UNIVERSITY OF OKLAHOMA

GRADUATE COLLEGE

OBSERVING SYSTEM SIMULATION EXPERIMENTS USING SMALL UNMANNED AERIAL VEHICLES IN VARIOUS CONFIGURATIONS TO IMPROVE HIGH-RESOLUTION FORECASTS OF CONVECTION

A THESIS
SUBMITTED TO THE GRADUATE FACULTY
in partial fulfillment of the requirements for the
Degree of
MASTER OF SCIENCE IN METEOROLOGY

BY

VIVEK SHENOY

NORMAN, OKLAHOMA
2021

OBSERVING SYSTEM SIMULATION EXPERIMENTS USING SMALL UNMANNED AERIAL VEHICLES IN VARIOUS CONFIGURATIONS TO IMPROVE HIGH-RESOLUTION FORECASTS OF CONVECTION

A THESIS APPROVED FOR THE
SCHOOL OF METEOROLOGY

BY THE COMMITTEE CONSISTING OF

Dr. Keith A. Brewster

Dr. Frederick H. Carr

Dr. Phillip Chilson

Acknowledgements

I wish to thank my advisors Dr. Keith Brewster, Dr. Frederick Carr, and Dr. Phillip Chilson for providing feedback on my thesis draft, as well as their constructive criticism that helped make this thesis the best it could be. I would especially like to extend my thanks to Dr. Keith Brewster and Andrew Moore for providing me with the resources, documentation, and code I needed to run the experiments. The work presented here wouldn't have been possible without the use of the University of Oklahoma's supercomputing resources.

The computing for this project was performed at the OU Supercomputing Center for Education & Research (OSCER) at the University of Oklahoma (OU) on Schooner. Thanks to the Director and System Administrators for providing this research tool. The verification and some of the post-processing were performed on the Center for Analysis and Prediction of storms research cluster (Stratus).

For previous work concerning use of unmanned aerial system vehicles in field site experiments, I would like to thank Dr. Phillip Chilson and Brian Greene for providing images, statistics, and descriptions of work done in this area of setup, deployment, and case studies for unmanned aerial vehicles.

Finally, I would like to extend special thanks to Dr. Keith Brewster and Dr. Frederick Carr for helping guide me through the research process when I encountered problems, and Andrew Moore for providing me with the files, documentation, and background concerning the research he conducted in 2018 that this work builds off of.

The research is supported by grants from the National Oceanic and Atmospheric Administration (NOAA) under the National Mesonet Program via the Cooperative Institute for Mesoscale Meteorology Studies (CIMMS, Part B), "Prototyping and Evaluating Key Network-of-Network Technologies", from the National Mesonet Program via Synoptics, Inc, "CASA DFW Testbed Operations and Data Impacts", and from a National Aeronautics and Space Administration (NASA) University Leadership Initiation (ULI) grant via Oklahoma State University.

Table of Contents

List of Tables

List of Figures

Abstract

There has been a lot of interest and development of small Unmanned Aerial Vehicles (sUAVs) to obtain atmospheric measurements for research and operations. Some have proposed a 3D Mesonet concept to add vertical profiling to mesonets such as the Oklahoma Mesonet. Observation System Simulation Experiments (OSSEs) are an effective tool to measure the impact of a proposed observing system before a complete set of observations are available, and thus are the ideal tool to study different configurations of sUAVs that may be deployed in such a 3D Mesonet.

In this OSSE study, a Nature Run is constructed using a short term 3 km and 1 km WRF nested model forecast covering Oklahoma and parts of surrounding states. Simulated sUAV profiles, as well as observations representing standard existing observations, are created from the WRF model forecast. The observations are then assimilated into the ARPS hourly for 6 hours. The case being examined is the May 20, 2013 severe weather outbreak in central and eastern Oklahoma. The sUAV system's ability to update the background forecast for conditions on May 20, focusing on convective initiation and early storm development in the afternoon, is assessed.

To examine the effect of adding simulated sUAV observations, experiments are run to test the impact of sUAV simulated observations at various max heights to 3 km. The number of simulated sUAV observations is also varied up to 108 sites. Additional experiments were run to test the impact of adjusting analysis parameters, changing the time interval of observations down to 30 minute intervals and adjusting the start time of the assimilation of data.

From the forecasts of convection in the OSSE experiments, we can clearly see positive impact from the addition of the sUAV observations in the convective initiation and early storm evolution. The quantitative impacts on the forecast state variables show clear positive dependence on the height of the sUAV data assimilated. There is also improvement in timing and placement of convection when the interval of consecutive UAV obs is reduced from hourly to every 30 minutes. However, there is not as much improvement in fitting the UAV sites to the average site density for 50 or fewer UAV sites, nor is there a clear linear relationship between delaying start times of consecutive hourly UAV obs and the areal coverage and placement of convective initiation. It is also found that decreasing the sUAV observation interval to 30 minutes from 1 hour while using 50 sites cannot replicate the results from using 108 sites.

Chapter 1. Introduction

a. Need for Additional Observations

Over time the resolution of operational numerical weather forecasting models has increased significantly. Previously when model grid spacing was 30 to 60 km, the number and density of conventional observations were sufficient. Now that the operational numerical models have increasing horizontal and vertical grid resolutions, there is a need for better spatial and temporal observations of mesoscale and storm-scale phenomena, especially in the lower boundary layer.

A National Research Council (NRC) committee concluded that a Network of Networks (NoN) is needed to address data gaps of mesoscale observations in the boundary layer (NRC, 2009). Integration of new observation systems into the architecture of a NoN is needed in addition to incorporation of existing observation systems. In additional to boundary layer deficiencies, gaps in observations in places such as mountains, coastlines and near urban areas should also be addressed.

The NoN architecture needs to provide a platform for both data providers and users to look up metadata, adjust standards of measurement, and enable operability between different systems. For example, a national database of metadata associated with each observation station should be accessible. A NoN also needs to give the user access to data, analysis tools, and models for utilizing these mesoscale observations (NRC, 2009).

The NRC recommendation for setting up a boundary layer profiling network for wind, temperature and moisture was approximately 400 sites in the continental United States. Instruments such as radiometers, interferometers, and wind and moisture lidars are very useful for continuous monitoring of diurnal boundary layer structure profiles in the lower troposphere. The spacing between the instrumentation sites should be approximately 125 kilometers but can acceptably range from 50 to 200 kilometers, depending on regional restrictions like terrain (NRC, 2009). These observations would supplement existing conventional observations such as surface METARs, rawindsondes, NEXRAD radars, satellite infrared and microwave soundings, atmospheric remote sensing via GPS radio occultation measurements, and aviation soundings taken by commercial aircraft. There has been more recent work demonstrating the utility of having more UAV observations in the boundary layer (NRC, 2018).

It is important for boundary layer measurements to be taken not only for the benefit of numerical weather prediction but for better understanding of the structure and evolution of convective storms. Crook (1996) shows that for two field experiments in northeastern Colorado for boundary layer forced convection, the vertical decrease in surface temperature and moisture with height in the boundary layer are both important factors in determining whether there is convective initiation or not. In this work it was also found that once convection has developed, the observational variability in moisture and its decrease with height in the boundary layer were the most important factors for determining the strength of the convection. However, at the horizontal boundary between convective storms and no convective storms, it is the observational variability in surface temperature and its decrease with height in the boundary layer that are most important for determining the strength of convection. In contrast, for specific measurements of convective

strength such as maximum vertical velocity, it was found that such measurements were most sensitive to surface potential temperature decrease with height in the boundary layer at the convective triggering boundary.

For rapidly developing convective weather phenomena, an Observation Simulation Experiment (OSE) study by Carlaw (2015) demonstrates that assimilation of non-conventional sources of weather observations such as temperature, dewpoint, wind and pressure data provided by weather provider Weatherbug can improve simulation of convective variables like low level vorticity and updraft speed and identification of tornado-like vortices (TLV) within the simulated supercell. Without the assimilation of non-conventional sources of weather observations (such as in the data denial experiments), no such TLV are present as quickly in the radar data as in the radar-observed storm. Due to the lack of sufficient spatial and temporal coverage of observations provided when using only non-conventional sources of weather observations, there is delayed formation of an intense TLV signature at the surface or no development of a TLV signature at the surface at all.

Work by Morris (2017) continued to examine the applications of non-conventional sources for better analysis and prediction of rapidly evolving convective phenomena such as mesocylones and associated severe weather, particularly hail. Counterintuitively, compared to just using conventional surface observation data, the addition of the non-conventional surface data from Citizen Weather Observation Program (CWOP) network and Earth Networks surface observations showed slight degradation of forecast temperature and dewpoint fields after 15 minutes into the forecast. However, incorporation of non-conventional CASA X-Band radial velocity data compared to just using conventional data from the Next-Generation Radar (NEXRAD) radar stations resulted in more accurate forecast supercell storm structure and forecasts of hail size (as confirmed by comparing model-derived hail characteristics to actual radar-observed hail). It is not known why the better forecast of surface temperature resulted from omission of non-conventional observations, but in this case there was a shallow layer of cold air in most of the domain whereas the storm was feeding off air from the southernmost part of the domain and just above the surface, so the effect on the surface temperature forecasts did not impact the hail forecasts. However, non-conventional sources can also be applied to convective setups where convection is not rooted in the boundary layer. Notably in the case study in Morris (2017), there was decoupling between the stable air at the surface and the unstable boundary layer aloft. Thus, addition of vertical profiles of temperature and moisture at the non-conventional observation stations might better resolve this paradox. Morris (2017) also addresses how non-conventional CASA X-Band radar can help sample missing low-level radial velocity data at smaller timer intervals, useful for analysis of rapidly developing surface based convective phenomena like mesocyclones and microbursts. Collection of temperature, moisture, and wind data by unmanned aerial vehicles (UAVs) at multiple levels can help identify such cases of elevated convection as well as identify any situation where frequent vertical sampling of the boundary layer is relevant.

It is important to not only study observations of temperature and moisture at specific levels but also look at how these observations vary with height in the boundary layer. Recall that in Crook (1996), the maximum vertical velocity was found to correlate better with the surface moisture decrease with height in the boundary layer than the surface temperature decrease with height in the boundary layer. This is relevant to the need for more accurate observations of both variables in the boundary layer, because the usual error (as computed using moist adiabats on a skew-T

diagram that are traced up from the surface to a higher level (e.g., 500 mb)) in surface moisture decrease with height in the boundary layer (1 g/kg) is 2.5 times greater than the usual error in surface potential temperature decrease with height in the boundary layer (1°C) – that is, a 1 g/kg error in moisture at the surface will result in just as much change of the 500 mb temperature as a 2°C error in temperature at the surface. As with Morris (2017), this indicates that gathering temperature and moisture data through more than just a few set levels of the boundary layer by UAVs will aid in better examination of storms and severe weather associated with the storms.

Weather observation data gaps for current and emerging aviation needs are present both in the lower boundary layer and upper troposphere (as well as in mountains, coastlines, and urban areas) according to the Lincoln Laboratories study for the FAA (Campbell, 2017). It noted that obtaining accurate and timely weather observations is one of the most significant factors in achieving good numerical weather prediction (NWP) performance. In addition to weather observations, numerical weather performance is affected by terrain, as well as other conditions like local cloud ceilings, visibility, and low level winds aloft. Outside of terrain effects, other naturally and artificially varying characteristics of the surface that affect evolution of the boundary layer are important. For example, the large spatial variability and characteristics of the urban canopy (i.e.: albedo, variation in building height) make forecasting in urban areas more complex than in less urban areas (NRC, 2012). This can be partially alleviated with use of urban canopy parametrization schemes in urban meteorology NWP models and airborne/spaceborne collection of urban land cover and thermal imaging data (NRC, 2012). Even outside of urban areas, collection of in situ measurements in the boundary layer by UAV for a more spatially dense layout of observing stations can help better capture missing data at finer spatial resolution and aid in examination of air-water-land coupled interactions and energy exchanges, which affect the initiation and development of convection (Chilson et al., 2019).

b. Potential for UAVs to Address Gaps

To help with the effort of creating a NoN for higher quality observing networks, more dense observation profiles in the lower boundary layer and assimilation of data from non-conventional airborne sources such as UAV platforms are needed (Chilson et al., 2019). Over the past few years, a number of different UAV designs have been tested. It is important to examine these to determine which designs are best suited to reduce observation error and take into account environmental effects that may skew the data (e.g., contamination of temperature data by direct solar radiation exposure, effects of turbulence on wind speed and direction data). For example, it was found that because of need for efficient aspiration of sensors, thermistors with ducted fans in the front of the body of the UAV are best for minimizing these effects (Greene et al., 2019).

Key design questions for a UAV network besides the design of the UAV platform include the maximum flight altitude, the spatial density of mesonet sites from which UAV are launched, and the time interval between collection of new UAV observations. In this study, the maximum height in which the UAV is able to operate is tested for altitudes from 122 m (400 ft, which is the current FAA legal operating limit for sUAV) to 3 km (which currently can be done legally in the US with Certificate of Waiver of Authorization, COA, from the FAA), the spatial density of stations from which UAV are launched ranges from 10 to 108 stations (Chilson et al., 2019), and timing between new observations ranges from every 15 minutes to 1 hour (Moore, 2018). The ideal range of these values is determined by observing system simulation experiments (OSSEs).

c. OSSEs

We can examine characteristics and potential benefits of the observing systems before they are widely deployed using OSSEs. An OSSE is an observing system simulation experiment where a model is used to represent the behavior of a physical system (here, the atmosphere) of interest. With the model results generated from a high-resolution model (Nature Run – see below), the results are then sampled so that they resemble a real or hypothetical observing system. These simulated observations are then inserted into a different model for the same time period to assess their relative value in reproducing the Nature Run results. This is an effective and inexpensive way to examine the design of newly implemented or enhanced observation networks or to provide a measure of how useful existing observation networks are. A look at the generic layout of an OSSE for Center of Analysis and Prediction of Storms (CAPs) at OU is provided in the figure below.

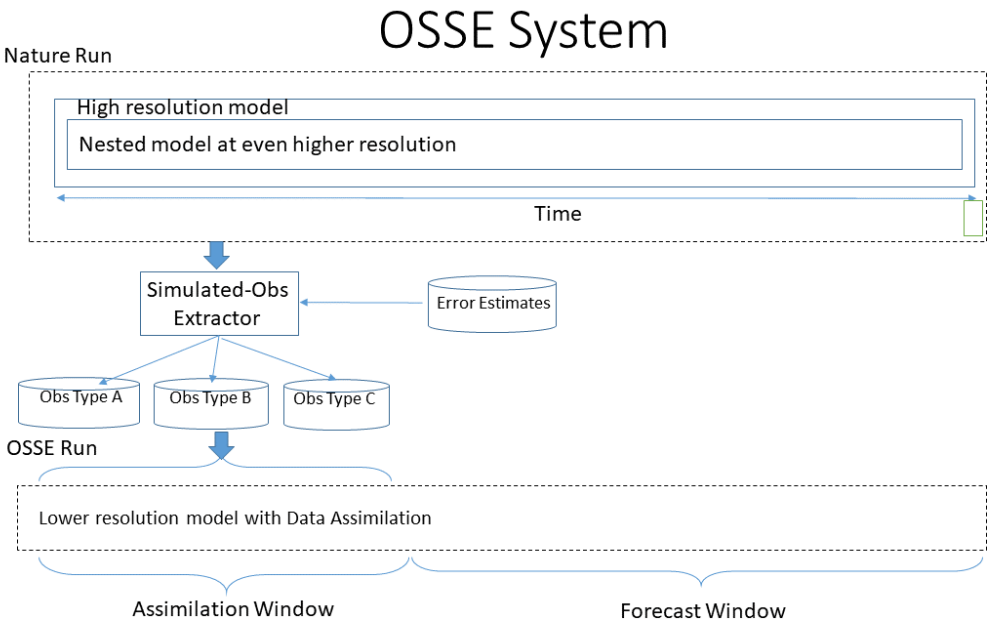

Figure 1. Layout of OSSE. Simulated observations in the Nature Run in the assimilation window are plugged into the lower resolution data assimilation/experimental model. This provides a quantitative measure of what the impacts of adding new proposed observation systems will be. The variables in these observations from the assimilation window in the Nature Run are then run in the Data Assimilation model to examine how they evolve during the following forecast window time period.

The four basic steps in the CAPS OSSE system are: 1) creation of the Nature Run (a high resolution NWP forecast that is intended to be a close depiction of the actual convective event), 2) creation of simulated observations by extracting data from the Nature Run and applying expected errors to those data, 3) assimilation of the created simulated observations into a second model (assimilation/experimental system), and 4) comparison of the forecast from the experimental system compared to the Nature Run. The goal of the OSSE is to test the impact and potential configurations of simulated observation data on the forecast. This is done by measuring how close

the forecast model with the simulated data gets to the Nature Run, compared to the system run without assimilation of simulated observation data.

With the use of simulated observations, OSSEs should simulate types of errors that are present in the real world such as representativeness, instrumental, calibration, random, and systematic errors. Instrumental error is due to in-built limits to precision in instruments designed to measure specific variables, such that the measured value of the variable is only an approximation of the actual value. Calibration errors occur because the accuracy of the instrument differs from a known, accepted calibration standard for that instrument. Random errors do not have a defined cause and can arise from natural fluctuations in data but nevertheless cause measured values to deviate from actual values. Systematic errors can arise because of introduced error from imperfect methods of observation or environmental effects interfering with measurements. Representativeness error accounts for the differences between what is measured by actual observations and what is present in the model simulations of these observations.

Representativeness errors stem from real world phenomena that are not represented correctly or are not accounted for at all in the forecast model, typically for phenomena occurring at smaller scales than those resolved by the model such as: wind gusts and turbulence, features in clouds, topography, sea surface temperature (SST), irregular and surface features at spatial scales smaller than the grid spacing, and changes in vegetation and soil moisture with time. Errors are assigned to the data based on expectations of representiativeness and instrument errors. When the Nature Run representativeness errors are reduced (so that the point measurement is more representative of the grid point in the model grid box), the simulated observations then plugged into the assimilating (or experimental) model run can provide a better quantitative measure of the effects of adding the predicted simulated observation systems as opposed to just using conventional observations alone. With decreased representativeness errors in the Nature Run, a better understanding of the accuracies of the analysis and forecast products that incorporate the new data is obtained (Hoffman & Atlas, 2016).

There has been work done in conducting OSSEs to better understand how additional simulated observations can capture data at a finer spatial and temporal scale than is otherwise missed by more conventional data sources. This work has been conducted since the late 1960s and 1970s (Atlas, 2017). Back then, OSSEs were performed to help design the observing systems needed for obtaining data from the Global Atmospheric Research Program (GARP) and included analysis of: the range of predictability for observations, needs for reference level data, and importance of asynoptic versus synoptic data assimilation. However, there were many limitations in these early OSSEs that precluded more extensive OSSEs from being undertaken. These limitations included generally using the same model for the Nature Run and the Assimilating Forecast (referred to as the identical twin problem), model dependence of results, and how the early OSSEs treated observational errors as random and uncorrelated (neglecting that in some observing systems, such as satellite, correlated observation errors are common) (Atlas, 2017). By the 1980s, these limitations had been mainly overcome and more extensive OSSEs have been conducted since then. However, most of the work in conducting OSSEs were considering space borne observation systems as the planned observation method of choice rather than other possible observation sources like mobile or stationary shorter-wavelength radars and mobile weather observation devices (e.g.: sensors in smartphone apps to measure temperature, pressure and wind, UAV). Thus, many of the

other proposed observing systems have been satellite radiance or satellite borne lidar systems. Satellite OSSEs are utilized for the purpose of testing the results of deploying new satellite observing systems for uses such as weather and climate prediction. In these tests, the possibilities of improving coverage and accuracy of weather observations collected from space were studied. These tests were useful in improving simulations examining how for example, the incorporation of satellite surface winds would improve NWP models. It is important to note that assimilation of microwave and infrared radiances from the space borne sources like the Global Navigation Satellite System/Radio Occultation (GNSS/RO) have been most responsible for improved forecast skill in OSSEs seen in recent years (Hoffman & Atlas, 2016). However, more recently, aircraft and UAVs have been deployed in OSEs and OSSEs to test how collection of more observations at finer horizontal and vertical scale (compared to conventional observations from weather stations on the ground) could improve analyses and forecasts of convective weather setups. As such, UAV are just one of the potentially new observing systems that can collect data which can be simulated in OSSEs. A more recent review of OSSEs is provided in a 2020 edition of *BAMS* (Zeng et al, 2020).

Simulating the results of assimilating observations from additional planned unconventional sources of weather data is useful in high resolution convection permitting models such as the Weather Research and Forecasting (WRF) and Advanced Regional Prediction System (ARPS) models at grid spacing less than 4 km, because at these smaller scales, the NWP models can better resolve mesoscale sized regional precipitation and temperature changes (and the smaller-scale topographical and lifting features that can induce these changes) than coarser weather models such as General Circulation Models (Li et al., 2019). The assimilation of observations in OSSEs at a finer spatial scale is also useful because in convection permitting models, they can allow for better representation of smaller-scale shorter-lived convective features like tornadoes and microbursts (Xue et al., 2006).

Work by Andrew Moore (2018) demonstrated via OSSEs how the addition of data collected by small UAV from the lower boundary layer (400 feet to 3 km above ground level (AGL)) assisted in better representation of lower boundary layer structure and more comparable results to the boundary layer data in the Nature Run. Specifically, within the initial 1 to 3 hour timeframe, the boundary layer temperature, moisture, and varying dimensions (i.e.: height of the boundary layer versus the layer encompassing the transition to the free atmosphere), as well as the timing of convective initiation in the assimilated runs of UAV data, were more similar to the Nature Run than the runs without the assimilated UAV data or no data cases. However, the resolution of observation data (especially on smaller scales), UAV observation station data layout and density, and sensitivities of convective initiation and maintenance of convection after initiation to boundary layer moisture are some factors that precluded runs with assimilation of UAV data from exactly matching the data in the Nature Run. This was the case even when the number of UAV observation stations and the spatial density of the stations were increased to 108 sites and 3 km maximum height of observations. This suggests that there is additional work that needs to be done in correcting for sensitivities of observation data to boundary layer moisture, particularly as OSSEs involving convective initiation cases are performed at higher resolutions and at smaller spatial and temporal scales. To this end, we plan to do experiments altering the timing and maximum height of UAV observations, as well as altering the number of UAV observations at a height in the

boundary layer. These experiments will be done to find the best combination that produces reflectivity, wind and moisture fields that best match the Nature Run.
To help with the effort of creating a NoN for higher quality observations in the lower boundary layer, assimilation of UAV data is needed. The maximum altitude, number and spatial density of mesonet stations from which UAVs are launched, and time interval between which new observations are collected by UAV are important to consider when gathering additional observations from the boundary layer via UAV. It is also important to examine the differences between UAV Design to best figure out which UAV designs are best to use to reduce observation error and take into account environmental effects that may skew the data (e.g., contamination of temperature data by direct solar radiation exposure, effects of turbulence on wind speed and direction data).

Work by Moore focused on varying maximum height at which observations were taken at mesonet sites by UAV. However, that work did not examine the effect of varying the frequency of the observations, nor did it examine more closely the lowest level of the boundary layer (around and below and below 1 km above ground level (AGL)) when varying the number of such UAV observations at that level. This paper aims to study the effects of varying the frequency of UAV observations (i.e.: how results change when observations are taken every 30 minutes, 2 hours, or 3 hours compared to every hour), examining the effect of changing the number of UAV mesonet sites (ranging from 10 to 108), and determining how changing the interval period and start of data collection affect results.

Chapter 2. Small UAV

It is important to describe the UAV setup that is envisioned for the OSSE testing. There are generally two types of small UAV being tested for making atmospheric measurements: fixed-wing aircraft and rotary (CopterSonde) aircraft.

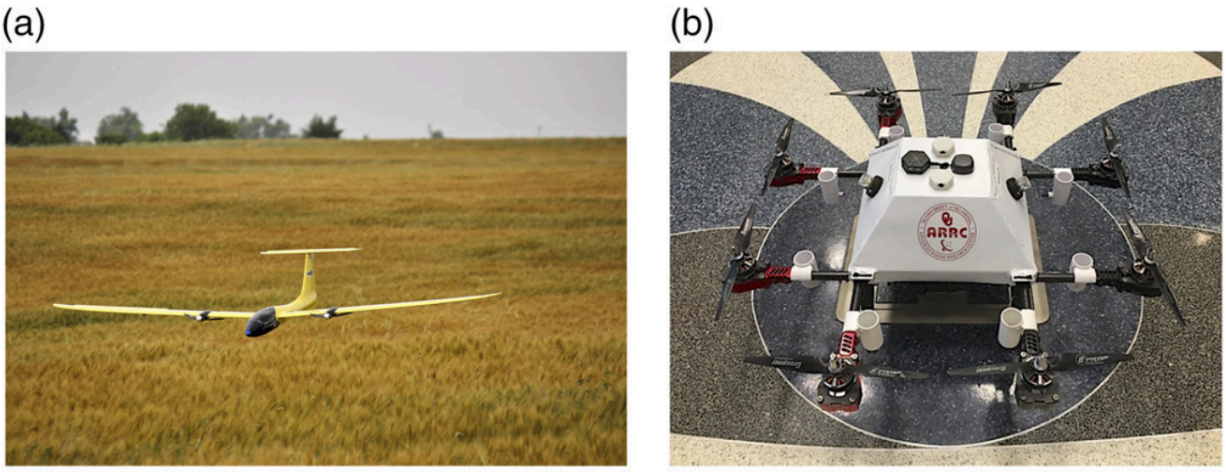

Figure 2. Fixed-wing aircraft (left, a)) and early version of OU CopterSonde Rotary-wing aircraft (right, b)) from Fig. 2. in Koch et al., (2018).

There are advantages and disadvantages among different UAV design and sensor configurations. Fixed-wing UAV aircraft have a more aerodynamically efficient design than rotary UAV and thus are more suited for carrying heavier equipment payload longer distances (Ackerman & Koziol, 2019). This means that fixed-wing UAV are potentially better for conducting flights where there needs to be a lot of instrumentation onboard. However, unlike rotary-wing UAV, fixed-wing UAV require a runway or catapult mechanism to launch, which precludes them from being used in settings with little open space free of obstacles or topographically hilly, forested areas (as are found in many parts of the mid-latitudes). Such launchings and landings generally also require active human participation and thus cannot be fully automated.

Among rotary-wing aircraft, there are two main design categories that have been tested by groups such as the National Severe Storms Laboratory, the National Weather Service, National Oceanic and Atmospheric Administration (NOAA), University of Oklahoma, University of Kentucky, University of Nebraska, DOE Atmospheric Radiation Monitoring (ARM) Southern Great Plains (SGP), and Choctaw Nation FAA UAV Integration Pilot Program (IPP) site : a forward facing (FF) design (with the ducted fan with sensors on the front of the body of the CopterSonde) and an arm propeller (AP) design (with sensors underneath the propellers of the CopterSonde). Greene et al., 2019 show that for UAV, a FF design is more effective than an AP design at reducing errors in wind measurements and reducing errors from solar radiation effects when measuring temperature. The effect of UAV design on wind measurements is important because orientation of rotary-wing UAV relative to the ambient wind can bias wind measurements. Regarding only temperature measurement precision however, it is still important to consider the types of rotary-wing design. For example, compared to the FF design, the AP design configuration is more effective in minimizing heating effects from the motor and from frictional heating at the propeller

tips. Still, because of the minimization of the solar radiation effects, minimization of torque effects on temperature measurements, and horizontal drawing of air in the FF design (as opposed to vertical ingestion of air from the propellers in the AP design, which can be problematic in stably stratified environments), thermistors attached to UAV had higher accuracy and precision for atmospheric measurements in the FF configuration than the AP configuration at a statistically significant level (Greene et al., 2019). Overall, an FF design of the UAV was thus found to be more desirable than an AP design. This is because of the drawbacks of the heavier ducted fan in the FF design on flight time of the rotary-wing UAV were less severe than expected for the current version of the OU CopterSonde UAV (see Figure 3) and were outweighed by the benefits of the ducted fan being more shielded from the effects of solar radiation in the FF design. For rotary-wing UAV in the FF configuration, future research is still needed to more closely examine if temperature measurements can be affected by heat from the main body of the aircraft (when the aircraft is not directly facing the wind), as well as determining the amount by which the presence of the rotary-wing UAV aircraft alters the vertical structure of the boundary layer environment around it.

Figure 3. Most recent (2019) version of rotary-wing OU Coptersonde, courtesy Brian Greene. The most apparent differences between the design of this most recent version and the version of the OU Coptersonde in Figure 2 is the more rectangular shaped, boxed body of the aircraft and more defined nose cone for drawing in air in the most recent version of the OU Coptersonde.

Collection of in situ boundary layer measurements by WxUAS coptersondes in a more spatially dense layout of observing stations can help better capture missing data at finer spatial-scale and aid in examination of air-water-land coupled interactions and energy exchanges that influence initiation and development of convection (Chilson et al., 2019). Better examination of air-water-land coupled interactions is helpful in better simulation of coupled OSSEs where information is drawn from various component models of the boundary layer, water cycle, and terrain effects. For a 3D Mesonet NoN to be set up that incorporates data from UAV, there are software and regulatory obstacles that need to be addressed before a 3D Mesonet network can be established. Additional applications and issues related to UAV sensing of the atmosphere are addressed in McFarquhar et al., 2020.

The CopterSonde can measure variables such as temperature, relative humidity, pressure, wind speed, and wind direction. The estimated errors that are being applied to the measurements to create the simulated observations are as stated in Table 1. in Chilson et al., 2019 The desired accuracy of temperature measurements are accurate within 0.2 degrees Celsius, desired accuracy of relative humidity measurements are accurate within 5.0%, desired accuracy of pressure measurements are accurate within 1.0 hPa, desired accuracy of wind speed measurements are accurate within 0.5 m/s, and desired measurements of wind direction measurements are accurate within 5 degrees azimuth (Chilson et al., 2019). The response time of the sensors on the CopterSonde to changing weather conditions is less than 5 seconds, although the preferred response time is ideally less than 1 second (Chilson et al., 2019). Response time of instruments from the UAV can vary depending on factors like metal type, ventilation, and design of the instruments, as well as the ascent rate of the CoperSonde (with standard ascent rate being 3 m/s, compared to typical 5 m/s ascent rate of other instrumentation like weather balloons used in rawinsonde observations). At a 3 m/s ascent rate, UAV observations are taken every 10 to 20 meters, with the UAV taking about 15 minutes to reach a height of 3 km after being launched from the ground. The faster the ascent rate of the UAV, the more lag there is in reporting variables at the various heights such as temperature and dewpoint, which can introduce error. However, a slower ascent rate, while helpful for reducing lag, increases the time it takes for the UAV to reach a certain height, which is not as good for obtaining near instantaneous observations with the UAV. All of this is applicable even in fair weather conditions without convection. Various intercomparison studies for studying the capabilities of different designs of remotely piloted UAV in fair weather conditions have been conducted. For example, the Lower Atmospheric Profiling Studies at Elevation - A Remotely-Piloted Aircraft Team Experiment (LAPSE-RATE, Barbieri, et al., 2019 and de Boer et al., 2020) was conducted in Colorado in July 2018.

The conditions in which the UAV operates are important to consider to assure adequate control of the UAV in data collection. Testing of a particular model of the UAV (the WxUAS, where UAS means Unmanned Aerial System) has shown that WxUAS is resilient in operating conditions such as: where the temperature ranges from -25°C to 30°C, wind speeds up to 25 m/s, altitudes up to 10,000 ft (3050 m) above sea level, and within clouds where relative humidity is close to or exceeds 100% (Chilson et al., 2019). The above are the following conditions required for assuring adequate control of WxUAS in data collection. The ability of the WxUAS to operate at high altitudes and within clouds is relevant to the capability of the WxUAS to remain airborne and maintain control for conditions of in-cloud air turbulence, high relative humidity, condensation, and icing (Chilson et al., 2019). This ability to withstand such conditions is needed in order for the WxUAS to capture timely observations aloft and for an extended period of time (1 to 2 hours) at regular intervals. However, the issue of the UAV being obscured by clouds (as per visual observation rules required by the FAA) is an issue that poses problems for operating UAV during overcast conditions or conditions with low cloud ceilings. This can hinder more extensive UAV missions during such conditions. Additionally, the ability to visually track the UAV from the ground is important because, by FAA rule, observation taking is halted once the UAV enters a cloud, even if the UAV has not reached the maximum planned height. Climatologically, clouds are not as impactful in impeding UAV operations in the western part of Oklahoma as in the eastern part of Oklahoma during all seasons, however UAV sites are located not just in part of Oklahoma but all across Oklahoma (i.e.: western, central, eastern) (Jacobs et al., 2020). This study will focus on the preconvective conditions leading up to convective initiation. Focusing on this time period

will alleviate some of these concerns since there are few clouds compared to after storms develop. By the time storms develop, there is development of widespread dense overcast associated with the storms and operation of UAV in/near active storms would pose issues with following and controlling the UAV.

Chapter 3. Experiment Design

In order to build off previous work done with OSSEs involving studies of initiation and propagation of convection, more OSSE experiments need to be performed where the UAV sample the lower boundary layer. There is an optimal maximum flight level height at which sampling of the boundary layer observations is most effective for predicting the structure and evolution of boundary layer moisture fields, as described in Moore (2018). From Moore (2018), it is clear that most of the improvement in depicting boundary layer moisture structure and magnitude of moisture (as measured using water vapor mixing ratio values) occurred when going from using UAV observations at a height of 400 feet AGL to using UAV observations at a height of 1 km AGL. However, in sample runs of the reflectivity and wind fields for simulated UAV observations at heights 400 ft, 1 km, 2 km, and 3 km AGL for 108 stations, it is found here that the structure and evolution of the reflectivity and wind field were most comparable with actual results for the experiments with the setup of simulated UAV observations at 2 km AGL with 108 stations. This is the motivation for conducting more OSSEs with simulated observations at 2 km than at other max heights, when the amount of simulated observation stations at 2 km is varied from 10 to 108. However, experiments will still be done for other max heights of the boundary layer (400 ft, 1 km and 3 km) but with the amount of observations in these OSSEs fixed at 108 since the assimilation of observations from max heights other than 1 km were found in Moore's work to be less impactful in depicting improvements to boundary layer moisture structure and magnitude of moisture values. While the only experiments varying the number of simulated UAV observations will be the experiments for simulated UAV observations at 2 km, the assimilation of simulated UAV observations in any experiment will still be performed for the purpose of seeing how that experiment generates the reflectivity and wind field showing the convective initiation and convective morphology of storms (as compared to actual observations of the reflectivity and wind field in the Nature Run).

By carrying out the proposed experiments, it will be seen which specific combination of the height and number of simulated UAV observations generate results that best match up with results from the Nature Run for the supercell event that unfolded in central Oklahoma and the Mid Mississippi Valley (see associated storm reports for this event in Figure 4). By finding the optimal combination of max height and number of simulated UAV observations, the results from this study can be compared with results from other OSSE studies looking at other convective events that have occurred in the Southern Great Plains and Mid Mississippi Valley region of the United States, in order to inform the design of a 3D Mesonet.

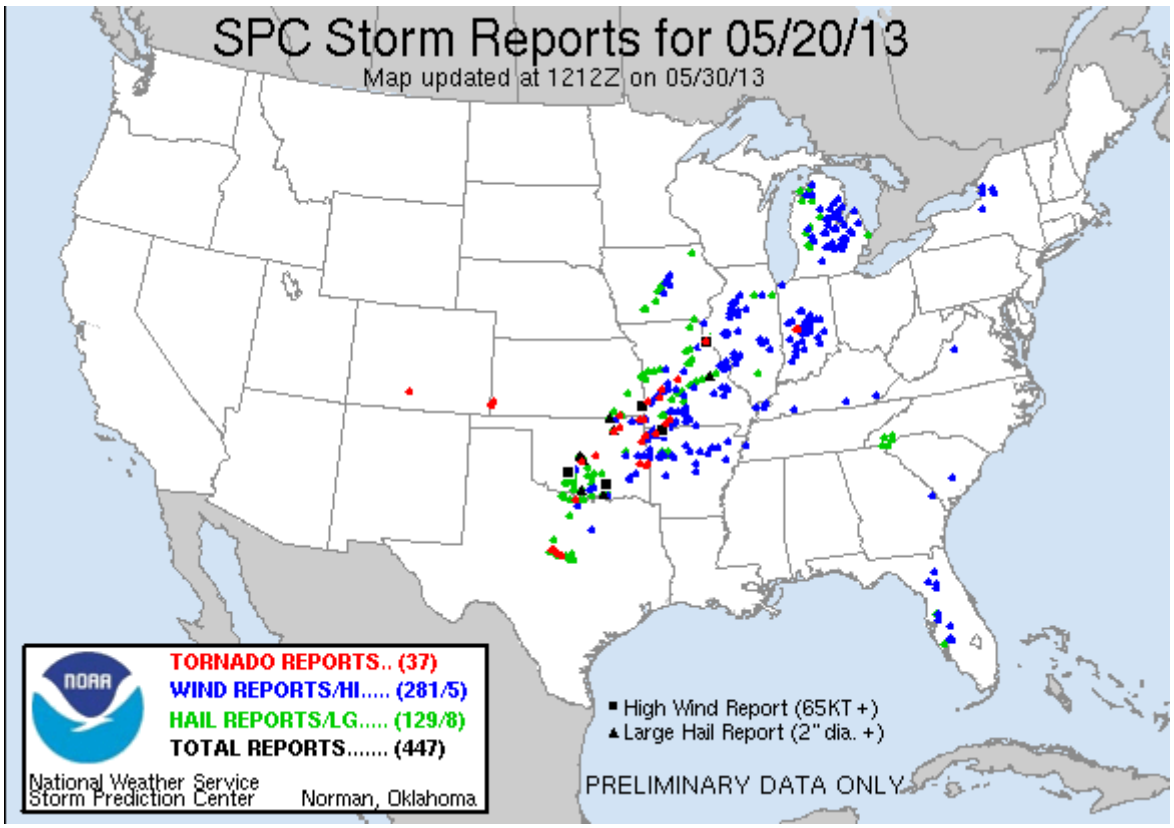

Figure 4. Map of storm reports (tornadoes in red, wind damage in blue, hail in green) from the National Weather Service Storm Prediction Center (SPC) for the May 20, 2013 supercell event that unfolded across the Southern Great Plains and Mid Mississippi Valley.

a. Planned Experiments

Table 1 shows the experiments that are conducted in this study. The first set of experiments used UAV observations at 108 mesonet sites for max heights at 400 ft, 1 km, 2 km, and 3 km AGL. The table also shows proposed tests where the number of stations is varied from 108 to 10 for UAV obs from a max height of 2 km AGL, tests of fitting the data to the average station spacing for 10, 25, and 50 stations when UAV obs from a max height of 2 km are used, tests of varying the interval time (between 3 hours, 2 hours, and 30 minutes instead of 1 hour) for a fixed number of stations (108) for UAV obs from a max height of 2 km, tests varying the start time of hourly UAV obs from a max height of 2 km (i.e.: start time at 1500 UTC and 1700 UTC instead of at 1200 UTC), and finally tests of what occurs in terms of environmental setup prior to convective initiation, the timing of convective initiation, and placement and coverage of storms along the dryline when reducing the number of stations (from 108 to 50) for 30 minute increment UAV obs from a max height of 2 km.

Unlike in previous work, the obs from max height AGL from which simulated UAV observations showed most improvement in convective initiation and storm structure position and motion in comparison to the Nature Run were simulated observations from a max height of 2 km, not a max height of 1 km as was found in work by Moore. So further examination of simulated observations at this height were examined by varying the number of simulated observations at 2 km from a maximum of 108 observations to a minimum of 10 observations, with an intermediate amount of observations (75, 50, and 25) in between, similar to the experiments varying the number of observations from 108 to 10 that Moore performed for simulated observations at 1 km. However, experiments for simulated observations at 400 ft AGL, 1 km AGL, and 3 km AGL were still performed, but with a fixed number of simulated UAV observations (108), because of how experiments at these heights yielded less similar convective initiation and storm structure position and motion than the UAV 2 km experiment when compared to the Nature Run.

Table of Planned Experiments
Tests of Maximum UAV Profile Height
3 km ARPS with IAU

Purpose	Name	FNL	Meso	UAV Height	UAV Sites	Interval Start Time
Baseline No Obs	No Obs					
Mesonet	Meso Only		X			Hourly 12 UTC
FNL	FNL Only	X				"
Baseline	NoUAV	X	X			"
Max Profile Hgt	FMU400ft108	X	X	400 ft	108	"
	FMU01km108	X	X	1 km	108	"
	FMU02km108	X	X	2 km	108	"
	FMU03km108	X	X	3 km	108	"
Station Density	FMU02km10	X	X	2 km	10	"
	FMU02km025	X	X	2 km	25	"
	FMU02km050	X	X	2 km	50	"
	FMU02km075	X	X	2 km	75	"
Density Fitted	FMU02km010f	X	X	2 km	10	"
	FMU02km025f	X	X	2 km	25	"
	FMU02km050f	X	X	2 km	50	"
Time Interval	FMU02km108a	X	X	2 km	108	3 hour
	FMU02km108b	X	X	2 km	108	2 hour
	FMU02km108c	X	X	2 km	108	30 min
	FMU02km050c	X	X	2 km	50	30 min
Start Time	FMU02km108d	X	X	2 km	108	1 h/15 UTC
	FMU02km108e	X	X	2 km	108	1 h/17 UTC

Table 1. Table of Planned Experiments for the study in this paper.

There's a cost associated with a more frequent time interval of observations, and there is a cost associated with having more UAV observation sites. That is why for the time interval experiments, experiments with observations taken every 30 minutes are tested for the full 108 sites and only 50 sites. The hypothesis being tested is whether it is acceptable to use fewer UAV sites (50 instead of 108; FMU02km50c versus FMU02km108c) when the time interval of UAV observations more frequent than every hour. If this is the case, it may be more advantageous to deploy the fewer 50

UAV sites if there is a more frequent time interval at which UAV observations are taken. Due to the time it takes a UAV to be recharged, the 30 minute sampling interval assumes each site has 2 UAVs in case one UAV is still being charged and cannot be immediately deployed (Meteomatics, 2020).

Before a map of the UAV sites is depicted, it is helpful to see maps naming the counties in the northern part of Texas and southwest Oklahoma where features such as convection, source advection of warmer temperatures, and the location of the dryline will be found.

Figure 5 shows the map of counties and their names in the northern part of Texas and Figure 6 shows the map of counties and their names in Oklahoma.

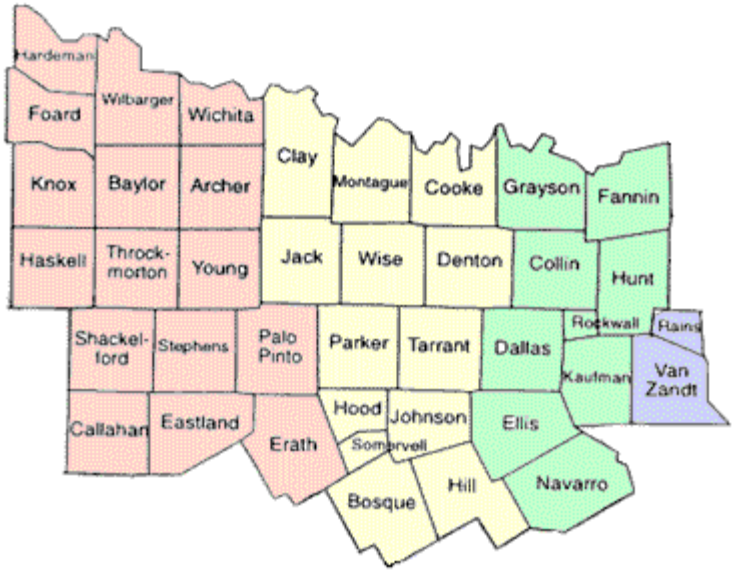

Figure 5. Map of showing location and name of counties in north central Texas courtesy https://www.sutori.com/item/north-central-plains-map.

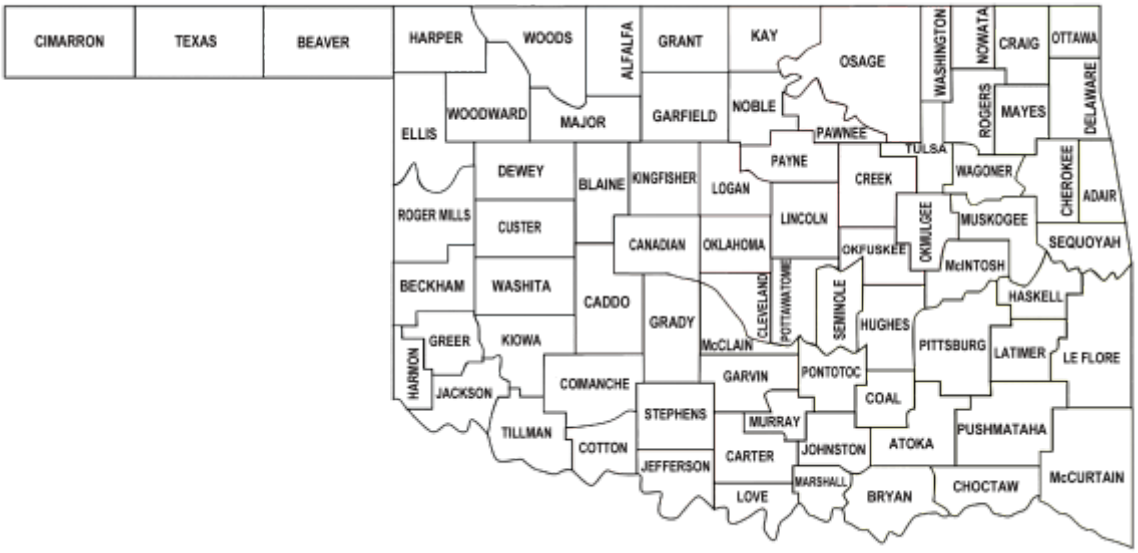

Figure 6. Map showing location and name of counties (bolded black text) in Oklahoma from Oklahoma State Auditor and Inspector website https://www.sai.ok.gov/images/okcountymap.png

These 108 mesonet stations will be situated across Oklahoma in the same layout and density as the 110 stations tested in Moore's work (Figure 7). Two stations out of the original 110 were omitted for the experiments done in this study: Hooker (HOOK) and Boise City (BOIS), both in the Oklahoma panhandle.

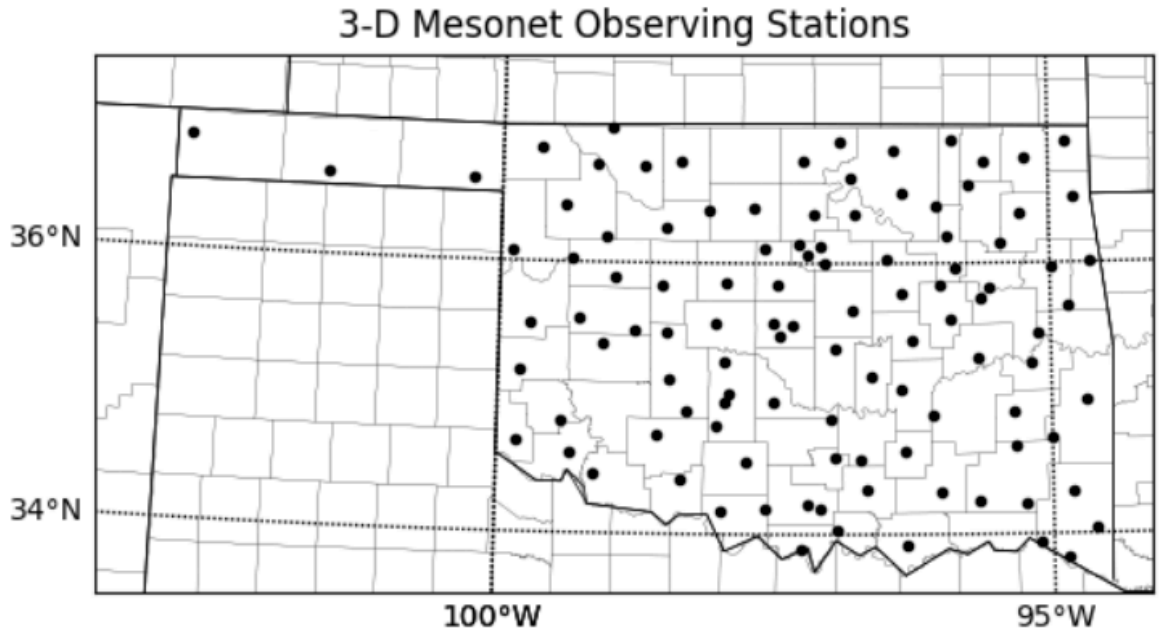

Figure 7. From Moore (2018), map outlaying locations of maximum number of mesonet stations used in the UAV OSSE experiments.

The layout of stations for 10, 25, 50, and 75 stations will be following Moore's work, where sites near major population centers and airports were eliminated and randomly thinned. This configuration for 10, 25, 50 and 75 stations is shown below.

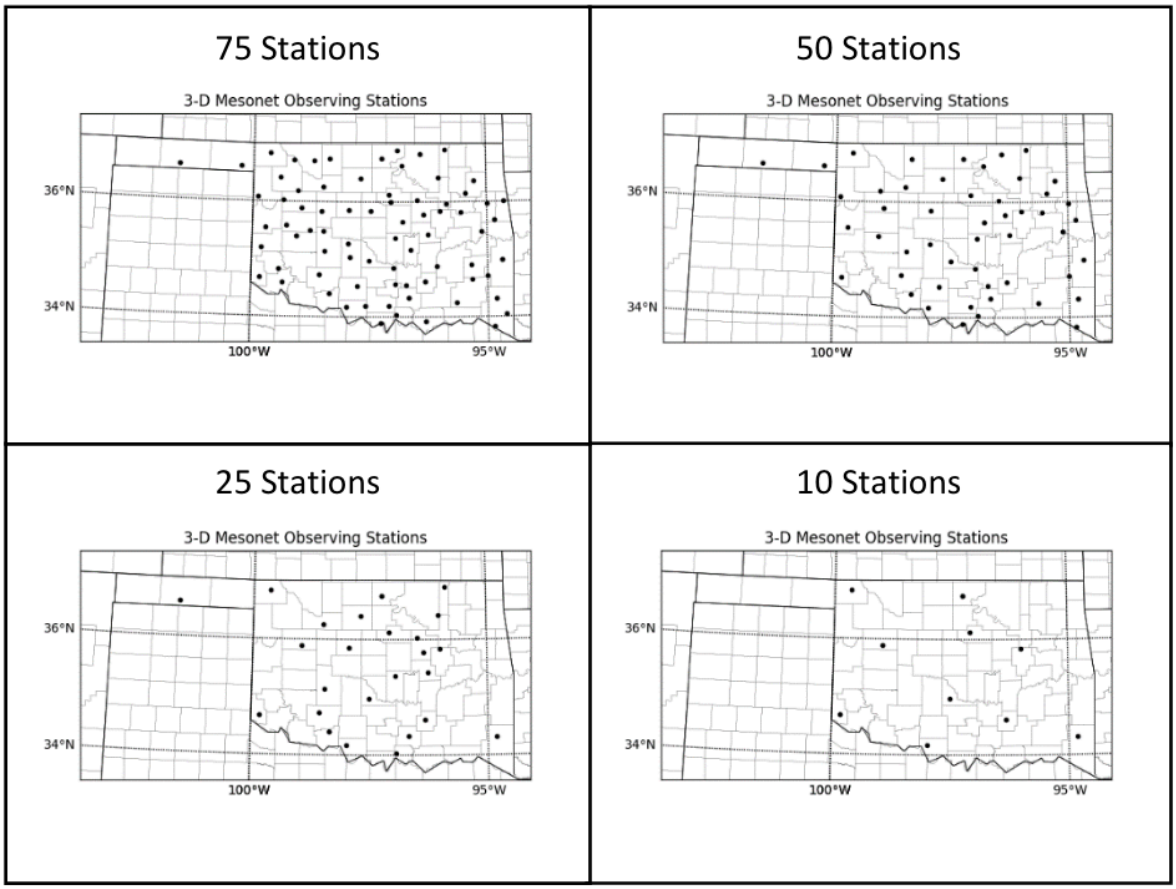

Figure 8. From Moore (2018), diagrams of mesonet station layout and density across Oklahoma for intermediate test cases where UAV observations from (clockwise moving from top-left): 75, 50, 10, and 25 mesonet stations are used.

b. ARPS with IAU OSSE System

A flowchart diagram of the ARPS with IAU OSSE System utilized here is shown in Figure 9. The Nature Run observations will be from the WRF model (nested at 1 km maximum resolution) instead of the ARPS model as was done by work in Moore (2018). The assimilating/experimental model will then be run using ARPS at 3 km resolution and will use the ARPS Data Analysis System (ADAS) to generate the analysis field of meteorological variables (e.g.: 2-m temperature, 2-m dewpoint temperature, 10-m wind speed and wind direction, water vapor specific humidity) and Incremental Analysis Updating (IAU) will apply the increments in an assimilation window in the ARPS model instead of using a cold start from the analysis fields every hour (which would introduce extra noise). Creation of simulated UAV vertical profiles at each mesonet site up to 3 km AGL of meteorological variables like temperature, moisture, and wind will be performed using the Nature Run output. This interpolation is done linearly in height above the ground for the first and following UAV observation levels.

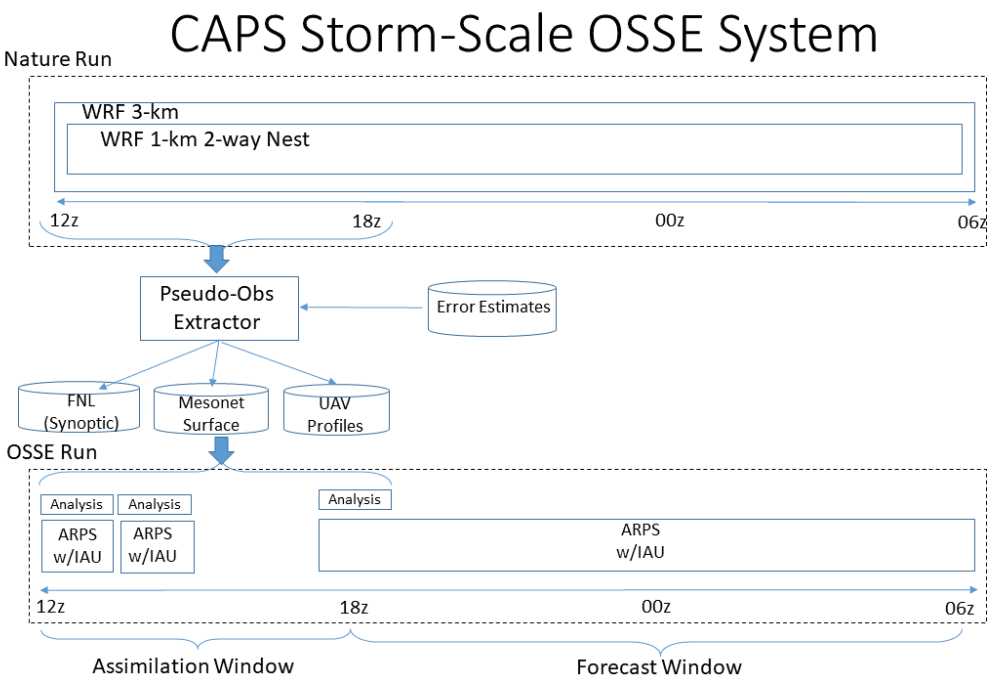

Figure 9. Flowchart diagram of the CAPS Storm-Scale OSSE System. Observations from the WRF 3 km (1 km nesting) Nature Run from 5/20 12 UTC to 5/20 18 UTC are input into the pseudo-obs extractor, which is used in creation of FNL, Mesonet and UAV observations. These observations are then assimilated in the Advanced Regional Prediction System (ARPS) with Incremental Analysis Updating (IAU) in the 12-18 UTC assimilation window to generate experimental forecasts for the period 5/20 18 UTC to 5/21 06 UTC.

Three observation types (FNL, Mesonet, and UAV) are used. The FNL data consisted of 3-hourly observations (here taken at 12 UTC, 15 UTC, and 18 UTC on May 20) and at 1 degree latitude by longitude resolution. The FNL observations are pseudo-obs representing operational synoptic/mesoscale alpha data such as the numerous operational data sets that go into the GFS FNL. FNL observations are from the GFS final analysis, and are needed because they represent all of the current observing systems, and OSSE experiments need to be compared to all the current

observing systems. With use of FNL observations, all the data from current observing systems is assimilated, which saves time and reduces complexity of code since assimilation of each individual current observing system doesn't need to be coded and run. The mesonet observations are used hourly during the assimilation window (nominally from 12 UTC to 18 UTC May 20), and the UAV observations are used every hour in the assimilation window for the initial set of experiments. Note that the start time interval of the forecast analysis and interval of consecutive UAV observations will be varied in later experiments to test the effect that this has on the resulting evolution of the reflectivity/wind and boundary layer moisture and vertical motion fields.

As was stated earlier, the Nature Run uses the WRF model and the forecast uses the ARPS model. For the work done by Moore (2018), the Nature Run used ARPS and the forecast model used WRF with hourly cycled analyses, and doing so meant that a cold start was done every hour that introduced model noise. This model noise was apparent in spurious convection across northern Texas and northeastern Oklahoma into southwestern Missouri, as well as excess area and coverage of convection in northern Texas, which acted to cut off inflow to developing storms in central Oklahoma. By using ARPS for the forecast model, IAU can be utilized. This approach gradually introduces the observational increments into the forecast model which reduces the high frequency noise introduced into the forecast model, which means less interference of spurious convection with factors such as storm inflow, outflow boundaries and less unneeded boundary layer overturning. These effects from spurious convection can affect the timing of initiation, position, intensity and motion of storms in west-central and central Oklahoma which are of key interest in this study.

The analysis procedure involves both the ARPS Data Assimilation System (ADAS) technique and the IAU, where ADAS creates the analysis increments that are then assimilated into ARPS using IAU. The ADAS technique incorporates data from sources ranging from surface observations like automated surface observing systems (ASOS) and Oklahoma mesonet observations, rawinsonde observations and profiler data, radar radial velocity and reflectivity, and radar retrieval output consisting of vertical profiles of wind, temperature, pressure, humidity, and rainwater (Brewster, 1996).

ADAS uses a type of successive correction scheme referred to as the Bratseth method (Bratseth, 1985). The ADAS technique is very well suited for in-situ data used in OSSE experiments such as this, which is another reason why it was chosen over other techniques like the ARPS 3DVar technique.

An advantage of the Bratseth scheme over other schemes like the Cressman scheme is that the relative error between the background field and the relative error between each observation source can be accounted for much as in a Statistical Optimal Interpolation (OI) scheme, and mathematically converges to Statistical OI (Bratseth, 1985).

The horizontal correlation distance is affected by separation not only in the horizontal (modeled as a Gaussian function of the ratio of displacement between two locations to the the horizontal correlation distance factor) but the vertical (which can be modeled as a function containing ratio of height separation to vertical correlation distance factor, or as a ratio of potential temperature surface separation to vertical correlation distance factor) (Brewster, 1996).

ADAS has the vertical correlation specified as a function of vertical height separation, which allows for analysis of single-level data such as surface observations, which can vary from when the boundary layer is deep and well mixed to when the boundary layer is shallow and inversions are present (Brewster, 1996).

In ADAS, the successive-correction analysis involves first correcting the background field for errors in large scale features through using a relatively long correlation scaling distance L_h, then reducing the correlation distance with each successive pass and also utilizing datasets that match the length scale of the observing system. This procedure was found by Carr et al., 1996 to generate the best successive-correction analysis (Brewster, 1996).

Six passes are used to account for the different densities of the observation types in the analysis (Table 2).

Analysis Pass	Horizontal Correlation Distance (km)	Vertical Correlation Distance (km)
1	320	200
2	240	250
3	160	200
4	110	150
5	70	100
6	40	75

Table 2. Table of analysis passes and horizontal and vertical correlation length scale associated with each analysis pass. Horizontal correlation distances are the values of xyrange and vertical correlation distances are the values of zrange, used in the ADAS input file.

Nearly all analysis control parameters for ADAS are read in from an ADAS input file. This input file also contains input variables for the ARPS domain and terrain, as well as file names of files containing expected errors for observations at multiple levels as a function of height.

On the ARPS grid, five variables are analyzed: u and v grid-relative winds, pressure, potential temperature, and RH* (analogous to dewpoint depression (i.e.: difference between air temperature and dewpoint temperature, which is a measure of how moist the air is)).

Because vertical velocity (w) is not well observed, it is diagnosed from the horizontal winds, with the wind velocity being set to zero at the ground and at the top boundary of the model. To allow for consistency with the analyzed horizontal (u-v) wind field, it is assumed that error in horizontal divergence is linear with height, with the w field being adjusted after error in horizontal divergence is removed, and the w field being found in each column in the model grid. Once this has been done, the total mass divergence is near zero, which ensures a smooth start to running the ARPS forecast model (Brewster, 1996).

RH* is the square root of relative humidity minus maximum relative humidity (1.0) and is used instead of specific humidity in the ADAS technique because of how even small changes in surface specific humidity can lead to unrealistically large, non-linear relative changes aloft, which affects 3-D weighting of obs (Brewster, 1996).

In addition to the ADAS technique used in the analysis, there is also the IAU Variable-Dependent Timing (VDT) technique that is applied in the assimilation window (the first 10 minutes of the model). IAU variable-dependent timing (IAU-VDT) allows for applying wind and latent heating increments early in the assimilation window while applying more hydrometeor increments later in the assimilation window to more accurately model vertical velocity before hydrometeors fall out of a parcel, in this way also better simulating hydrometeor growth (Morris et al., 2021). No matter which analysis technique is used in concert with the IAU method (whether ADAS or ARPS 3DVar), IAU is not applied here to analyzed pressure and vertical velocity increments because these fields are not well enough observed at scales being modeled (3 km) (Morris et al., 2021), and because they respond quickly to increments from other variables.

c. Nature Run and ARPS for 20-May-2013

The domain of the Nature Run 3 km run is depicted in Figure 10. The 1-km inner nest (d2) encompasses all of Oklahoma, parts of northern Texas, the Oklahoma and Texas Panhandle regions, southern Kansas and southeast Missouri, as well as the southeasternmost parts of Colorado, easternmost portions of New Mexico, and westernmost portions of Arkansas.

The domain for the OSSE experiments is similar to the Nature Run but not exactly the same. More specifically, the domain for the experiments has to be contained within the domain for the Nature Run.

The ARPS domain is shown in Figure 11. The western portion of the ARPS domain incorporates less area at the boundaries than the Nature Run, with the western part of the ARPS domain only covering southeastern Colorado. A similar portion of southern Kansas as in the Nature Run is covered for the extreme northern portion of the ARPS domain. However, because of effects from the boundaries, this domain will be trimmed slightly at the edges, especially at the top (where vertical axis slices above 500 km are omitted) and to the east (where all data to the east of 700 km is omitted) when generating plots of variables like reflectivity.

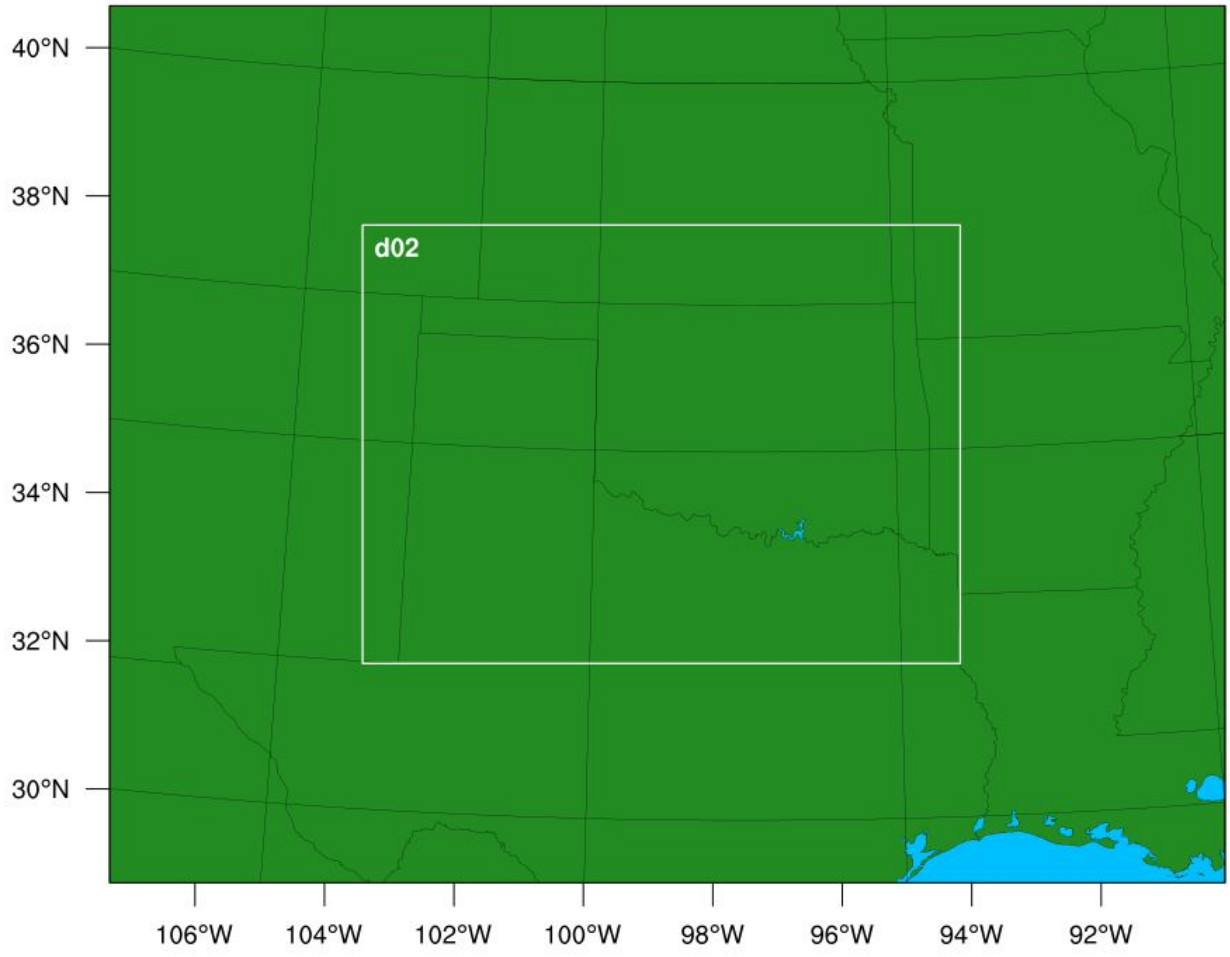

Figure 10. The 3 km resolution domain for the Nature Run. The nested inner 1-km domain is outlined in white and is labeled as d02.

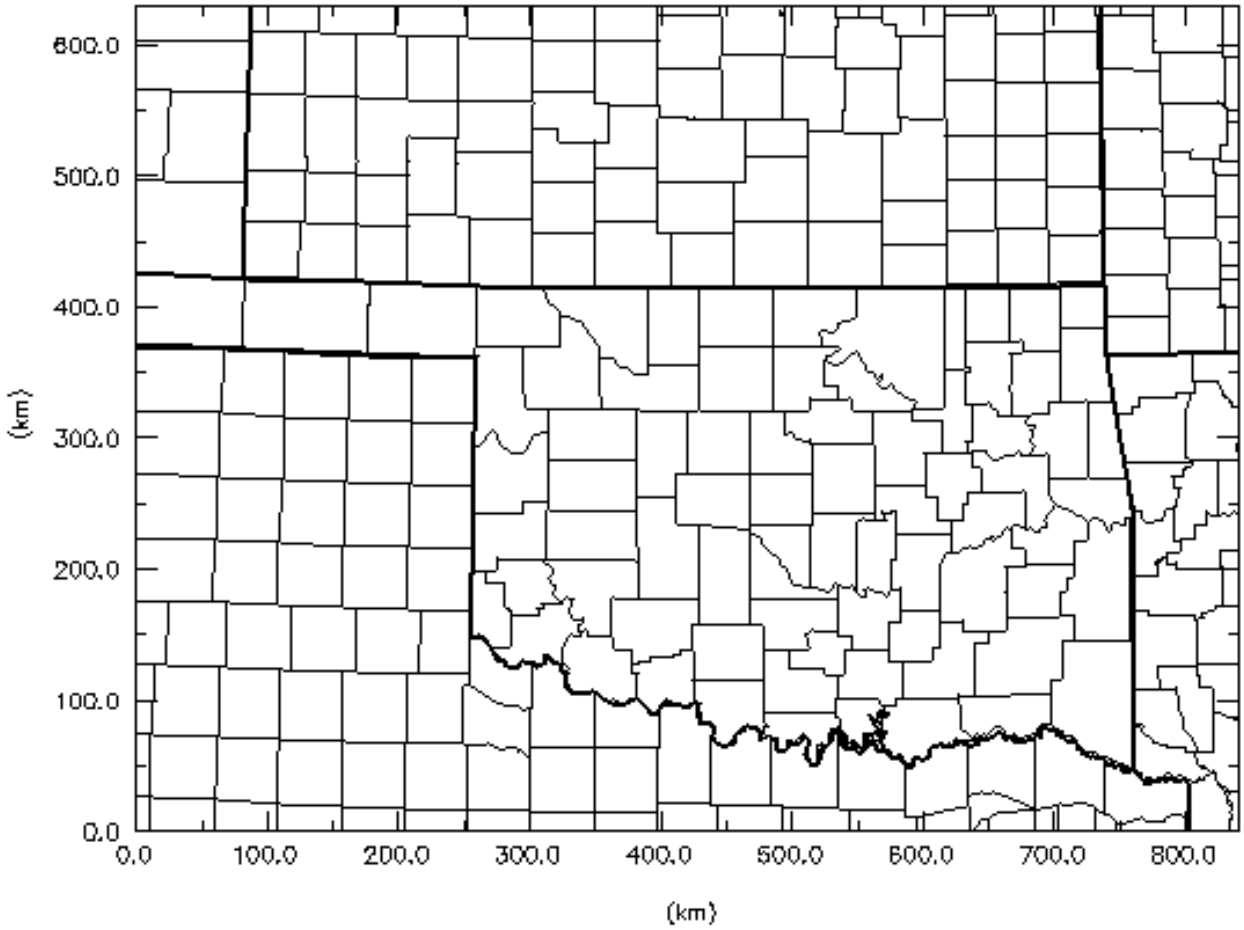

Figure 11. The 3 km resolution domain used for the ARPS forecast model.

The OSSE experiments used different parameters for the ARPS model compared to the WRF Nature Run; some of these parameters were similar to those used in the Nature Run, such as microphysics option, turbulence and mixing options, and damping options.

The precipitation scheme used for both the WRF and ARPS models are 2-moment schemes, where not only is the mass of precipitation taken into account, but the size distribution of precipitation and size sorting effects are taken into account. 2-moment schemes differ from single moment (1-moment) schemes in that effects from size distribution of precipitation like outflow development, strength of cold pool, and effects on strength and area of downdraft are not as well simulated compared to when size distribution of precipitation is also taken into account. To avoid the identical twin problem between the Nature Run model and ARPS forecast model, the microphysics 2-moment schemes differ between the WRF and ARPS model. For the WRF nested model, the Thompson 2-moment scheme is used, whereas for the ARPS model, the multi-moment bulk microphysics parametrization 2-moment scheme with diagnosed alpha (MYDMd) is used with all moist processes activated, graupel and hail processes accounted for, no convective cumulus

parameterization and grid-scale condensation, and cloud ceiling limited by the lifted condensation level (LCL) of a surface-based parcel.

Additionally, some other important parameters to note that the Nature Run used are: the rrtmg scheme (Atmospheric and Environmental Research, Inc., 2019) for shortwave radiation and longwave radiation, the MYNN Monin-Obukhov similarity theory (Dudhia, 2010) for surface-layer option for use with MYNN-PBL, the Noah Land-Surface Model for the land-surface option set before running real, the MYNN 2.5 level TKE scheme for the boundary-layer option, no cumulus parametrization for the cumulus physics option, heat and moisture fluxes from the surface being included, cloud effect included for optical depth in radiation vertical velocity damping turned on, turbulence and mixing option set so that 2nd order diffusion terms are evaluated on coordinate surfaces, eddy coefficient option of type Horizontal Smagorinsky first order closure, upper level damping set to consider w-Rayleigh damping (dampcoef inverse time scale [1/s]), and a damping depth (zdamp) of 5000 meters.
A summarized list of these important parameters is shown in Table 3.

Variable	Meaning	Value	Description	Section
mp_physics	Microphysics option	8	Thompson Graupel Scheme	&physics
ra_sw_physics	Shortwave radiation option	4	rrtmg	&physics
ra_lw_physics	Longwave radiation option	4	rrtmg	&physics
sf_sfclay_physics	Surface-layer option	5	MYNN Monin-Obukhov similarity for use with MYNN-PBL	&physics
sf_surface_physics	Land-surface option	2	Noah Land-Surface Model: Unified NCEP/NCAR/AFWA scheme with soil temperature and moisture in four layers, fractional snow cover and frozen soil physics	&physics
bl_pbl_physics	Boundary-layer option	5	MYNN 2.5 level TKE Scheme	&physics
cu_physics	Cumulus option	0	No cumulus	&physics
isfflx	Heat and moisture flux	1	Heat and moisture fluxes from surface	&physics
icloud	Cloud effect to the optical depth in radiation	1	Includes cloud effect on optical depth in radiation	&physics

w_damping	Vertical velocity damping	1	Vertical velocity damping is turned on	&dynamics
diff_opt	Turbulence and mixing option	1	2nd order diffusion terms evaluated on coordinate surfaces	&dynamics
km_opt	Eddy coefficient option	4	Horizontal Smagorinsky first order closure	&dynamics
damp_opt	Upper level damping	3	Uses w-Rayeligh damping where dampecoef is of inverse time scale	&dynamics
zdamp	Damping depth from top of model in meters	5000.	Same as meaning	&dynamics

Table 3. Table of some important parameters used in the Nature Run model. Each row corresponds to a different parameter. The columns give the parameter name, meaning, value used for the parameter, a short description, and the section the parameter was in for the Nature Run namelist.input file.

A complete list of all the parameters and their values that were included in the Nature Run settings are listed in Appendix A.

As with the Nature Run, there were set values for cloud and radiation, turbulence and mixing and damping parameters for the ARPS model. For the ARPS model, no METAR radar and satellite data was directly used (those being represented by the FNL data), there was no smoothing applied to analyze moisture and in-cloud w fields, the radiation physics option used Atmospheric radiation transfer parameterization, the radiation was computed at staggered points, radiative longwave scheme used transmission functions in CO_2, O_3, and three water vapor bands with cooling rates computed up to 0.01 mb, control parameter for turbulence and mixing was set to 1.5 TKE turbulent mixing, the isotropic subgrid scale turbulence was assumed to be anisotropic, the type of 1.5 TKE formulation used was the PBL parameterization for an unstable boundary layer (Sun & Chang (1986)), the full turbulence formulation computing both horizontal and vertical terms was performed, 2nd order computational mixing was turned off, surface physics was set to calculate surface fluxes from stability-dependent surface drag coefficients and predicted surface temperature and surface volumetric water content, a distinction was made between land and water surfaces in surface physics calculations, PBL depth was determined diagnostically, specified PBL depth was 1400 meters, heating and moisture fluxes were distributed quadratically with a flux distribution depth of 200 m, acoustic wave divergence damping was set to have anisotropic divergence turned on, and Rayleigh damping was defined as the difference between the total and external fields in the external boundary condition file.

Variable	Meaning	Value	Description
mphyopt	Microphysics option	8	2-moment bulk physics scheme (MYDMd)
moist	Moist processes	1	Moist process activation
graupel_ON	Graupel initiation	1	Graupel initiation is allowed
hail_ON	Hail initiation	1	Hail initiation is allowed
cnvctopt	Convective cumulus parameterization	0	Convective cumulus parametrization and grid-scale condensation turned off
ceilmin	Cloud ceiling	2	Cloud ceiling limited by LCL of surface-based parcel
cloudopt	Cloud analysis	1	Complex cloud analysis using all possible data sources
cldwopt	In-cloud w adjustment	0	In-cloud w fields not adjusted
radopt	Radiation physics	2	Radiation computed using Atmospheric radiation transfer parametrization
radstgr	Staggered computation of radiation	1	Radiation computed at staggered points on x-y plane
rlwopt	Radiative longwave scheme	1	Transmission functions used for various gases with cooling rates computed up to 0.01 mb
tmixopt	Control parameter for turbulence and mixing	4	1.5 TKE formulation
trbisotp	Isotropic sub-grid scale turbulence	0	Anisotropic turbulence
tkeopt	Type of 1.5 TKE formulation	3	PBL parameterization for unstable boundary layer (Sun & Chang 1986)

Variable	Meaning	Value	Description
tmixvert	Turbulence formulation computation	0	Computation of both vertical and horizontal terms
cmix2nd	2^{nd} order computational mixing	0	2^{nd} order computational mixing turned off
sfcphy	Surface physics	4	Calculated from stability-dependent surface drag coefficients and predicted surface temperature and surface volumetric water content
landwtr	Distinction between land and water surface physics	1	Distinction made between land and water surfaces for surface physics calculations
pbldopt	PBL depth determination	2	PBL depth determined diagnostically
pbldpth0	Specified PBL depth in meters	1400.	Specified PBL depth set to 1400 meters
tqflxdis	Distribution of heat and moisture fluxes	1	Heat and moisture fluxes distributed quadratically through PBL
dtqflxdis	Distribution depth of heat and moisture fluxes in meters	200.	Heat and moisture fluxes distributed through depth of 200 meters
divdmp	Acoustic wave divergence damping	2	Anisotropic divergence damping enabled
raydmp	Rayleigh damping	2	Damping difference between total and external fields defined in external boundary condition file.

Table 4. Table of some important parameters used in the ARPS forecast model for the OSSE experiments. Each row corresponds to a different parameter. The columns give the parameter name, meaning, value used for the parameter, and a short description as described in the ARPS input files.

A table of similar microphysics, radiation, turbulence and mixing, and damping parameters used in the ARPS forecast model is listed in Table 3. Similar to the Nature Run, a complete list of all the parameters and their values that were included in the ARPS settings are listed in Appendix B.

d. Comparison of Nature Run to Observed KTLX Radar Data

To assess the validity of the Nature Run, simulated reflectivity data from WRF level 10 (~2 km AGL) was compared with the observed 0.50 degree elevation angle scan radar data from the Twin Lakes radar site near Oklahoma City (KTLX, Figure 12) during the afternoon and evening (local time) on May 20, 2013.

Nature Run	KTLX Radar
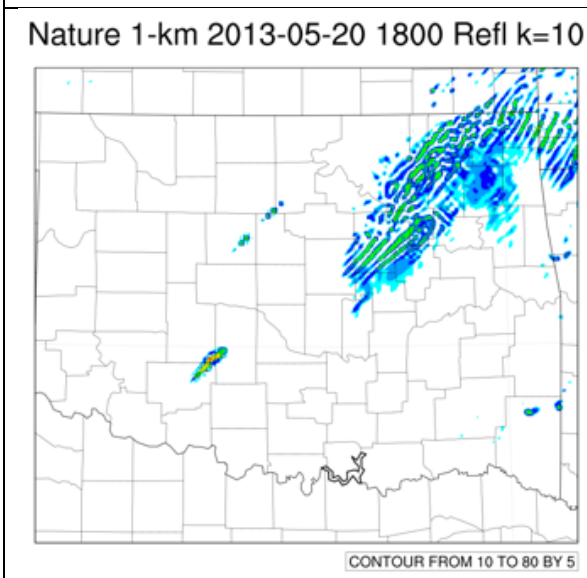	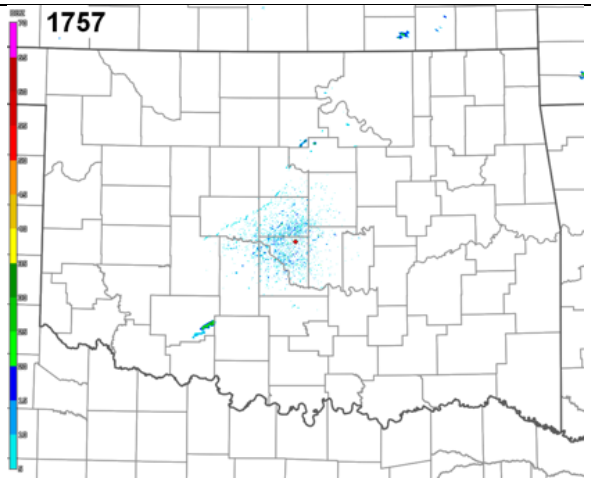
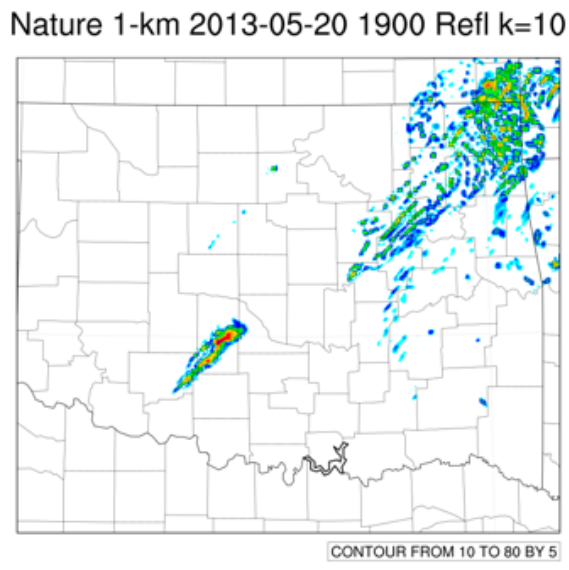	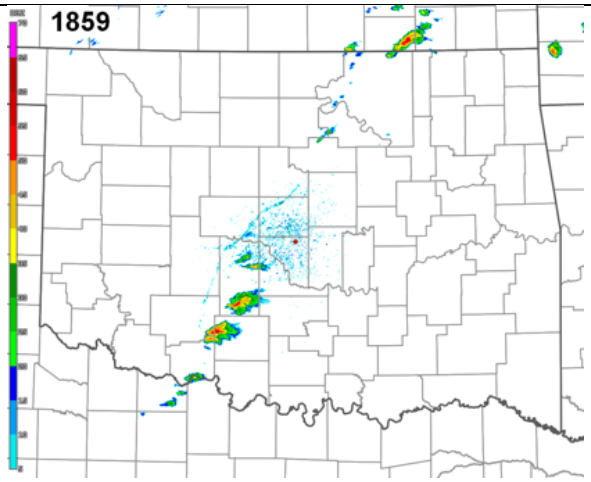

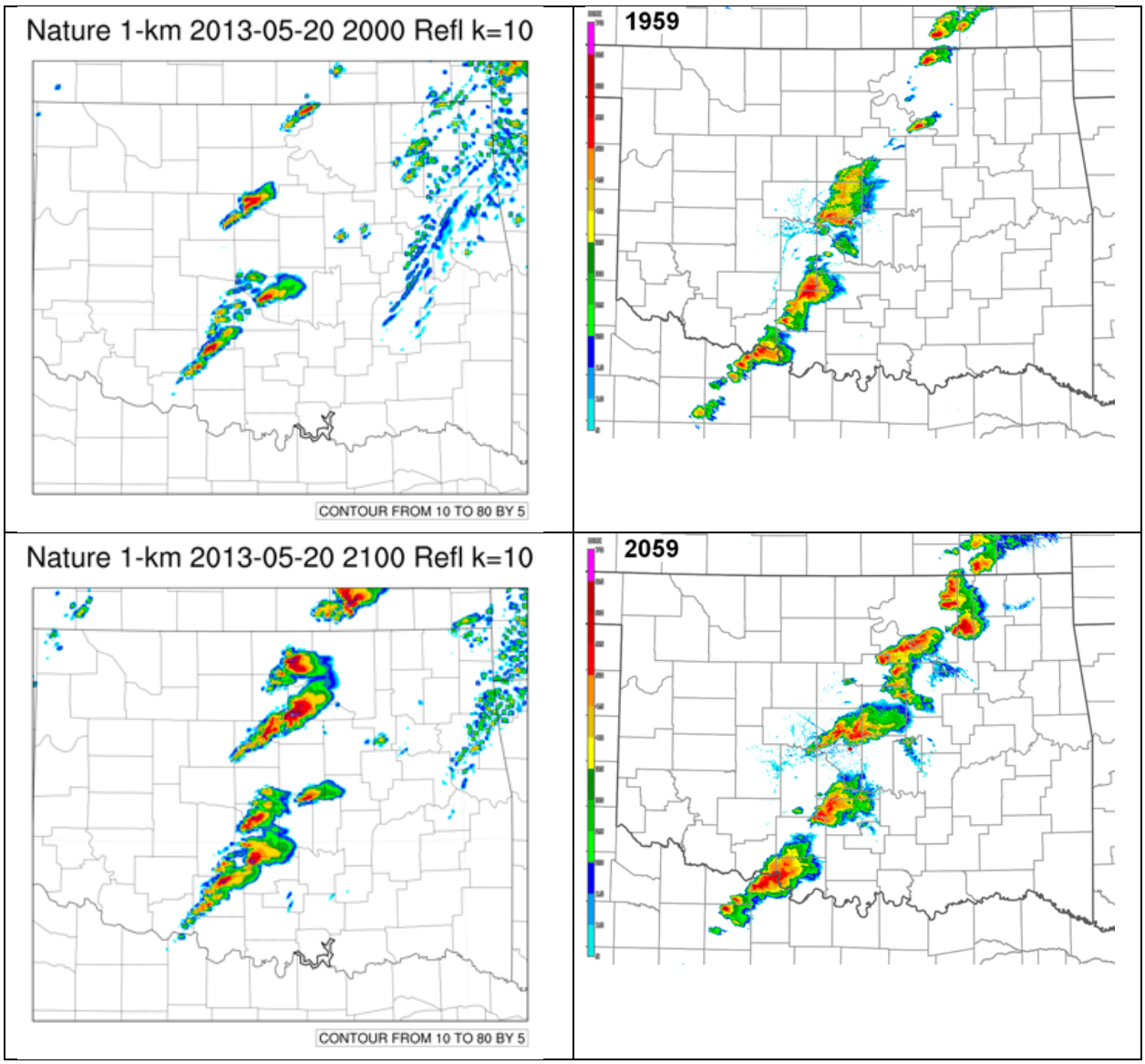
Nature 1-km 2013-05-20 2000 Refl k=10
CONTOUR FROM 10 TO 80 BY 5
1959
Nature 1-km 2013-05-20 2100 Refl k=10
CONTOUR FROM 10 TO 80 BY 5
2059

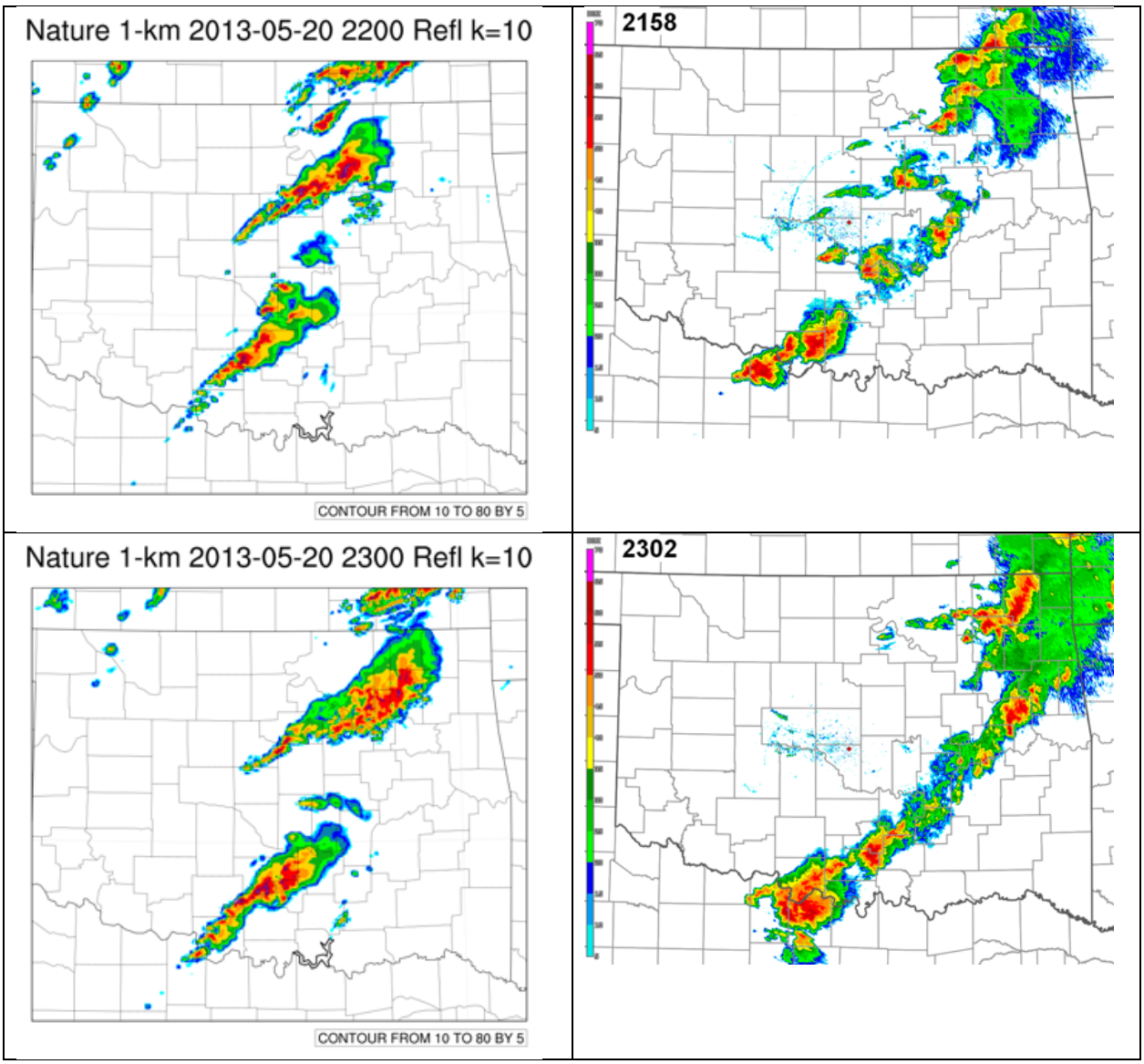
Nature 1-km 2013-05-20 2200 Refl k=10
CONTOUR FROM 10 TO 80 BY 5
2158
Nature 1-km 2013-05-20 2300 Refl k=10
CONTOUR FROM 10 TO 80 BY 5
2302

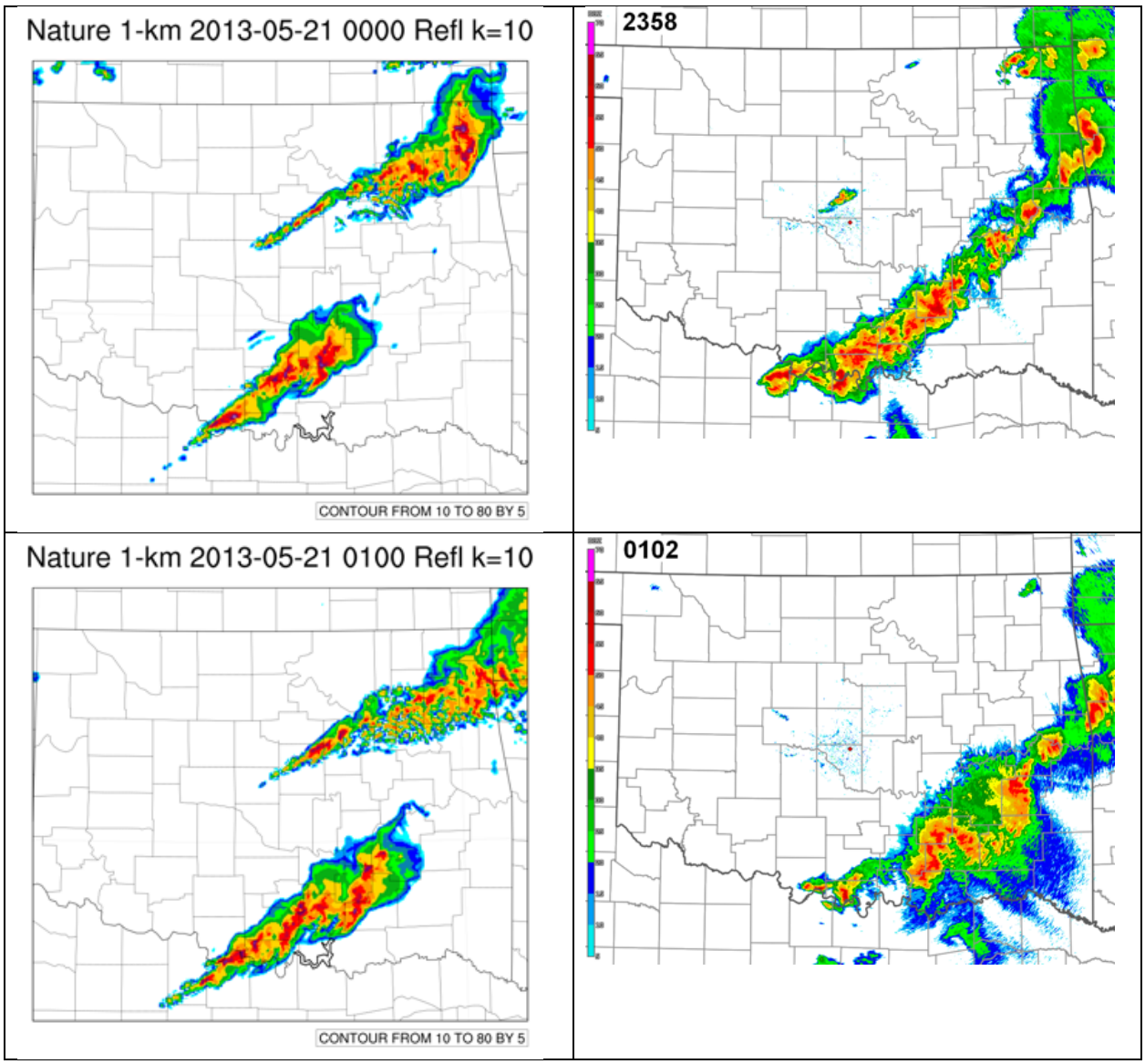
Nature 1-km 2013-05-21 0000 Refl k=10
CONTOUR FROM 10 TO 80 BY 5
2358
Nature 1-km 2013-05-21 0100 Refl k=10
CONTOUR FROM 10 TO 80 BY 5
0102

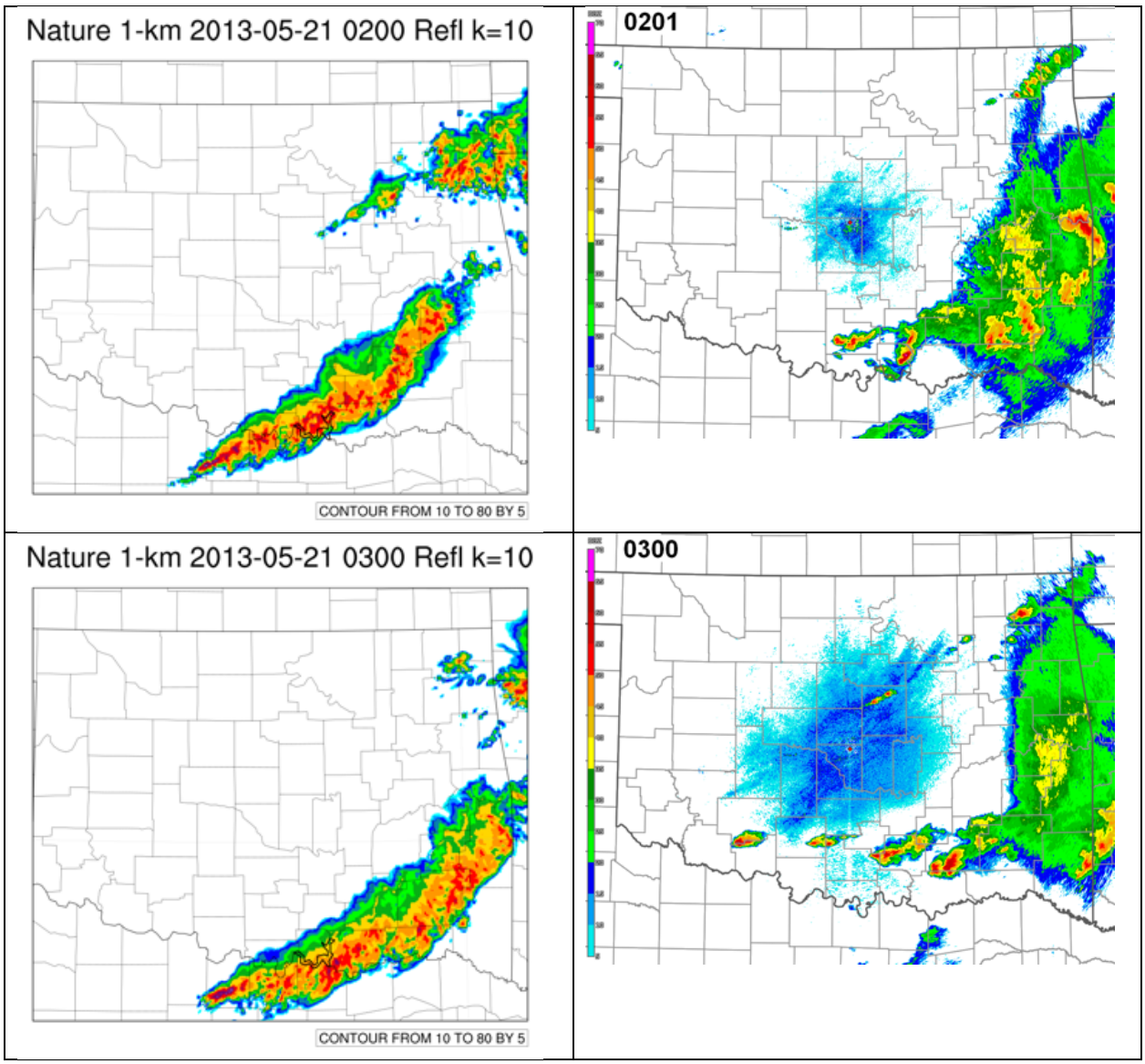

Figure 12. Comparison of nested 1 km Nature Run (left) reflectivity radar data (see right panel for dBZ color scheme) from level 10 (~ 2 km) and actual, observed radar data during the event from 0.5 degree elevation angle reflectivity scans from the KTLX radar site. The KTLX images are hourly and cover the same forecast period (18 UTC May 20 to 03 UTC May 21) as the Nature Run images do.

In the Nature Run and KTLX radar data, initiation of storms along the dryline in Grady County has occurred by 1900 UTC, with these storms moving into Cleveland County by 2000 UTC and a line of storms developing in southwest Oklahoma extending from Cotton County up into Cleveland County. By 2100 UTC, convection has split into three main areas, namely in southwest Oklahoma, north-central Oklahoma, and southeast Kansas for both the Nature Run and the KTLX radar data. However, past this point, the Nature Run and the KTLX radar data begin to diverge.

The biggest difference between the Nature Run data and the KTLX radar data was that in the actual radar data from KTLX, the supercell storms congeal into a single, continuous quasi-linear convective system (QLCS) line segment, whereas in the Nature Run, there remain separate

supercell clusters that develop into separate, northern and southernmost QLCS segments. This difference was judged to be minor enough to be acceptable, as the timing, location and intensity of convective initiation in southwest to west-central Oklahoma and supercell storm propagation through central Oklahoma (including Cleveland County) in the Nature Run showed the same pattern of convective initiation and propagation as the KTLX radar data.

After 0000 UTC, the KTLX radar data shows that the QLCS that forms is more or less continuous from northeast to southwest, with a clear bowing structure only showing up at 0100 UTC May 21, but the reflectivity in the eastward moving QLCS becomes weaker over time, presumably as the QLCS shifts away from the KTLX radar site and higher heights of the QLCS (where reflectivity is lower) are sampled. The Nature Run data does not show the QLCS being continuous in extent from northeast to southwest from 0100 UTC to 0300 UTC, but that instead there are northern and southern portions of QLCS that develop, with the northern portion moving more quickly to the east than the southern portion, with the southern portion of the QLCS developing to the northeast as it also shifts east. This lagging behavior of the southern portion of the QLCS is also seen in the KTLX radar images, but to a lesser extent and with the QLCS showing reflectivity filled in continuously from northeast Oklahoma to south-central Oklahoma.

Since the Nature Run was shown to be a suitable benchmark with which to compare the OSSE experiments, the reflectivity images from the Nature Run are generated from the entire period of 1200 UTC May 20 to 0300 UTC May 21 in 15 minute increments. The Nature Run reflectivity from level k = 10 (which is around 2 km AGL) for the entire forecast period (1800 UTC May 20 to 0300 UTC May 21) is shown in Figure 13. The Nature Run was interpolated to the ARPS model grid in order to facilitate comparison of results at exactly the same model resolution and height. Selected images from this series will be used in the following section to judge the results of the OSSE experiments.

00 minutes	15 minutes	30 minutes	45 minutes
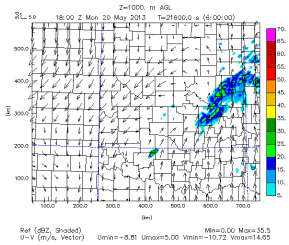	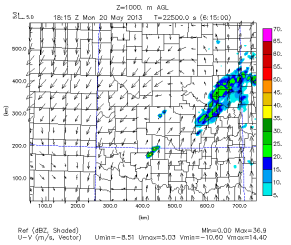	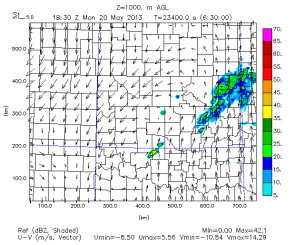	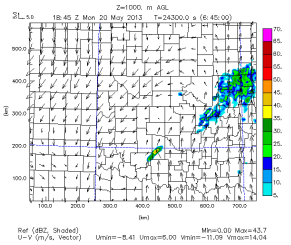
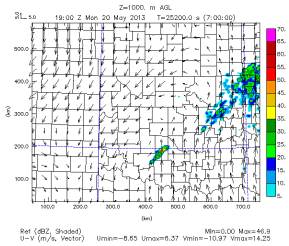	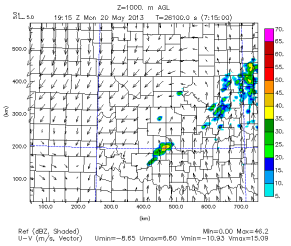	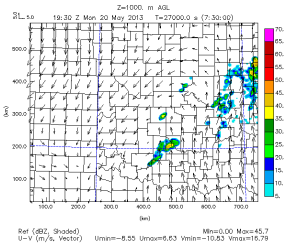	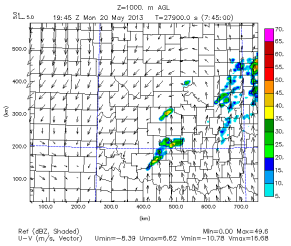
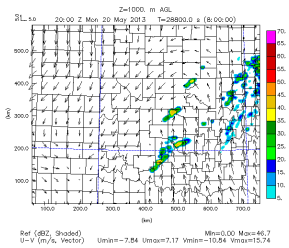	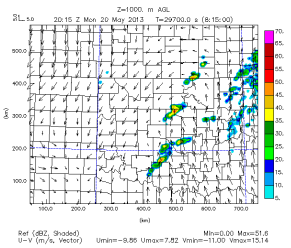	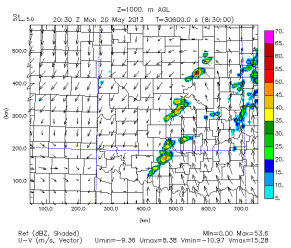	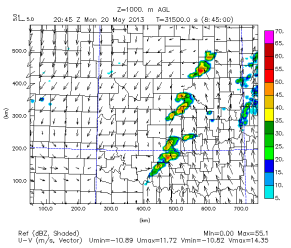
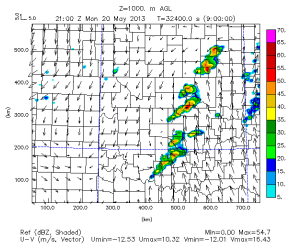	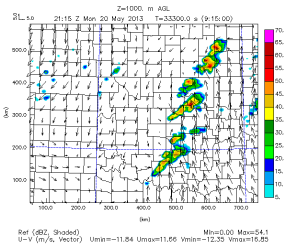	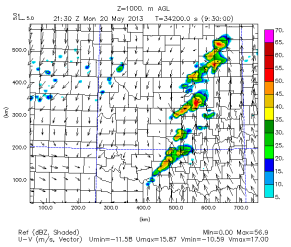	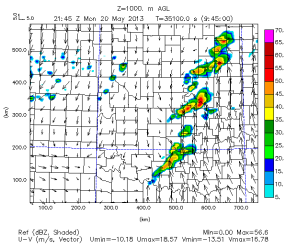
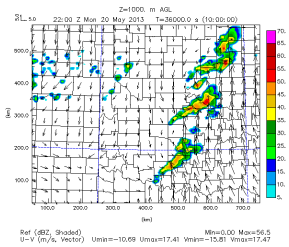	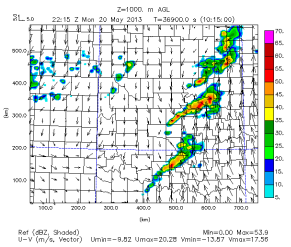	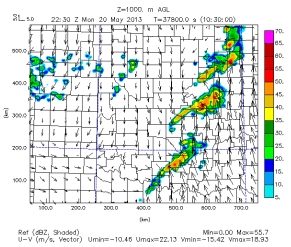	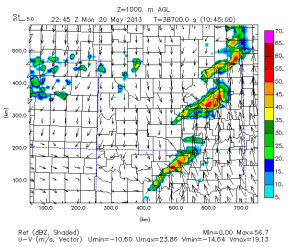
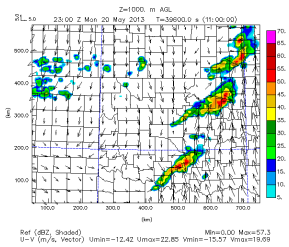	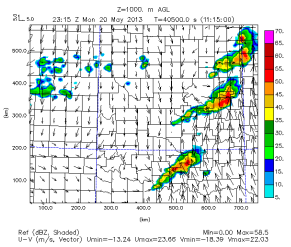	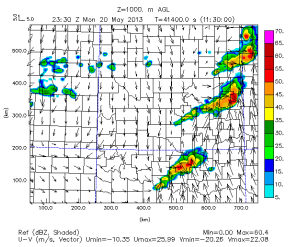	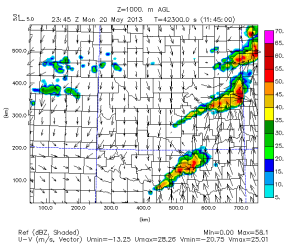

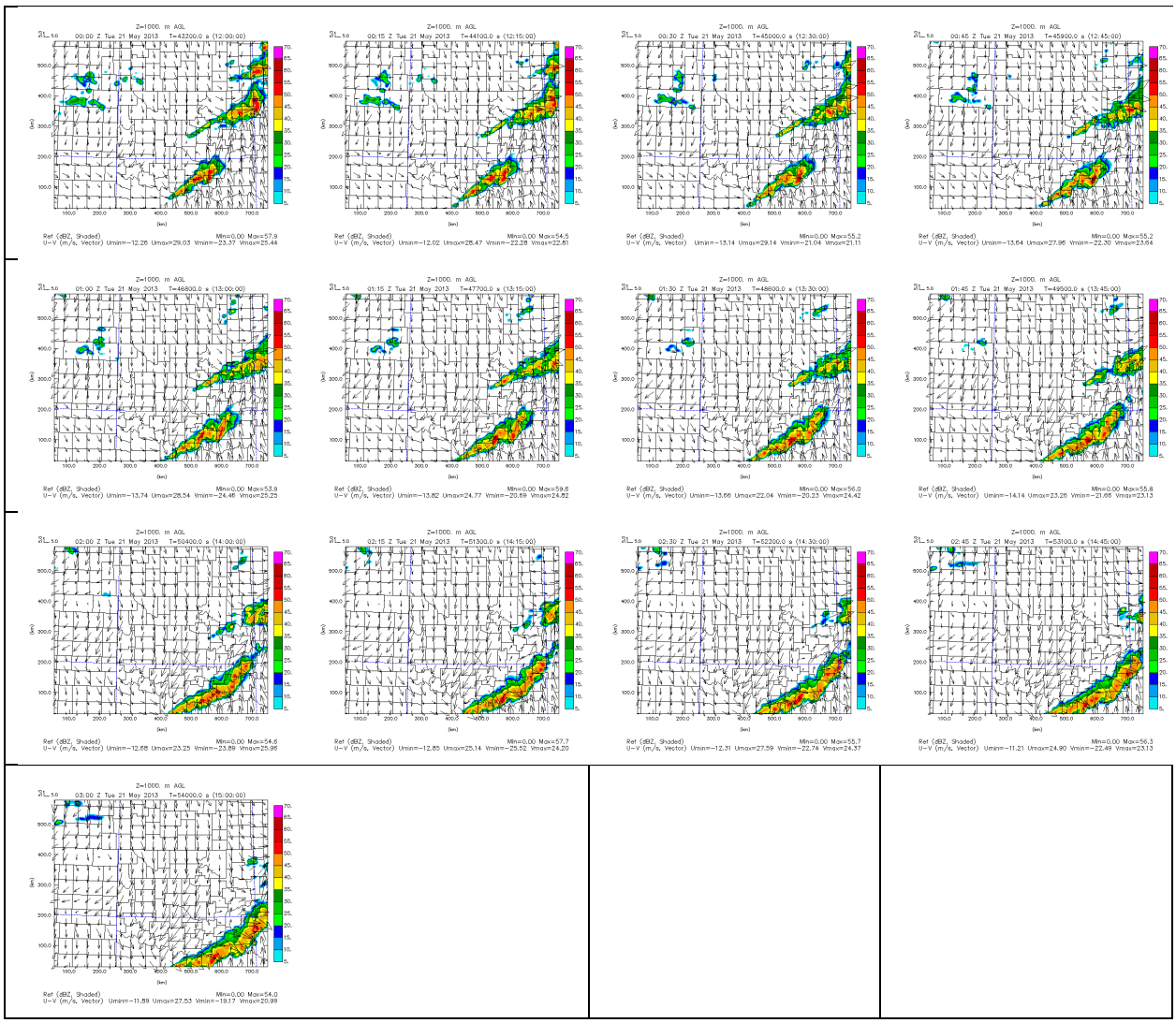

Figure 13. Nature Run simulated reflectivity (dBz, colors) and winds (scale top-left) at 1 km AGL every 15 min from 1800 UTC May 20 to 0300 UTC May 21. Each row corresponds to a forecast hour block. The columns are every 15 minutes, 0, 15, 30, and 45 minutes after the hour, respectively. The chronological sequence of the radar images from the Nature Run can be viewed by going from left to right in each row.

Comparison of the OSSE experiments will focus on a few key features in the reflectivity/wind fields during the forecast period: a) initiation of storms around 1900 UTC to 1930 UTC May 20, b) development of supercell storms in the 2000 UTC to 2300 UTC timeframe (where storms move into Cleveland County anywhere from 1945 UTC to 2000 UTC and storms congeal into a QLCS pattern after exiting Cleveland County by 2130 UTC to 2230 UTC), and c) at 0000 UTC, where the supercell storms have move east of Cleveland County are have taken on the form of separate linear convective segments in southeast Oklahoma and northeast Oklahoma.

Beyond 0000 UTC (0100 UTC to 0300 UTC May 21), much of the features show nonlinear interactions and difference in propagation speed of the QLCS line segments, but coverage and density of the QLCS segments are relatively similar.

Chapter 4. Experiment Results

The first step for testing the potential benefits of UAV observations in various configurations was to compare the results of experiments at various max heights with and without simulated UAV observations. Comparison of how well each experiment itself simulated convection and moisture/wind fields is done by comparing that experiment to the Nature Run. Without UAV observations, only GFS/FNL data and surface mesonet data observations from the Oklahoma Mesonet will be used, but with UAV observations, GFS/FNL, surface mesonet, and UAV data are incorporated. Addition of UAV data will also mean addition of surface data, since data from the surface is captured from the UAV every time it ascends from the ground to a given height at regular intervals (e.g.: every 15 minutes, or 30 minutes, or 1 hour, or 3 hours).

a. Synoptic Weather Conditions

The synoptic conditions for the time at the beginning of the forecast period (1800 UTC May 20) are shown in order to delineate regions along features of interest like the dryline and warm front. These features will be referenced when comparing how the placement of storms differs between the Nature Run and each set of OSSE experiments.

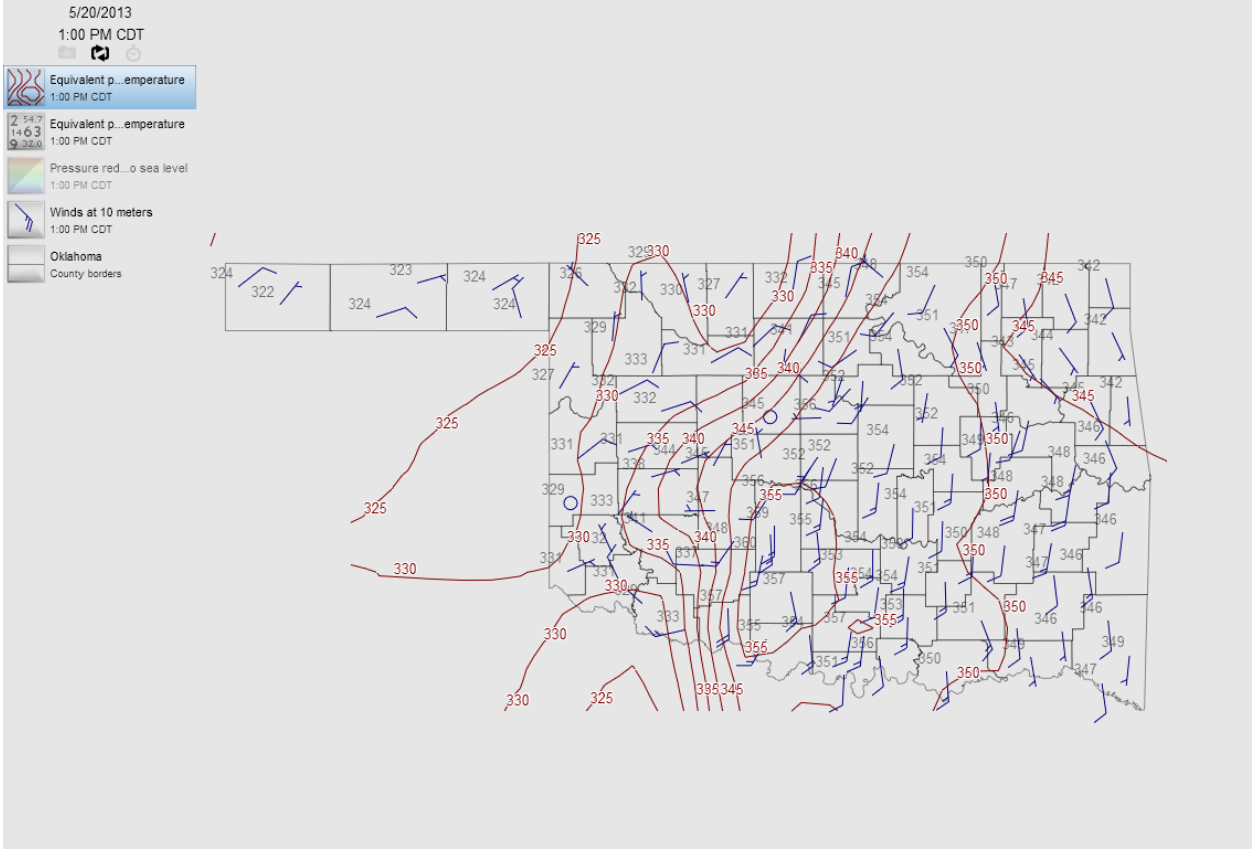

Figure 14. Map of equivalent potential temperature (°K contours) and 10-m wind barbs (knots) generated in WeatherScope using Oklahoma Mesonet data for 1800 UTC (1:00 PM Central Daylight Time) May 20.

A map of equivalent potential temperature (theta-e) at the start of the free forecast period (1800 UTC) is shown in Figure 14 to help determine the placements of the dryline and the warm front across Oklahoma at the time. The tightly-spaced theta-e contours outline the boundary of the dryline in west-central Oklahoma and warm front extending across northeast Oklahoma. The dryline is located across west-central Oklahoma delineating the region between more moist, higher theta-e air to the east and drier, lower theta-e air to the west. Specifically, it can be seen that the dryline stretches from Grant and May counties in the northern part of Oklahoma to the boundary between Tillman and Cotton counties in southwest Oklahoma.

The kink in the theta-e contours in northeast Oklahoma and change in wind direction in this region show a warm front extending from Delaware County in northeast Oklahoma to approximately Logan-Payne-Lincoln counties in north-central Oklahoma.

The pattern of winds show that a low pressure region is present along the dryline around northeast Caddo County. This area of low pressure is shown in the following surface station map (Figure 15).

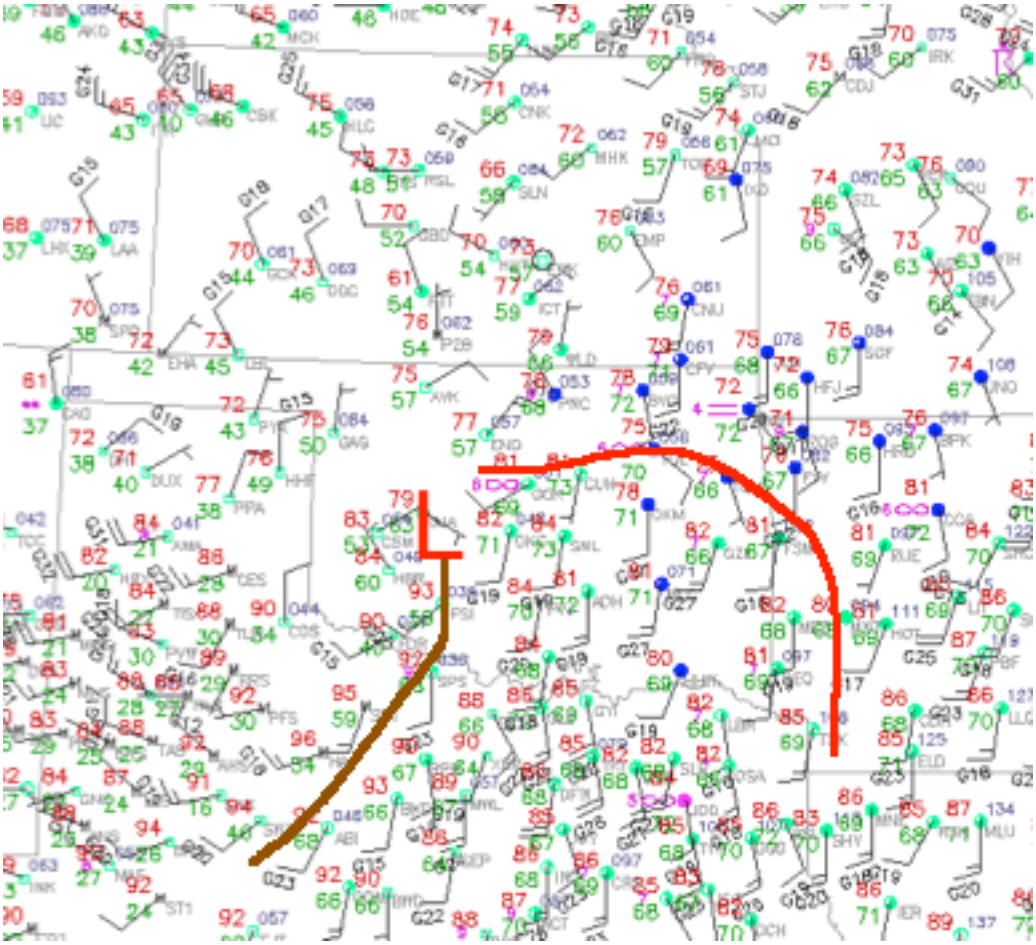

Figure 15. Surface station plot at 1800 UTC May 20 courtesy of NCAR MMM Image Archive (https://www2.mmm.ucar.edu/imagearchive/). Standard surface meteorological plot including temperature (°F), dew point temperature (°F), wind barbs (knots), sea level pressure (hundredths of hPa), locations of the dryline (brown) and the warm front (red) are indicated.

As indicated in Figure 15, the dryline stretches from west-central Oklahoma to southwest Oklahoma and farther south into Texas, and the warm front stretches from north-central Oklahoma to northeast Oklahoma, and into westernmost Arkansas. Overcast conditions are seen for most areas along the warm front, in contrast to partly cloudy skies seen along and ahead of the dryline.

b. Evaluation of Results without UAV Observations

To begin the evaluation of each OSSE experiment, the Nature Run is compared to runs without the UAV data (No Observation Data at all, Mesonet observations only, FNL observations only), and will be shown pertaining to a) convective initiation on the dryline in south and central Oklahoma around 1930 UTC May 20, b) supercell storm development (2000 UTC to 2100 UTC), c) storm propagation through central Oklahoma from 20 UTC through 23 UTC, and d) propagation of the QLCS segment(s) through eastern Oklahoma after 23 UTC (00 UTC will be used for comparison).

Following these, plots of reflectivity for the No UAV (FNL and Mesonet observations only), FMU400ft108, FMU01km108, FMU02km108, and FMU03km108 experiments will be shown at these same stages.

These were judged as the stages that need to be the focus of examination, in order to gauge how the OSSE experiments performed with simulating convection compared to the Nature Run.
Simulated reflectivity was plotted using microphysics variables from the ARPS forecast model.

For the horizontal reflectivity plots in both the Nature Run and the ARPS, the reflectivity is simulated at the same height (1 km AGL), so that low level reflectivity features that might seen on radar can be examined more closely. Output from the Nature Run interpolated to the same height (1 km AGL) and to the ARPS 3km grid is used so that direct comparisons can be made.

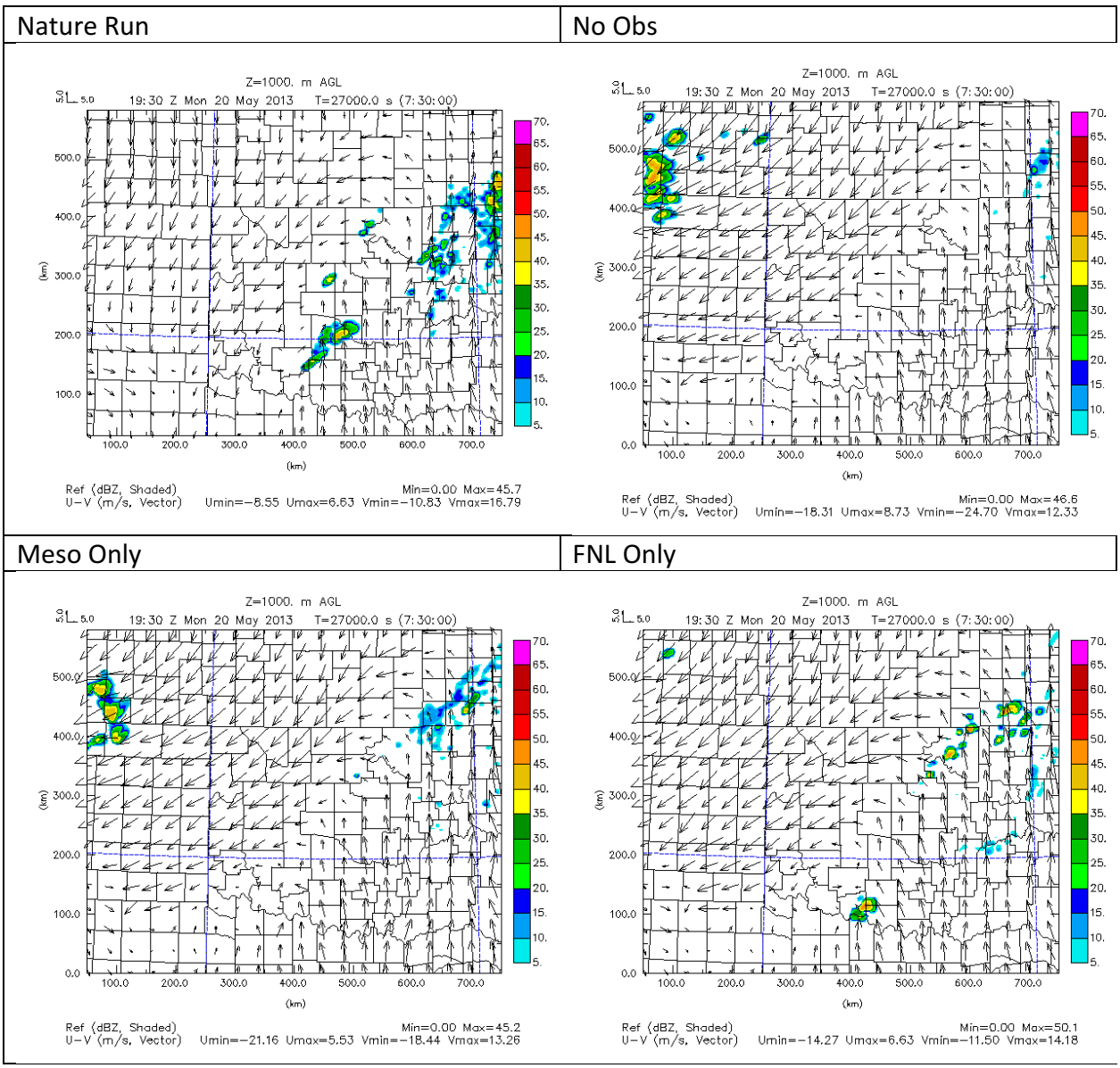

Figure 16. Simulated reflectivity (dBZ, color scale), and wind at 1 km AGL, 1930 UTC. Nature Run, No Observation data, Meso Only data, and FNL Only data.

With no observation data, no convection is simulated in central Oklahoma at 1930 UTC, unlike the Nature Run, which has convection in Grady County (Figure 16). Similarly, using Mesonet data only, and FNL data only is not sufficient to have convection initiation in central Oklahoma at 1930 UTC. However, with the addition of FNL data, some convection appears across north-central and northeastern Oklahoma (also apparent in the Nature Run), and a small spurious cell appears near the Red River, but there is no convective initiation in central Oklahoma.

c. Examination of Maximum Height of UAV Profiles

Nature Run	No UAV
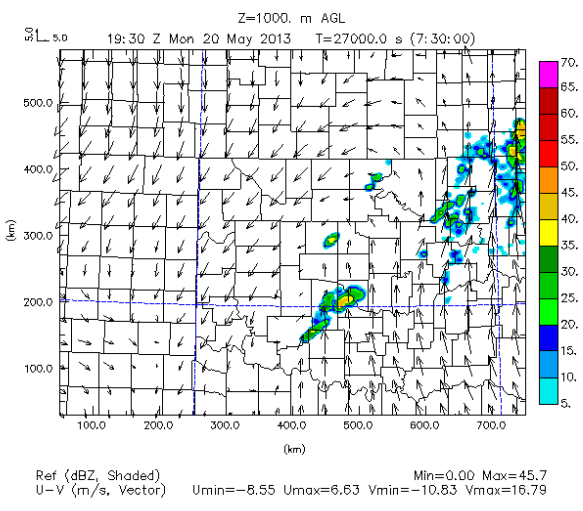	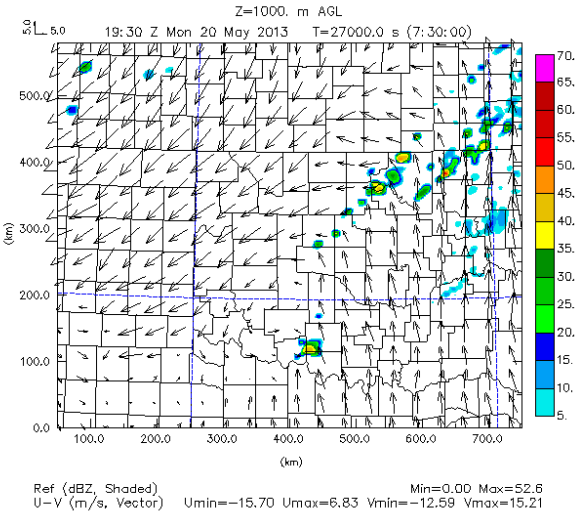
FMU400ft108	**FMU01km108**
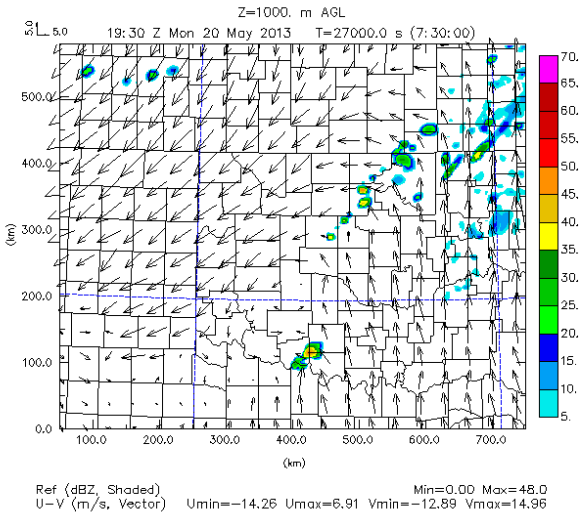	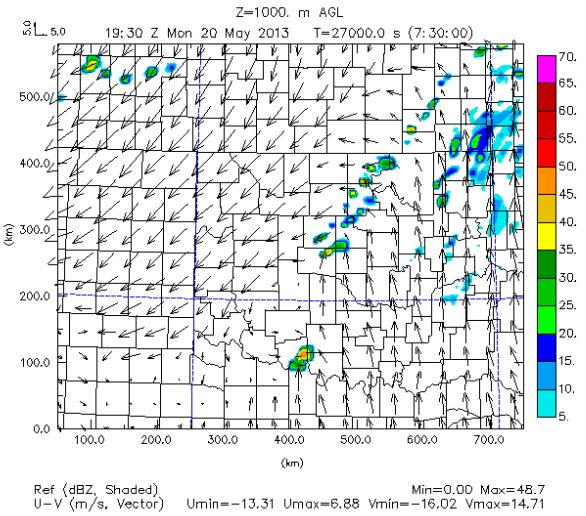

Figure 17. As in Figure 16, but Nature Run, No UAV, UAV obs from max height of 400 ft with 108 stations data, and UAV obs from max height of 1 km with 108 stations.

No UAV experiment combines Mesonet and FNL data, (Figure 17 top-right panel) and creates some convection in north-central Oklahoma, along the warm front, and near the Red River at 1930 UTC, but not in central Oklahoma along the dryline. The experiments with data up to 400 ft at 108 stations (FMU400ft108) and with data to 1 km AGL (FMU01km108) experiments show similar patterns, but with more convection present in north-central Oklahoma in the FMU01km108 experiment.

Nature Run	FMU02km108
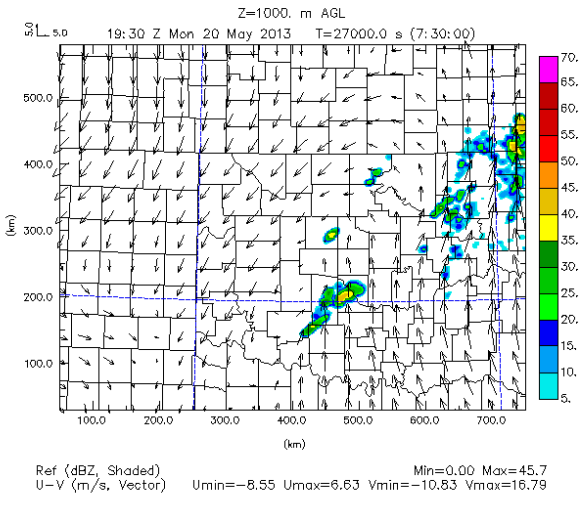	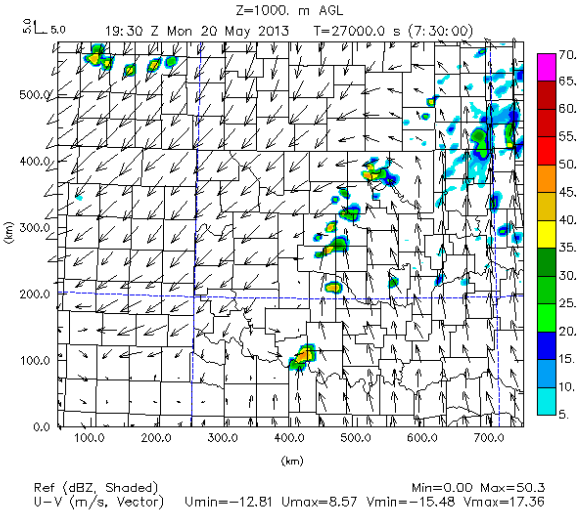
FMU03km108	
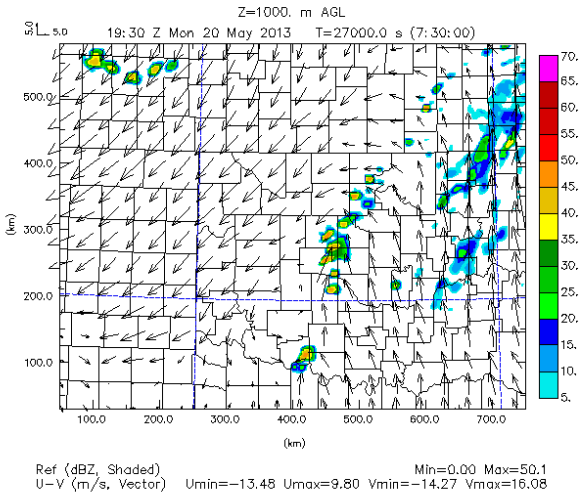	

Figure 18. As in Figure 16, Nature Run, UAV obs from max height of 2 km with 108 stations data, and UAV obs from max height of 3 km with 108 stations.

It can be seen that at 1930 UTC, convection along the dryline in west-central Oklahoma (Kingfisher to Grady counties) is in the vicinity of Cleveland County in both the FMU02km108 experiment and the FMU03km108 station experiment, just as in the Nature Run experiment. However, there is more small-scale convection in northeastern Oklahoma in the FMU03km108 station experiment, which is not as prevalent as in the FMU02km108 station experiment.

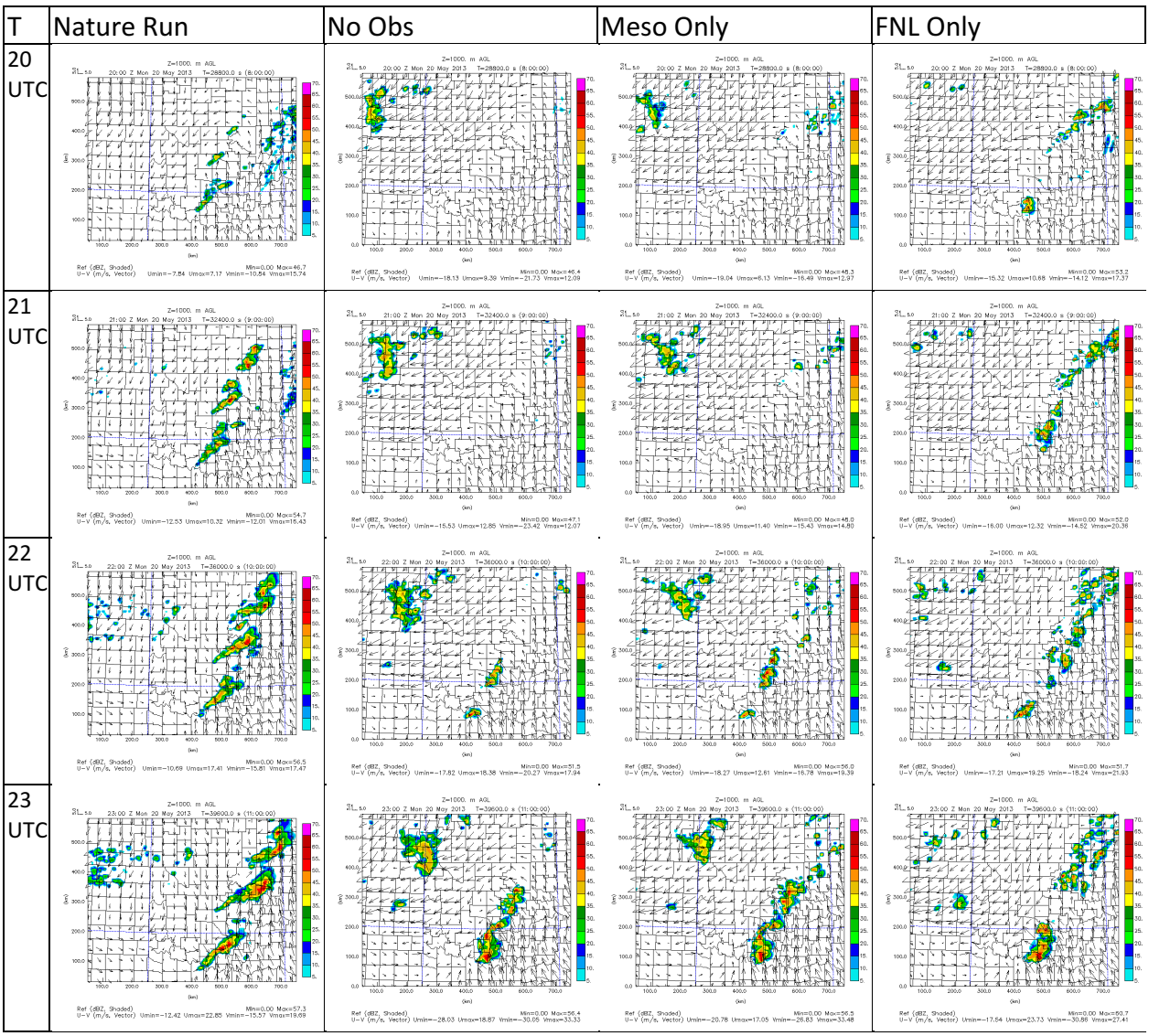

Figure 19. As in Figure 16, but for Nature Run, No Observation, Meso Only, and FNL Only experiments (columns) for times 20 UTC, 21 UTC, 22 UTC, and 23 UTC (rows).

As at 1930 UTC, the Meso Only and FNL Only experiments best recreate the Nature Run reflectivity for the experiments without UAV data in the period 2000 UTC to 2300 UTC. For the No Obs and Meso Only experiments, convective initiation in south-central Oklahoma (Cotton-Jefferson counties) is delayed until 2200 UTC.

However, there is better formation of the supercell and multicell storms in than the No UAV and FNL Only experiments along the warm front from central Oklahoma to southeastern Kansas in the compared to the Meso Only experiment.

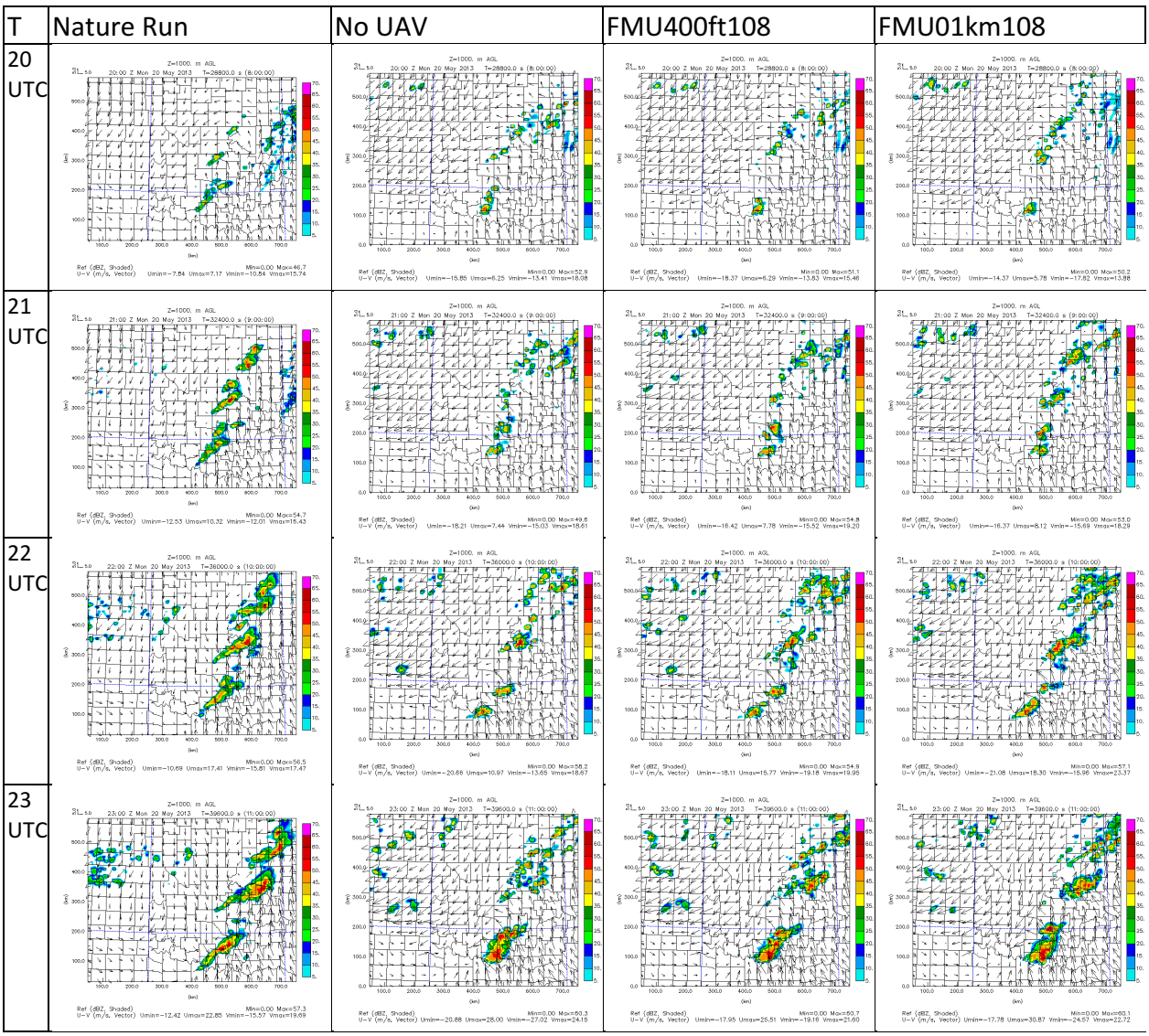

Figure 20. Simulated reflectivity (dBz, color scheme) and winds (scale top-left) at 1 km AGL for times 20 UTC, 21 UTC, 22 UTC, and 23 UTC. Nature Run, No UAV, FMU400ft108, and FMU02km108 experiments.

From 2000 UTC through 2300 UTC, the No UAV experiment consistently underrepresents the amount of convection across north-central Oklahoma (Logan to Kay-Osage counties), consistent with delayed and more sparse convective initiation, while the FMU400ft108 and FMU01km108 experiments have better coverage and intensity of convection in north-central Oklahoma. All of the experiments simulate the formation of a QLCS cluster in southern Oklahoma (eastern Cleveland County down to Carter-Love counties), but with a slighter greater spatial coverage than in the Nature Run.

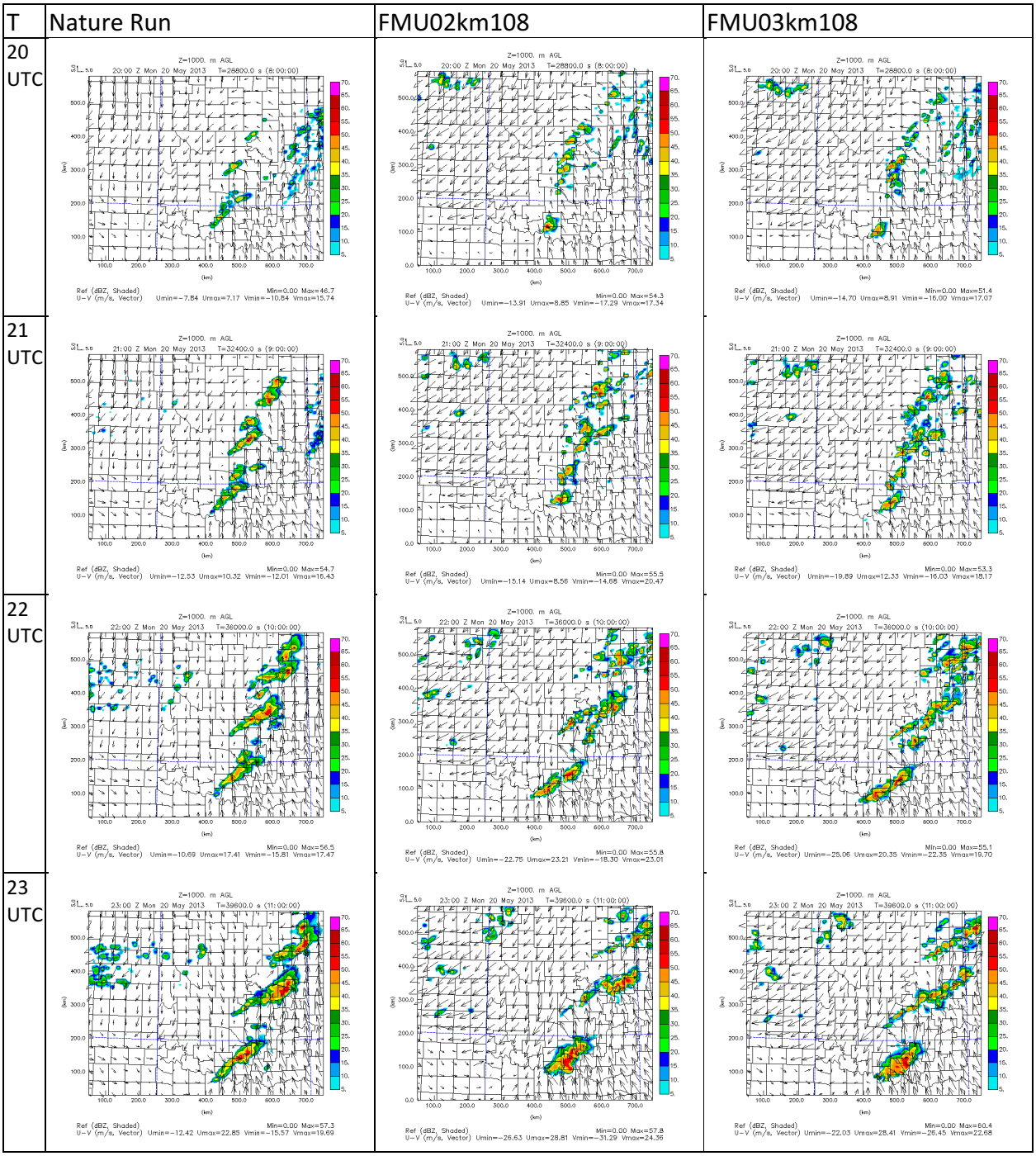

Figure 21. Simulated reflectivity (dBz, color scheme) and winds (scale top-left) at 1 km AGL for times 20 UTC, 21 UTC, 22 UTC, and 23 UTC. Nature Run, FMU02km108, and FMU03km108 experiments.

In comparison to the Nature Run, the FMU02km108 experiment again does the best job simulating the northern portion of developing supercell convection along the dryline in north-central Oklahoma and the southern portion of developing QLCS along the advancing dryline in south-central Oklahoma. As at 1930 UTC, for the period from 2000 UTC to 2300 UTC, the

FMU03km108 experiment has too much small-scale convection in north-central and northeast Oklahoma (in the corridor stretching from Logan to Craig counties).

Regarding the timing of convective initiation, coverage, intensity and placement of storms, and the least amount of small-scale convection in the 1930 UTC to 2300 UTC time window, the FMU02km108 experiment was most similar to results from the Nature Run, while the No Obs and Meso Only experiments were the least similar and lacked substantial convective coverage, particularly along the dryline.

Nature Run	No Obs
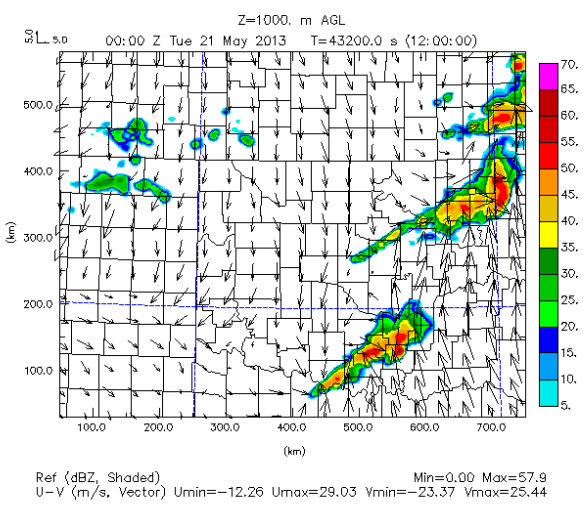	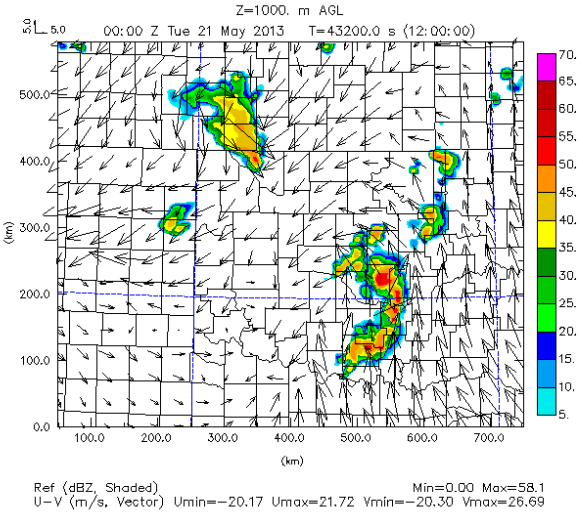
Meso Only	**FNL Only**
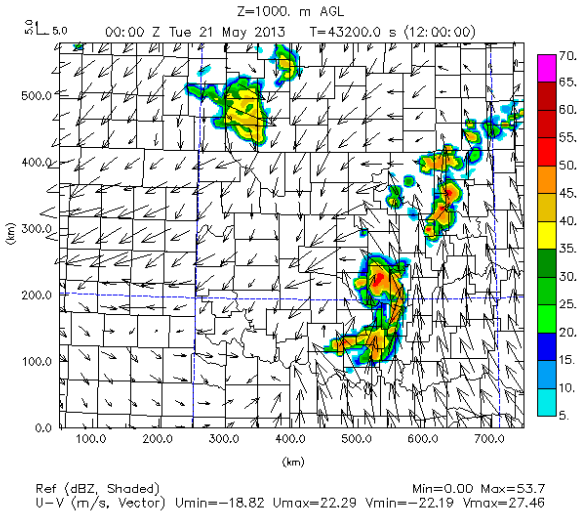	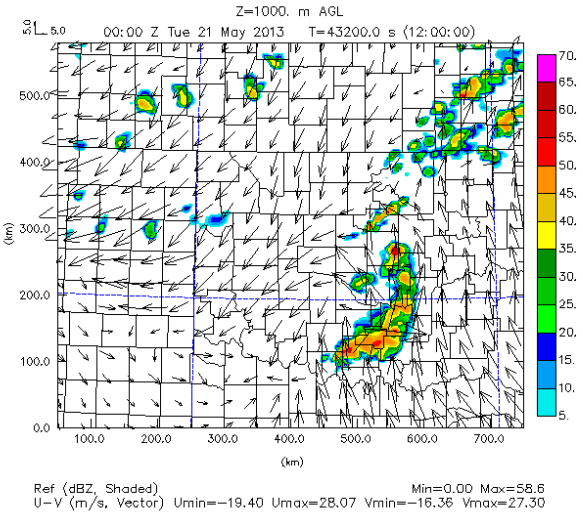

Figure 22. Simulated reflectivity (dBz, color scheme) and winds (scale top-left) for time 00 UTC May 21. Nature Run, No Obs, Meso Only, and FNL Only experiments.

Now that there has been examination of the initial timing, coverage and intensity of supercell storms, the evolution of the storms after 2300 UTC (when they had moved east to form two separate clusters of QLCS) will be examined.

As in the Nature Run, by 00 UTC the OSSE experiments show that the configuration of the supercell storms had transitioned to a more QLCS-like pattern. However, the No Obs and Meso Only experiments consistently show a complete bowing structure to the QLCS unlike the separate, more linear shaped areas of convection seen to the northeast (Ottawa County down to Tulsa County) and southwest (Hughes County down to Jefferson-Love counties) in central Oklahoma for the Nature Run. It is only with the addition of FNL Only data that there is a more linear structure to storms in central Oklahoma.

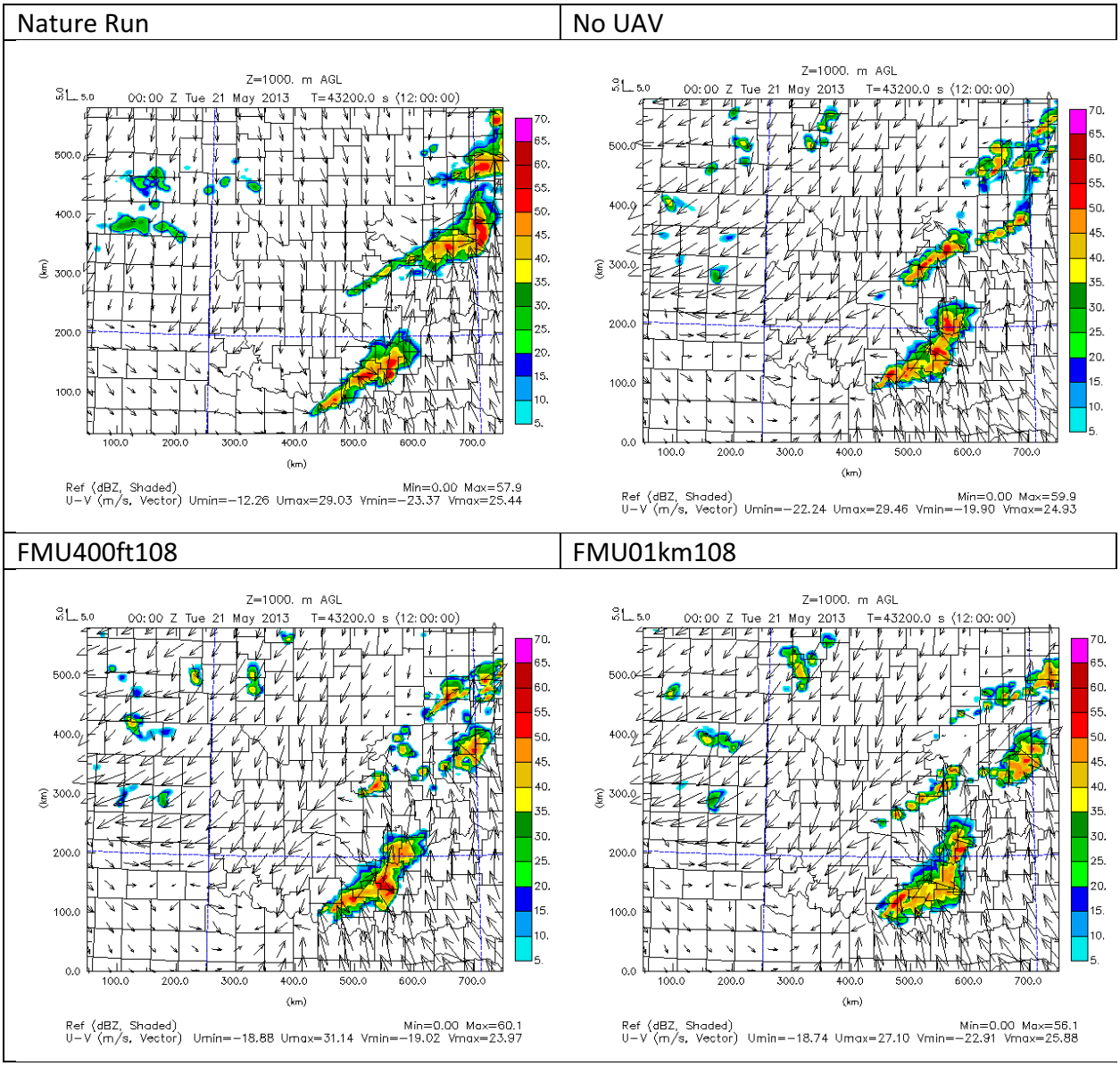

Figure 23. Simulated reflectivity (dBz, color scheme) and winds (scale top-left) at 1 km AGL for time 00 UTC May 21. Nature Run, No UAV, FMU400ft108, and FMU01km108 experiments.

As with addition of FNL Only data, addition of combined FNL and mesonet data (No UAV) shows largely the same pattern that the Nature Run has, with a more linear storm mode and separate areas of convection in northeast and southeast Oklahoma. Both the FMU400ft108 and FMU01km108 experiments show the main area of the northern portion of convection is farther east (Wagner to Ottawa counties), which is more similar to the position in the Nature Run than either of the other two experiments. However, in the the FMU400ft108 experiment, the line extending northeast from Payne county to the area of convection in the northeast corner of Oklahoma is reduced in coverage and intensity.

Nature Run	FMU02km108
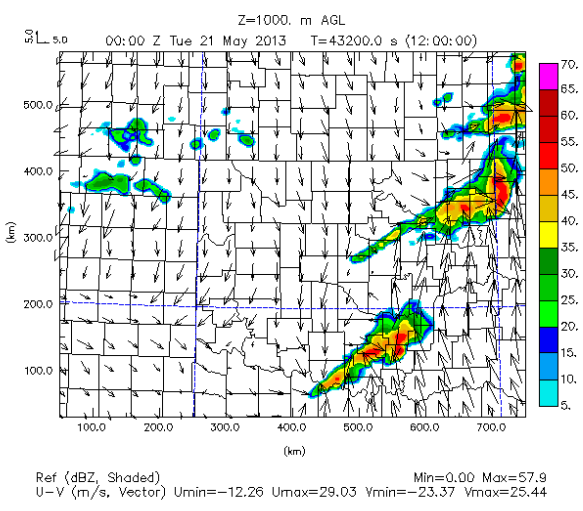	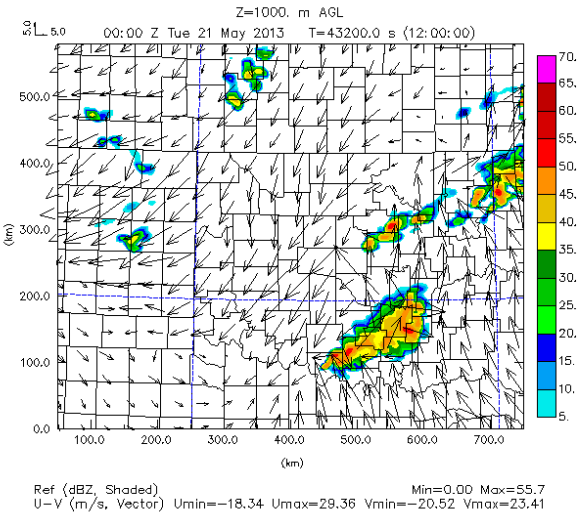
FMU03km108	
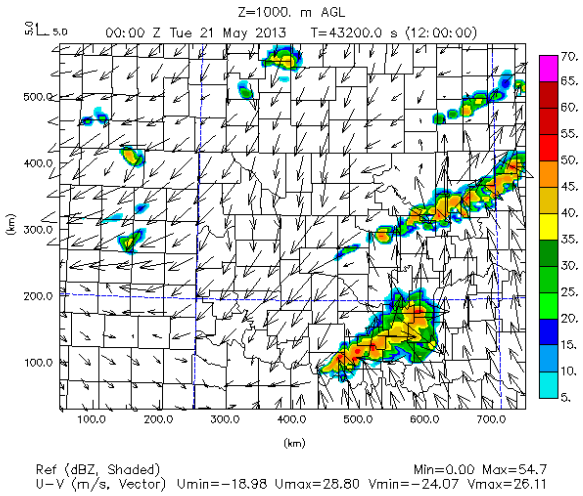	

Figure 24. Simulated reflectivity (dBz, color scheme) and winds (scale top-left) at 1 km AGL for time 00 UTC May 21 for Nature Run, FMU02km108, and FMU03km108 experiments.

The shape of southern portions of QLCS convection is nearly identical in the FMU02km108 and FMU30km108 experiments compared to the Nature Run, whereas for the FMU03km108 experiment, the line of cells running from Payne County to the northerast corner of Oklahoma is more narrow than in the Nature Run and FMU02km108 experiments. However, there are more distinctive, continuous northern and southern QLCS segments in the FMU03km108 experiment compared to the FMU02km108 experiment, and these distinctive northern and southern QLCS segments are more similar in coverage and placement to in the Nature Run. Of all of the OSSE experiments, the FMU01km108 experiment and FMU03km108 experiments seem most similar to the Nature Run at 0000 UTC. They are all nearly the same with the southern QLCS but the depiction of the northern QLCS, including its trailing convective line is somewhat better simulated for the FMU01km108 and FMU03km108 experiments.

Generally, as more data are added and UAV observations from higher max heights are taken, the position of the southern portion of convection exhibits a very slight shift to the southwest (with northeastern portion farther south-southwest to Hughes County instead of Okfuskee County), and just crosses the Red River region (as in the Nature Run) for the FMU03km108 experiment, but not extending as far southwest in the other experiments. While the position of the southern portion of convection is most similar to the Nature Run for the FMU03km108 experiment, when considering both the size, shape, and position of the northern and southern portions of convection at 0000 UTC, it is the FMU01km108 experiment that produces horizontal reflectivity at 1000 m AGL that is qualitatively most similar to the Nature Run.

In order to see why there were differences between the timing of convective initiation and ensuing evolution of convective storms, boundary layer cross-sections of moisture variables such as relative humidity, specific humidity (g/kg), winds, reflectivity (dBz), and cloud water mixing ratio (g/kg), were examined for a set vertical cross-sections through Oklahoma at 1800 UTC. Each vertical cross-section ranged from 0 km (Oklahoma/Texas panhandle region) to 700 km (eastern Oklahoma) from Y = 85.5 km (Red River region) to Y = 295.5 km (central Oklahoma north of Cleveland County. Figure 25 shows a map of the ARPS domain and where these horizontal cross-sections are located.

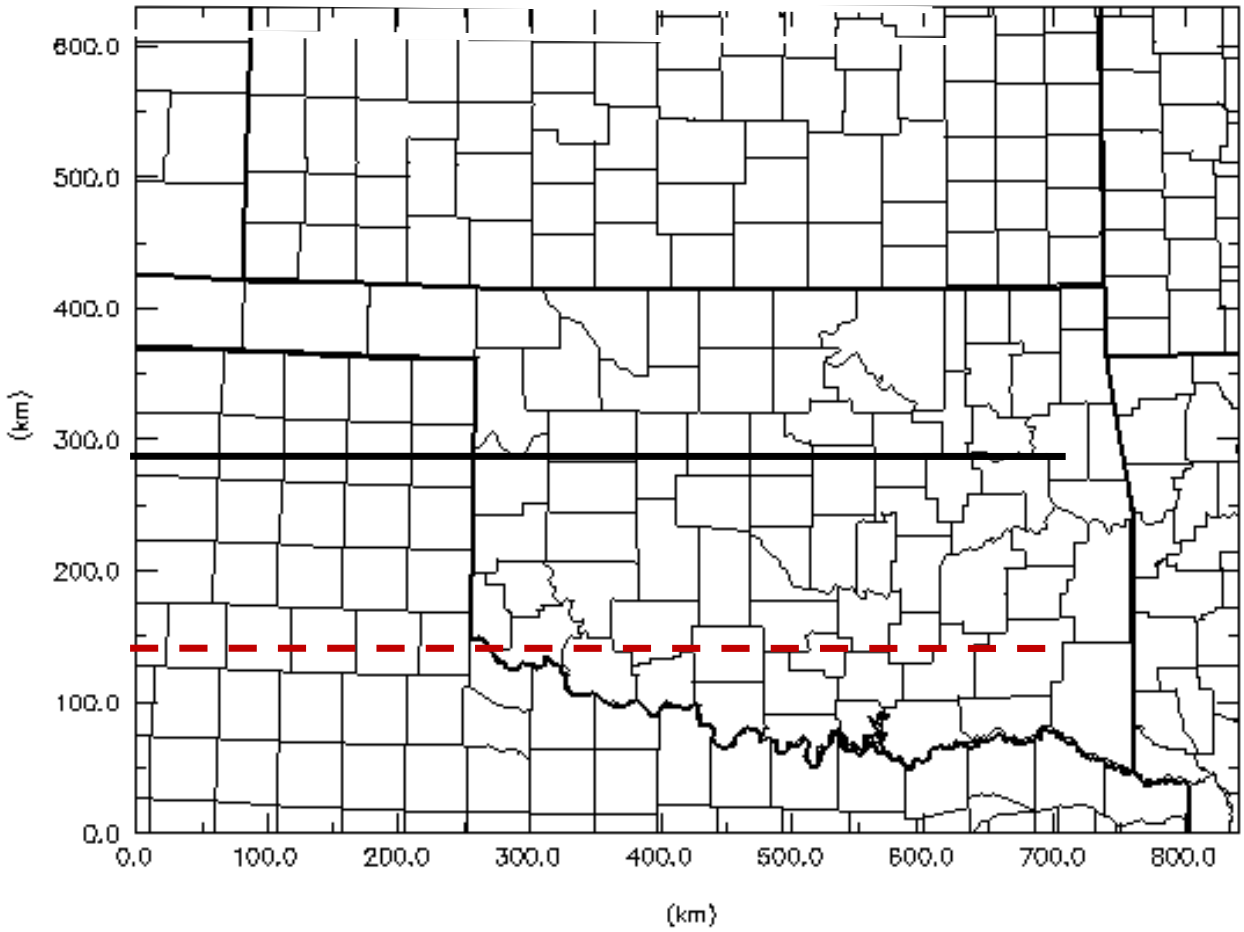

Figure 25. Map showing range of horizontal slices (Y = 85.5 km to Y = 295.5 km) taken for generated boundary layer cross-section of moisture variables for each experiment at 1800 UTC. The red dashed line corresponds to the Y = 85.5 km horizontal slice and the black solid line corresponds to the Y = 295.5 km horizontal slice.

Out of all the variable examined, the relative humidity and specific humidity cross-sections provide the best representation of the boundary layer structure for each of these horizontal slices. The cross-sections of specific humidity (Figure 26 and following) show both color shaded contours for mixing ratio values (ranging from 0 g/kg to 20 g/kg) and motion vectors (m/s) in the plane, denoting both moisture content of the air and direction of eastward and vertical motion, respectively. For the relative humidity cross-sections, in the following discussion values of 0.50 to 0.70 (tan to light green shading) represent regions of moderate relative humidity, while values of 0.70 and above (green shading) represent regions of high relative humidity. For the specific humidity cross-sections, values of 10 g/kg to 14 g/kg (light green shading) represent moderate levels of water vapor mixing ratio and the height of the 10 g/kg light green contour can represent the overall height of the moist boundary layer.

While the specific humidity cross-sections conveys information about both the magnitude of moisture throughout the boundary layer and the wind field, including vertical motion, the relative humidity cross-section is also useful because it depicts the regions of the boundary layer where relative humidity is at a maximum, where rising air is potentially near saturation that would create

cloud and release latent heat, and also the overall shape of the region of highest relative humidity, which is useful for delineating the boundary between drier air to the west and moister air to the east for the lower portion of the boundary layer. This was also able to be seen in the specific humidity cross-sections but as not as distinctly, presumably due to temperature effects across the region near the dryline.

Also, while vertical cross-sections were taken for slices from Y = 85.5 km to Y = 295.5 km, the overall pattern from west to east of the moisture field for slices taken at Y = 295.5 km were not much different except for how the position of the dryline was farther east with northward extent through Oklahoma, and how the top of the moist boundary layer changed from having a peak height closer to the center of the domain (450 to 500 km) to having a peak height closer to the eastern part of the domain (650 to 700 km). Additionally, as the position of the dryline shifted east, so did the area of maximum horizontal convergence (as shown by the length and density of vertical motion vectors in the water vapor mixing ratio cross-sections) was farther east corresponding to the dryline. Here we compare the maximum height of the moist boundary layer (which was taken as the maximum height of the light green shaded contours, as mentioned previously) and the shape and vertical extent of the area of maximum horizontal convergence at the dryline to judge how the OSSE experiments performed relative to one another and relative to the Nature Run.

The horizontal slice at Y = 217.5 km is chosen for discussion herein since this is the region in the Nature Run where convective initiation first occurs across part of west-central Oklahoma. The goal is to see how the boundary layer moisture structure and magnitude was setup leading up to the time of convective initiation in the region where storms first formed in the Nature Run.

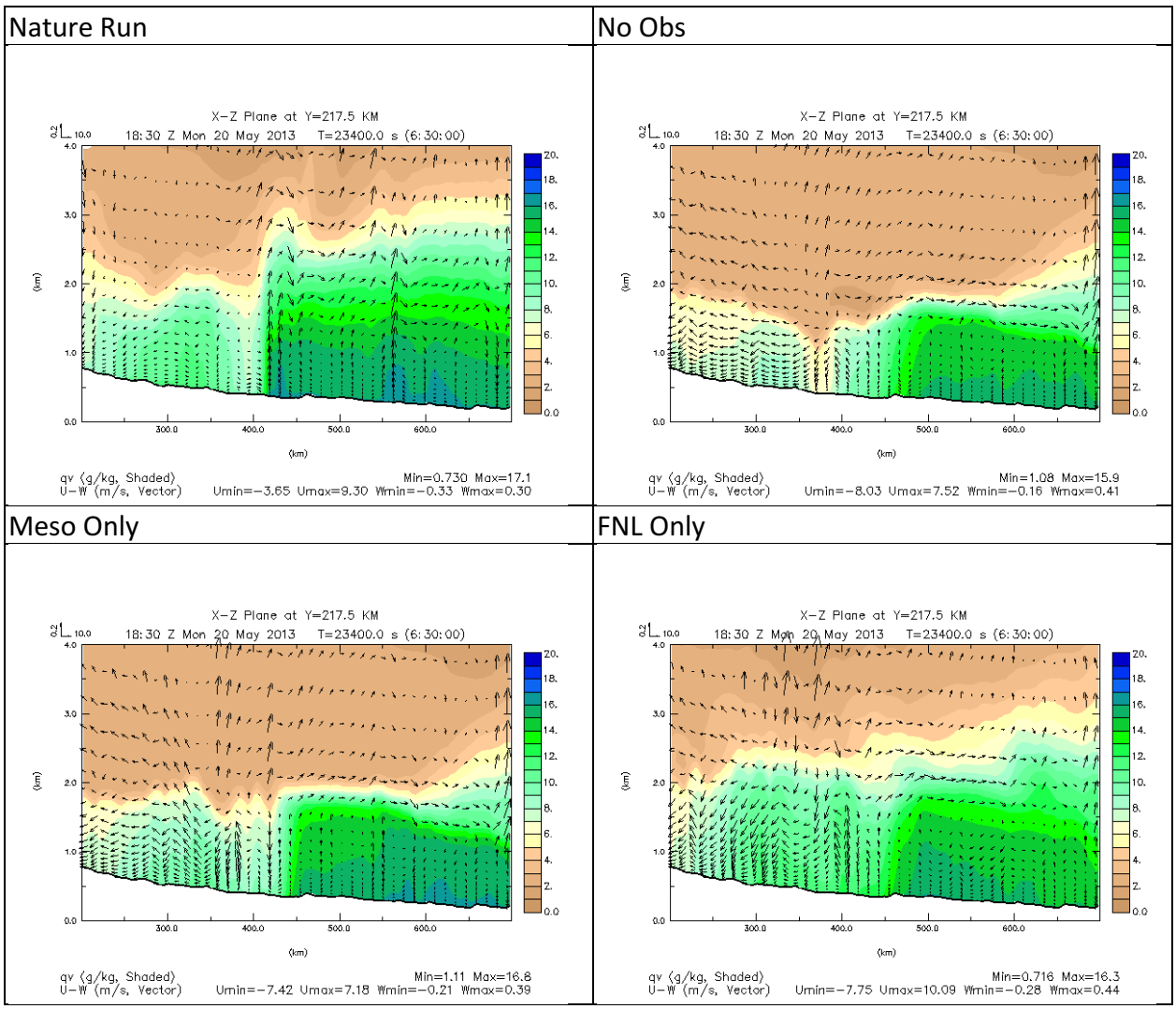

Figure 26. East-west vertical cross-sections of specific humidity (g/kg) (colorbar at right) and winds in plane for 1830 UTC at Y = 217.5 km. Nature Run, No Obs, Meso Only, and FNL Only experiments.

Compared to the Nature Run, both the No Obs and Meso Only experiments show the average height of the moist boundary layer east of the dryline only up to 1.0 km mean sea level (MSL) for most of the domain, whereas in the Nature Run the average height of the moist boundary layer extends to around 2.0 km MSL west of the dryline at 450 km (eastern Grady County)), and approximately 3.0 km MSL (with height increasing with eastward distance) east of 450 km. Both the No Obs and Meso Only experiments show this general pattern of increasing boundary layer moisture height with increasing eastward distance, but the average height of the boundary layer increases up to 2.5 km MSL only east of 600 km (Hughes-Okfuskee counties).

Despite the similarities between the No Obs and Meso Only experiments, there are some differences regarding whether the moisture peak seen in the Nature Run just east of the dryline is present and where it sets up. In the No Obs experiment, the narrow peak in boundary layer moisture seen in the Nature Run is not seen, and instead there is a minor localized peak in moisture around 475 km and a slight depression around 2.0 km MSL at 450 km, with intrusion from drier air aloft.

The Meso Only experiment, in contrast, shows a localized peak of boundary layer moisture farther west, behind the dryline, around 400 km, but with the height of the peak just below 2.0 km MSL. The Nature Run shows a region of strong vertical motion around 425 km, although the region of strong vertical motion extends higher up in the boundary layer for the Nature Run than in the Meso Only experiment. The data assimilation and forecast carry the impact of observations vertically, but the effect of observations being carried vertically for mesonet observations appears to be limited. Compared to the No Obs experiment, adding mesonet data helps better define the dryline, but the dryline is not as strong as when adding more data because mesonet data is only located at the surface.

Looking at the Nature Run experiment versus the FNL Only experiment, it is seen that compared to in the No Obs and Meso Only experiments, there is no clearly defined moisture peak showing the location of the dryline, and the average height of the moist boundary layer in the FNL Only experiment is much closer to the average height east of the dryline seen in the Nature Run. However, there is no defined moisture peak visible, with a more dome-shaped, gradual staircase pattern being seen instead, with the average height of the moist boundary layer increasing from around 2.25 km MSL to 2.75 km MSL at 400 km, and from 2.75 km MSL to around 3.0 km MSL at 650 km (Pittsburgh-Haskell counties). Concurrent with no visible moisture narrow moisture peak, there is no strong, narrow region of convergence and upward vertical motion, as shown by lack of density of stronger upward wind vectors, except within a region from 0.5 km MSL to 1.5 km MSL east of the dryline at around 500 km in Cleveland County.

For the FMU400ft108 experiment (Figure 27), the moisture peak associated with the dryline remains and is better defined than in the No UAV experiment, although still much less peaked in shape than in the Nature Run. The vertical velocity at the dryline is stronger at higher levels above 1.75 MSL than in the Nature Run. When looking at the FMU01km108 experiment, the max height of the moist boundary layer is similar to the FNL Only, No UAV, and FMU400ft108 experiments and the difference between height of the moist boundary layer west, versus east, of the dryline is still less apparent than in the Nature Run. However, the moisture intrusion at the dryline is more similar in width and peaked shape compared to the Nature Run than in the previous experiments. There is also better resolution of higher specific humidity (16 g/kg to 20 g/kg dark green to blue shaded contours) at the lowest levels near the dryline, in better agreement with the Nature Run.

Figure 27 also depicts how with the use of both FNL and Mesonet data in the No UAV data experiment, there is not much change compared to the separate FNL Only and Meso Only experiments in the overall structure of the max height of the moist boundary layer, except that the structure of the moist boundary layer becomes even more flattened and stair-case shaped in between the jumps in average height. Moisture peaks at 325 km (Washita County) and 400 km (Caddo County) and associated regions of strong convergence extend from the surface to 2.25 km MSL and from just above the surface to 3.0 km MSL, respectively, behind the dryline. The FMU400ft108 experiment shows much the same structure regarding the max height of the moist boundary layer as in the No UAV and FNL Only experiments, but with disappearance of the narrow peak of moisture at 275 km and a weaker, more diffuse convergence of winds in that region.

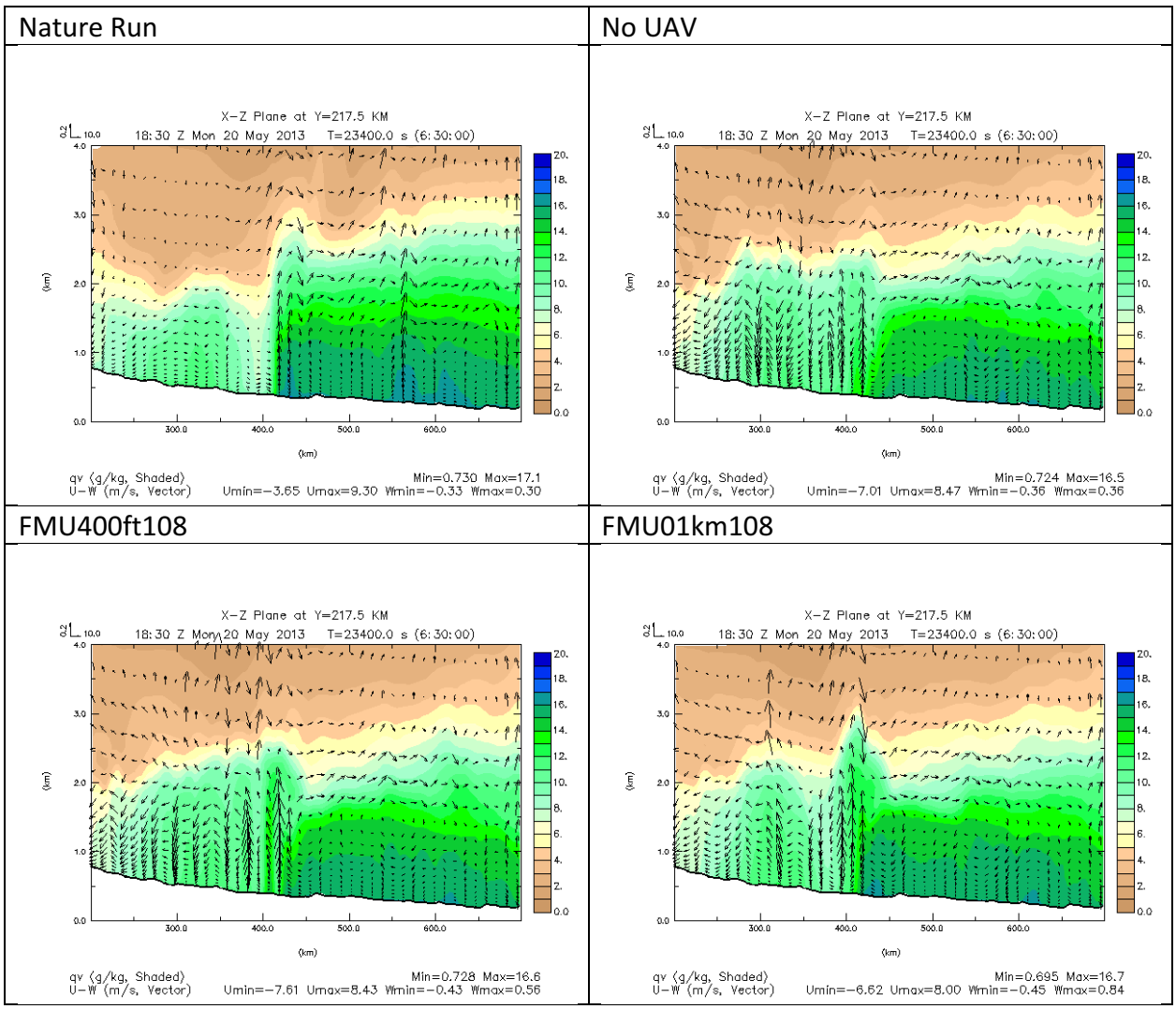

Figure 27. As in Figure 26. Nature Run, No UAV, FMU400ft108, and FMU01km108 experiments.

With the FMU02km108 experiment (Figure 28), the flattened, staircase shaped pattern seen in the FNL Only, No UAV, FMU400ft108, and FMU01km108 experiment is no longer evident, with the difference between height of the moist boundary west versus east of the dryline being more apparent, while the increase in average height of the moist boundary layer is more gradual, much like in the Nature Run. From 600 km and eastward (Hughes-Okfuskee to Le Flore-Sequoyah counties) however, the increase in average height of the moist boundary layer is a bit higher in magnitude, as seen by the higher slant of the 10.0 to 14 g/kg light green to green shaded contours at 600 km and eastward in the FMU02km108 experiment compared to in the Nature Run. In the region around 400 km at the dryline, there is a more rounded peak to the moisture intrusion. As with the Nature Run, this relative highest peak of moisture is associated with a region of strong upward motion from near the surface to around the top of the moist boundary layer intrusion, but like the FMU400ft108 experiment, the vertical motion above 1.75 km MSL in the FMU02km108 experiment is much stronger than in the Nature Run. Higher pooling of high specific humidity values up to 1.0 km MSL east of the dryline is evident in the FMU02km108 experiment compared

to the FMU01km108 experiment, although the shape of this pooled relative maximum in low level moisture is more broad than in the Nature Run.

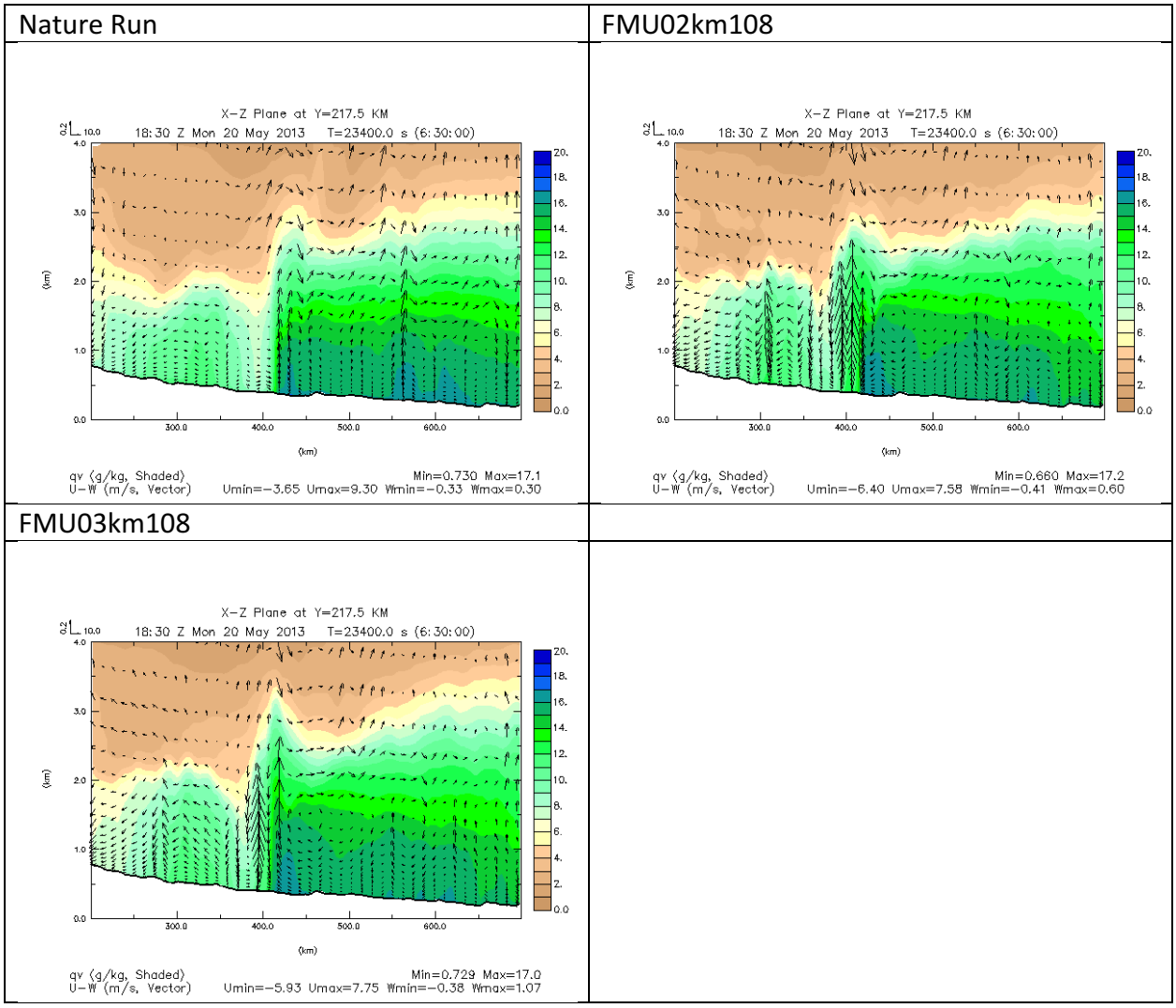

Figure 28. As in Figure 26. Nature Run, FMU02km108, and FMU03km108 experiments.

With the FMU03km108 experiment, the structure and magnitude of the moist boundary layer is much like that seen in the FMU02km108 experiment, with the exception being along the dryline. Here, the intrusion of moisture takes on a sharper peak with increased downward motion west of the dryline from about 2.0 km MSL extending down to the surface. This might indicate too much mixing and suppression of convection at the dryline compared to in the Nature Run and the OSSE experiments with max height of obs being at lower levels. Additionally, there is a sharper increase in the height of the moist boundary from 500 km (Cleveland County) eastward compared to the previous OSSE experiments, as well as a moister atmospheric profile from 2.75 km MSL to 3.0 km MSL, even compared to the Nature Run. This indicates too much moisture at higher levels of the boundary layer east of the dryline than is present in the Nature Run.

The most significant differences between the Nature Run and OSSE experiments were related to the height of the moist boundary layer west and east of the dryline, the shape of the highest peak of moisture intrusion along the dryline, and the structure and magnitude of vertical velocity in the moisture intrusion at the dryline (as shown by the different lengths and change in area covered by the wind vectors).

The least difference was in the magnitude and shape of the moisture profile in the lowest levels of the atmosphere (from the surface to 1.0 km MSL). Most of the OSSE experiments showed the same pattern of this between each other, with the height of the moistest part of the boundary layer (shown in 16 g/kg and 20 g/kg dark green and blue shaded contours, respectively) extending from the surface to 0.75 km MSL from 1.25 km MSL. All the OSSE experiments had slightly lower and more downward slanted profiles of the moistest, lower portion of the lower boundary layer east of the dryline compared to the Nature Run, indicated a lack of more substantial overrunning low level moisture farther east of the dryline at low levels in the OSSE experiments. The Nature Run showed a more even height and flat slope of the moistest, lower portion of the atmosphere east of the dryline, with dark green to blue shaded contours indicating relatively high levels of moisture consistently extending to an average height 1.25 km MSL east of the dryline, and having a more, wavy pattern than in the OSSE experiments, with peaks at 450 km (eastern Grady County) and around 550 km (Pottawatomie County), and troughs around 525 km (eastern Cleveland County) and 700 km (Le Flore-Sequoyah counties).

Overall, as with the plots of horizontal reflectivity, it is the FMU02km108 experiment that comes closest to resembling the Nature Run. The experiments that are the least similar to the Nature Run are the No Obs and Meso Only experiments, mainly because of the decreased average height of the moist boundary layer (specifically east of the dryline) and associated muted regions of vertical velocity. The second most similar OSSE experiment to the Nature Run is the FMU03km108 experiment, given the appearance clear height differences of the moist boundary west versus east of the dryline, even though there is too much moisture at higher levels east of the dryline in the FMU03km108 experiment compared to the Nature Run. Despite the closest similarity being between the FMU02km108 experiment and the Nature Run, the strength of the vertical motion is still too strong above 1.75 km MSL for the FMU02km108 experiment compared to in the Nature Run, with the region of strongest vertical motion and associated downward motion couplet noticeably narrower in the FMU02km108 experiment than in the Nature Run.

In all of the experiments, the dryline separating drier air to the west (as seen by tanner shades indicating lower specific humidity ratio values) and moister air to the east (as seen by the greener shades indicating higher specific humidity values) is set up within the region from 400 km to 450 km (Caddo to Grady counties). The greatest change between the OSSE experiments without UAV data is from adding data from FNL profiles, which increases the average height of the moist boundary layer by 1 to 2 kilometers compared to the No Obs and Meso Only experiments. In contrast, addition of UAV data does not show much change in average height of the moist boundary layer, except for an increasing contrast in height of the moist boundary west versus east of the dryline when UAV data from max heights above 400 ft are added.

While vertical cross-sections of specific humidity and vertical motion are instrumental in examining the structure of the boundary layer prior to convective initiation, factors such as mixing,

entrainment of drier air from aloft or west of the dryline, and areas of evaporation below cloud base complicate examination portions of the boundary layer closest to saturation and resultant cloud formation. To better hone in how the structure and magnitude of the most saturated portions of the boundary layer compares between the Nature Run and OSSE experiments, plots of relative humidity can be examined. Note that white regions represent areas where relative humidity is less than 50%. In the locations with relative humidity of 1.00, there can be expected to be regions of condensation leading to clouds (since these regions are saturated and assumed to be within cloud), and potentially enhanced vertical velocity with additional buoyancy from latent heat release.

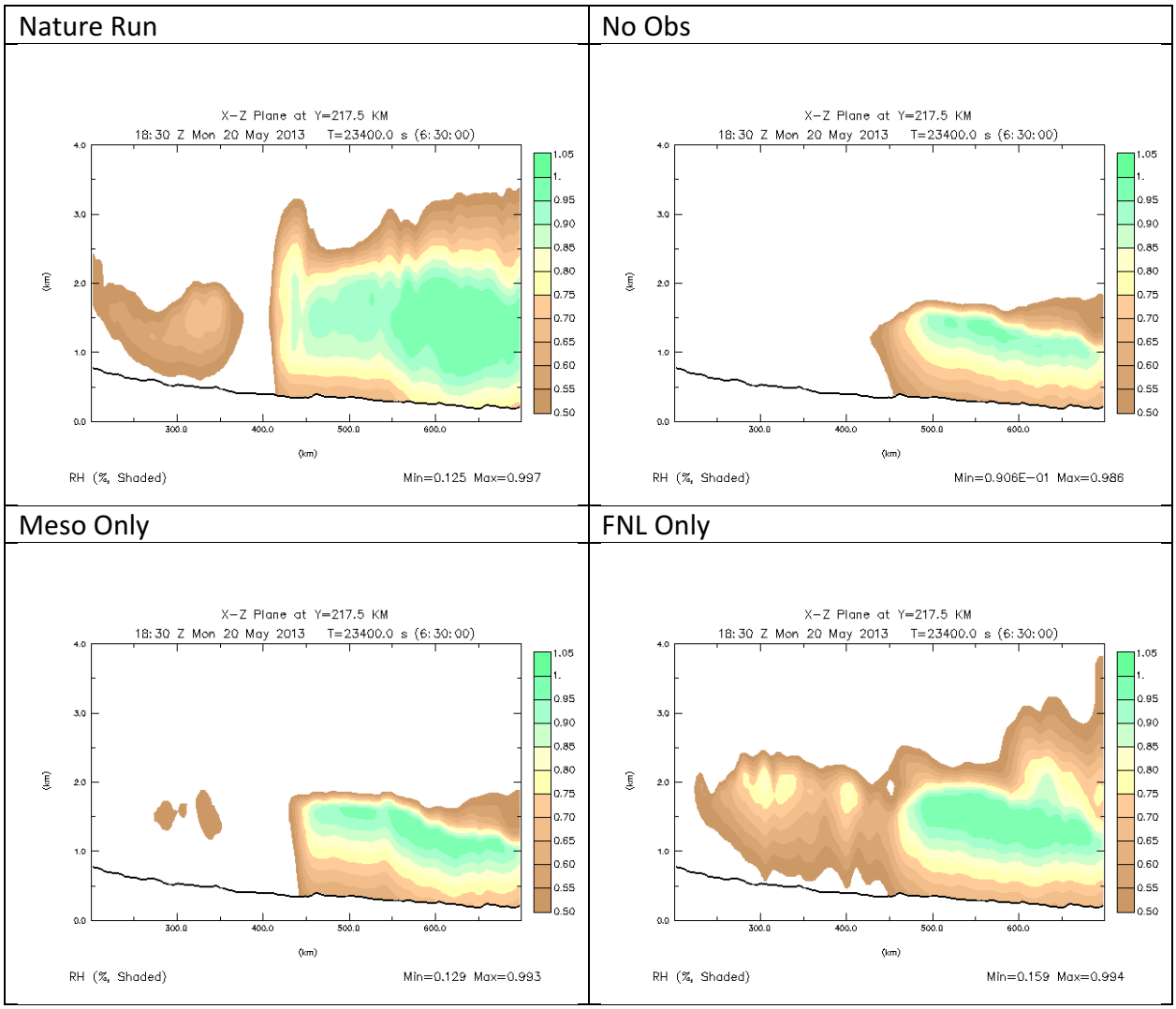

Figure 29. Vertical cross-sections of relative humidity (values from 0.50 to 1.00) (colorbar at right) for 1830 UTC at Y = 217.5 km. Nature Run, No Obs, Meso Only, and FNL Only experiments.

The Nature Run plot (Figure 29) indicates a peak of relatively moist air at 425 km (Grady County) extending from the surface to 3.25 km MSL. This demarcates the dryline. East of 400 km, the layer of near saturated air (relative humidity 0.90 and above) is concentrated within a layer from 1.0 km to 1.5 km MSL, with depth of this layer increasing east of 500 km (Cleveland County). West of the dryline, the air is nowhere close to saturation (as indicated by the 0.50 to 0.60 brown and 0.50

and below white shaded contours), The same structure and outline of the top of the moist boundary layer as seen in the water vapor specific humidity plots is not observed in the plots of relative humidity, with height of the boundary layer (as outlined by the 0.75 to 0.85 yellow shaded contours) staying capped around 2.25 km MSL. As with the plots of water vapor specific humidity, the No Obs and Meso Only experiments show a much shallower layer of air close to saturation east of the dryline than the Nature Run. However, when comparing the No Obs and Meso Only experiments, it can be seen that with the addition of mesonet data, the sharp vertical boundary between less moist air to the west and more moist air to the east at the dryline becomes better defined, as well as a more apparent increasing depth of air close to saturation in the 1.0 km to 1.5 km MSL layer. However, the height of the more moist air still reaches a lower height at and east of the dryline boundary (1.75 km MSL) compared to the Nature Run (2.25 km MSL). With the addition of FNL data, much like when FNL data was used for created the water vapor specific humidity plots, the depth of the layer of air closest to saturation increases, from 0.5 km-1.75 km MSL to 0.5 km-2.0 km MSL. These plots show that for the No Obs, Meso Only, and FNL Only data experiments, there was still imminent condensation leading to latent heat release occurring along the dryline like in the Nature Run, but that this latent heat release and vertical motion didn't extend as high up into the atmosphere along and east of the dryline as in the Nature Run.

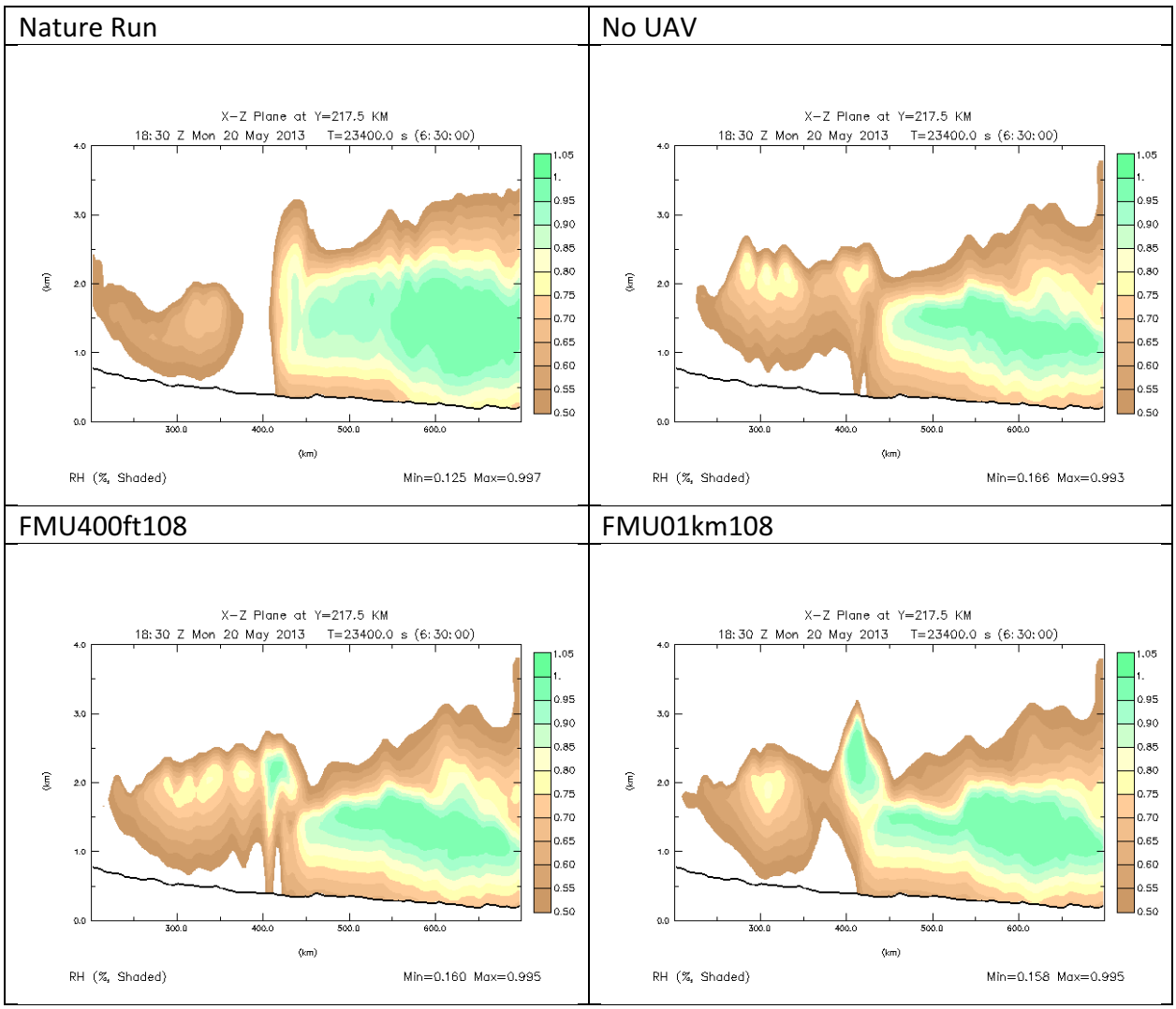

Figure 30. As in Figure 29. Nature Run, No UAV, FMU400ft108, and FMU01km108 experiments.

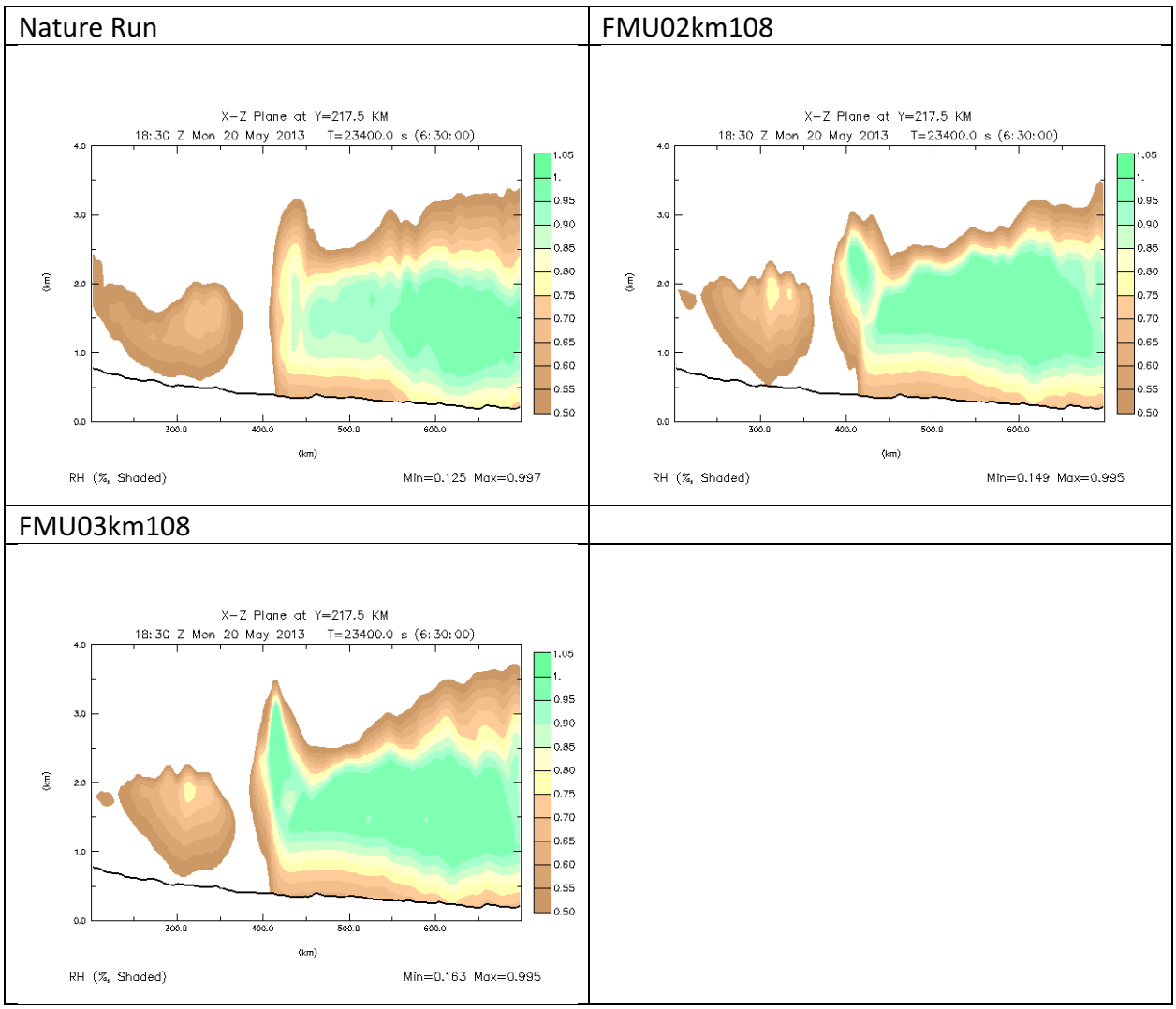

Figure 31. As in Figure 29. Nature Run, FMU02km108, and FMU03km108 experiments.

Comparing the Nature Run to the No UAV and FMU400ft108 experiments (Figure 30), it can be seen that there is not a lot of difference between the structure and depth of the layer closest to saturation for the No UAV and FMU400ft108 experiments. Compared to the Nature Run however, both experiments show a less sharp and less vertically oriented peak of the moistest air at the dryline and concurrently a less well defined dryline, with sporadic higher levels of moisture around 2.0 km MSL. Much as with the water vapor specific humidity plots, the FMU01km108 experiment generates results that more similar to the Nature Run than the No UAV and FMU400ft108 experiments. This is mainly because of the more defined peak of air closest to saturation at the dryline and the increasing depth of this moistest air with eastward extent being more apparent than the previous OSSE experiments.

Compared to the previous OSSE experiments, the FMU02km108 experiment (Figure 31) shows a larger depth of air close to saturation (value of 0.90 and above) in the moisture intrusion peak at the dryline and increasing depth of this layer of air east of the dryline. This region of near saturation extends higher into the atmosphere as the max height of UAV obs is increased, but becomes more

narrow as well. This shows that with experiments with higher max height of UAV obs, there is increasing height of near saturated air at the dryline prior to convective initiation. Still, compared to the Nature Run, this layer of air closest to saturation is not as vertically oriented at the dryline, with the sporadic moisture around 2.0 km MSL evident at 400 km. The FMU03km108 experiment on the other hand is less similar to the Nature Run than the FMU02km108 experiment, because the air at and east of the dryline that is closest to saturation is much more extensive in terms of depth and maximum height compared to the Nature Run, specifically east of 500 km (Cleveland County). This is in agreement with how there was much greater moisture at higher levels east of the dryline in the plots of water vapor specific when comparing the Nature Run to the FMU03km108 experiment.

Therefore, much as with the OSSE experiments producing data for the horizontal reflectivity and specific humidity vertical cross-section plots, the FMU02km108 experiment generates results of imminent latent heat release and ensuing vertical motion that best match those in the Nature Run, and the No Obs and Meso Only experiments generate results that are least similar to those in the Nature Run. Also, as with the specific humidity cross-section plots, the FMU01km108 experiment is more similar to the Nature Run than the No UAV and FMU400ft108 experiments, while the FMU03km108 experiment generates too much depth and unrealistically tall height of layers of air closest to saturation near and east of the dryline.

From plots of horizontal reflectivity at level 10, specific humidity vertical cross-sections at Y = 217.5 km, and relative humidity vertical cross-sections at Y = 217.5 km, it can be seen that in any situation, it is the preconvective environment in the FMU02km108 experiment that qualitatively, best resembles what is seen in the preconvective environment in the Nature Run. It is also seen from these plots that addition of FNL profile data in the data assimilation period helps with increasing resolution of moisture fields in the forecast period through a larger depth in the atmosphere at and east of the dryline, which is useful for simulating features like increased latent heat release through a deeper extent of the boundary layer, low topped convection, detrainment of moister air into higher levels of the atmosphere, convective initiation from lifting of shallow layers of air near saturation, downdraft strength and locations of outflow boundaries, and magnitude of moisture in layers of air close to saturation as communicated through max ranges of radar reflectivity in the early period of convective initiation, and peak water vapor specific and relative humidity values in core layers of relatively moist air at and east of the dryline.

In order to quantitatively assess which OSSE experiment (No Obs, Meso Only, FNL Only, FMU400ft108, FMU01km108, FMU02km108, FMU03km108) generated results with the least error compared to the Nature Run, and why addition of FNL data greatly reduced differences (in reference to the Nature Run) compared to the No Obs and Meso Only OSSE experiments, quantitative analysis was performed by examining the mean absolute error of thermodynamic variables like potential temperature (pt) and water vapor specific humidity (qv). This quantitative verification was performed by comparing the values of these variables every 5 minutes at several levels for each OSSE experiment to the values in the Nature Run interpolated at the 3 km ARPS grid for those same times and levels. The reference values in the Nature Run for these thermodynamic variables at these times and levels were taken as the truth, and used to compare the mean absolute error of each OSSE experiment to the other OSSE experiments that were conducted.

The quantitative analysis is shown as line graphs with different color and styled lines corresponding to different OSSE experiments (Figure 32 and following). The x axis is time 0 hours after assimilation/forecast start time at 1200 UTC May 20 to 15 hours after the assimilation/forecast start time (0300 UTC May 21). Error (measured in mean absolute difference from the Nature Run) is shown as the ordinate.

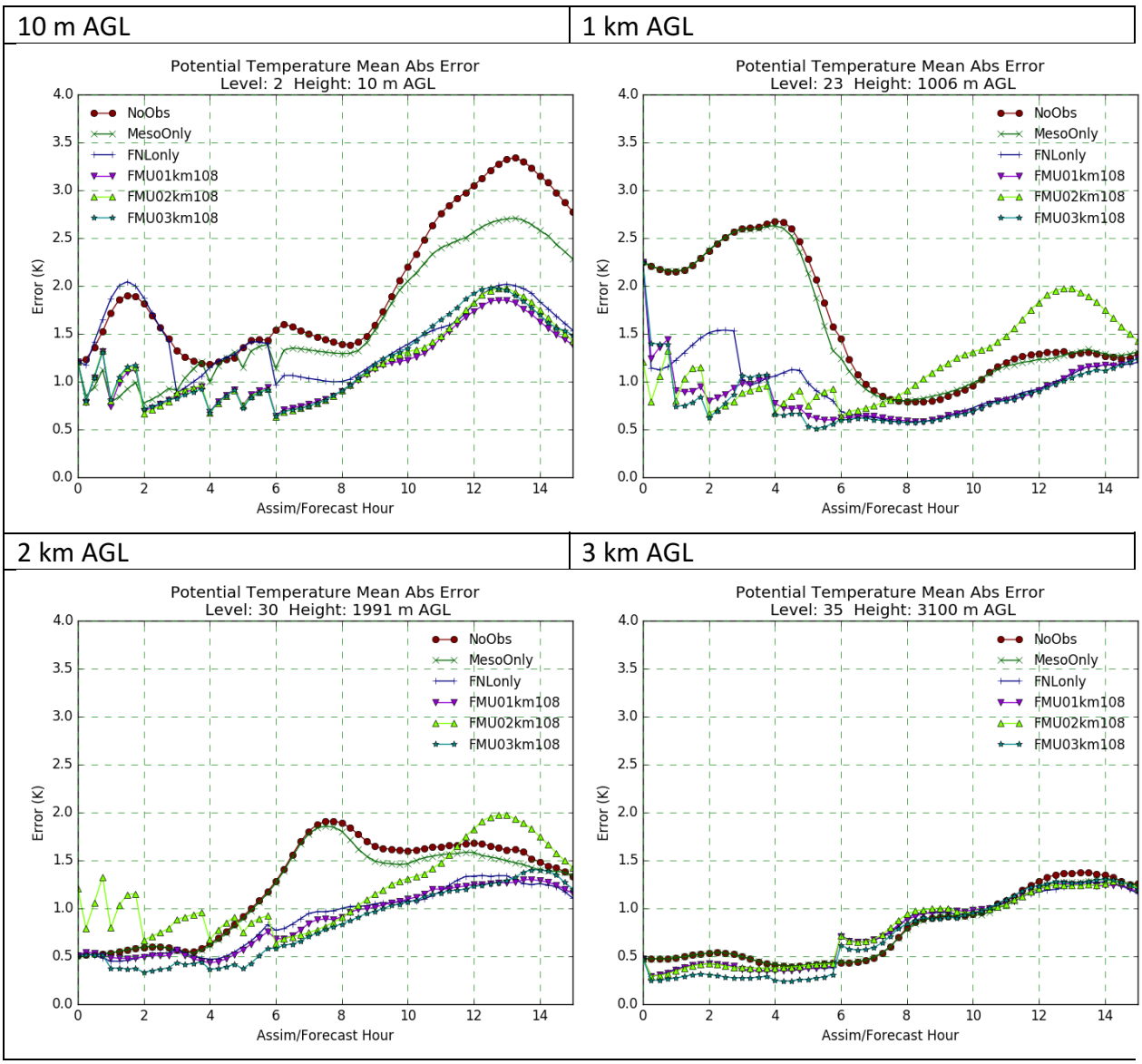

Figure 32. Forecast error time-series plots of Mean Absolute Error for Potential Temperature at heights 10 m, 1 km, 2 km, and 3 km AGL from 1200 UTC May 20 to 15 hours forecast (03 UTC May 21). Mean Absolute Error in Potential Temperature (°K), for six experiments as indicated in the legends.

Consider potential temperature mean absolute error at height 10 m, 1 km, 2 km AGL, and 3 km AGL for 6 of the OSSE experiments (No Obs, Meso Only, FNL Only, FMU01km108, FMU02km108 and FMU03km108) shown in Figure 32. Note that there is progressively less error throughout the assimilation period (0 to 6 hours) at all levels as more data (particularly Meso Only and FNL data) is added. Specifically, errors in the potential temperature data at all levels decrease slightly with addition of Mesonet data, drastically with addition of FNL data, less drastically with the combination of Mesonet and FNL (No UAV) data, and then to a smaller additional extent with addition of UAV observations from higher max heights (e.g.: 2 km max height versus 1 km max height). Adding mesonet observations had the greatest impact at reducing error at the 10 m level but little impact at 1 km, 2 km, and 3 km AGL. This is not unexpected since mesonet obs are taken at the surface and the effects of the mesonet obs are not spread in the analysis more than a few 100

m above the surface. It is apparent that addition of FNL data yields the most decrease in mean absolute error, with the decrease most pronounced during the assimilation period (0 to 6 hours) at 10 m and 1 km, at the end of the forecast period (10 to 14 hours) for at 10 m, the start of the forecast period (6 to 10 hours) at 2 km, and through the assimilation period (0 to 6 hours) at 3 km. Additionally, Figure 32 shows that the most improvement in adding additional data and UAV observations from higher max heights occurs at 10 m, followed by 1 km, and then 2 km. In contrast, there is not much noticeable improvement in adding data for a height of 3 km AGL except when looking at the FMU02km108 and FMU03km108 experiments. This is along the lines of what we'd expect, as it is only with the FMU02km108 and FMU03km108 experiments that we get better modeling of thermodynamic variable fields compared to the Nature Run at higher heights like 3 km AGL. For the addition of UAV data, the saw tooth pattern in the beginning of the forecast period (0 to 6 hours) at 10 m, 1 km, and 2 km AGL shows integration of the data and then the forecast error wandering up slightly, with a correction at the next hour. However, with each successive insertion the error is decreasing, so the magnitude of the saw tooth pattern becomes less throughout the assimilation period. This saw tooth pattern is not observed at 3 km AGL, possibly because compared to the other heights, mean absolute error in potential temperature is already relative low for all experiments even with no data. This is likely due to this level being mostly above the mixed boundary layer and generally better forecasted by the background model.

However, note that for 8 to 15 hours into the forecast period, error is somewhat greater for the FMU02km108 experiment than the FMU03km108, FMU01km108, Meso Only, and No Obs experiments for levels 1 km and 2 km AGL, but about the same for the level at 3 km AGL and less than the FMU03km108 experiment at level 10 m. While before this, at levels 10 m, 1 km, 2 km AGL and 3 km AGL, the level of mean absolute error in potential temperature is roughly the same for the FMU02km108 and FMU03km108 experiments. This quantitatively shows that the FMU02km108 experiment doesn't necessarily provides results closer to the Nature Run than the FMU03km108 experiment overall for all levels of the boundary layer when considering simulation of thermodynamic variables like potential temperature. The advantage of the FMU02km108 experiment over the FMU03km108 experiment is in simulating lower mean absolute error of potential temperature for the lowest plotted height (10 m AGL) and highest plotted height (3 km AGL) early on in the data assimilation period (0 to 6 hours) and for later in the forecast period from 8 to 15 hours.

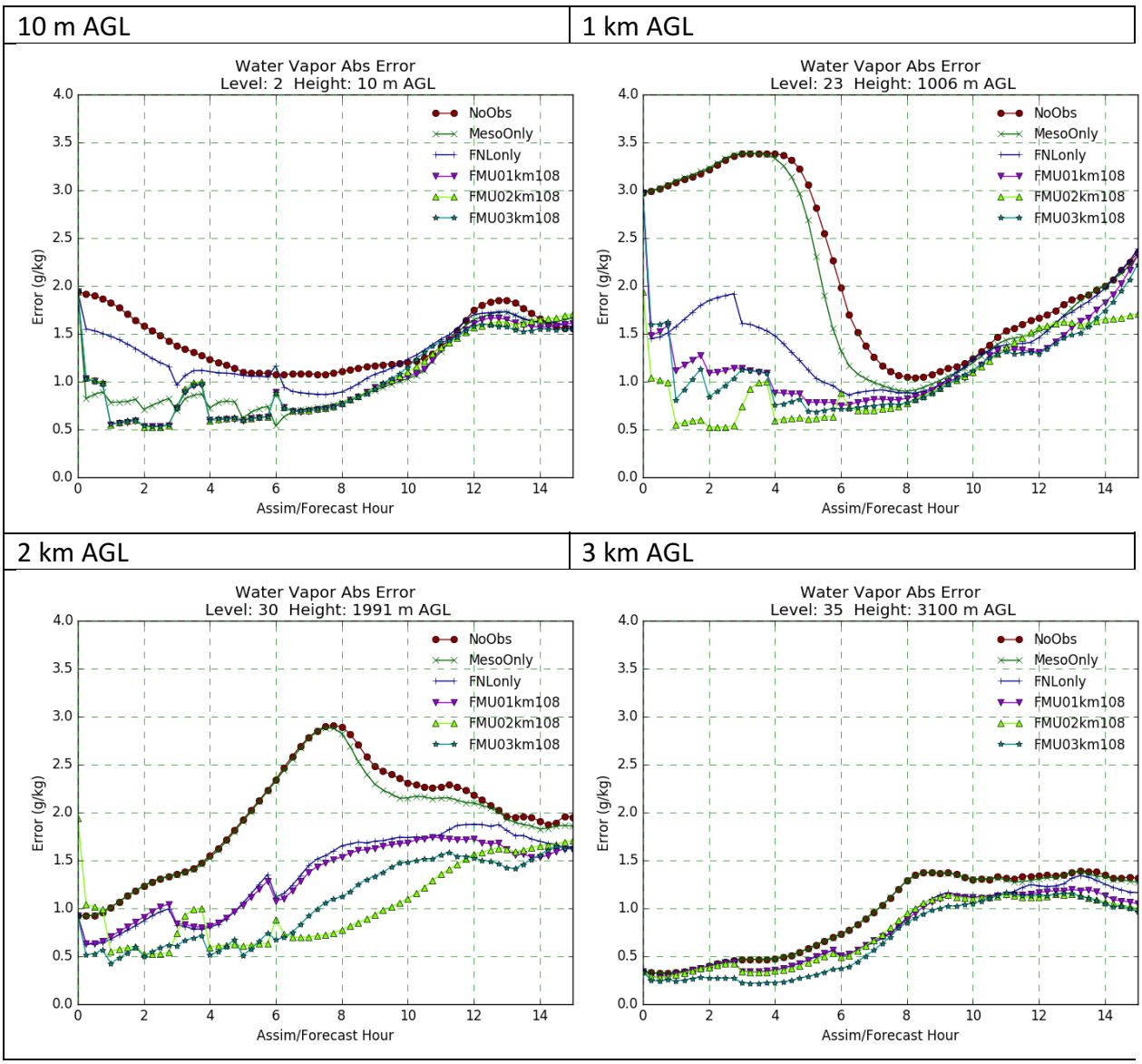

Figure 33. Forecast error time-series plots of Mean Absolute Error for Water Vapor Specific Humidity (g/kg) at heights 10 m, 1 km, 2 km, and 3 km AGL for 1200 UTC May 20 to 0300 UTC May 21. Mean Absolute Error in Water Vapor Specific Humidity (g/kg) for six experiments as indicated in the legend.

Plots of specific humidity mean absolute error at heights 10 m, 1 km, 2 km, and 3 km AGL AGL were constructed for the same 6 OSSE experiments (No Obs, Meso Only, FNL Only, FMU01km108, FMU02km108, and FMU03km108) are shown in Figure 33.

Here with the addition of more data, including UAV observations from higher max heights, the mean absolute error throughout the forecast period is reduced compared to the baseline (No Obs) for all other OSSE experiments at all levels, with the most decrease in error occurring mostly within the assimilation period (from 0 to 6 hours) for the OSSE experiments at 1 km AGL and for the early portion of the free forecast period (6 to 10 hour window) for the OSSE experiments at 2 km AGL. In contrast, there is not much change in mean absolute error of water vapor specific humidity at the lowest level (10 m) or the highest level (3 km) listed out of all the four plots, as

pre and post addition of UAV data, mean absolute error in specific humidity is relatively low compare to at other levels. This differs from how mean absolute error of potential temperature was significantly decreased at the lowest level (10 m AGL) at the beginning and end of the forecast period when more data was added for the OSSE experiments, but is similar to the lower overall mean absolute error in potential temperature for all experiments at the highest level (3 km AGL).

It is worth noting that the background fields for specific humidity started with the least error at 10 m and 3 km AGL compared to at 1 km and 2 km, due to a better background forecast at these levels, so this partially explains why the mean absolute error of specific humidity did not decrease as much at 10 m and 3 km AGL. However, unlike with potential temperature, there is consistently the pattern that mean absolute error is noticeably lower for the FMU02km108 experiment than the FMU03km108 experiment in the forecast period (6 hours to 11 hours) for all levels. There is less mean absolute error in specific humidity for the FMU03km108 experiment compared to the FMU02km108 experiment in the 11 to 15 hour forecast time window at 10 m AGL, 1 km AGL, and 2 km AGL, but not all at level 3 km AGL (where the mean absolute error for the FMU02km108 experiment remains lower than the FMU03km108 experiment. This indicates at lower levels below 3 km AGL, there is not much difference in the assimilation period when modeling vertical profiles of moisture concerning whether you add UAV obs from a max height of 2 km or 3 km AGL, as both yield a similar reduction in mean absolute error of specific humidity compared to the baseline (No Obs). Also, it indicates that at lower levels below 3 km AGL, there is actually more error in modeling moisture later in the forecast period (specifically the 11 to 15 hour window) when assimilating UAV obs from a max height of 2 km instead of UAV obs from a max height of 3 km. The only improvement in simulating consistently lower mean absolute error in specific humidity for the FMU02km108 experiment over the FMU03km108 experiment is applicable at the highest plotted level (3 km AGL).

What Figure 32 and Figure 33 demonstrate is that generally, adding more data that encompasses a greater depth of the boundary layer (as when using FNL data instead of Mesonet data) results in decreases of mean absolute error compared to the Nature Run for thermodynamic variables like potential temperature and a water vapor specific humidity. The least error for the thermodynamic variables throughout the forecast period consistently occurs in the FMU03km108 experiment at levels 1 km and 2 km AGL, where the max height of UAV observations is 3 km. So even though qualitative analysis of vertical cross-sections of water vapor specific humidity and relative humidity suggest the most improvement in modeling moisture fields at higher levels (2 km and above) at the end of the assimilation period/start of the forecast period at 1800 UTC was obtained with UAV observations from max heights of 2 km and not 3 km, quantitative analysis shows that all else equal, adding UAV observations using UAV obs from a max height of 3 km AGL decreases overall error of the OSSE experiment compared to the Nature Run for thermodynamic variables during the entire window, but especially for the forecast period following the assimilation period in 1 to 2 km AGL layer. Still, for this set of experiments, we prefer the UAV obs from max height of 2 km data due to the most qualitative similarities between the Nature Run and FMU02km108 experiment for the plotted horizontal reflectivity and vertical cross-sections of moisture in the boundary layer and how storm forecasts are more sensitive to moisture than temperature (Crook, 1996), despite quantitatively, much larger error growth in potential temperature and specific humidity at later hours at 1 km and 2 km AGL with assimilation of UAV obs from max height of 2 km compared to assimilation of UAV obs from max height of 3 km data.

By means of the IAU Data Assimilation, vertical cross-sections of water vapor specific humidity and relative humidity indicate that addition of observations at low levels (from Mesonet, FNL, and UAV observations at max heights of 400 ft and 1 km AGL) can affect moisture aloft in comparison with the No Obs data experiments, but mainly in horizontal convergence/updraft areas, with the most improvement seen in magnitude and structure of moisture in low levels (surface to 2 km AGL). However, the plots of horizontal reflectivity, vertical cross-sections of water vapor mixing ratio and relative humidity, and quantitative analysis line graphs showing mean absolute error of water vapor specific humidity at multiple levels all show that increased moisture at and above 2 km AGL is more apparent when adding UAV observations from max heights at 2 km or 3 km AGL for the 108 station UAV setup, specifically for the highest level (3 km AGL), which is the only level where addition of UAV obs from a max height of 3 km results in noticeably higher error in the forecast period than addition of UAV obs from a max height of 2 km. Therefore, as hypothesized before, we can expect that the utility of assimilating UAV obs from higher max heights of 2 km and 3 km will be most apparent in reducing forecast errors for modeled temperature and moisture fields for higher levels of the boundary layer (2 km and 3 km AGL).

d. Examination of Number of UAV Sites (Station Density)

Now that we have qualitatively and quantitatively analyzed how assimilation of Mesonet, FNL and UAV observations from 2 km for 108 UAV observations input from the data assimilation window for the FMU02km108 experiment compare to the baseline No Obs data, it is worth studying how reducing the number of UAV observations affects how similar results in the OSSE experiments are to the Nature Run. Since the max height of UAV observations for 108 UAV observations which generally gave the best results compared to the Nature Run out of all the other max heights was 2 km, tests will be conducted looking at how decreasing the number of UAV observations (from 108 to 75 down to 10; see Table 1.) affects forecasts for horizontal plots of reflectivity and vertical cross-sections of moisture when assimilating 3-hourly FNL data, hourly Mesonet data, and hourly UAV observations from a max height of 2 km.

Nature Run	FMU02km108
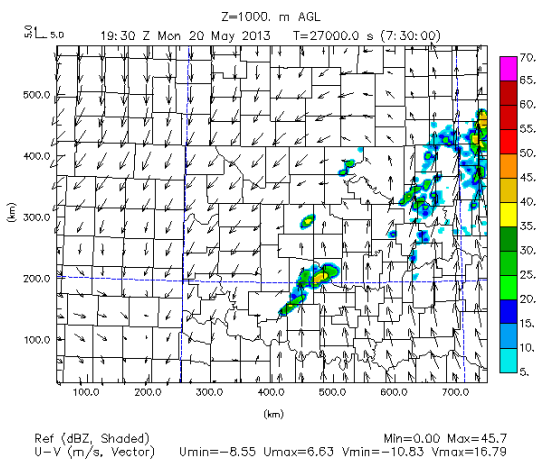	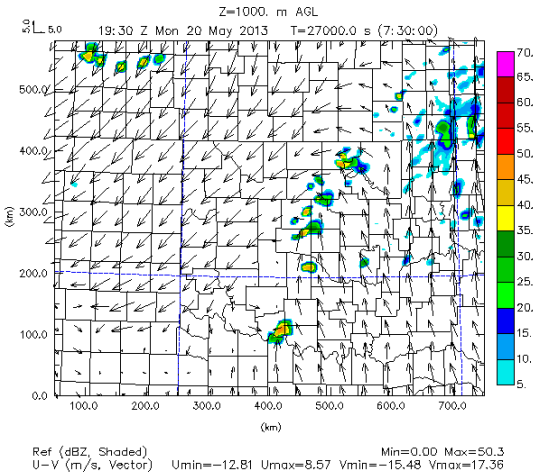
FMU02km075	**FMU02km050**
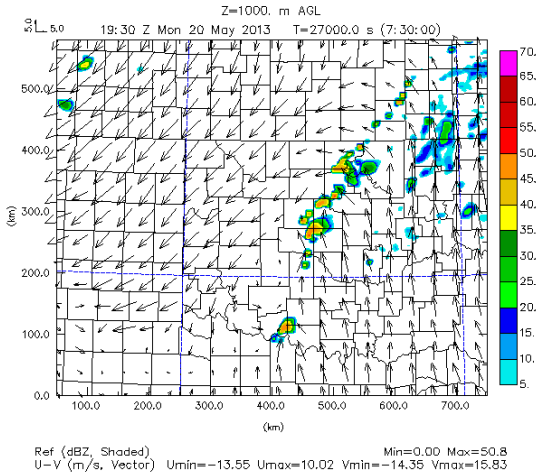	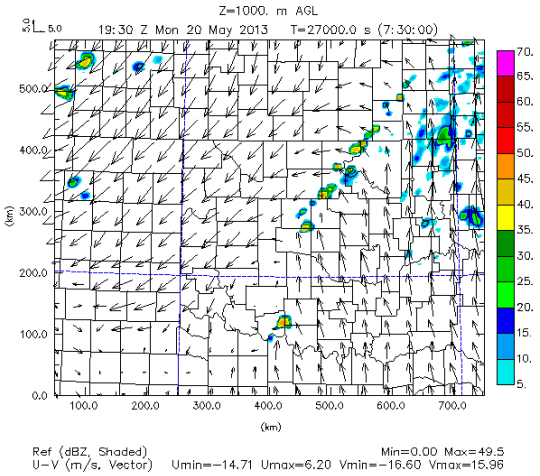

Figure 34. As in Figure 16. Nature Run, UAV obs from max height of 2 km with 108 stations (FMU02km108), 75 stations (FMU02km075), and 50 stations (FMU02km050).

Nature Run

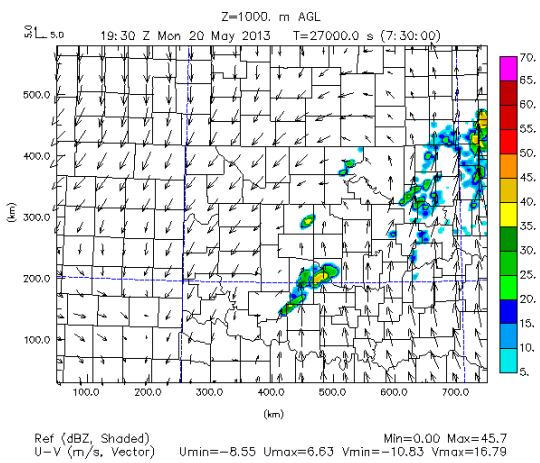

FMU02km025

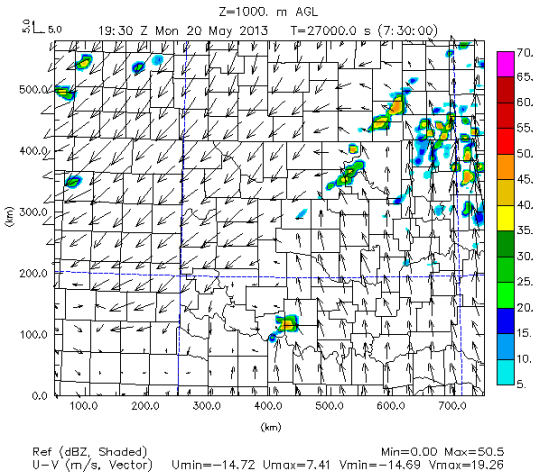

FMU02km010

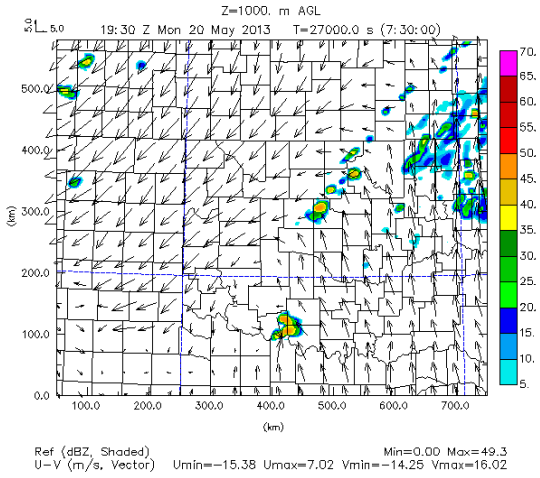

Figure 35. As in Figure 34. Nature Run, UAV obs from max height of 2 km with 25 stations (FMU02km025) and 10 stations (FMU02km050).

Concerning convection along the dryline in central Oklahoma and the warm front in northeast Oklahoma, Figure 34 and Figure 35 indicate that the FMU02km108 experiment best matches results from the Nature Run, while the FMU02km025 experiment is least similar because of unusually large intensity of spurious convection in southeast Kansas and southwest Oklahoma that is not present in the Nature Run and is more intense than in the FMU02km010 experiment (which is the other least similar experiment to the Nature Run at this time).

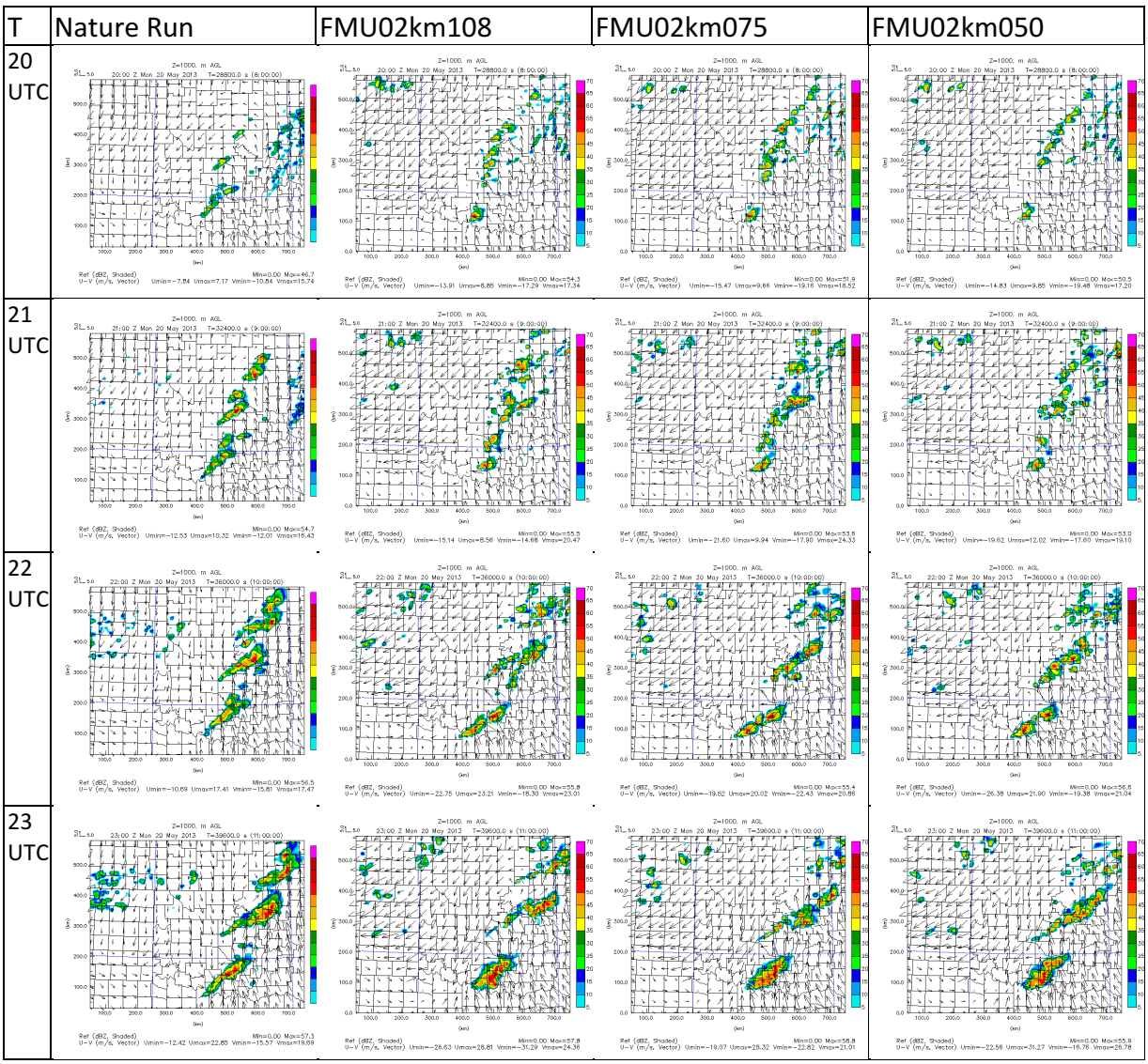

Figure 36. As in Figure 20. Nature Run, UAV obs from max height of 2 km with 108 stations, 75 stations, and 50 stations data experiments.

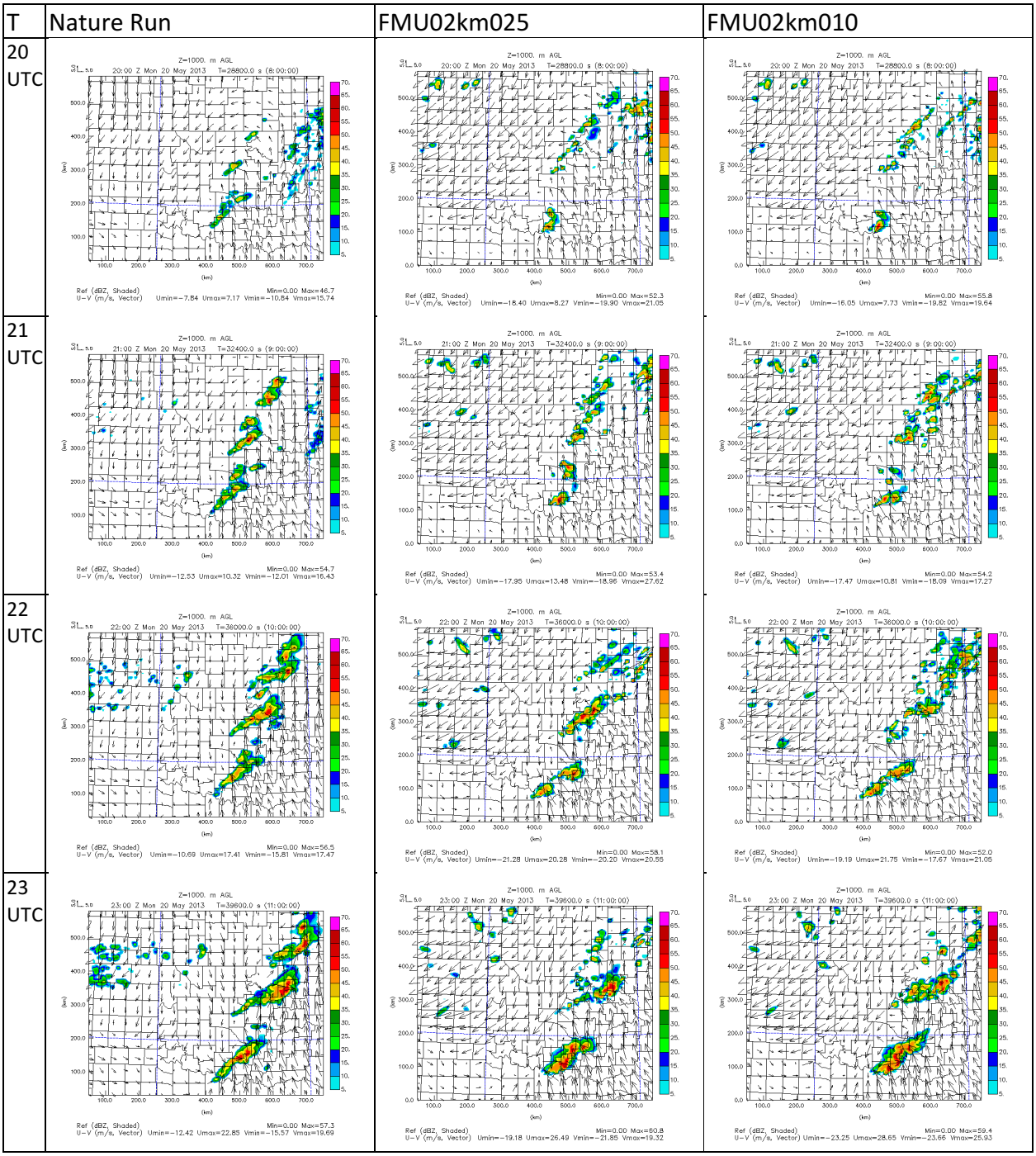

Figure 37. As in Figure 36. Nature Run, UAV obs from max height of 2 km with 25 stations, and 10 stations experiments.

Plots of reflectivity in the Figure 36 and Figure 37 show that compared with the Nature Run, the FMU02km108 experiment provides the closest match with how storms move northeast through Cleveland County from 2000 to 2100 UTC, go on to form three separate areas of convection in southwest Oklahoma, eastern parts of north-central Oklahoma, and southeast Kansas, and form a relatively thin width, eastward moving, southern portion of the QLCS in southern Oklahoma. Due to the absence of more consistently filled in reflectivity in northern and northeastern Oklahoma

and southeastern Kansas in the FMU02km025 and FMU02km010 experiments, these experiments are the least similar to the Nature Run out of all the other UAV obs at 2 km max height OSSE experiments, even though overall the FMU02km025 and FMU02km010 experiments are still quite similar to the Nature Run in simulating the rest of the convective features.

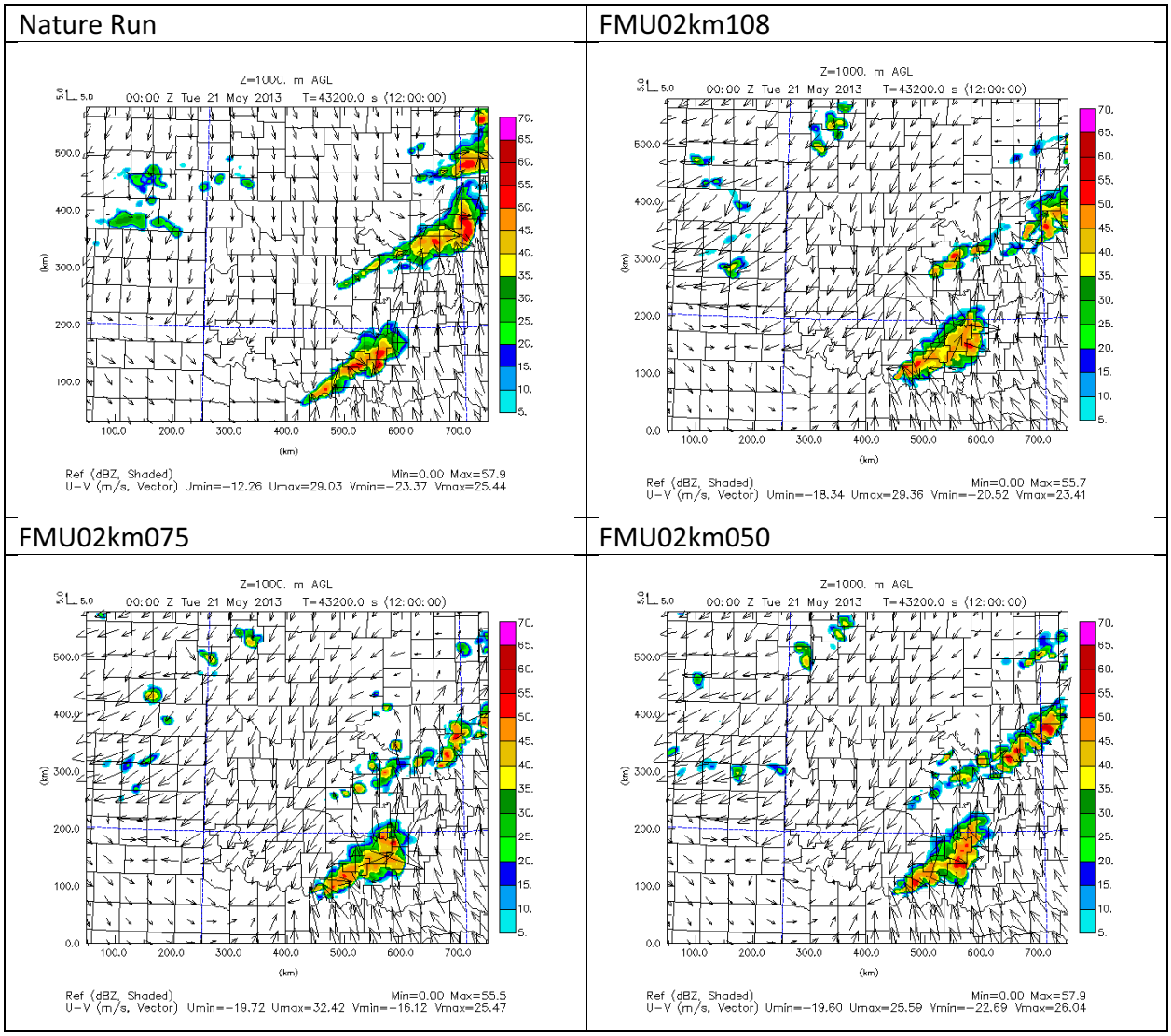

Figure 38. As in Figure 34, except for 00 UTC May 21. Nature Run, UAV obs from max height of 2 km with 108 stations, 75 stations, and 50 stations.

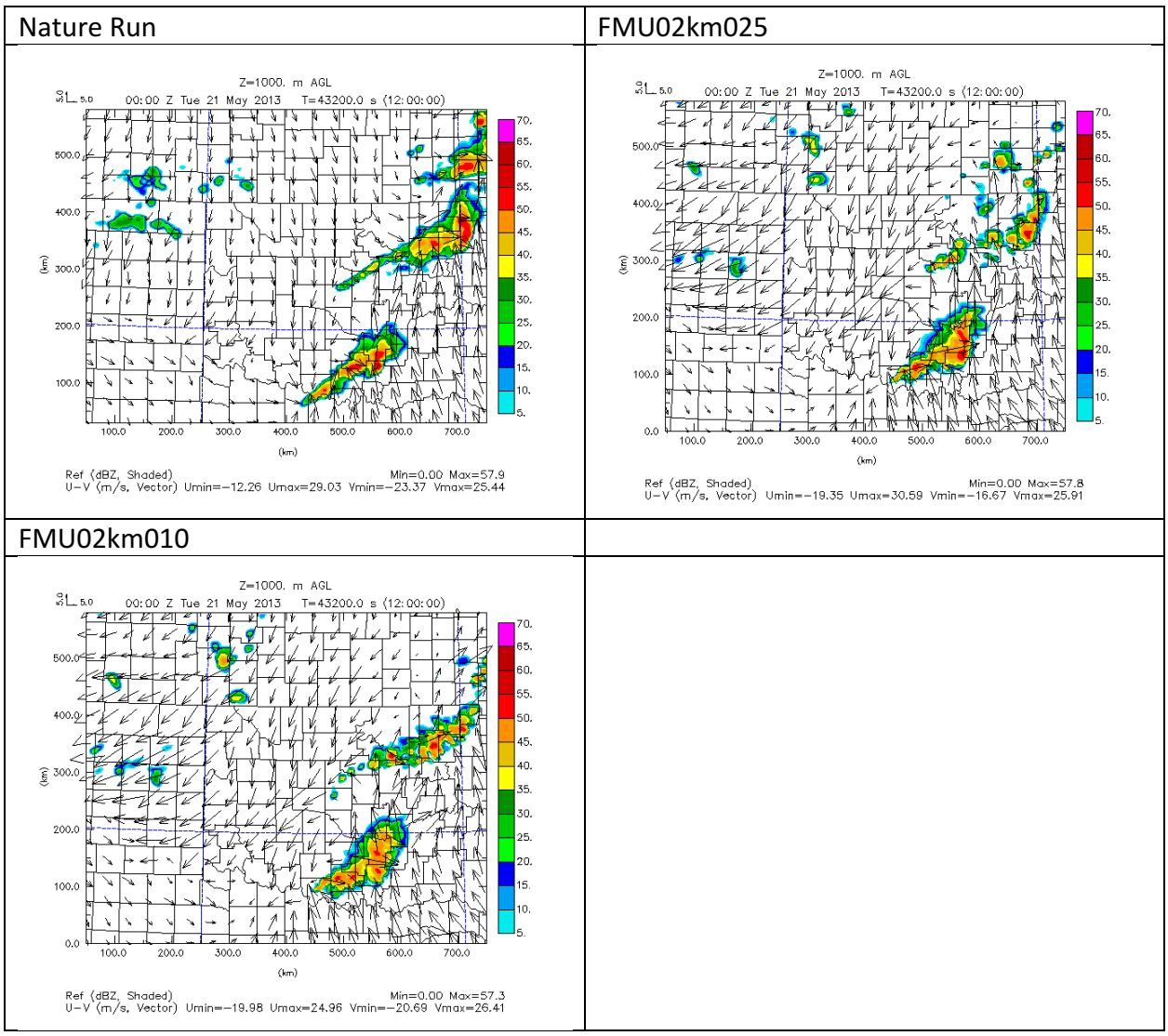

Figure 39. As in Figure 34. Nature Run, UAV obs from max height of 2 km with 25 stations, and 10 stations.

Figure 38 and Figure 39 depict that with respect to evolution, orientation and continuous structure of the QLCS convection in northeastern Oklahoma (Ottawa County down to Tulsa-Osage-Pawnee counties) at 0000 UTC, the FMU02km050 experiment actually has the closest results to the Nature Run, with the FMU02km075 and FMU02km050 experiments being the least similar because of the sporadic, discontinuous nature of the QLCS convection in northeastern Oklahoma (specifically from Rogers to Payne counties) compared to the Nature Run.

Similar to the prior analysis for max height of the UAV data, plots of boundary layer vertical cross-sections at the end of the assimilation window (1800 UTC) shortly before convective initiation are examined to see the results of how changing the number of stations for UAV obs with max height of 2 km compares with the Nature Run in the height and structure of the boundary layer.

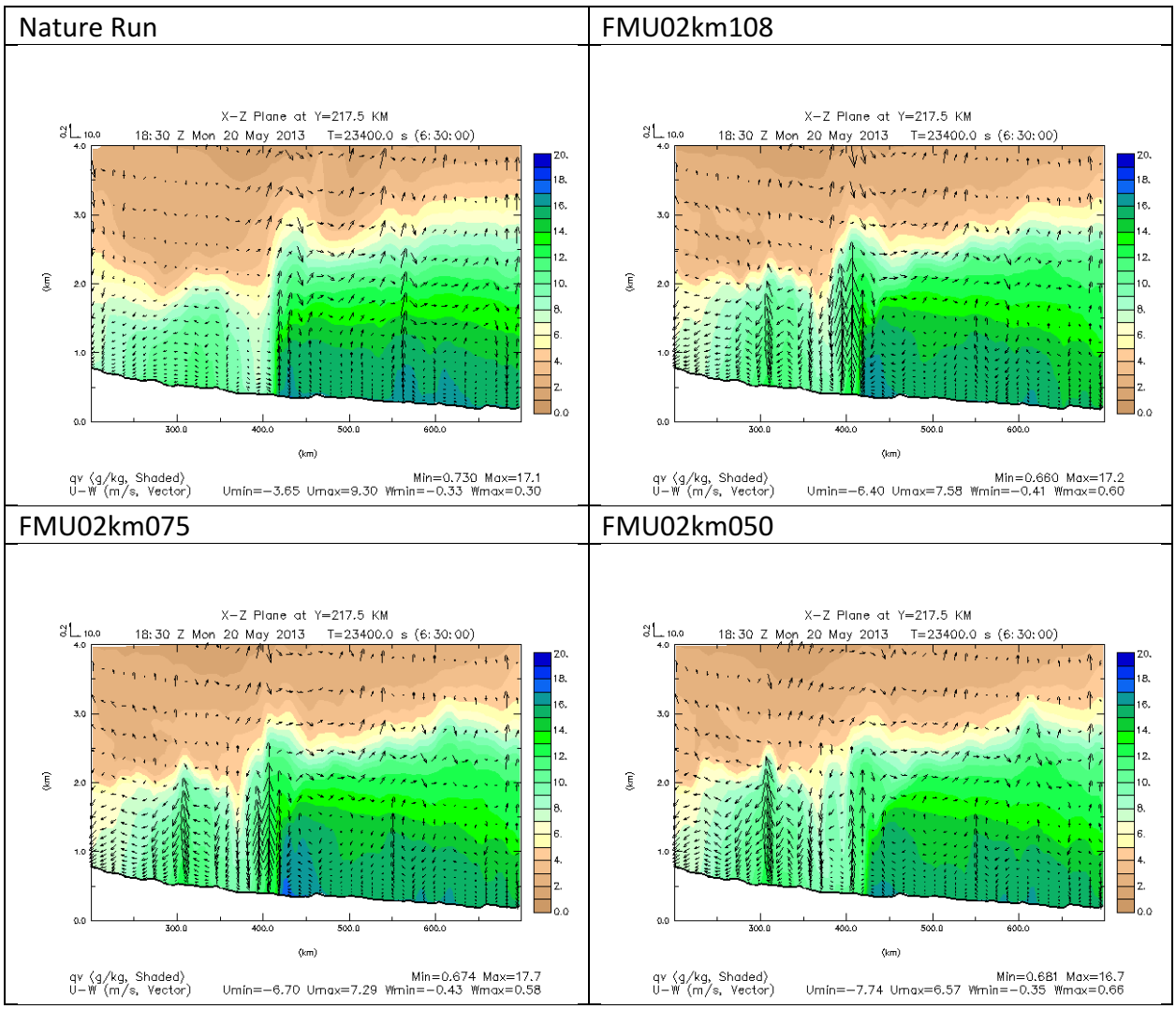

Figure 40. As in Figure 26. Nature Run, UAV obs from max height of 2 km with 108 stations data, 75 stations data, and 50 stations data.

As noted earlier, the FMU02km108 experiment provides the most comparable results to the Nature Run in terms of considering the configuration (height, shape and magnitude of values) of the moist boundary layer. When examining how reducing the number of stations to 75 and then 50 in the OSSE experiments for UAV obs at a max height of 2 km affects results, it can be seen that while the overall configuration of the moist boundary layer does not change much in terms of the overall height of the moist boundary west versus east of the dryline. However, when reducing the number of stations from 108 to 75, the FMU02km075 plot shows more broadening of the region of vertical motion at the dryline. Reducing the number of stations down to 50, the FMU02km050 plot of specific humidity shows that the region of upward vertical winds at the dryline becomes more diffuse, while a second set of upward vertical winds is apparent at 300 km in Washita County. Due to the disappearance of a single column of strongest vertical winds at the dryline boundary and appearance of a secondary set of upward vertical winds west of the dryline FMU02km050 experiment is less similar to the Nature Run and the FMU02km108 experiments than the FMU02km075 experiment.

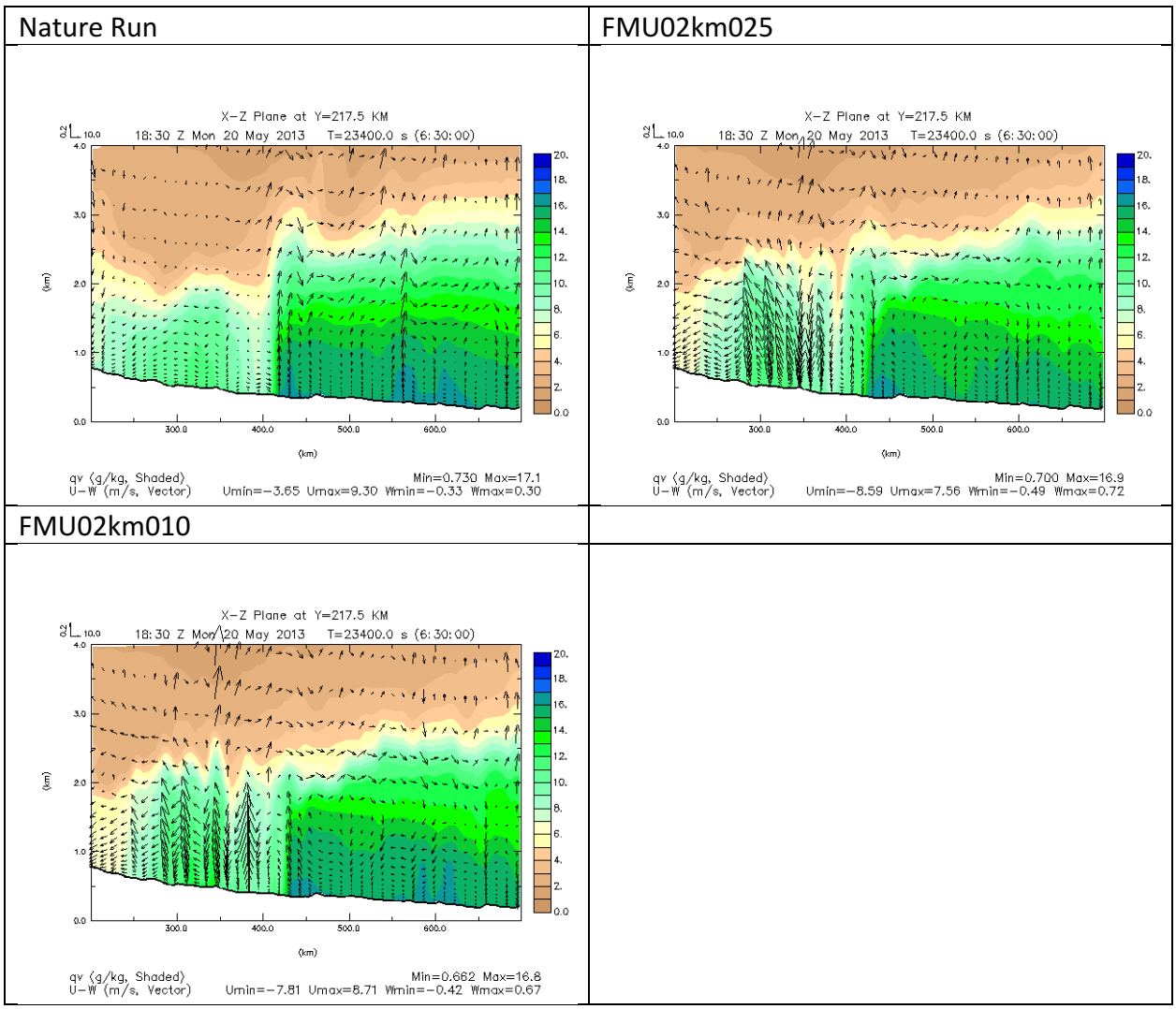

Figure 41. As in Figure 40. Nature Run, UAV obs from max height of 2 km with 25 stations data, and 10 stations data.

As evident from the disappearing 16 to 20 g/kg dark green to blue shaded contours in the lowest few meters of the atmosphere just east of the dryline as the number of UAV obs is decreased, there is also decreasing low level moisture east of the dryline in the FMU02km050 experiment compared to the Nature Run and FMU02km075, FMU02km108 experiments.

As with the FMU02km108 experiment, the profile of this very moist bottom layer east of the dryline is relatively slanted from west to east even as the number of UAV obs is decreased, instead of being more evenly flat shaped like in the Nature Run.

Continuing with reducing the number of stations down to 25 (Figure 41), it is seen how the shape of the top of the moist boundary becomes more flattened and stair-case shaped when compared to the Nature Run as well as the FMU02km108, FMU02km075, and FMU02km050 experiments. Additionally, the region of upward vertical winds at the dryine becomes even more diffuse, while a layer of upward vertical winds from around 300 km to 350 km (behind the dryline in Washita to

Caddo counties) develops from the surface extending up to 2.0 km MSL, with pockets of drier air entraining in between the relative maximums in vertical velocity. As has been the case for the progression of fewer UAV obs in OSSE experiments, the FMU02km025 experiment shows a less clearly defined boundary layer moisture gradient outlining the dryline region, as well as the continued disappearance of a moisture intrusion and single column of upward vertical winds contained in that moisture intrusion at the dryline boundary.

Finally, reducing the number of stations down to 10 shows that the single peak of vertical velocity along the dryline vanishes and instead, there are multiple weak peaks of vertical velocity extending from the surface to around 2.0 km MSL between 300 and 350 km (Washita and Caddo counties) and even farther west around 275 km (Beckham-Roger Mills counties). In comparison to the Nature Run and the FMU02km108, FMU02km075, FMU02km050, and FMU02km025 experiments, the FMU02km010 experiment gives the least realistic results in this regard.

Therefore, overall it is found that in comparison to boundary layer profiles of specific humidity and winds, the FMU02km108 experiment is the most similar to the Nature Run and the FMU02km010 experiment is the least similar, with noticeable diminishing returns from using less than 75 UAV obs when seeking the presence of a single defined moisture intrusion and associated maximum magnitude in upward vertical winds at the dryline boundary. This could explain why convective initiation and placement of storms is significantly degraded when less than 75 UAV obs are used.

Moving on to examination of relative humidity boundary layer profiles, comparison of the Nature Run with the OSSE station density experiments (Figure 42) shows how there is increasingly less area and upward extent o near saturated air at the dryline when the number of UAV obs is decreased below 75. Again, this is a possible explanation for why convective initiation and placement of storms becomes less similar to the Nature Run once the number of UAV obs is decreased below 75.

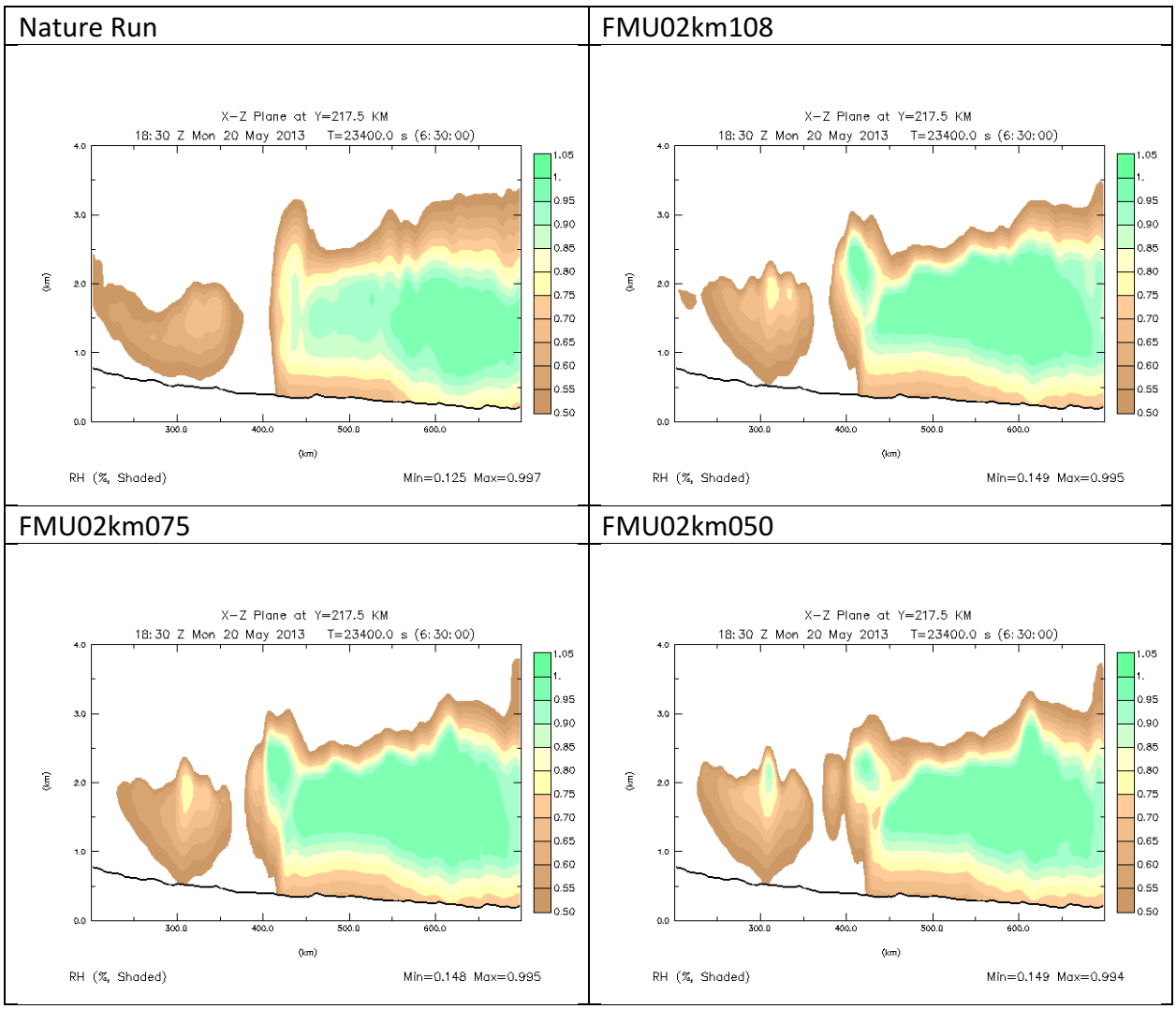

Figure 42. As in Figure 29. Nature Run, UAV obs from max height of 2 km with 108 stations data, 75 stations data, and 50 stations.

However, it is not only at the dryline that changes are seen. In the FMU02km108 experiment there are relatively high values of relative humidity and regions of air closest to saturation in a pocket of air around 2.0 km MSL at 400 km east of the dryline boundary from 425 km onward (Grady County to Le Flore-Sequoyah counties), as in Nature Run. The relatively high levels of relative humidity indicating air closest to saturation have the same configuration in the FMU02km108 experiment and when reducing the number of stations down to 75, with similar minima and maxima of relative humidity.

However, when reducing the number of stations down to 50, the pocket of air closest to saturation becomes drier (as indicated by increasing yellow shaded contours), a secondary maxima in air closest to saturation appears in the layer of air at 2.0 km MSL west of the dryline at 300 km (Washita County), and the layer of air closest to saturation east of the dryline takes on a more dome shaped structure rather the increasing depth from west to east seen in the Nature Run, FMU02km108 experiment, and FMU02km075 experiment. Much like prior figures, this indicates

a cutoff at 75 stations beyond which reducing the number of stations results in the poorer configuration and shape of the moisture profile at and east of the dryline, which can result in later convective initiation and displacement of areas of convective initiation compared to in the FMU02km108 and FMU02km075 experiments and the Nature Run.

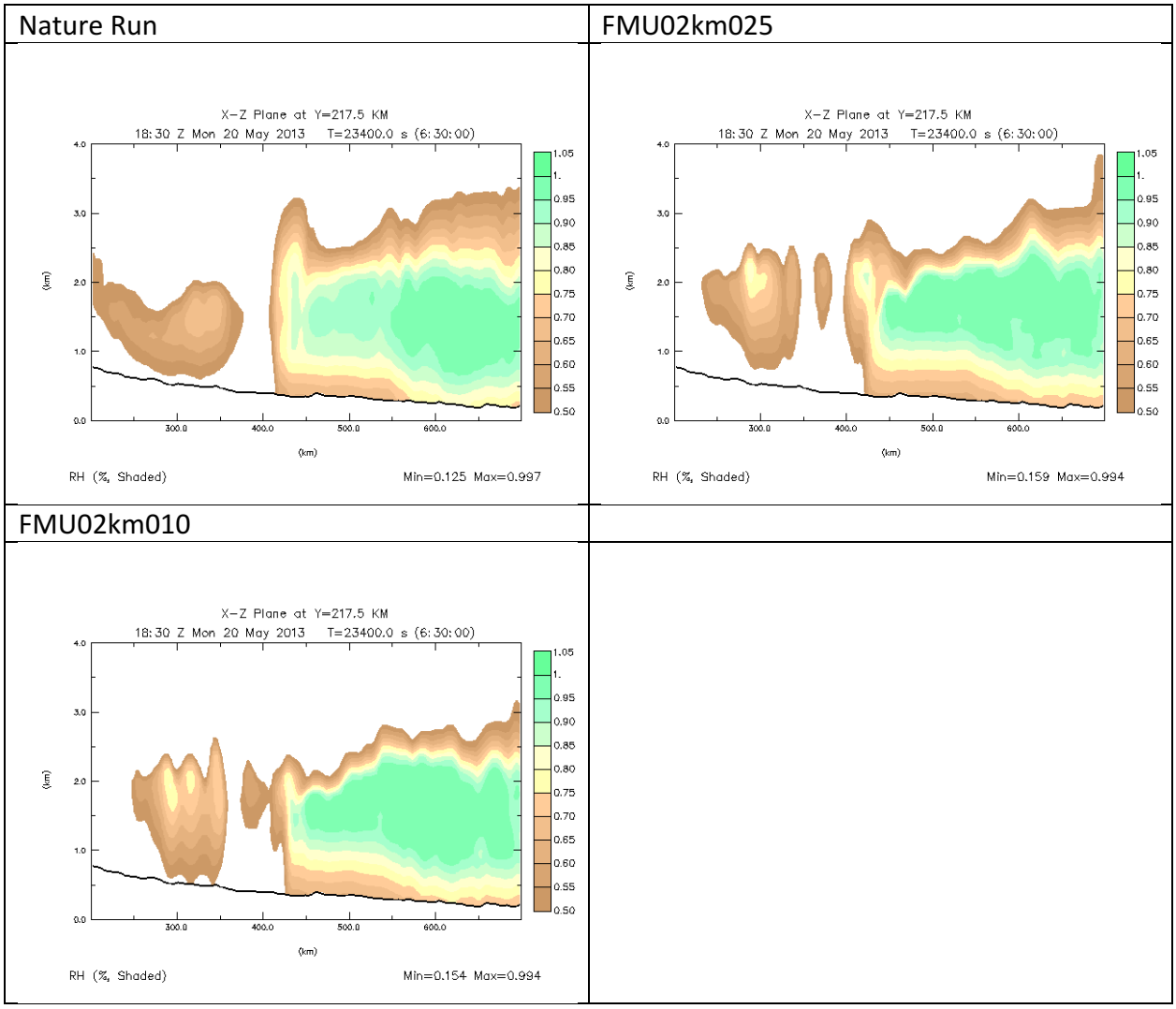

Figure 43. As in Figure 42. Nature Run, UAV obs from max height of 2 km with 25 stations data, and 10 stations.

Reducing the number of stations to 25 (Figure 43) shows much the same result seen when reducing the number of stations before, but with less difference in the configuration and depth of the air closest to saturation at and east of the dryline when reducing the number of stations to 25 from 50 than from 75 to 50. The layer of air closest to saturation shows less of an increase in height or

depth east of the dryline than the Nature Run and FMU02km108, FMU02km075, and FMU02km050 experiments. Unlike with the FMU02km075 and FMU02km050 experiments, the pockets of air at 2.0 km MSL west of the dryline at 300 km in Washita County dry out (as evident by the disappearance of green shaded contours and appearance of more brown shaded contours among the yellow shaded contours). The flattened, dome-shaped pattern as outlined by the relative humidity shaded contours is even more apparent than in the FMU02km108, FMU02km075, and FMU02km050 experiments, specifically east of the dryline

When the number of stations is further reduced to 10, the profile is even less similar than in the Nature Run or any of the previous OSSE experiments (FMU02km108, FMU02km075, FMU02km050, and FMU02km025). The biggest difference is that while the dryline boundary between air closer to saturation to the east and air farther from saturation to the west is still apparent, the pocket of air in the 2.0 km MSL layer at the dryline dries out further (as evident by the appearance of white shaded contours among the yellow and brown shaded relative humidity contours). Surprisingly, the trend of the relative humidity contours the delineate the top of the moist boundary (specifically in the region east of the dryline) becoming increasingly flattened with fewer number of stations is not continued, with the outline of the relative humidity shaded contours in the FMU02km010 experiment having less flatness and more bumps from 500 km and eastward (Cleveland to Le Flore-Sequoyah counties), possibly indicated more small-scale convective noise from lack of sufficient number and density of observations.

Figures 42 and Figure 43 show that again when considering configuration of the boundary layer at Y = 217.5 km, the FMU02km108 and FMU02km075 experiments generate preconvective moisture profiles most similar to the Nature Run, while the FMU02km010 experiment generates preconvective moisture profiles least similar to the Nature Run.

Therefore, again it is seen that using 108 or 75 stations when conducting OSSE experiments for UAV obs from a max height of 2 km gives the most similar configuration of the boundary layer at the time (1800 UTC) before convective initiation, specifically when regarding the changes in depth of the layer of air closest to saturation at and east of the dryline boundary. The relative humidity plots show specifically that the region of imminent latent heat release and ensuing vertical motion along the dryline, along with overall magnitude and extent of near-saturation east of the dryline, are best modeled for a larger number of stations (108 or 75) when using UAV obs from a max height of 2 km.

e. Optimizing Analysis Parameters for Station Density

The prior experiments examining the effect of varying the number of UAV sites were all run using the same set of analysis parameter settings (values most appropriate for the 108 station data case). This is done in order to utilize the 108 station data in the best way possible and to remove analysis settings from the variability among the OSSE experiments. Doing this provides a baseline for using the same analysis parameters for all cases, however the experiments with the smaller number of stations have significantly larger observation spacing (see Figure 44, which shows the average station spacing decreases non-linearly with the increasing number of stations). Then analysis parameters can be changed to study how the forecast results change when the analysis parameters are a more appropriate match to the actual station spacing. The actual data spacing in some of the more sparse site cases is much wider than the analysis correlation coefficient length parameter in the final pass (see Table 2), which potentially can lead to overfitting of the data and making the analysis noisier. The objective is for the analysis to interpolate in the space between the stations, not draw a bulls-eye around the stations.

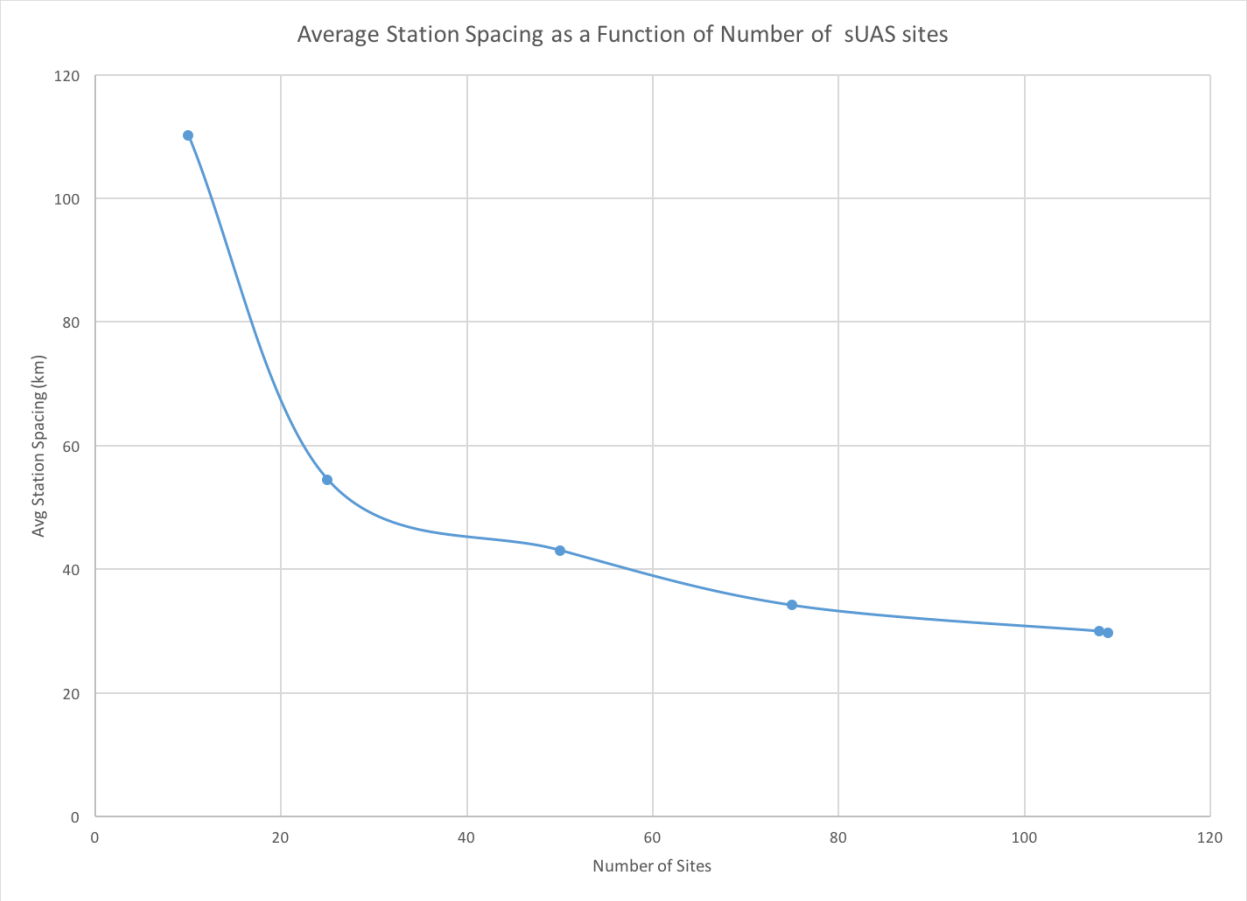

Figure 44. Line graph of average station spacing (km) versus number of UAV sites.

To test whether there would be improvement of results from better matching the analysis parameters to the station density, we repeated these experiments by changing the iterations in which the data were used – withholding the data from the analysis iterations where the correlation distance parameters were shorter compared to the data spacing (see Table 2). In addition, for the

most sparse case of 10 stations, the UAV data were added to one earlier iteration to insure the data were involved in multiple iterations. We will refer to these tests as the "fitted experiments". In the OSSE experiments with 75 and 108 UAV sites the station spacing is sufficiently close to utilize the smallest correlation distance, so experiments were not repeated for these cases.

As with the original unfitted experiments, the fitted experiments will compare results of differing number of UAV observations (this time only 10, 25, and 50) using plots of reflectivity and boundary layer moisture, in comparison to one another and the Nature Run.
First in order to see whether the data points in the unfitted and fitted experiments for 10, 25, and 50 in comparison to the 108 station UAV observations from a max height of 2 km are sufficiently different than the baseline original experiments, plots of temperature and humidity for a height in the lower boundary layer such as 1000 m AGL at 1800 UTC are generated to see if the data points have continuous interpolation between stations or create bulls-eye around the stations. The analyses from the lowest levels are not used for this because we presume the results there are dominated by the mesonet data being available at the surface.
If the data have more continuous and smooth fields for variables like temperature and specific humidity for the fitted experiments compared to the Nature Run and the unfitted experiments, it will be confirmation that the fitted experiment does a better job of analyzing thermodynamic and moisture fields than the unfitted experiment does.

As the number of stations increases, the fit of the length scale in the sixth pass is more appropriate, so to see what the effect is for simulation of thermodynamic and moisture fields, the difference between plots of horizontal temperature/wind and specific humidity across the domain at 1000 m AGL at the beginning of the forecast period (1800 UTC May 20) will be examined for the Nature Run and the fewest number of stations (10 stations) for fitted and unfitted experiments. This will be done to demonstrate if there is improvement of plotted thermodynamic and moisture fields in the fitted experiment (i.e.: the plotted fields in the fitted experiment are more similar to the Nature Run) compared to the unfitted experiment.

In order to do this, the results of how the data is assimilated compared to how the data is analyzed before assimilation will be examined for the temperature/wind and specific humidity fields for the FMU02km108, FMU02km010, and FMU02km010f OSSE experiments. This is compared to the forecast from the Nature Run valid at 1800 UTC, which is the source of the 1800 UTC simulated data.

When we first examine the temperature and wind fields (Figure 45), the only major difference between the plots is that this set of experiments show higher values of temperature in southwest Oklahoma and north Texas compared to the Nature Run. This is most apparent in northwest Texas and southwest Oklahoma and is because we have used no data other than the 1 degree FNL data outside of Oklahoma. There is not much apparent difference regarding the spreading of temperature contours between the unfitted FMU02km010 experiment and the fitted FMU02km010f experiment.

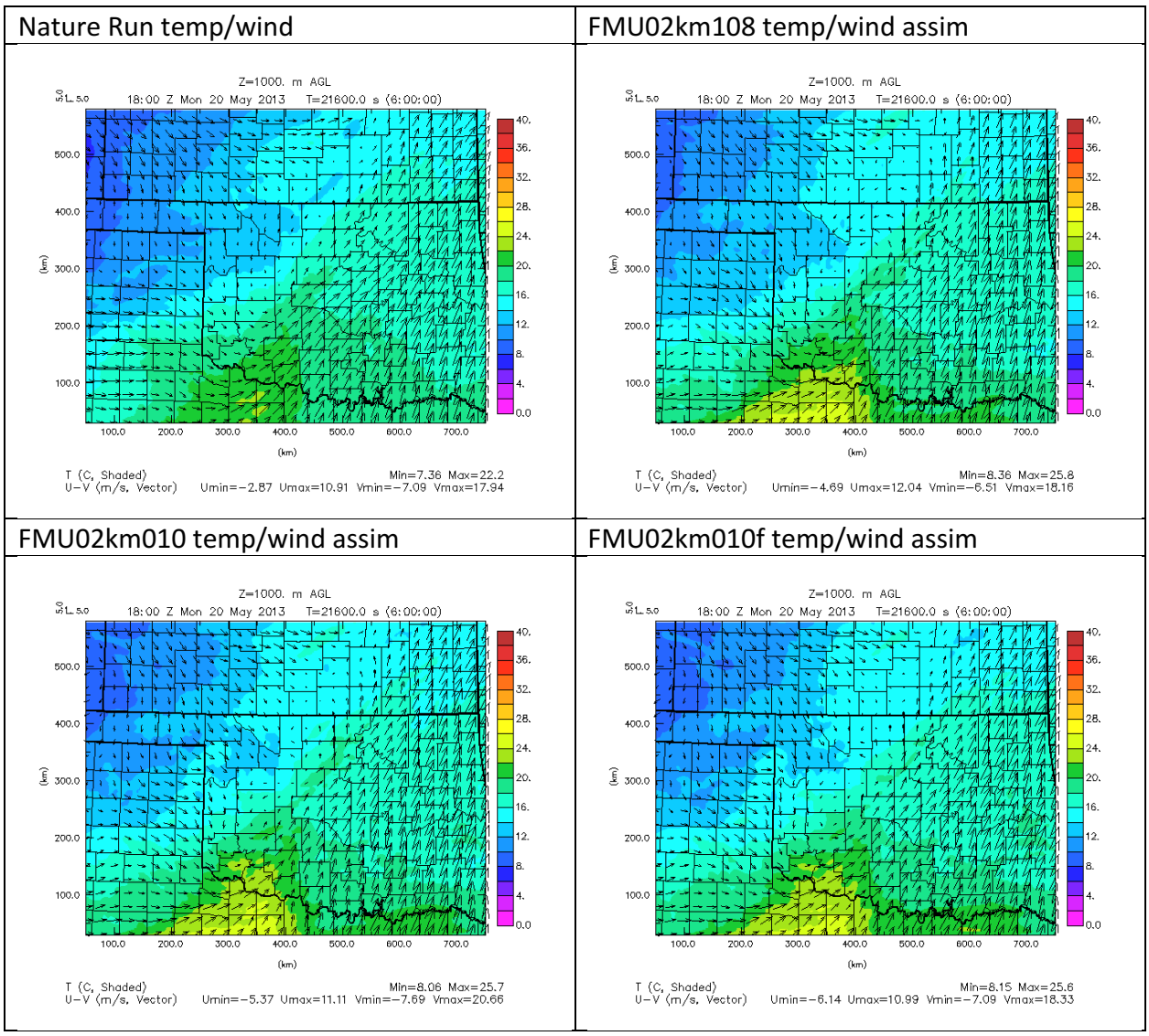

Figure 45. Plot of temperature (deg Celsius) and U-V winds (vectors, length proportional to magnitude of wind speed) at 1000 m AGL for the Nature Run at 1800 UTC, and the FMU02km108 experiment assimilated data, FMU02km010 assimilated data, and FMU02km010f assimilated data at 1800 UTC.

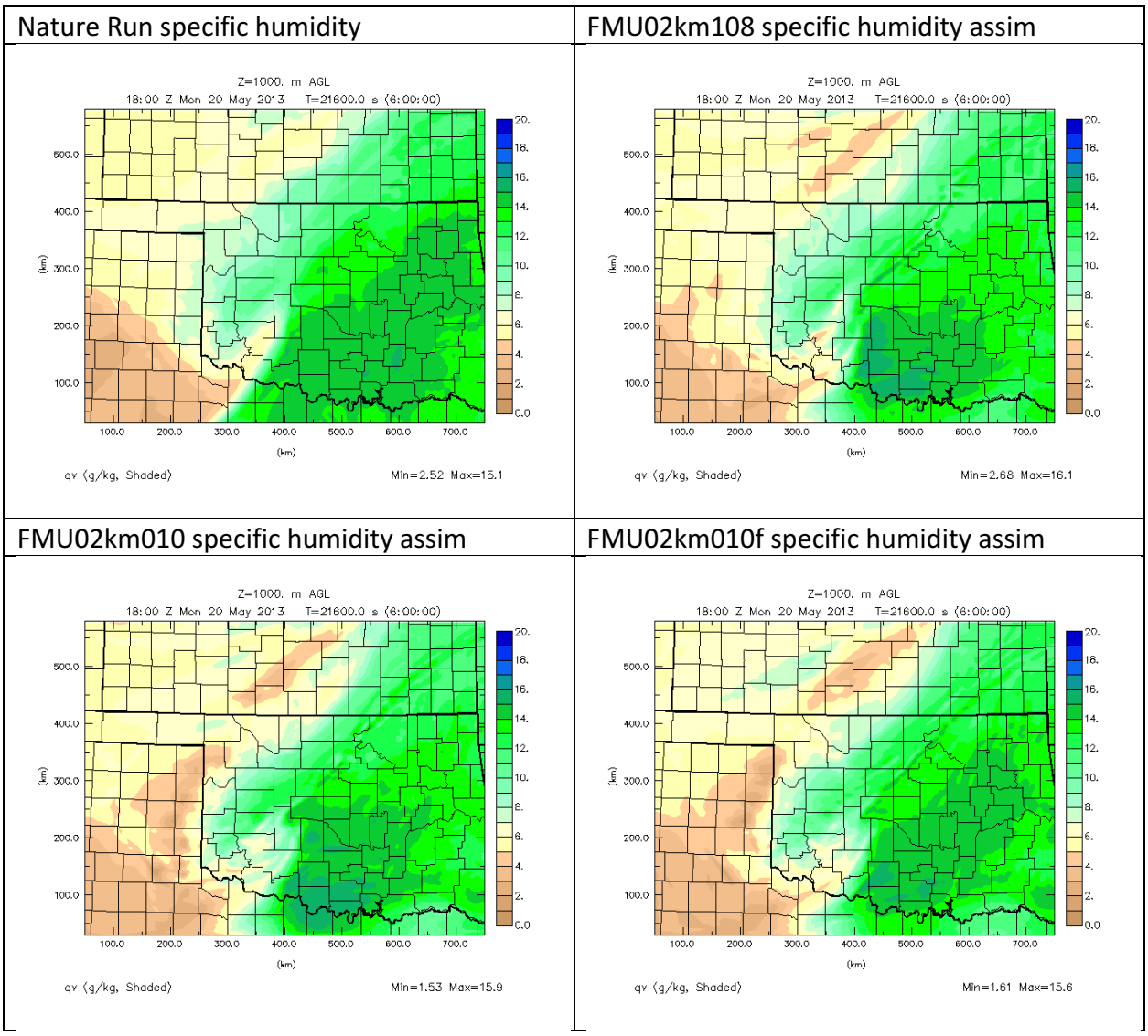

Figure 46. As in Figure 43, but for specific humidity (g/kg).

When we examine the specific humidity field at 1800 UTC (Figure 46), what stands out is the pocket of higher levels of moisture exceeding 15 g/kg in south-central Oklahoma (in Stephens-Carter-Jefferson counties) that are not present in the Nature Run, and to a much smaller extent in the FMU02km010f experiment. Comparing the fitted and unfitted 10 station experiments to the Nature Run, we see that the fitted experiment has more spreading of moisture into northeast Oklahoma (specifically Muskogee-Okmulgee-Wagner-Cherokee and surrounding counties) than the FMU02km010 experiment, leading to slightly higher values of moisture there and is thus more similar to the Nature Run than the FMU02km010 experiment, both in terms of spreading of moisture into northeast Oklahoma and lower magnitude bulls-eyes of higher magnitude moisture in southwest Oklahoma. This suggests that the fitted 10 station experiment is more properly spreading the moisture increments across a larger area and drawing more continuous fields of moisture instead of overfitting concentrated moisture values, which may include positive random error added as occurs in the FMU02km108 and FMU02km010 experiments.

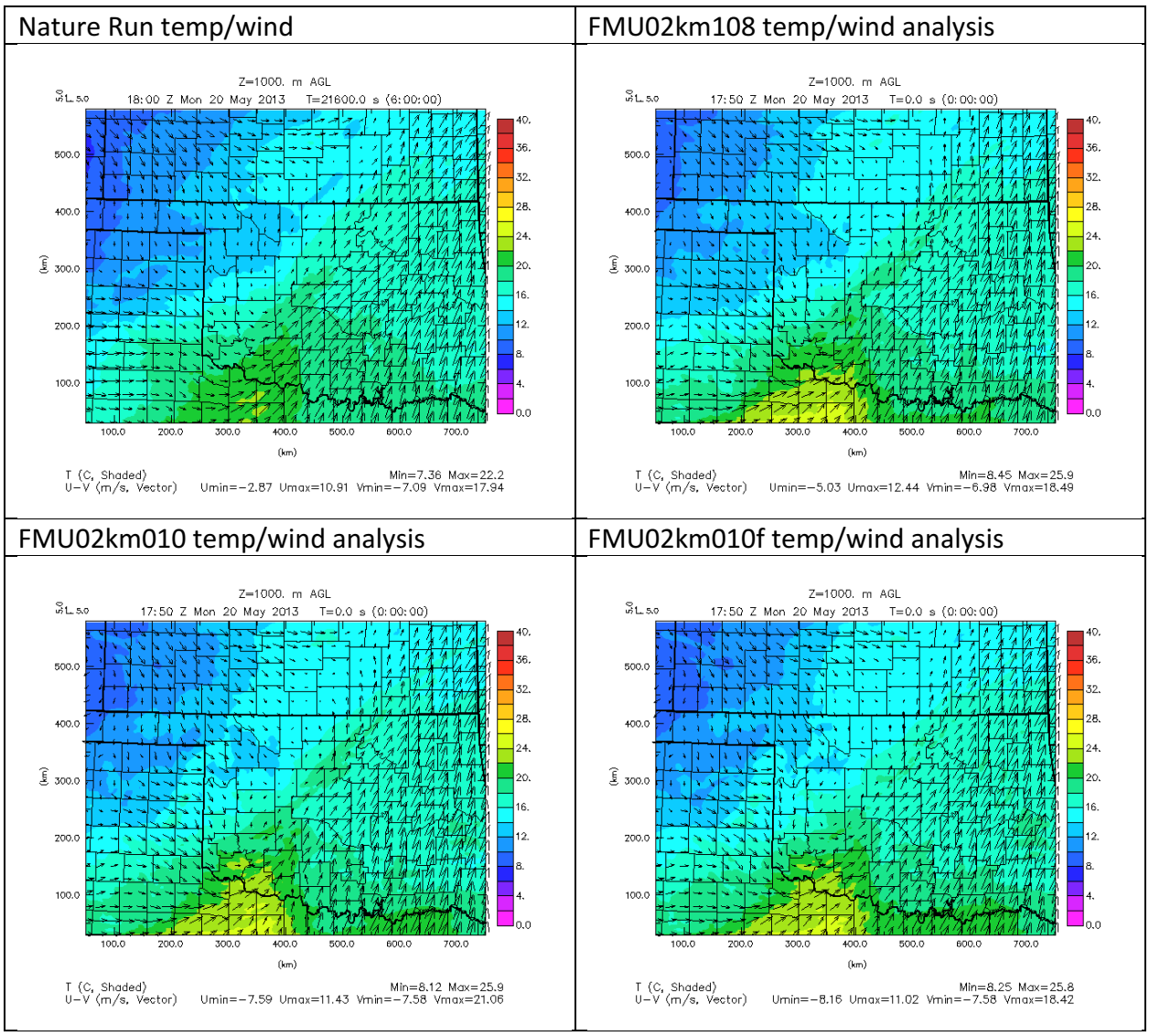

Figure 47. As in Figure 43, but for the analysis fields of temperature/wind before data is assimilated at 1800 UTC.

To see if these same results are seen for the analysis fields in the OSSE experiments before the increments are assimilated just prior to 1800 UTC, the Nature Run, FMU02km108 analysis at 1750 UTC, FMU02km010 analysis at 1750 UTC, and FMU02km010f analysis at 1750 UTC are examined as well (Figure 47).

As before, plots of temperature/wind are examined first to see if there is any difference between the runs for the thermodynamic and kinematic fields before examination of the moisture field is done.

Similar to in Figure 45, there is not much difference between the Nature Run and the OSSE experiments other than how there is a higher magnitude of temperature in southwest Oklahoma and north central Texas (in the same counties in north Texas and southwest Oklahoma as mentioned in description of Figure 45). Temperatures are highest in this region in the

FMU02km108 experiment, about the same in the FMU02km010 and FMU02km010f experiments, and lowest in the Nature Run. Elsewhere there are slightly lower temperatures in FMU02km010f near the warm front boundary in north-central Oklahoma, northeast of Canadian County. What the results in Figure 45 and Figure 47 indicate is that as far as modeled temperature fields are concerned, the fitting of data spacing to the correlation parameters does not make much difference.

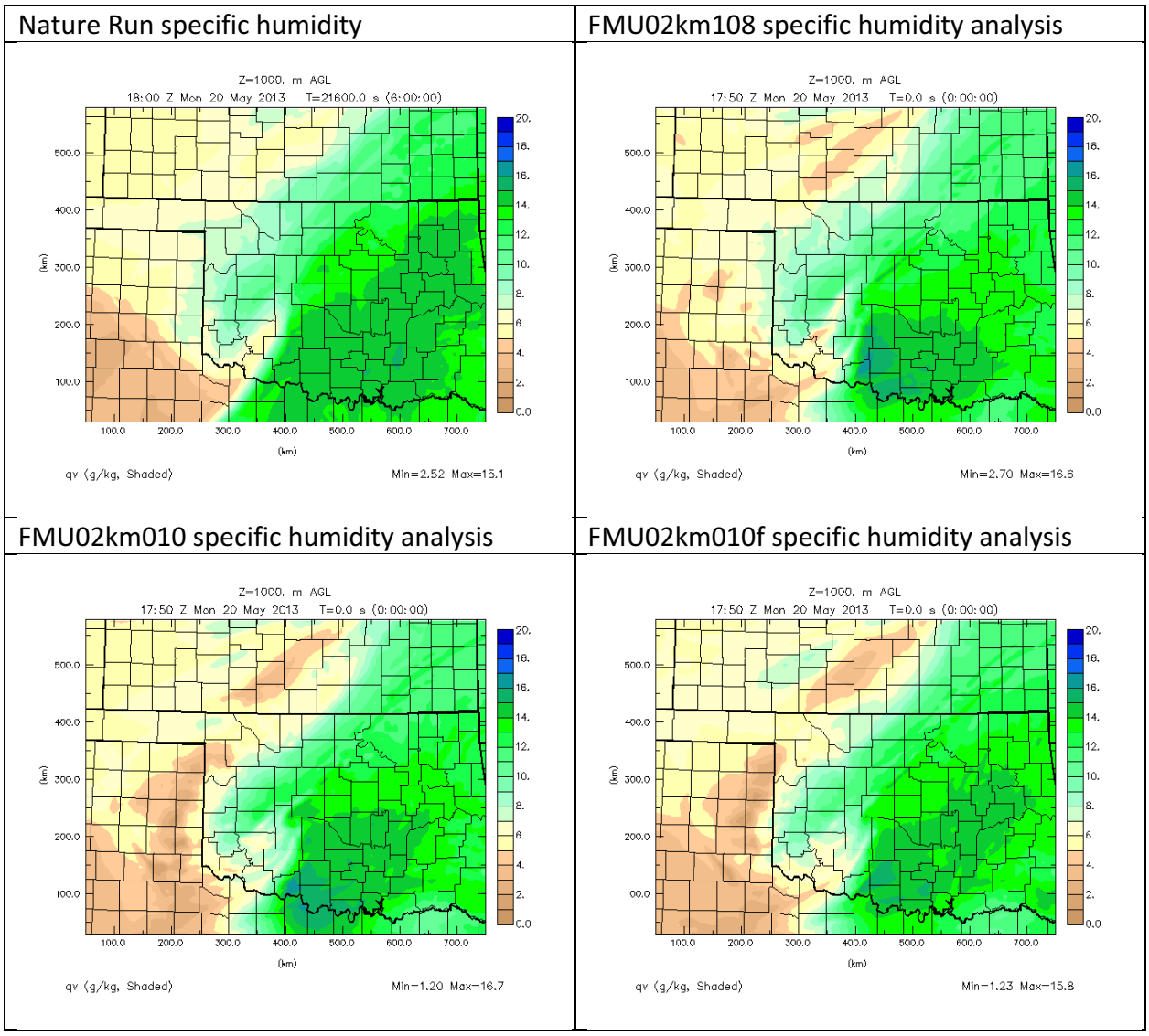

Figure 48. As in Figure 44, but for analysis fields of specific humidity at 1800 UTC. Note plots are labelled for the background data time of 1750 UTC.

In the 1800 UTC specific humidity analyses (Figure 48) as in the assimilated states (Figure 46), there is a consistent pattern of more widely spread moderate levels of specific humidity into northeast Oklahoma in the FMU02km010f experiment, as evidenced by the extension of the 14 g/kg contour into northeast Oklahoma (same counties as found in Figure 46) in the FMU02km010f experiment). Overall, compared to the Nature Run and the other OSSE experiments, specific humidity is best spread out across the domain for the FMU02km010f experiment, while there is a more concentrated area of relative high specific humidity (18 g/kg, as evidenced by blue shaded

contours) in Cottons-Stephens-Jefferson counties in southwest Oklahoma for the FMU02km108 and FMU02km010f experiments. Therefore, we see that the result in the assimilated state is directly due to the improved analysis.

Now that it has been shown that there is value in fitting the data at least as far as simulating moisture fields more comparable to the Nature Run, reflectivity images will be shown for the same stages of convection that have been covered before. This will be done in order to see how fitting the data affects results of timing, intensity, coverage, and overall evolution of convection between the Nature Run, FMU02km108 experiment, and 10, 25, and 50 station fitted and unfitted experiments.

Nature Run	FMU02km108
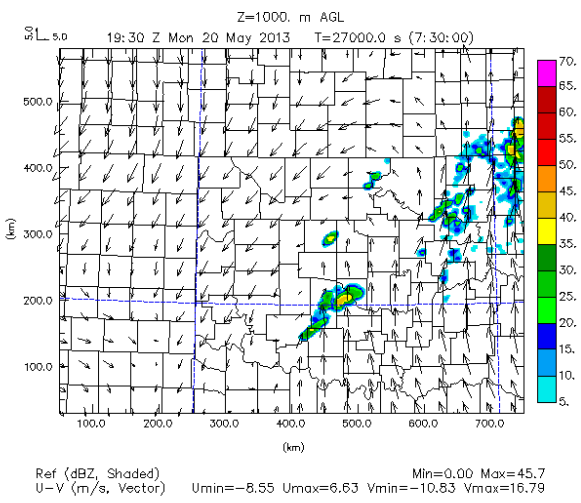	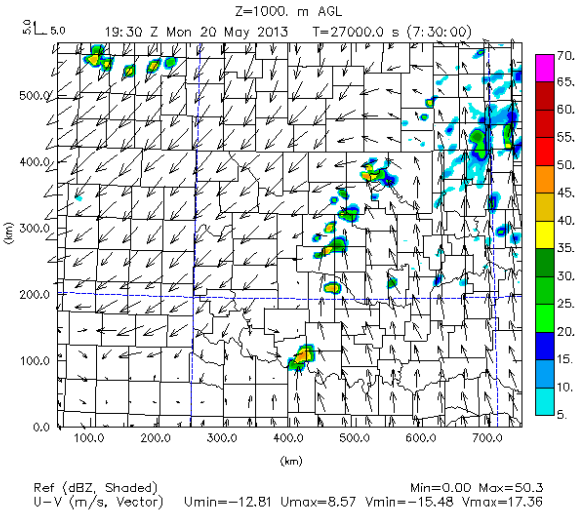
FMU02km010	FMU02km010f
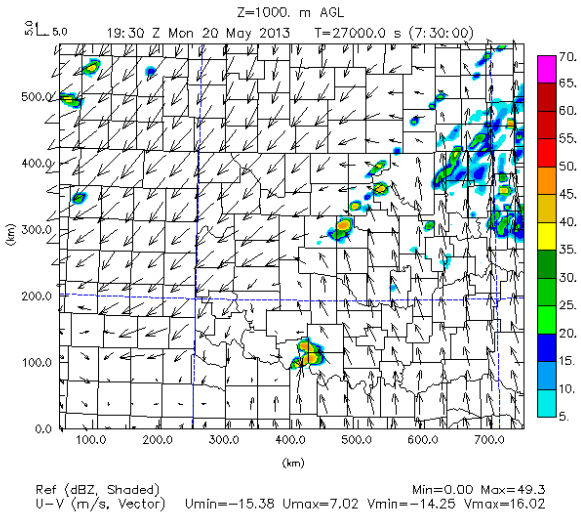	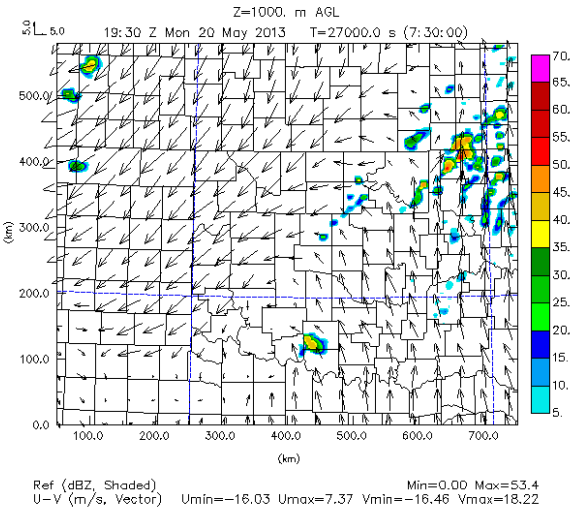

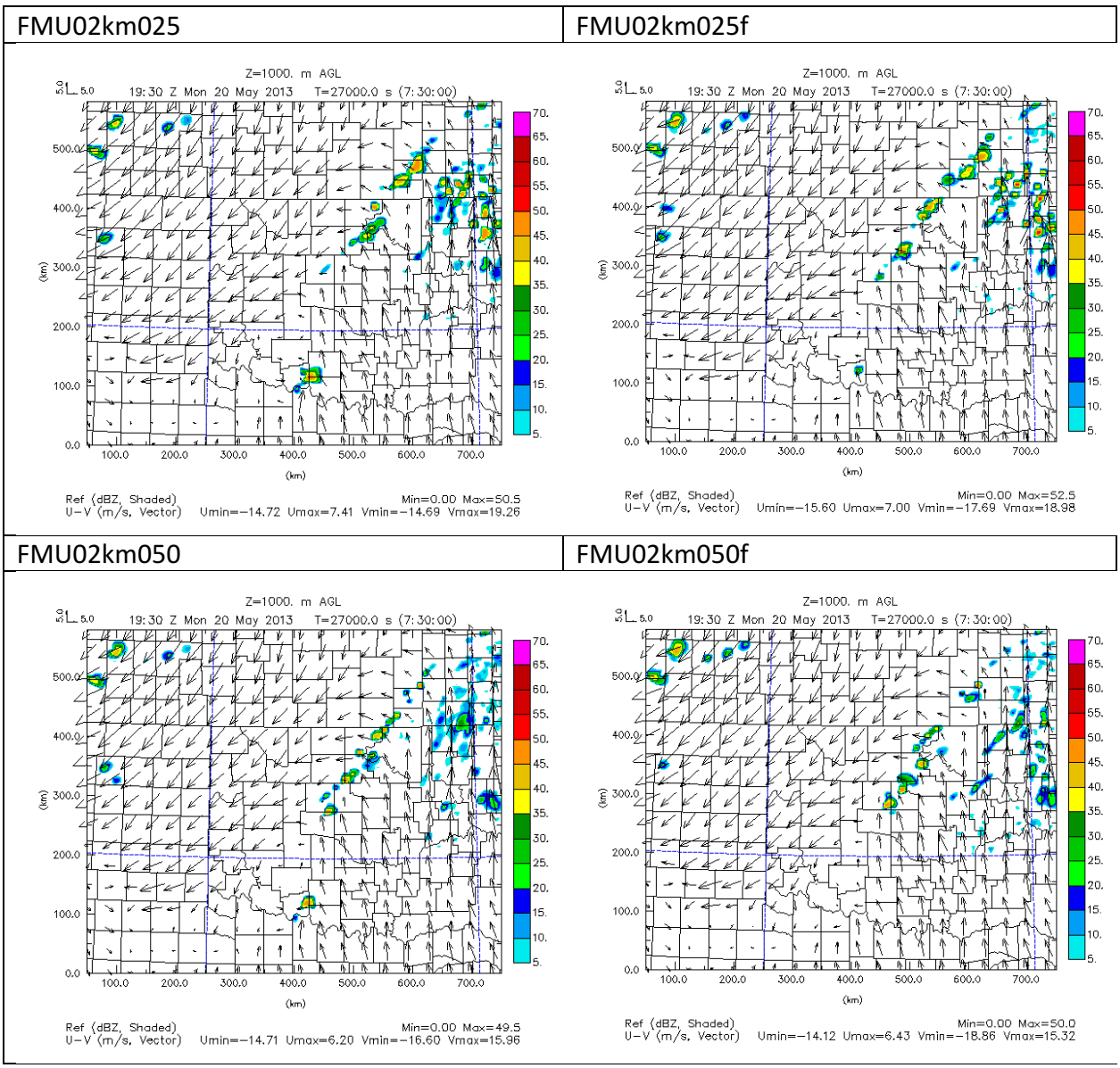

Figure 49. As in Figure 16. Nature Run, UAV obs from max height of 2 km with 108 stations, 10 stations unfitted and fitted, 25 stations unfitted and fitted, and 50 stations unfitted and fitted data.

Comparing the FMU02km010 and FMU02km010f experiment, Figure 49 shows that at 1930 UTC, there is somewhat lower intensity of convection across north-central Oklahoma in the FMU02km010f experiment compared to the FMU02km010 experiment, but a higher intensity of convection across central to northeast Oklahoma along the warm front compared to in the FMU02km010 experiment. In this way, the results of the FMU02km010f experiment are more in line with the Nature Run. However, neither the FMU02km010 nor FMU02km010f experiment was able to initiate convection in Grady County along the dryline as in the Nature Run, but instead they each have a spurious cell in southwest Oklahoma in the Red River region. So fitting the analysis to the 10 station dataset improves the forecast but is not enough to solve the most important challenge for this forecast system.

Examination of the FMU02km025 and FMU02km025f experiment reflectivity at 1930 UTC shows little difference between the experiments with the exception of a higher intensity reflectivity signature in Cotton-Stephens-Jefferson counties for the FMU02km025 experiment. Otherwise, the general pattern of convective lines through Logan-Payne-Pawnee-Osage counties and convection in northeast Oklahoma is similar to in the Nature Run.

Focusing on the reflectivity at 1930 UTC for the FMU02km050 and FMU02km050f experiments, we see how again there is not much difference between the two experiments, but for this fitted experiment the spurious reflectivity signature in Cotton-Stephens-Jefferson counties does not appear, so it is successful in removing that spurious convection. Still the 50 station fitted experiment does not have convection initiation in Grady County.

Note that although not shown, in the FMU02km010f, convective initiation has begun in Jefferson County by 1900 UTC, around the same time that convection has initiated in the northern part of Clay County in north Texas in the FMU02km010 experiment. The beginning stages of convection have developed along the border between Jefferson County in Oklahoma and Clay County in north Texas by 1900 UTC in the FMU02km025 experiment, but not until 1930 UTC in the northeastern part of Cotton County in the FMU02km025f experiment. The beginning stages of convection show up in southern Cotton County by 1915 UTC in the FMU02km050 experiment, but not until 2030 UTC in Stephens County in the FMU02km050fexperiment.

Overall, this compares with convective initiation (of storms that move into Cleveland County) occurring as early as 1845 to 1900 UTC from Caddo to Grady County in the FMU02km108 experiment and in Grady County in the Nature Run.

For all sets of OSSE experiments (i.e.: fitted and unfitted experiments for 10, 25, and 50 stations) however, we consistently see that while storms do form along the dryline and move into Cleveland County, the storms form too far south (near the Red River region) compared to the Nature Run (where storms form along the dryline in Grady County).

Nature Run	FMU02km108
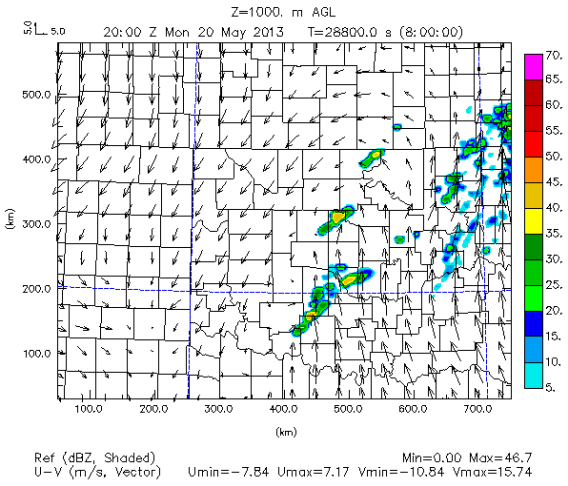	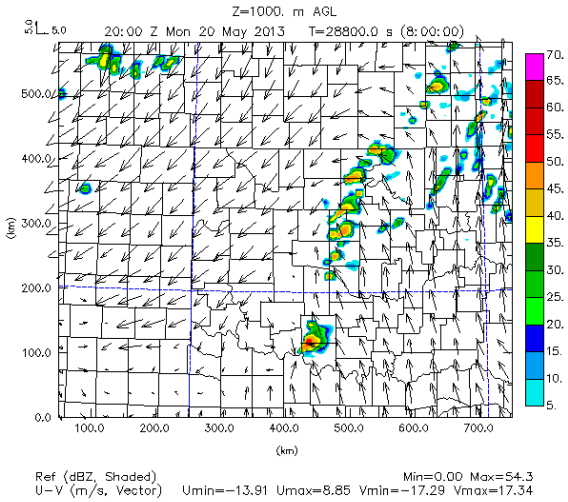
FMU02km010	FMU02km010f
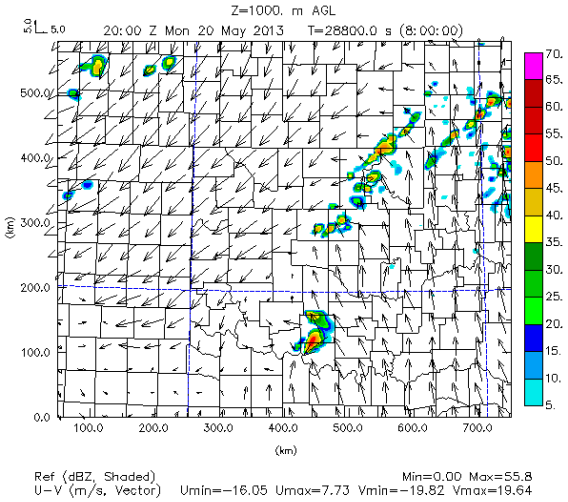	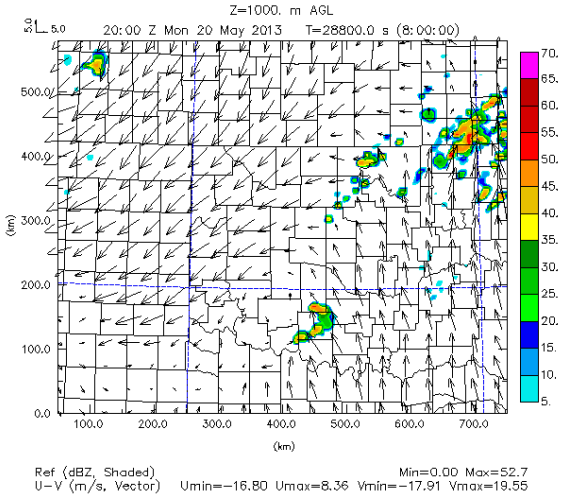

FMU02km025	FMU02km025f
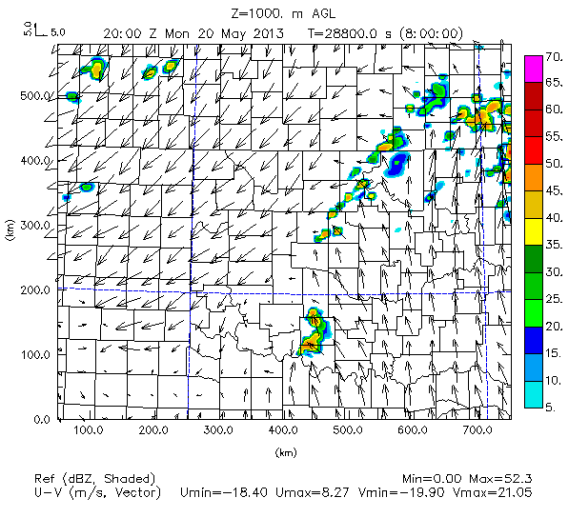	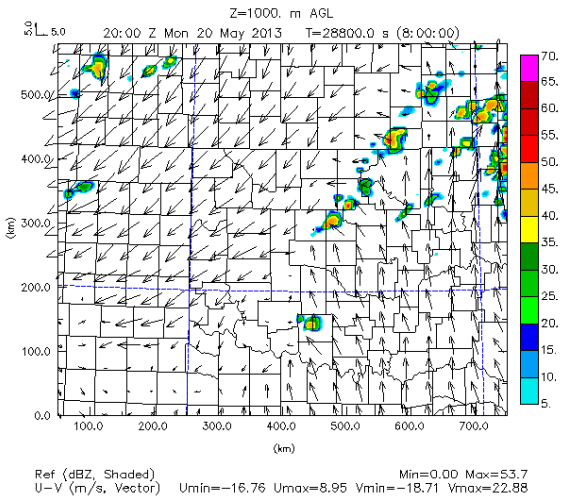
FMU02km050	FMU02km050f
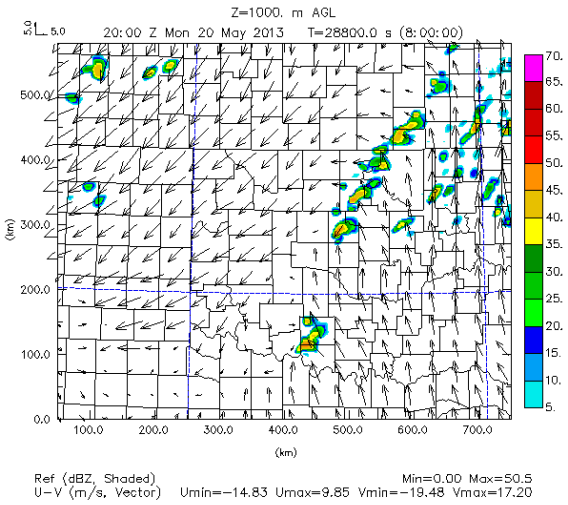	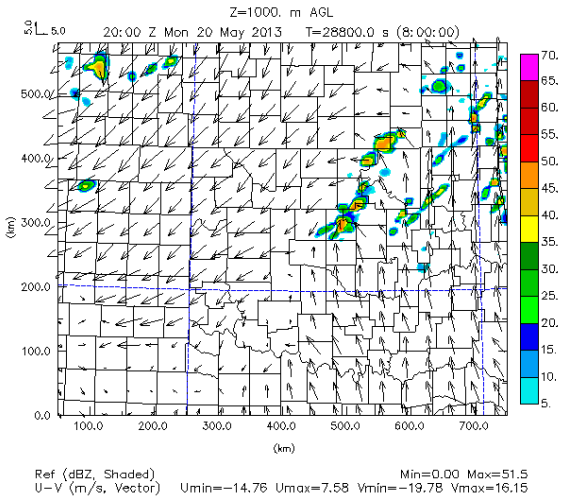

Figure 50. As in Figure 16, but for time 20 UTC. Nature Run, UAV obs from max height of 2 km with 108 stations, 10, 25, and 50 stations unfitted and fitted data.

Comparing the FMU02km010f experiment to the FMU02km010 experiment (Figure 50) shows that at 2000 UTC, there is much less convective activity in north-central Oklahoma in the, and that there is higher intensity convection in northeast Oklahoma in the FMU02km010f experiment compared with the FMU02km010 experiment. The FMU02km010 experiment is more similar to the Nature Run in resolving these features. In both the FMU02km010 and FMU02km010f experiments, convection in south-central Oklahoma is still southwest of Cleveland County in Grady-Stephens-Jefferson counties. This differs from the Nature Run, where convection is already located over Cleveland County by 2000 UTC. The main difference between convection in central Oklahoma for the 10 station unfitted versus fitted experiments is that there is a higher intensity of convection in Jefferson County in the FMU02km010 experiment and in Stephens-Grady counties in the FMU02km010f experiment.

Figure 50 shows that the main difference between the FMU02km025 and FMU02km025f experiments is that there is a greater coverage of convection in southwest Oklahoma (in the Stephens-Carter-Jefferson counties area) in the FMU02km025 experiment in comparison with the FMU02km025f experiment. In both experiments, unlike in the Nature Run, there is no convection on the dryline in Grady County Oklahoma at the time.

At 2000 UTC, the FMU02km050 experiment shows similar intensity and coverage of convection in north-central and northeast Oklahoma as in the FMU02km050f experiment. However, convection in Carter-Stephens-Jefferson counties that is modeled in the FMU02km050 experiment is not seen at all in the FMU02km050f experiment. Both the FMU02km050 and FMU02km050f experiments differ from the Nature Run in how the Nature Run shows convection in west-central Oklahoma near the vicinity of and over Cleveland County at the time.

By 2100 UTC (Figure 51), the FMU02km010 and FMU02km010f experiments both show splitting supercell behavior, but such behavior is not as prevalent in the FMU02km010f experiment, in better agreement with the Nature Run. Convection across Kay-Noble-Pawnee-Payne-Logan counties that is apparent in the Nature Run at this time is missing in the FMU02km010f experiment but some appears in the FMU02km010 experiment. The FMU02km010 experiment also does a better job of simulating coverage and intensity of convection in eastern parts of north-central Oklahoma and southern Kansas compared to the FMU02km010f experiment, although storms in the northeast part of the domain have moved farther east in the FMU02km010 and FMU02km010f experiments than in the Nature Run.

The splitting supercell behavior (seen of the storms that develop northeast closer to Cleveland County) is much more subdued in the FMU02km025f experiment compared to the FMU02km025 experiment, making the behavior of convection in central Oklahoma in the FMU02km025f experiment more similar to the Nature Run. While both the FMU02km025 and FMU02km025f experiments show convection located in the vicinity of Cleveland County, in agreement with the Nature Run. Compared to the Nature Run, there is better coverage of convection in north-central Oklahoma and south-central Kansas in the FMU02km025 experiment than in the FMU02km025f experiment. The convection, especially at the Oklahoma-Kansas border, is too sparse in the FMU02km025f experiment compared to the Nature Run. Both the FMU02km025 and FMU02km025f experiments model a similar amount of convective activity in northeast Oklahoma, but with there being more scattered convection in this region in the FMU02km025f experiment, in contrast to the Nature Run and FMU02km025 experiment.

By 2100 UTC, the FMU02km050 experiment still shows better agreement with the Nature Run in terms of convective coverage and intensity, specifically with regards to the batch of convection that stretches from Stephen County to Cleveland County in the FMU02km050 experiment, but that is still to the southwest in Grady-Garvin-McClain counties in the FMU02km050f experiment. However, the FMU02km050f experiment performs slightly better having less extraneous, scattered convection in northeast Oklahoma and southeast Kansas that is seen in the FMU02km050 experiment but not in the Nature Run.

Nature Run	FMU02km108
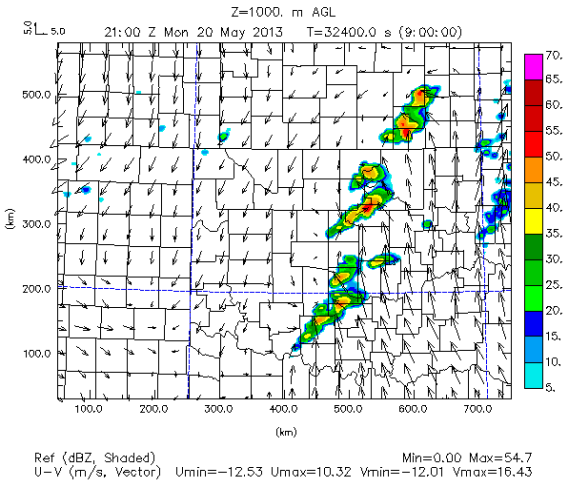	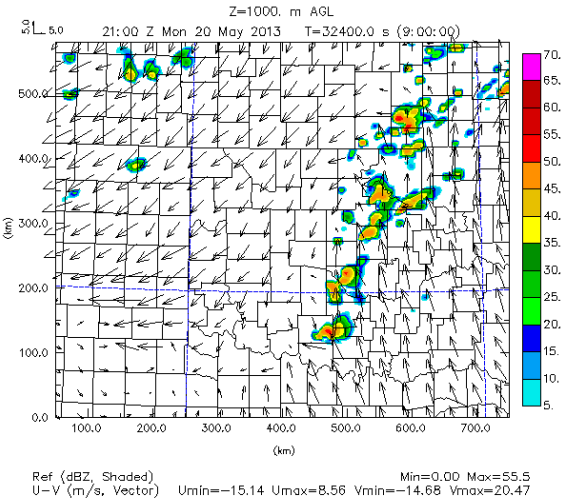
FMU02km010	FMU02km010f
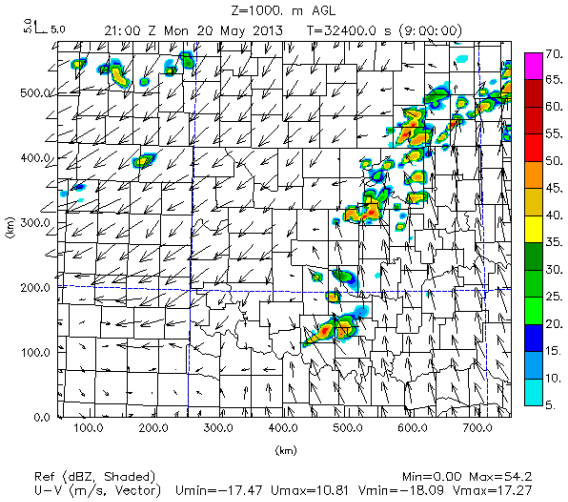	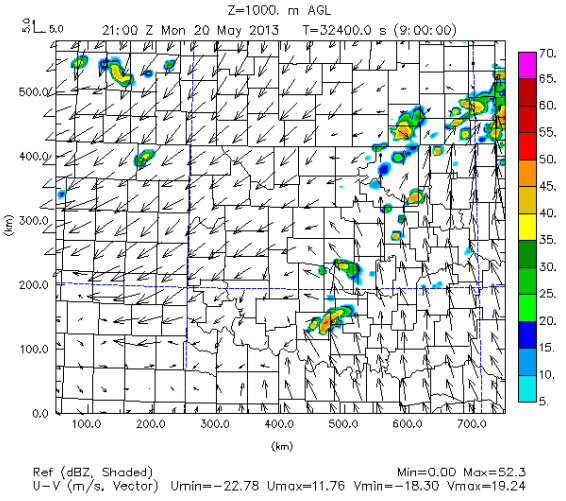

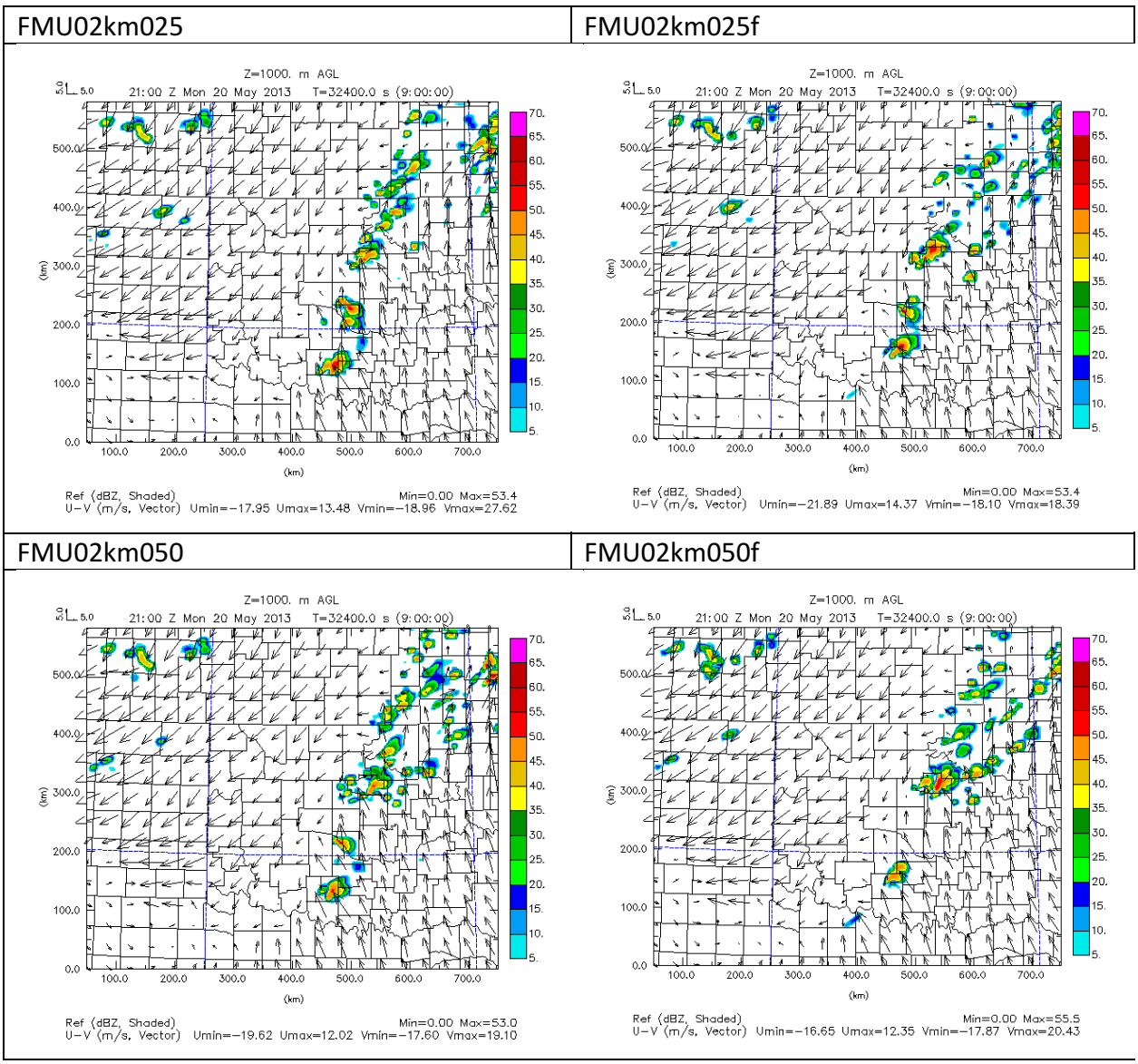

Figure 51. As in Figure 16, but for time 21 UTC. Nature Run, UAV obs from max height of 2 km with 108 stations, 10, 25, and 50 stations unfitted and fitted data.

The results in Figures 49 through 51 indicate that while the fitted experiments do a better job in reducing extraneous convective noise in northeast Oklahoma in the earlier portion of the forecast period (1930 UTC to 2100 UTC) and while modeling more subdued splitting supercell behavior in the 10 station and 25 station experiments, the fitted experiments don't always do a better job compared to the unfitted experiments in modeling placement and coverage of storms along the dryline. Thus, the general pattern that is seen is that while the fitted experiments for 10, 25, and 50 stations reduce extraneous convection in north-central and northeast Oklahoma, they generate forecasts less similar to the Nature Run than the unfitted experiments in terms of simulating the proper configuration and shape of convection.

The benefits of fitting the data therefore only seem to carry so far as to reduce overall extraneous convection in north-central and northeast Oklahoma and reducing the amount of splitting supercell

behavior when storms are in the vicinity of Cleveland County, but can end up modeling poorer configuration of convection in southwest and central Oklahoma, specifically when storms are supposed to be located over Cleveland County within an hour of convective initiation at 2000 UTC (see the results for the FMU02km010f and FMU02km050f experiments), as in the Nature Run. Additionally, for the overfitted experiments for 25 and 50 stations, there is actually earlier convective initiation (by 15 minutes to up to an hour and longer, respectively) of storms in southwest Oklahoma in the 1930 UTC to 2030 UTC window compared to in the fitted experiments for 25 and 50 stations, making the timing of convective initiation more similar to the Nature Run for the unfitted experiments than the fitted experiments for the 25 and especially 50 station setups. This notable difference in timing of convective initiation is not seen in the FMU02km108 setup or the Nature Run, nor is it seen in the FMU02km010 and FMU02km010f experiments.

Due to nonlinear interactions between storms and inadequate resolution of the model to examine smaller-scale convective features like downdrafts, differences between the Nature Run and the fitted and unfitted experiments for 10, 25, and 50 stations are not compared here for the forecast period after 2100 UTC.

Turning to the cross-section near the dryline (Figure 52), for the most part the fitted experiments seemed close to the corresponding unfitted experiments. However, there were some differences. For example, in the wind fields, it is apparent that there is very focused upward vertical motion at 350 km (Caddo County) and just east of 400 km (i.e. just west of Grady County at the dryline) for the Nature Run and the fitted and unfitted experiments. However, these focused, narrower corridor of upward vertical motion west and east of the dryline appears to be much more defined in the unfitted 25 and 50 station experiments than the fitted 25 and 50 station experiments. This differing configuration of boundary layer moisture at the dryline between the fitted and unfitted experiments could explain part of why convective initiation is so similar for the 25 and 50 station unfitted experiments but not for the 25 and 50 station fitted experiments.

Nature Run	FMU02km108
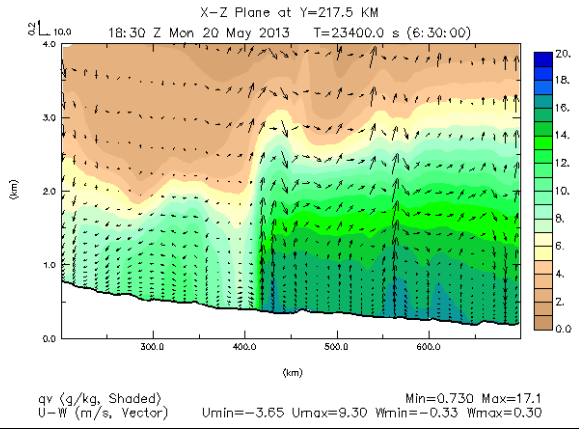	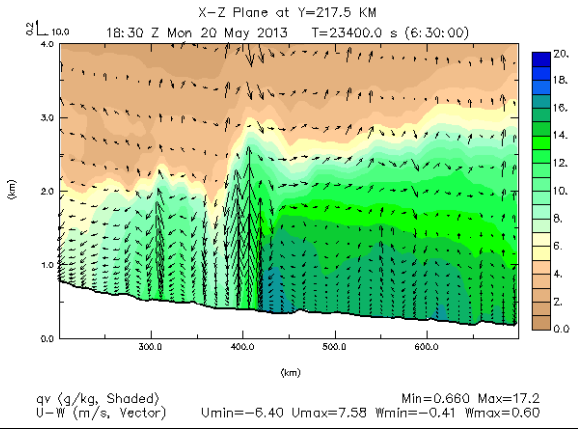
FMU02km010	FMU02km010f
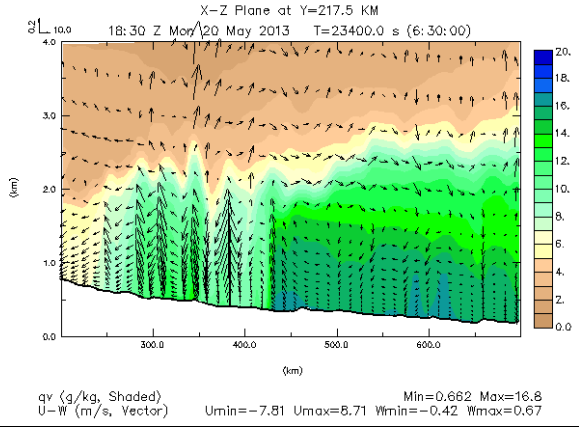	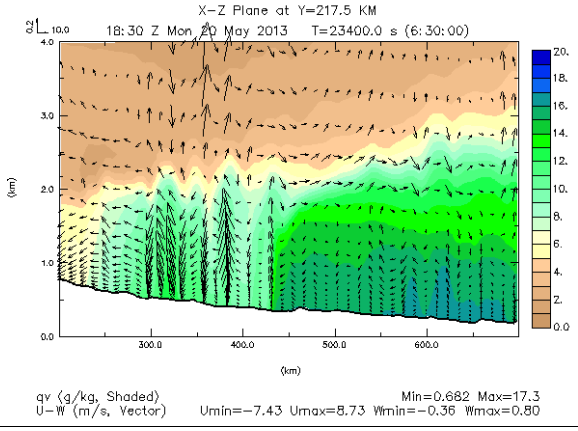

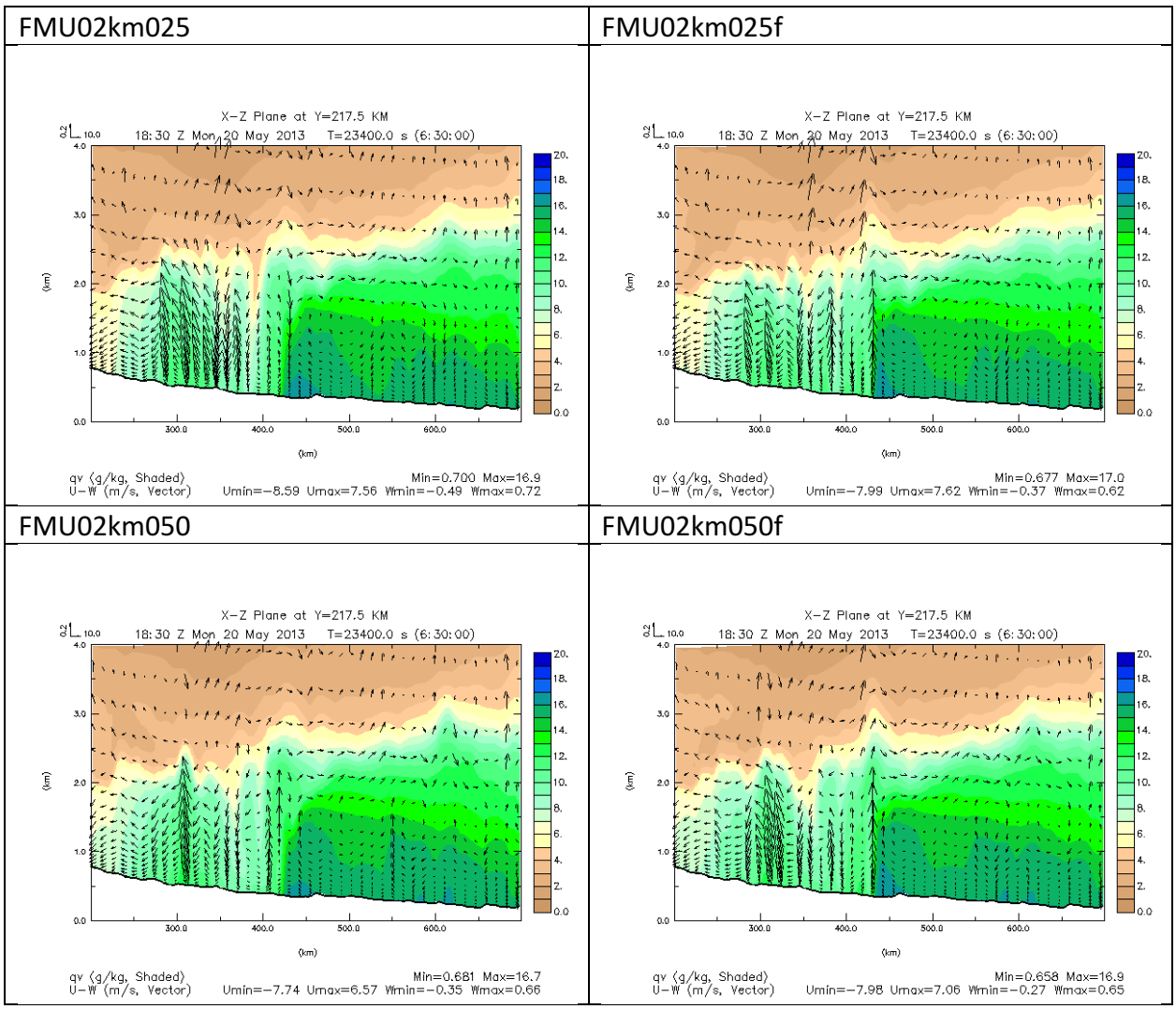

Figure 52. As in Figure 26. UAV obs from max height of 2 km with 108 stations, 10 stations unfitted and fitted, 25 stations unfitted and fitted, and 50 stations unfitted and fitted data.

In addition to the wind fields, the specific humidity fields show that for the Nature Run, the most humid air (as outlined by the 14 g/kg darker green shaded contour) is dome shaped east of the dryline all the way to Sequoyah County and reaches a maximum height of about 1.5 km MSL at 575 km (Pottawatomie and Seminole counties). This dome shaped layer of humid air becomes less and less defined flattened and more slanted downward from west to east when looking at the FMU02km108 experiment and then the experiments for the fitted 10 station, unfitted 10 station, fitted 25 station, and so on. However, this difference is not very large between the fitted and unfitted experiments.

Examination of the updraft region near the dryline shows that there is too much westward pooling of the highest moisture (as defined by the presence of the 20 g/kg blue shaded contour being confined to just east of the dryline in the FMU02km108 experiment) compared to the Nature Run. The fitted and unfitted 25 and 50 station experiments show that the peaked shape of the moisture intrusion at the dryline is much more similar to the Nature Run than the corresponding unfitted

experiments, although the moisture intrusion reaches a same peak height of around 2.5 km MSL. However, in all of the experiments except for the fitted 10 station experiment, the fitted experiments simulate a more similar range of values of vertical motion and shape of areas of higher moisture in the lower boundary at and east of the dryline. Even so, it is likely that the lower value of maximum vertical velocity and lack of pooling of moisture just east of the dryline in the fitted 25 and 50 station experiments that explains the later convective initiation in these experiments compared to in the corresponding unfitted 25 and 50 station experiments.

Nature Run	FMU02km108
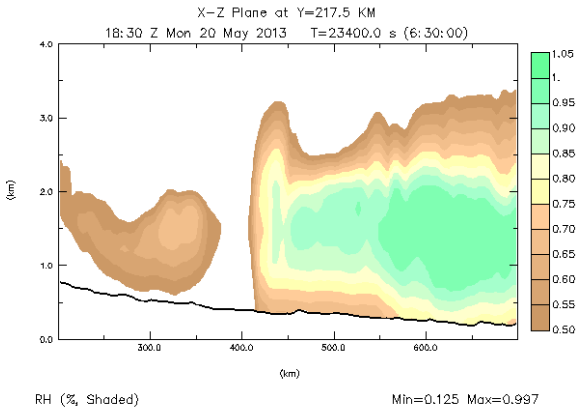	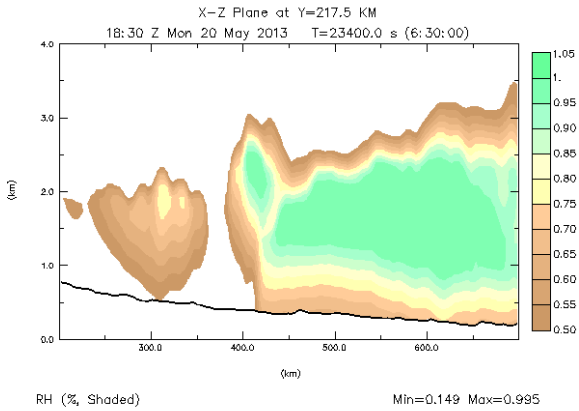
FMU02km010	FMU02km010f
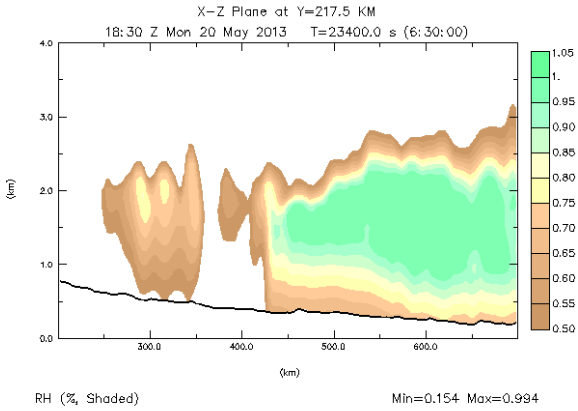	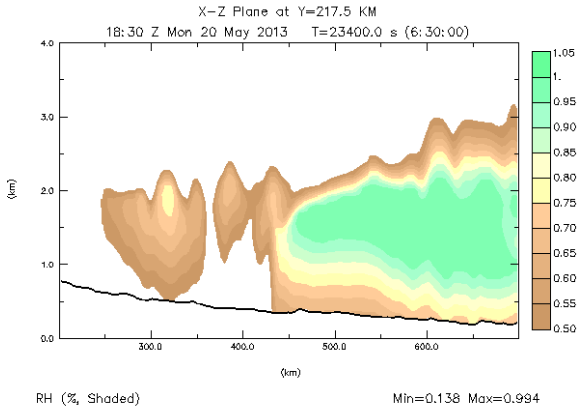
Continued on next page…	

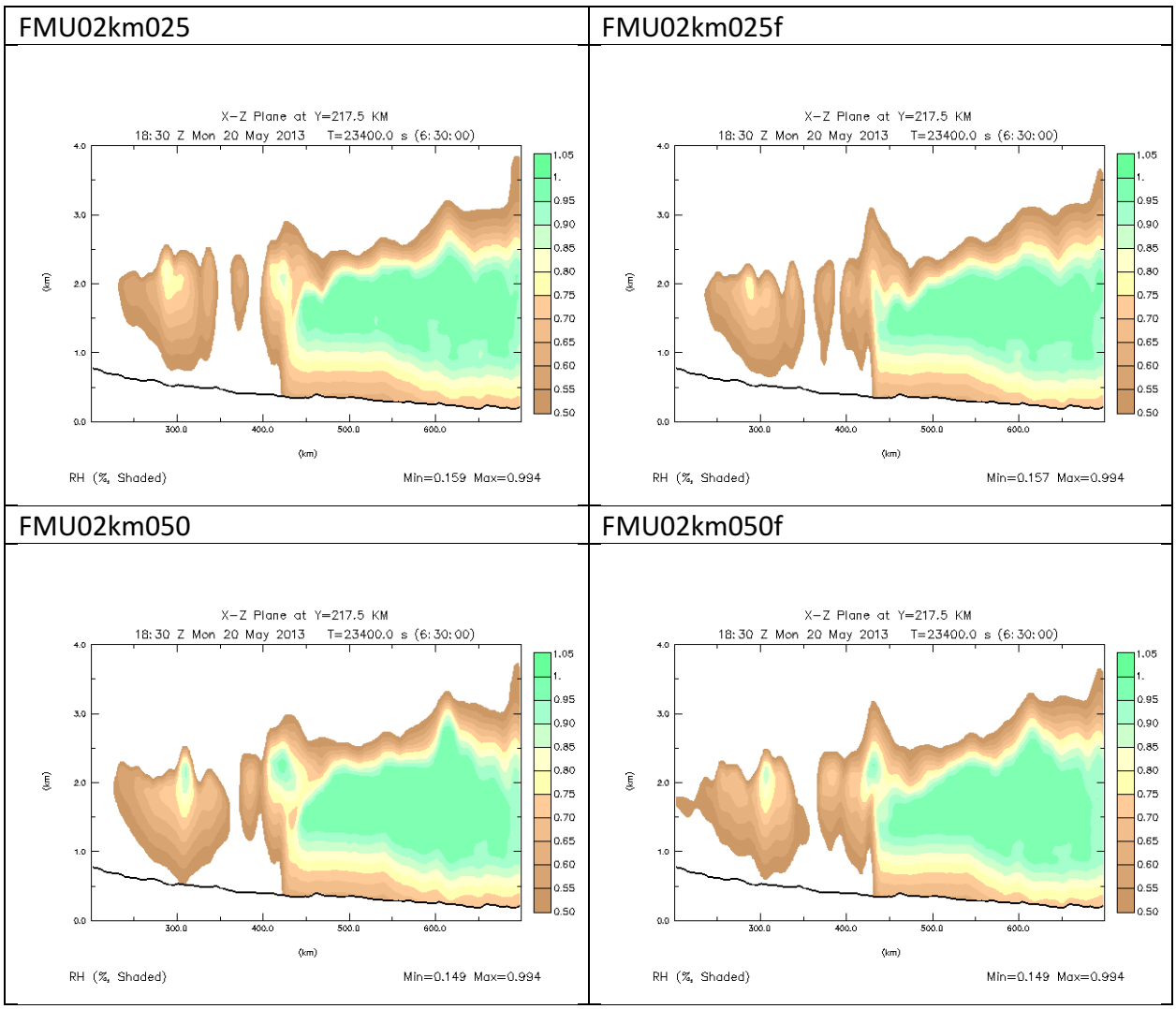

Figure 53. As in Figure 29. Nature Run, UAV obs from max height of 2 km with 108 stations, 10 stations unfitted and fitted, 25 stations unfitted and fitted, and 50 stations unfitted and fitted data.

To see how close the convective initiation is setting-up near the dryline, we can look at plots of relative humidity for this same cross-section.

Examination of boundary cross-sections of relative humidity between the Nature Run and the rest of the OSSE experiments (shown in Figure 53) in the preconvective environment at Y = 217.5 km again shows slightly wider pockets of near saturation at the top of the boundary layer at the dryline for the unfitted experiments than in the fitted experiments. This provides one reason why convective initiation is sooner to occur in the fitted experiments than in the unfitted experiments for 25 and 50 stations, but does not explain why timing of convective initiation between the 10 station fitted and unfitted experiments does not differ.

Relative humidity contours show that for the 25 and 50 station fitted and unfitted experiments, the fitted experiments have a more defined cutoff of higher relative humidity in the 0.5 km MSL to 2.5 km MSL layer east of the dryline, as well more humid air (as defined by the 0.95 green shaded

contour shaded contour) being less extensive east of the dryline in the fitted experiments. This suggests that although the boundary between air closer to saturation and air farther from saturation is better depicted in the 25 and 50 station fitted experiments, there is a lack of moisture depth east of the dryline compared to the corresponding 25 and 50 station unfitted experiments. This could explain at least part of why convective initiation is delayed in the 25 and 50 station fitted experiments compared to the corresponding unfitted experiments. By contrast, the 10 station fitted experiment, although not showing a more defined vertical demarcation between more humid air to the east and drier air to the west, shows a similar area and depth covered by the most humid air.

An interesting pattern to note is drier air west of the dryline (in Caddo County) in all of the fitted experiments compared to the corresponding fitted experiments (as seen by the presence of more brown and less yellow shaded contours west of the dryline in the fitted experiments, closer to what is seen in the Nature Run). So while moisture extent and depth east of the dryline does not show improvement when fitting the data, it appears that there is some improvement in drying out the environment west of the dryline.

The smaller areal coverage and depth of the most humid air east of the dryline in the 25 and 50 station fitted experiments compared to the 25 and 50 station unfitted experiments is a possible reason why convection is much later to initiate in the 25 and 50 station fitted experiments than the corresponding unfitted experiments. The absence of such differences between the fitted and unfitted experiments for 10 stations correspondingly also explains the lack of difference between the timing of convective initiation between the fitted and unfitted 10 station experiments. This indicates that the setup of regions of imminent latent heat release isn't much better simulated for the fitted and unfitted 25 and 50 experiments than the FMU02km108 experiment, although there is improvement at the dryline in simulating a more constrained dryline boundary and drier air west of the dryline in the fitted experiments.

The smaller area and depth of the most humid air east of the dryline in the 25 and 50 station fitted experiments can be expected to be associated with weaker condensation and latent heating, and hence faster convective initiation in the unfitted experiments for 25 and 50 stations compared to the fitted experiments for 25 and 50 stations. It is this factor of more humid air just east of the dryline (especially from 450 km to 500 km) in the lower boundary layer in the 25 and 50 station unfitted experiments that best explain why convection is sooner to initiate and develop into the Grady County area just east of the dryline in the unfitted experiments for 25 and 50 stations compared to the fitted experiments for 25 and 50 stations.

f. Time Interval Between UAV Obs

The number of stations is important to consider, but two other network and assimilation design factors to also consider are the interval time between consecutive UAV obs and the start time in the 1200 to 1800 UTC window that observations are assimilated. For the previous experiments, the UAV obs are assumed to be taken hourly starting at 1200 UTC and extending to 1800 UTC. This is true no matter what the configuration, number, and max height of UAV obs have been.

For this new series of experiments, we vary the interval for UAV obs from hourly (FMU02km108 experiment) to every 3 hours, every 2 hours, and every 30 minutes (FMU02km108a, FMU02km108b, and FMU02km108c experiments, respectively), with the start time of UAV obs assimilation in all these experiments remaining at 1200 UTC. By changing just the interval of UAV obs while fixing the max height UAV obs (at 2 km) and the number of stations (at 108), we can diagnose how changing the interval for UAV obs affects the simulations.

At 1930 UTC (Figure 54), all runs show that convection has initiated by this time. Convection initiates at 1915 UTC at the border between Wichita County in north Texas and Cotton-Jefferson counties in Oklahoma in the FMU02km108a experiment, at 1900 UTC in Wichita-Clay counties in north Texas in the FMU02km108b experiment, and from 1845 UTC to 1900 UTC in north Texas in northern Clay County developing northeast into Cotton-Jefferson counties in the FMU02km108c experiment. This is in comparison to initiation of convection at 1900 UTC at the border between Wichita County in Texas and Cotton County in Oklahoma in the FMU02km108 experiment, and in Comanche-Caddo-Grady counties from 1745 to 1830 UTC in the Nature Run.

Nature Run	FMU02km108a, 3 hour interval
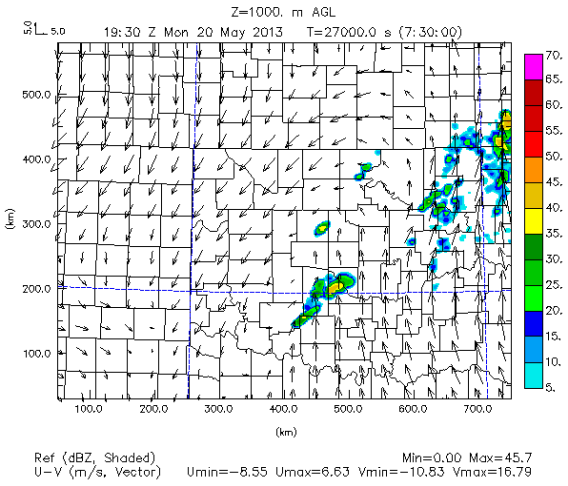	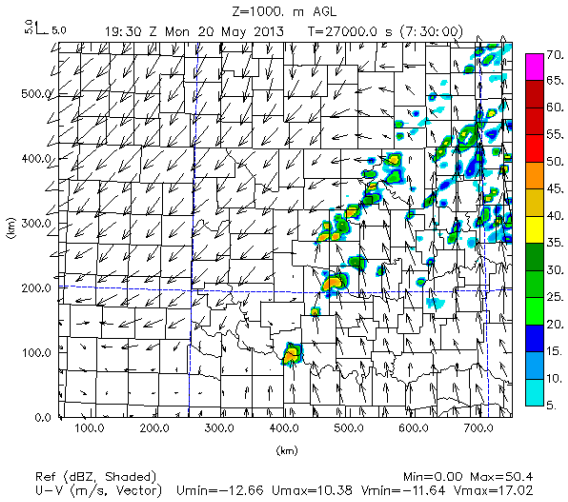
FMU02km108b, 2 hour interval	FMU02km108, 1 hour interval
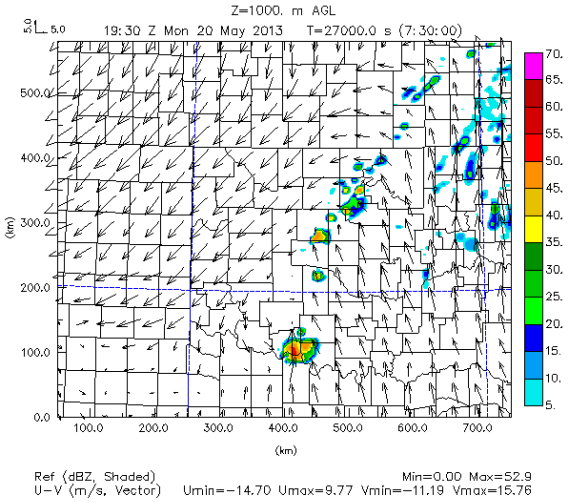	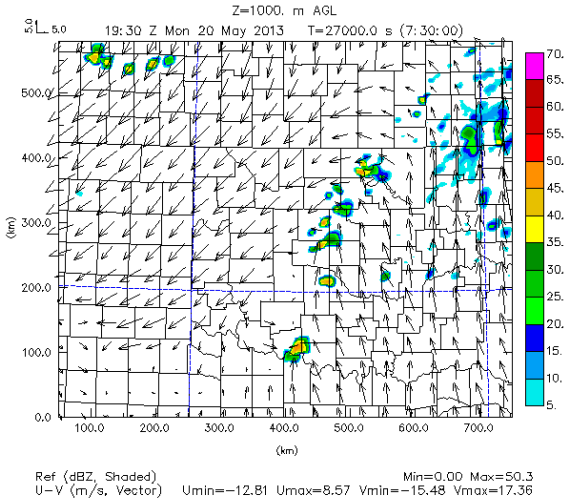
Continued next page…	

FMU02km108c, 30 minute interval	
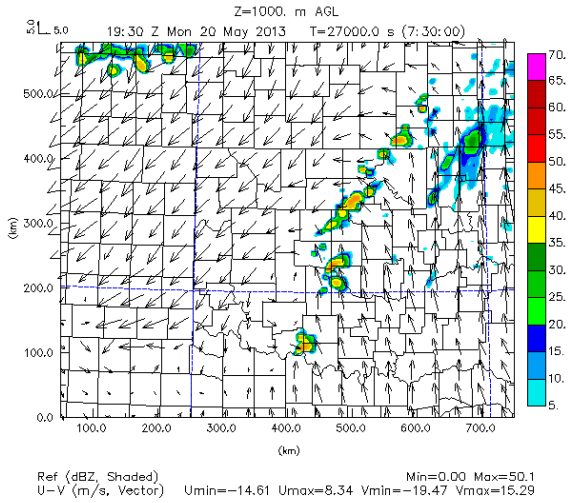	

Figure 54. As in Figure 49, but for set of experiments where the number of stations is fixed at 108 but the interval of consecutive UAV obs is varied from 3 hours to 30 minutes.

Convection is quickest to initiate in the FMU02km108c experiment, where UAV obs are taken every 30 minutes starting at 1200 UTC. Compared to the FMU02km108 experiment (where UAV obs are taken every 1 hour starting at 1200 UTC), this marks an even earlier time for convective initiation, and is closer to timing of convective initiation in the Nature Run than the FMU02km108 experiment. In all the experiments, the convection initiates at the dryline in north Texas-southwest Oklahoma as would be expected, but with county specific differences in location and timing of convective initiation.

In terms of having storms located over the McClain-Cleveland County area and just west of those counties near the dryline in central Oklahoma at 1930 UTC as in the Nature Run, the FMU02km108a and FMU02km108c experiment do a better job of representing this than the FMU02km108b and even FMU02km108 experiment. This is somewhat counterintuitive, since the FMU02km108b experiment is using UAV obs every 2 hours starting at 1200 UTC while the FMU02km108a experiment is using UAV obs every 3 hours starting at 1200 UTC, and so it would be expected that the FMU02km108b experiment would give better placement of convection compared to the FMU02km108a experiment considering that there is more data at 2 hour intervals than at 3 hour intervals, which allows for better temporal resolution of features.

Apart from timing and placement of convection in central Oklahoma, the other apparent difference between the runs at 1930 UTC is that there is more convective activity in northeast Oklahoma in the FMU02km108a and FMU02km108c experiments compared to the rest of the experiments and the Nature Run. This might indicate that UAV obs taken at too short or too long an interval might result in initial excess spotty convection in this region.

Nature Run	FMU02km108a, 3 hour interval
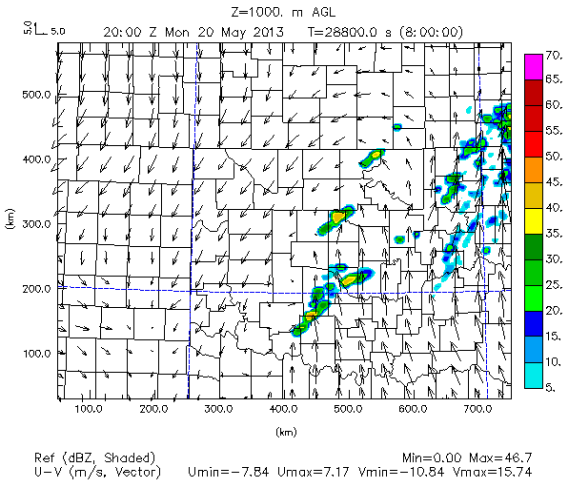	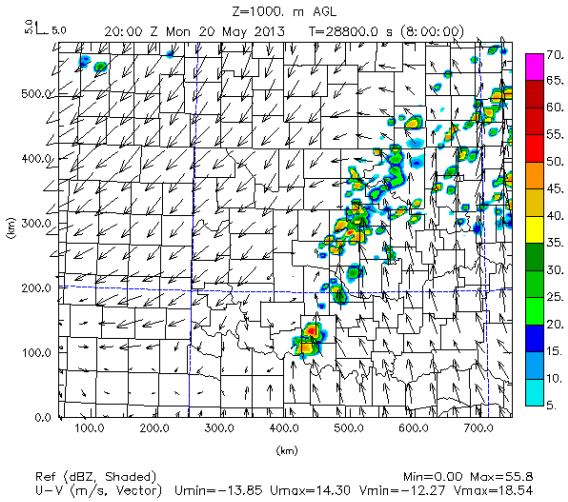
FMU02km108b, 2 hour interval	FMU02km108, 1 hour interval
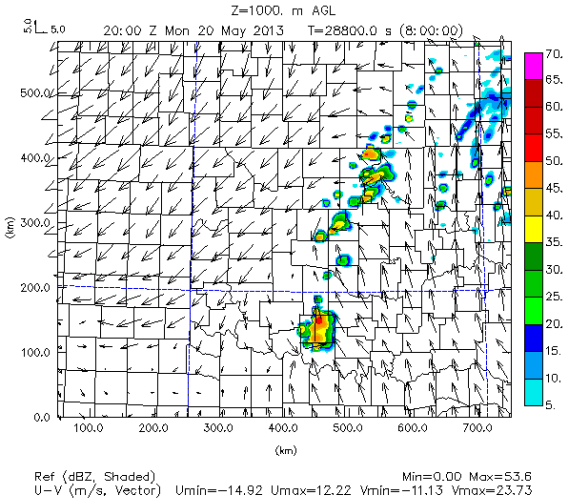	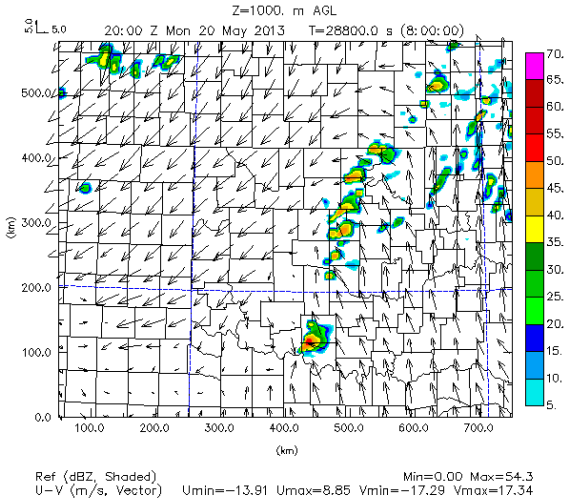
Continued next page…	

FMU02km108c, 30 minute interval	
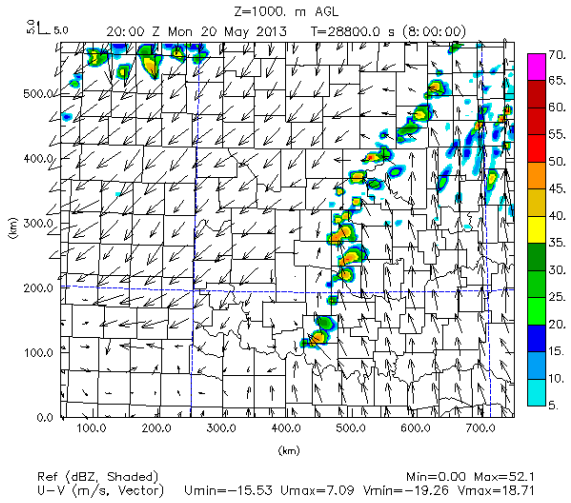	

Figure 55. As in Figure 50, but for set of experiments where the number of stations is fixed at 108 but the interval of consecutive UAV obs is varied from 3 hours to 30 minutes.

By 2000 UTC, the main difference between the set of experiments is the amount of scattered convection in north-central and northeast Oklahoma. In the FMU02km108a and FMU02km108c experiments, there is again excess convective activity compared to the other experiments, but this time more focused more in north-central Oklahoma from Oklahoma to Osage counties. There is not as much excess convective activity in this region for the FMU02km108 and FMU02km108b experiments, again indicating that UAV obs taken at too large or too short an interval can result in some spurious convection where it should not be present.

The other major difference at this time is in the position and intensity of storms in southwest Oklahoma. In the Nature Run, there are moderate intensity storms in the area of Comanche-Grady-Stephens counties. This compares with higher intensity storms in Cotton-Stephens-Jefferson counties in the FMU02km108 and FMU02km108a experiments. In the FMU02km108b experiment, this extent of higher intensity storms is located farther east to mostly encompass Stephens County, but the intensity and extent of storms in southwest Oklahoma still is excessive compared to the Nature Run. Only in the FMU02km108c experiment is the intensity and extent of convection in southwest Oklahoma a better match to the Nature Run. What this suggests that is that when varying the timing of UAV obs, once convection has initiated, the best results of convection in terms of intensity and placement at the dryline are when there is the shortest interval (30 minutes) between UAV obs.

Nature Run	FMU02km108a, 3 hour interval
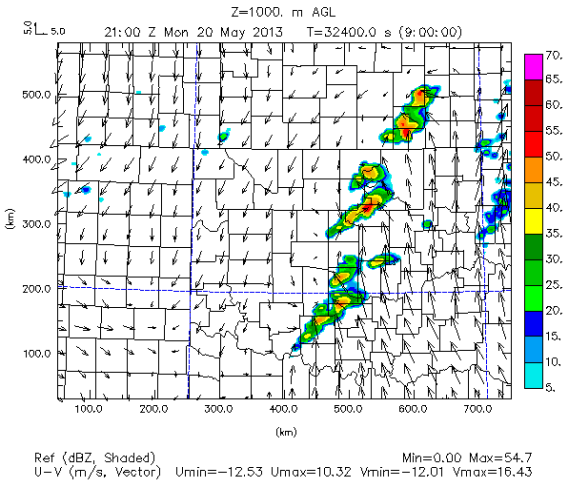	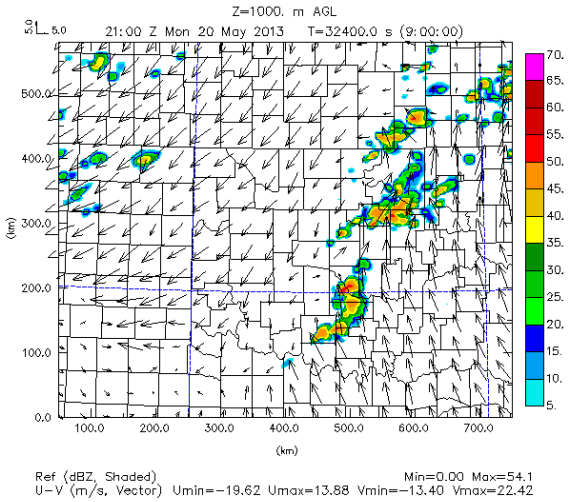
FMU02km108b, 2 hour interval	FMU02km108, 1 hour interval
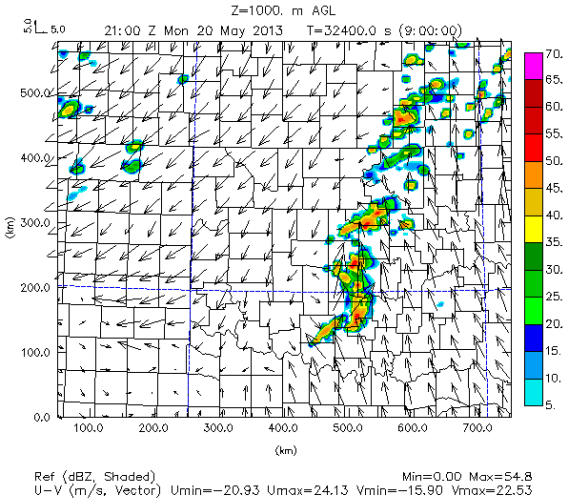	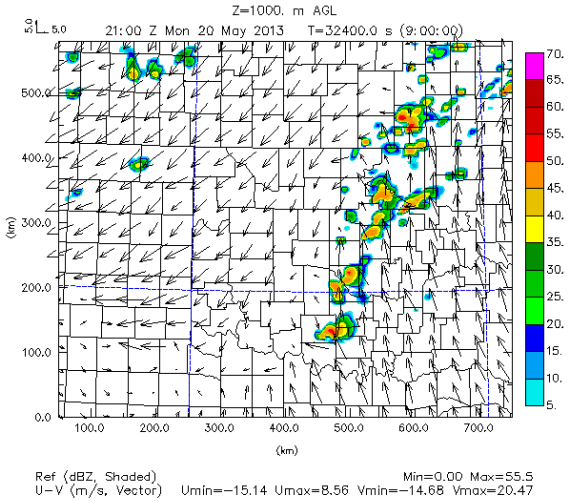
Continued next page…	

FMU02km108c, 30 minute interval	
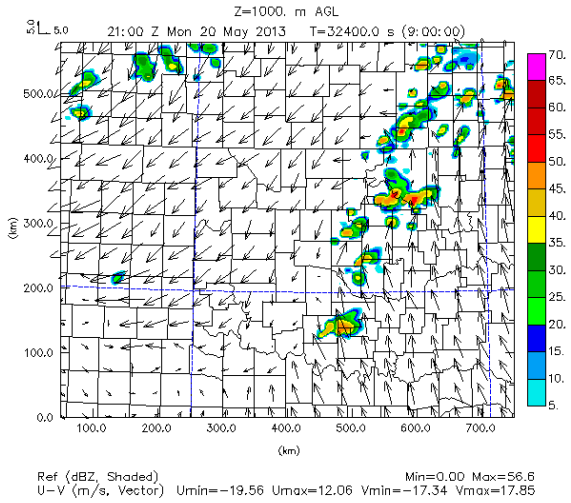	

Figure 56. As in Figure 51, but for set of experiments where the number of stations is fixed at 108 but the interval of consecutive UAV obs is varied from 3 hours to 30 minutes.

An hour later at 2100 UTC, much like the Nature Run, the FMU02km108a and FMU02km108b experiments show two line segments of storms, a northern and southern segment. The southern segment extending from Cleveland to Cotton-Stephens-Jefferson counties acquires more of a bowing shape in the FMU02km108a and FMU02km108b experiments in comparison to the Nature Run. For the FMU02km108 and FMU02km108c experiments, the storms in east-central Oklahoma are more isolated at 2100 UTC than the other experiments, with local high intensity storms in Stephens-Garvin, Cleveland-Pottawatomie, and Lincoln to Osage counties. This is a possible indication that with shorter intervals between UAV obs, the timing of segmentation and modeling of continuous nature of the line of storms along the dryline is less accurate compared to when there are longer intervals between UAV obs.

Since small differences between the experiments become less reliable with increasing forecast time due to nonlinear interactions between storms, specifically at scales like 3 km, reflectivity is not examined for this set of experiments past 2100 UTC.

To examine differences between the boundary layer structures prior to convective initiation and how this might have affected the timing and placement of convection, vertical cross-sections of specific humidity and relative humidity will be examined as in the prior experiments. The focus will be in southwest Oklahoma where the Y = 217.5 km cross-section is located and which includes through the dryline region in southern Oklahoma where storms first form.

Nature Run

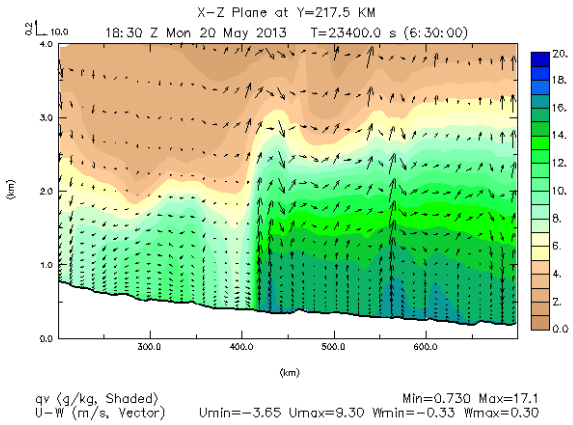

FMU02km108a, 3 hour interval

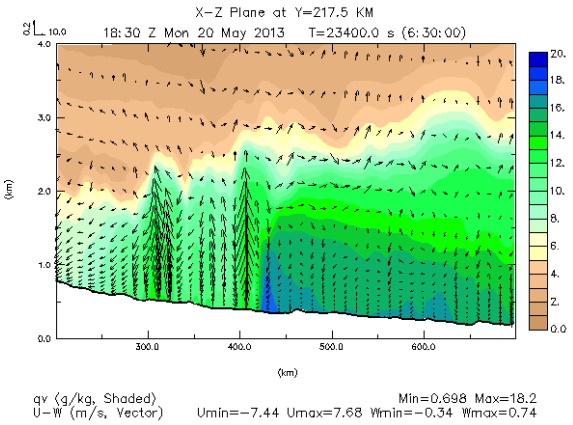

FMU02km108b, 2 hour interval

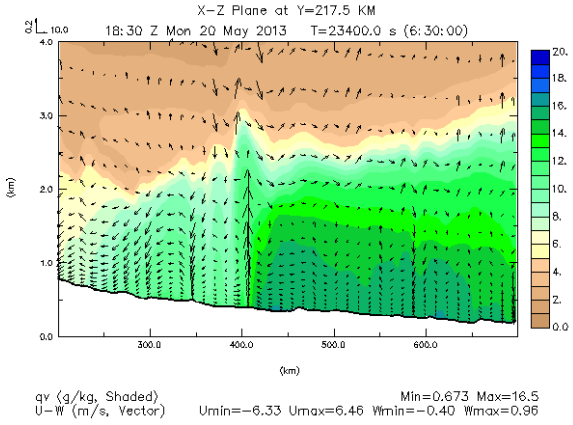

FMU02km108, 1 hour interval

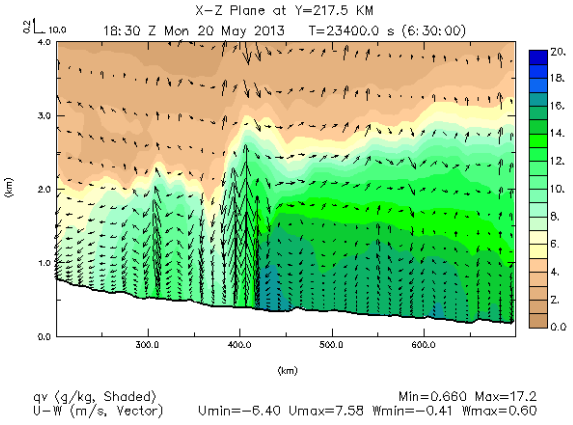

FMU02km108c, 30 minute interval

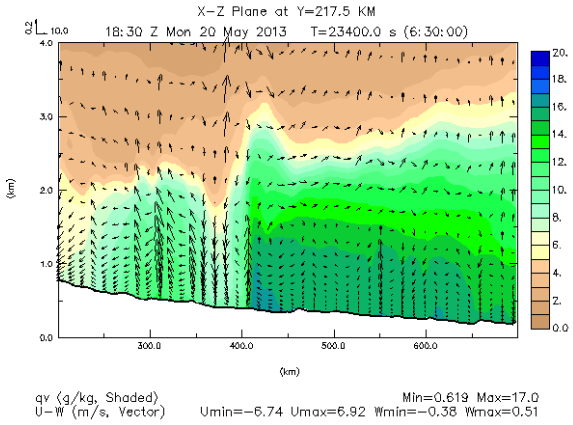

Figure 57. As in Figure 52, but for set of experiments where the maximum height of obs is 2 km and number of stations is fixed at 108, but the interval of consecutive UAV obs is varied from 3 hours to 30 minutes.

Figure 57 shows that a significant improvement in the peaked shape of the moisture intrusion at the dryline is seen as the interval of consecutive UAV obs is progressively reduced from 3 hours to 2 hours to 1 hour and then 30 minutes. In the FMU02km108a experiment, this moisture intrusion is not as apparent as in the rest of the OSSE experiments. In the rest of the OSSE experiments, the maximum height of the moisture intrusion is around the same as in the Nature Run (2.50 km MSL to 2.75 km MSL).

Already this suggests there is improvement in modeling the convergence on the dryline leading to improvements in the height of the moisture intrusion and low level pooled moisture along the dryline when using shorter intervals between consecutive UAV obs.

Looking at the overall boundary layer, the specific humidity vertical cross-sections for this set of experiments shows that when the interval of consecutive UAV obs is every 3 hours, there is far too much humid air in the lowest 500 meters of the boundary layer east of the dryline compared to the Nature Run (as seen by the presence of 18 g/kg, the dark blue shaded contours in the FMU02km108a experiment compared to the rest of the OSSE experiments in the figure and the Nature Run). Conversely, when the interval of consecutive UAV obs is every 2 hours, there is drier air, a max of 16 g/kg in the lowest meters of the boundary layer east of the dryline compared to the Nature Run. The area of pooled humid air east of the dryline becomes more comparable to the Nature Run in the FMU02km108 and FMU02km108c experiments, although it is the experiment where the interval of consecutive UAV obs is every 30 minutes that has closest resembles the shape and extent of this region of pooled humid air in the Nature Run east of the dryline in the lower levels.

Reducing the UAV obs interval from 1 hour to 30 minutes also shows a smoother wind field associated with the moisture intrusion (as seen by the consistently smaller density and size of wind vectors in the moist intrusion in the FMU02km108c experiment that is more similar to the Nature Run compared to in the FMU02km108 experiment). However, again this reverses the prior pattern seen when reducing the UAV obs interval from 2 hours to 1 hour where the couplet of upward and downward velocity vectors near the dryline becomes more robust (wider and somewhat stronger).

To see whether there were any other factors like different locations and area of cloud formation along and east of the dryline might explain the timing of convective initiation, vertical cross-sections of relative humidity were studied for this same region.

Nature Run

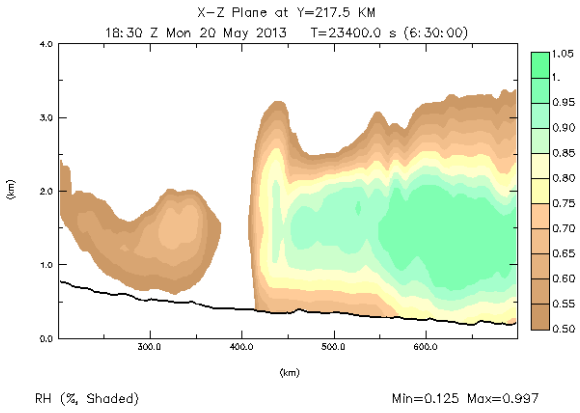

FMU02km108a, 3 hour interval

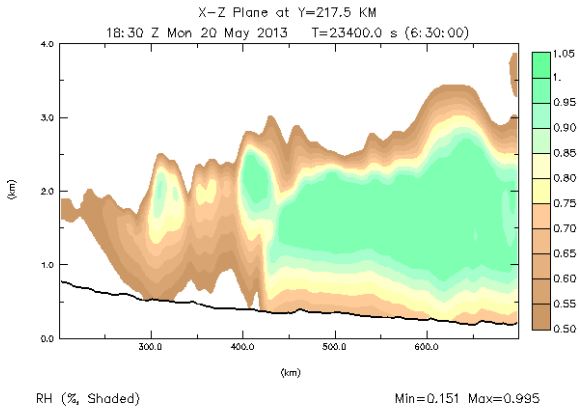

FMU02km108b, 2 hour interval

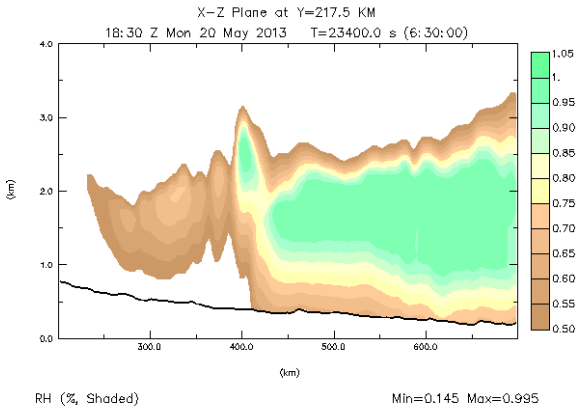

FMU02km108, 1 hour interval

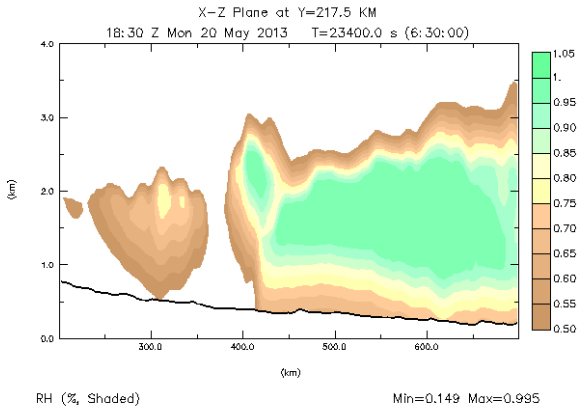

FMU02km108c, 30 minute interval

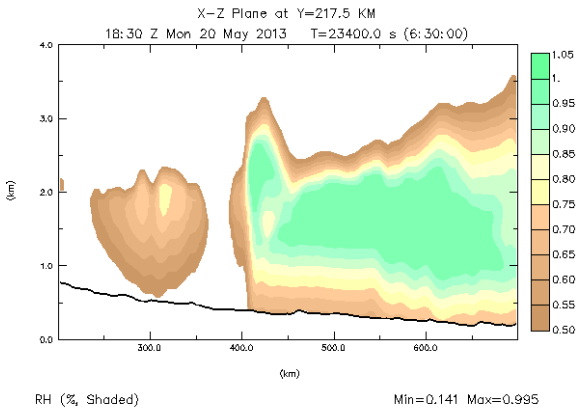

Figure 58. As in Figure 53, but for set of experiments where the number of stations is fixed at 108 but the interval of consecutive UAV obs is varied from 3 hours to 30 minutes.

Figure 58 shows how the most apparent difference when reducing the interval of consecutive UAV obs are the presence of drier air west of the dryline (as indicated by the larger extent of brown and white shaded contours rather than yellow shaded contours in experiments with a small interval between consecutive UAV obs), and a sharper, vertical delineation between more humid air east of the dryline and drier air west of the dryline. What this suggests is that there is stronger diurnal heating, narrower, concentrated vertical updrafts along the dryline and faster initiation of convection as the interval between consecutive UAV obs is decreased.

The FMU02km108a experiment with UAV obs interval being every 3 hours displays a sinusoidal shape of the top of air layer closer to saturation (as shown by the green shaded contours), with a peak around 600 km (Hughes-Okfuskee counties) and troughs in height of these more humid air layers from 450 km to 600 km (Grady east to Cleveland and Pottawatomie counties) and from 650 km and east (from Latimer-Haskell to Le Flore-Sequoyah counties).

The FMU02km108b experiment shows that when the UAV obs interval is decreased from the 3 hours to 2 hours, the shape of the most humid air layer takes on more of the shape as seen in the Nature Run, with an increasing height with further eastward extent from 2.5 km MSL to 3.0 km MSL. This is also seen for the FMU02km108 and FMU02km108c experiments, indicating that as UAV obs interval is decreased, there is less entrainment of drier air aloft east of the dryline and presence of moister air near saturation aloft, even prior to convective initiation. This can contribute to earlier and more widespread convection in OSSE experiments with a small interval between consecutive UAV obs, in addition there being better pooling of moisture at lower levels east of the dry line and smoother wind fields and more defined peak of moisture intrusion in the updraft along the dryline (as was seen from the plots of specific humidity).

g. Sensitivity to the UAV Observation Start Time

We also wanted to test the effect of changing the start time of UAV obs assimilation while leaving the UAV obs interval at 1 hour. By starting assimilation later, forecast turnaround time might be improved for better nowcasting utility and potentially a cost savings for collecting fewer observations, keeping in mind that by starting later, fewer data would then be available to guide the simulated fields toward the Nature Run. To this end, experiments were run where hourly UAV obs at 108 sites start at 1500 UTC (FMU02km108d) and 1700 UTC (FMU02km108e) and compared to the previous runs starting at 1200 UTC.

Nature Run	FMU02km108, 1200 UTC
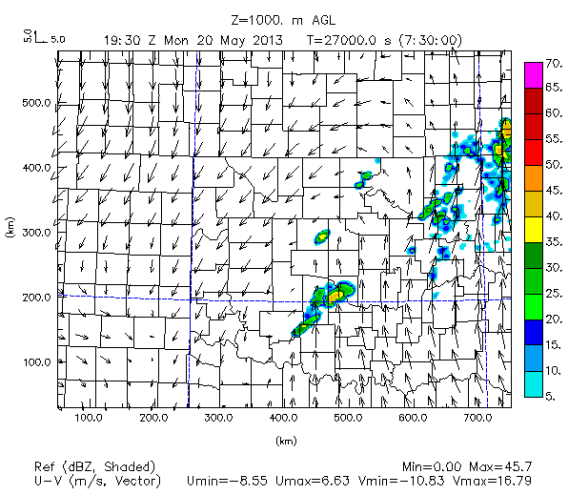	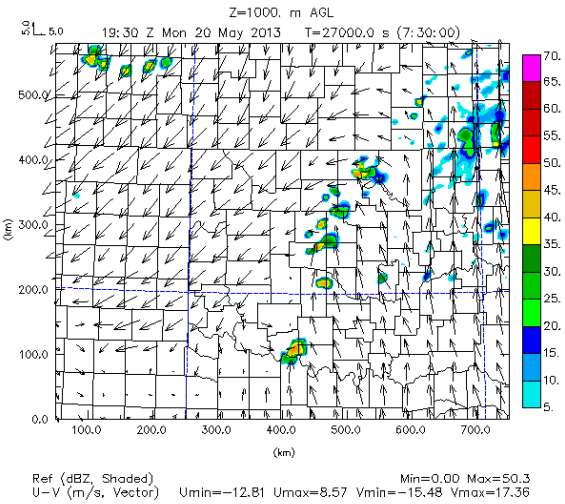
FMU02km108d, 1500 UTC	**FMU02km108e, 1700 UTC**
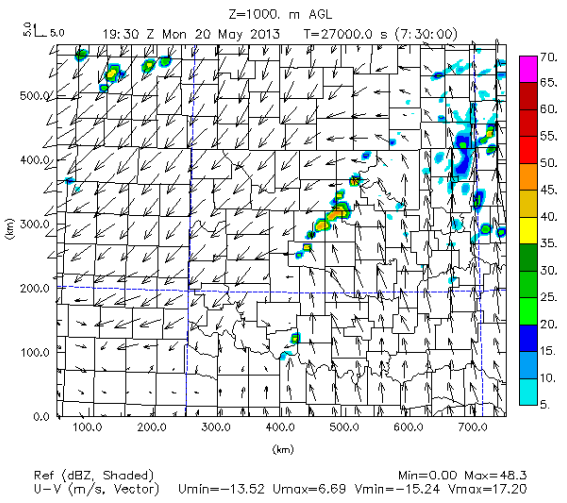	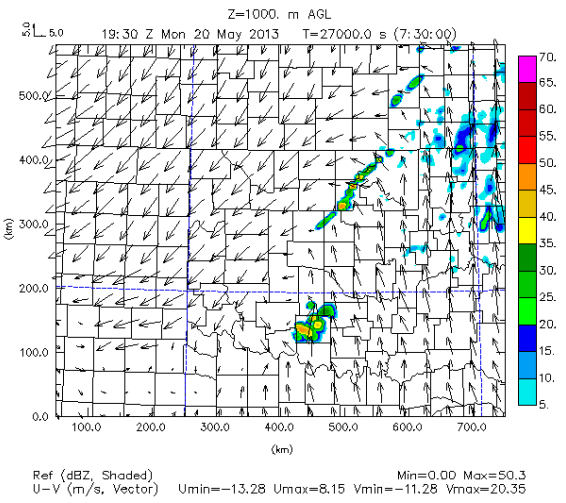

Figure 59. As in Figure 49, but for set of experiments where number of stations is fixed at 108, but where start time of UAV obs is varied. Nature Run, 12 UTC, 15 UTC, 17 UTC.

Convection initiates at 1930 UTC in Cotton County in the FMU02km108d experiment and at 1845 UTC in Cotton County in the FMU02km108e experiment (Figure 59). The timing of convection is similar to in the Nature Run, however convection forms too far south compared to the Nature Run. While the timing of convective initiation is closer to the Nature Run for the FMU02km108e experiment where assimilation of UAV hourly obs start at 1700 UTC instead of 1200 UTC, the timing of convective initiation at the dryline is later than the Nature Run for the FMU02km108d experiment where assimilation starts at 1500 UTC instead of 1200 UTC.

Compared to the FMU02km108 and FMU02km108d experiment, the FMU02km108e experiment (where hourly UAV assimilation starts at 1700 UTC) has the closest placement of convection across southwest Oklahoma (in Stephens and Grady counties) compared to the Nature Run and FMU02km108 experiment. However, the placement, coverage, and intensity of convection is the least similar to the Nature Run and FMU02km108 experiment for when the start time of hourly UAV obs begins at 1500 UTC in the FMU02km108d experiment. Additionally, storms in Grady County that later move into Cleveland County (as shown in the Nature Run) are only present in the FMU02km108 experiment.

In this regard, having later start times of hourly UAV obs (where less data is used than for the period closer to the time of convective initiation) is detrimental to forecasted timing, coverage, and intensity of storms during the period where storms are initiating along the dryline. It seems that 6 hours of assimilated data are needed in this case that starts with 24h old background data.

Nature Run	FMU02km108, 1200 UTC
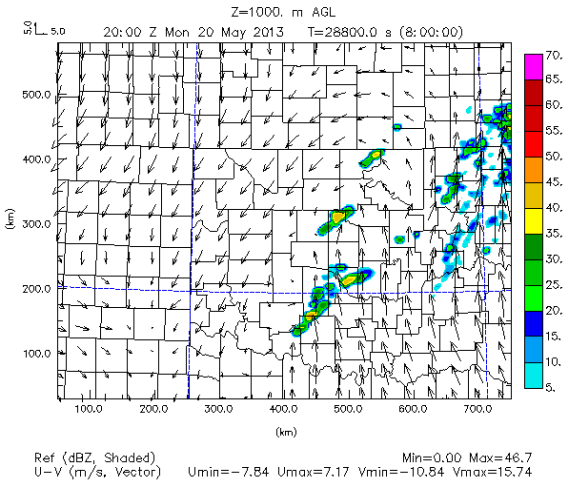	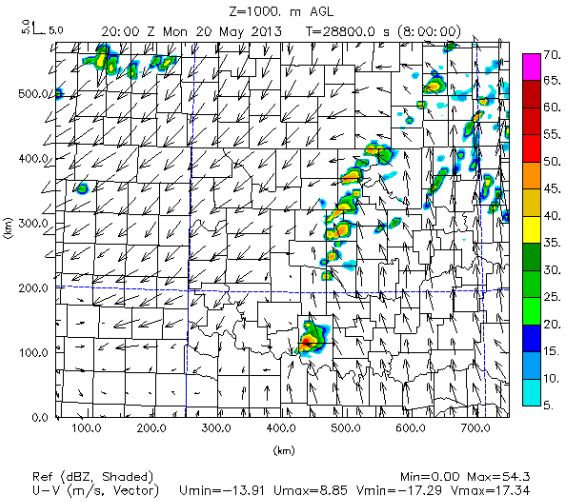
FMU02km108d, 1500 UTC	**FMU02km108e, 1700 UTC**
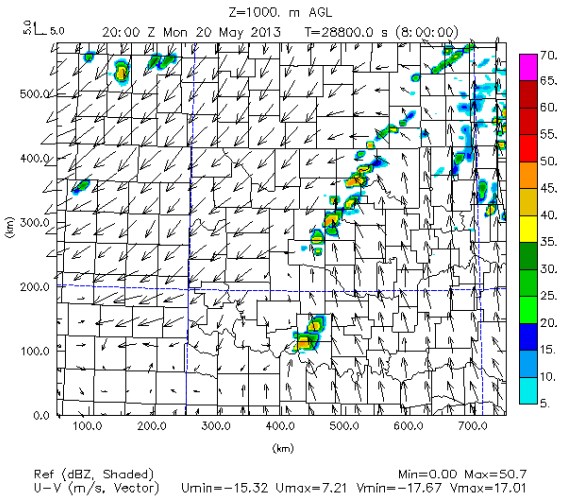	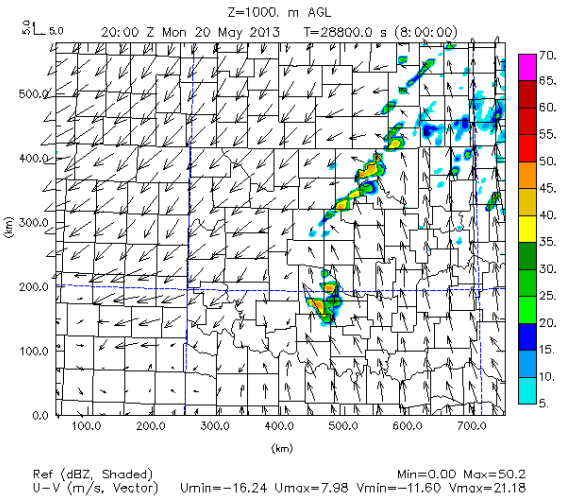

Figure 60. As in Figure 50, forecasts at 20 UTC, but for set of experiments where number of stations is fixed at 108, but where start time of UAV obs is varied. Nature Run, 12 UTC, 15 UTC, 17 UTC.

When using a later start time for UAV hourly obs, the 1930 UTC horizontal reflectivity plots show less scattered convection in north-central Oklahoma than in the FMU02km108 experiment, but also a linear band of convection from Kingfisher to Osage counties that are considerably more extensive than line segments in the Nature Run. So while convective organization around time of convective initiation appears to be better represented in north-central Oklahoma with later start time of hourly UAV obs, there is still spurious convection that is simulated in this area early on in the forecast period.

Comparison of simulated reflectivity at 2000 UTC show, it is only the FMU02km108e experiment that generates the closest match to the Nature Run in terms of placement of the southwest portion of convection along the dryline. The FMU02km108 and FMU02km108d experiments show similar placement of trailing convection farther southwest in Oklahoma compared in the Nature Run and

the FMU02km108e experiments. As before, this suggests there is no better modeling placement of convection in southwest Oklahoma along the dryline when using a later start time of hourly UAV obs (1500 UTC versus 1200 UTC), but perhaps some benefit to simulating convective organization of storms when using the start time of hourly UAV obs closer to the time of convective initiation.

As in the 1930 UTC simulated reflectivity plots, organization of storms in north-central Oklahoma is much more small-scale in the experiments where the start times hourly UAV obs are delayed until 1500 UTC and 1700 UTC (FMU02km108d and FMU02km108e, respectively). However, as at 1930 UTC, there is still too much convection compared to the Nature Run in the corridor extending from Oklahoma to Osage County, which again shows that in this region of north-central Oklahoma, there is no clear improvement in reducing bands of spurious convection when using later start times for hourly UAV obs.

Nature Run	FMU02km108, 1200 UTC
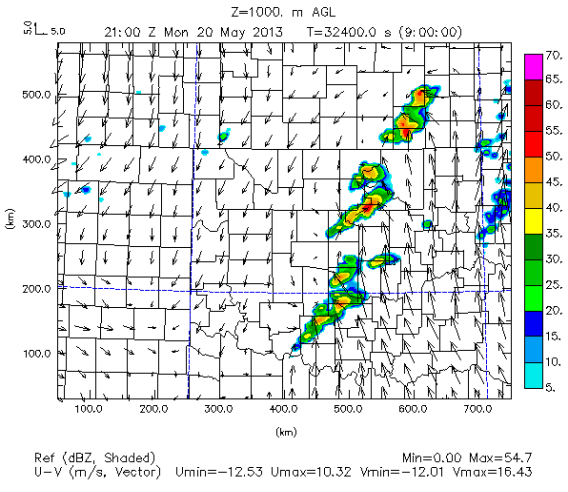	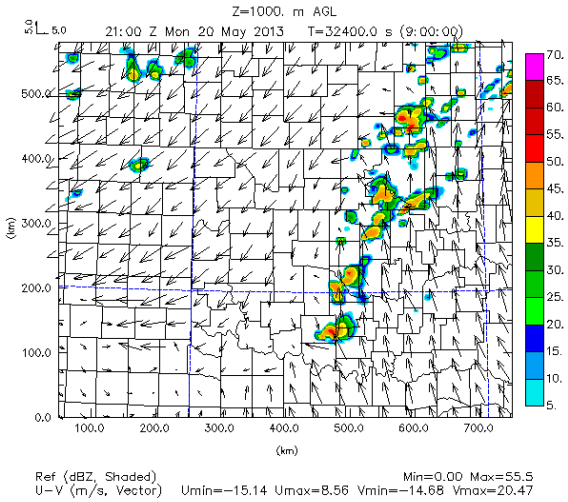
FMU02km108d, 1500 UTC	**FMU02km108e, 1700 UTC**
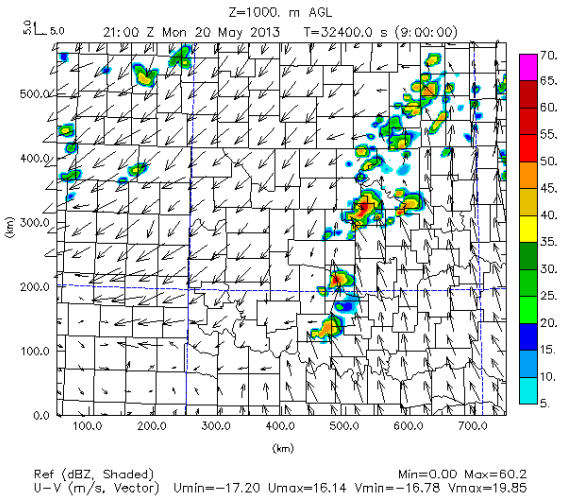	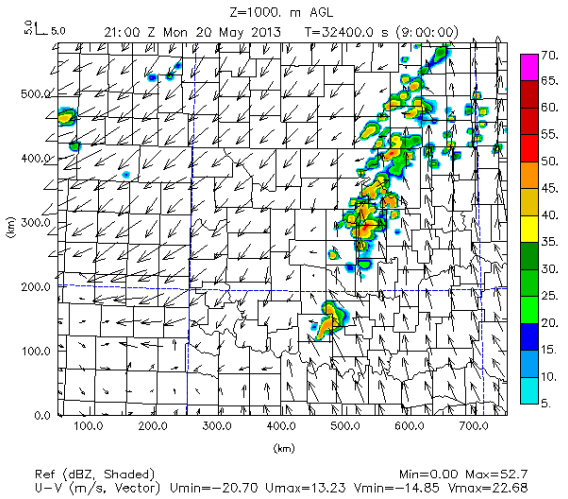

Figure 61. As in Figure 50, but 21 UTC, for set of experiments where number of stations is fixed at 108, but where start time of UAV obs is varied. Nature Run, 12 UTC, 15 UTC, 17 UTC.

By 2100 UTC (Figure 61) the only consistent improvement that the FMU02km108d and FMU02km108e experiments show is better alignment of storms from the northeast to southwest across north-central Oklahoma. For the case where hourly UAV obs start closest to the time of convective initiation (FMU02km108e, when there is the least data used) there is an absence of convection over Cleveland County at this time unlike in the Nature Run and the other experiments.

To study possible reasons for why convective initiation timing varied depending on when hourly UAV obs assimilation began (1200 UTC, 1500 UTC, or 1700 UTC), vertical cross-sections of specific humidity and relative humidity were examined at Y = 217.5 km for this set of experiments.

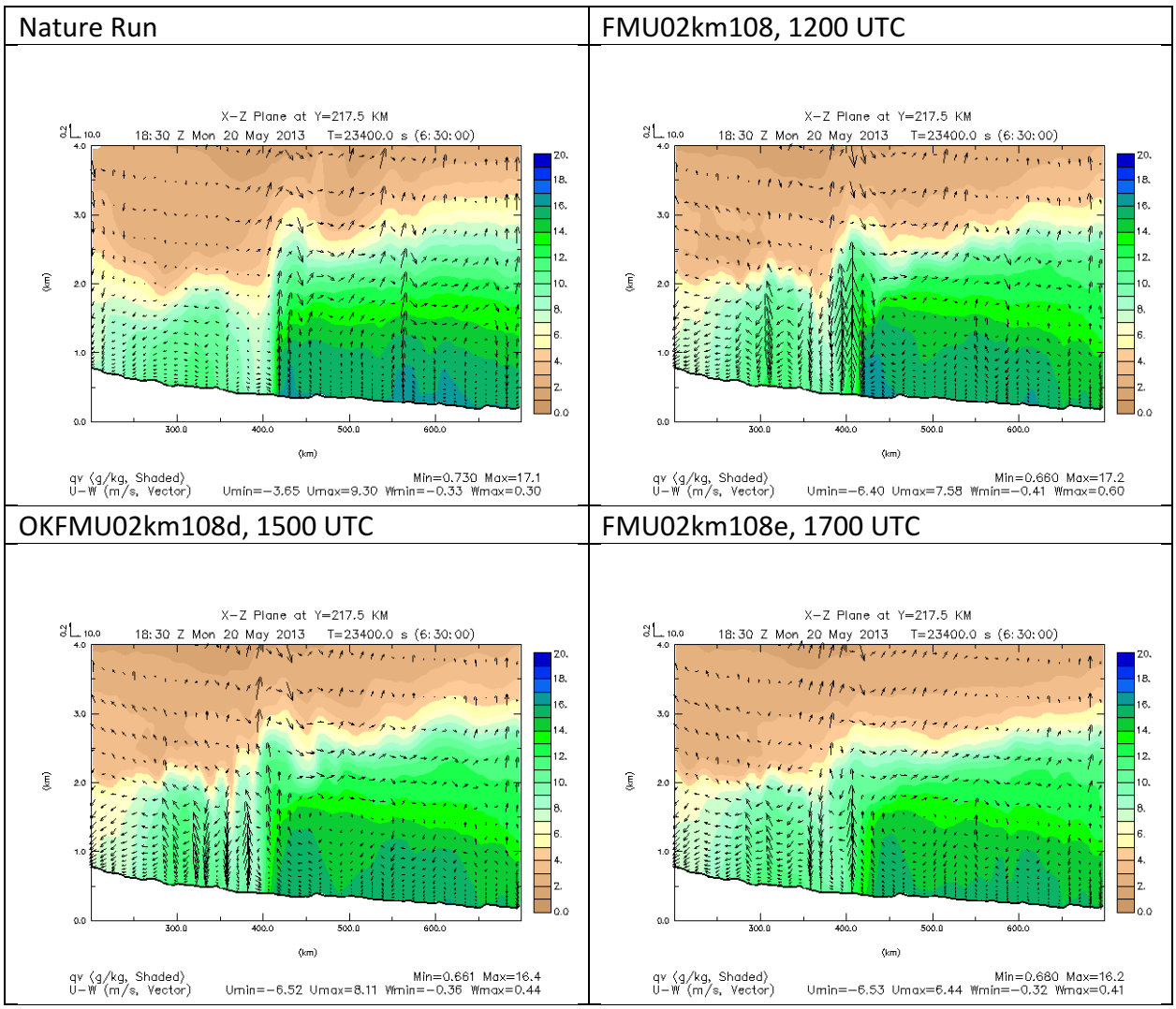

Figure 62. As in Figure 52, but for set of experiments where number of stations is fixed at 108, but where start time of UAV obs is varied; Nature Run, 12 UTC, 15 UTC, 17 UTC.

Figure 62 shows that delaying the start time of UAV obs from 1200 UTC results in a progressively less defined peak region of moisture and vertical motion at the dryline, as well as a less steep, plateaued shape of the boundary layer moisture profile both west and east of the dryline (as shown by the outline and shape of the 12 g/kg green shaded contour). Additionally, there is consistently a lower magnitude of low level moisture (as indicated by lack of 18 g/kg blue shaded contour in the lowest meters of the boundary layer east of the dryline in the FMU02km108d and FMU02km108e experiments), and a less well defined moisture intrusion peak region along the dryline. However, there is also increased moisture west of the dryline when delaying start time as evident from the larger area of 8 to 10 g/kg light green shaded contours west of 400 km in the FMU02km108e experiment than the FMU02km108d experiment, and the FMU02km108d experiment compared to the FMU02km108 experiment. This is observed especially around 250 km and 350 km in the 1.0 km to 1.5 km MSL layer. The dome of air outlined by the 14 g/kg dark green contour and extending up to 1.25 km to 1.5 km MSL also shows that flattening and a less slanted slope when delaying the start of UAV obs. Already this shows that the magnitude of

boundary layer moisture profile in Grady County is not necessarily improved linearly as start time is delayed, as there is less buildup of moisture in the lowest levels east of the dryline and less dry air west of the dryline when this is done.

As with the experiments changing only the UAV obs interval, the magnitude of maximum vertical motion and the range of vertical motion are far too great in the FMU02km108 experiment, but are more comparable to the Nature Run for this set of experiments where the UAV obs start time is delayed. However, the FMU02km108e experiment with start time at 1700 UTC still exhibits the closest match of maximum and minimum vertical velocity to the Nature Run.

This all shows that delaying the start time of UAV obs to 1700 UTC does demonstrate worsening outline of regions of moister air east of the dryline and the overall strength of upward and vertical motion in the boundary layer. Reduced moisture gradient west and east of the dryline and smaller buildup of lower level moisture east of the dryline (which can lead to weaker updrafts and reduced latent heating as this air needs to be lifted farther up to reach saturation) explain part of why placement and coverage of storms is generally worse as start time of UAV obs is delayed.

Since convection initiates along the dryline sooner in the FMU02km108e experiment than the FMU02km108d experiment however, it appears that the lack of moisture at lower levels east of the dryline is compensated for by the better simulation of wind fields and boundary layer structure and magnitude of moisture in the FMU02km108e experiment compared to the FMU02km108 and FMU02km108d experiments with earlier start times of UAV obs (1200 UTC and 1500 UTC, respectively).

To examine how the differences in incipient regions of latent heating and cloud cover along the dryline might differ between the experiments, plots of relative humidity for this set of experiments were examined.

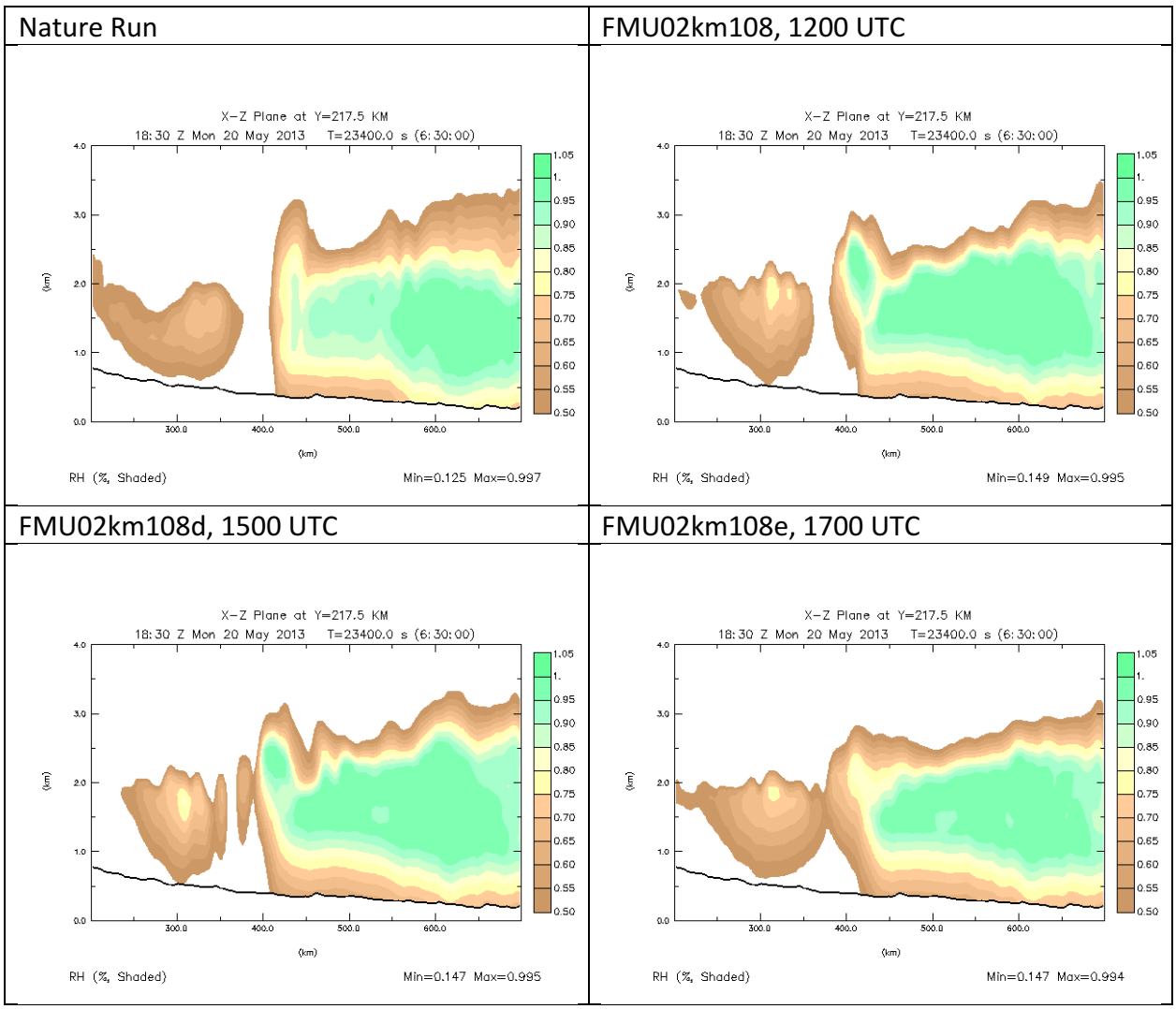

Figure 63. As in Figure 53, but for set of experiments where number of stations is fixed at 108, but where start time of UAV obs is varied; Nature Run, 12 UTC, 15 UTC, 17 UTC.

Vertical cross-sections of relative humidity for this set of experiments (Figure 63) show that when the start time of hourly UAV obs is closest to the time of convective initiation, the leading edge of air near saturation at and east of the dryline from 1.0 km to 3.0 km MSL is not as steep and vertically oriented as in the Nature Run. This issue is only increased when delaying start time of hourly UAV obs, as the leading edge of more humid air in green (0.85 to 0.90) and spring green (0.90 to 0.95) shaded contours along the dryline only becomes less vertically oriented and more slanted downward from west to east in the FMU02km108d experiment with start time at 1500 UTC and then the FMU02km108e experiment with start time at 1700 UTC, indicating less vertically oriented, robust updrafts at the dryline. Even so, the range of maximum and minimum relative humidity does not change much between the OSSE experiments, except for reduced magnitude of maximum and minimum relative humidity in the FMU02km108d experiment compared to the FMU02km108 experiment, and reduced magnitude of maximum relative humidity in the FMU02km108e experiment compared to in the FMU02km108d experiment. Even still, the presence of more humid air slanting westward with height as the start time of hourly UAV

obs is delayed would indicated less capping, faster destabilization, and faster convective initiation when the start time is delayed from 1500 UTC to 1700 UTC, and from what is observed in the plots horizontal reflectivity from 1800 UTC to 2100 UTC during the window of convective initiation, this is exactly what is observed when comparing the FMU02km108, FMU02km108d, and FMU02km108e experiments to the Nature Run.

Overall, unlike previous experiments (where other factors like structure and magnitude of vertical motion along the dryline explained differences in convective initiation and placement of storms), it appears that differences in the structure and magnitude of boundary layer moisture along and east of the dryline from delaying start time comprise the largest factor in explaining why convective initiation occurs faster along the dryline in the FMU02km108e experiment compared to the FMU02km108d experiment, as well as why storms are quicker to move into Grady County in the FMU02km108e experiment as in the Nature Run.

h. Trade Off Between Obs Interval and Obs Density

One last aspect that this study will look at is whether decreasing the interval between UAV obs from 1 hour to 30 minutes (when UAV obs start time is fixed at 1200 UTC) could allow for a smaller number of stations (as in the FMU02km050c experiment) to be used to get similar results (in terms of timing of convective initiation, placement, coverage, and intensity of storms, and boundary layer configuration prior to convective initiation) to when the maximum number of stations (as in the FMU02km108c experiment) are used. Testing this is important, because if it turns out that decreasing the interval of UAV obs may allow for a lesser number of stations to be used, then it will be less expensive to set up and deploy a UAV network, yet have available the same total volume of UAV observations. To test this, the FMU02km108c and FMU02km050c experiments will be compared to the Nature Run and FMU02km108 experiment.

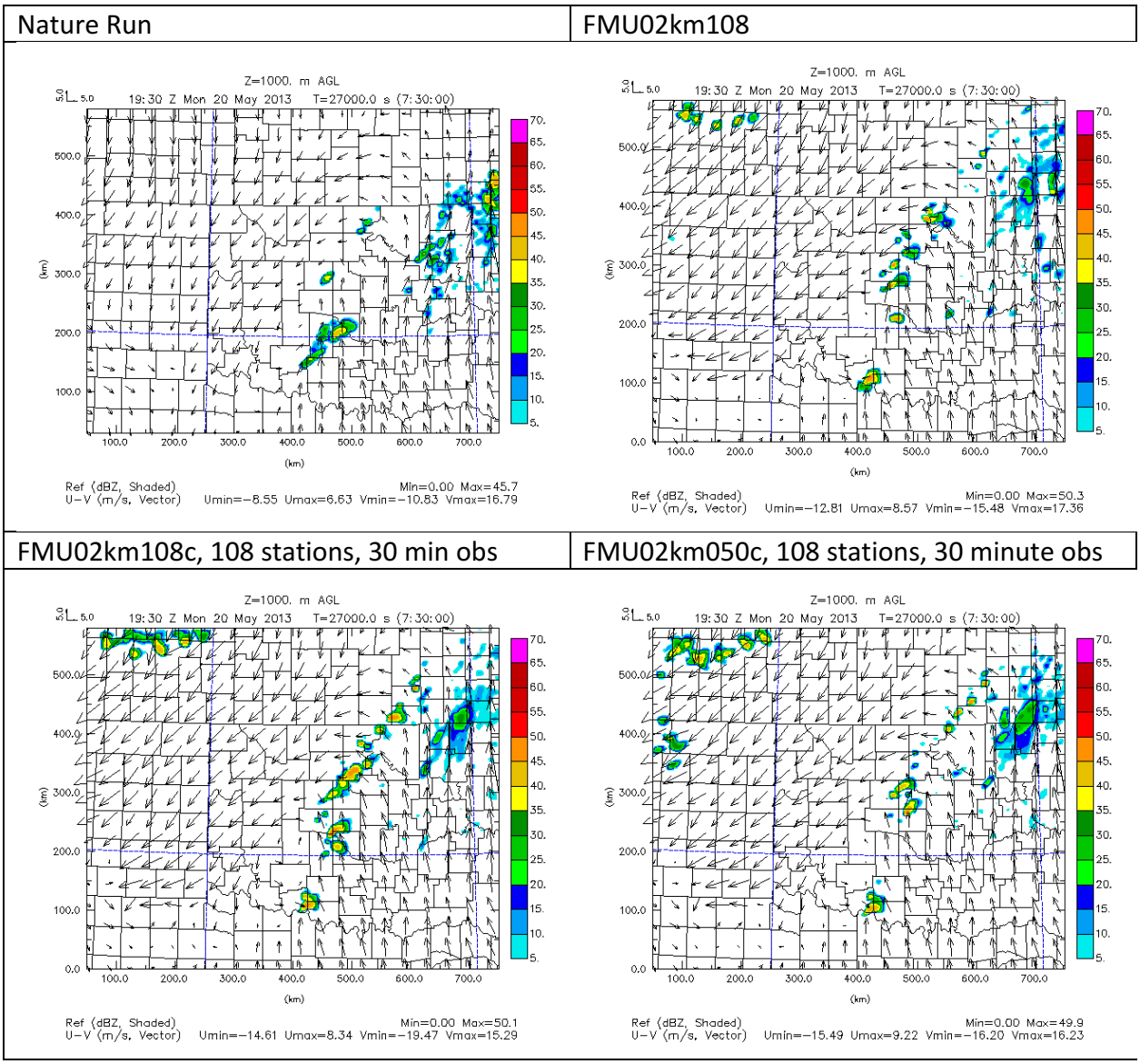

Figure 64. As in Figure 49, but for set of experiments where frequency of UAV obs for bottom experiments is 30 minutes instead of 1 hour. Bottom-left, 108 stations, bottom-right, 50 stations.

Convection that will later move into Cleveland County initiates from 1845 UTC to 1900 UTC in north Texas in northern Clay County developing northeast into Cotton-Jefferson counties in the FMU02km108c experiment, and at 1900 UTC in Hardemann-Wilbarger County in the FMU02km050c experiment. Therefore, convective initiation along the dryline is already delayed by at least 30 minutes in the FMU02km050c experiment compared to the Nature Run. This is again in comparison to initiation of convection at 1900 UTC along the Red River in southern Cotton County Oklahoma in the FMU02km108 experiment, and in Comanche-Caddo-Grady counties from 1745 to 1830 UTC in the Nature Run.

By 1930 UTC (Figure 64), convection is present in southwest Oklahoma (Cotton-Stephens-Jefferson counties) for the OSSE experiments (FMU02km108, FMU02km108c, and FMU02km050c) but not stretching from Stephens to Grady and Stephens counties as in the Nature Run. So in all the OSSE experiments in this set of experiments, at 1930 UTC, after convection has initiated, the storms are still located too far southwest along the dryline compared to the Nature Run. So in all this set of OSSE experiments at 1930 UTC after convection has initiated, storms are still located too far southwest along the dryline compared to the Nature Run

The FMU02km050c experiment has less scattered convection at 1930 UTC in north-central Oklahoma compared to the FMU02km108 and FMU02km108c experiments. This is in better agreement with the Nature Run, specifically regarding placement and coverage of convection in Logan County. However, convection in the FMU02km050c experiment still shows convection farther east compared to the Nature Run at 1930 UTC in north-central Oklahoma.

Nature Run	FMU02km108
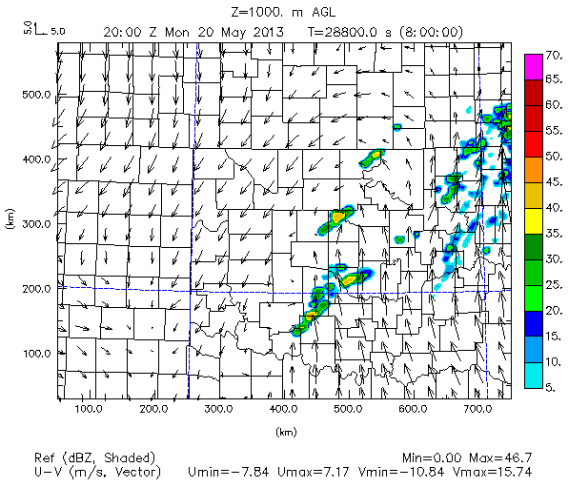	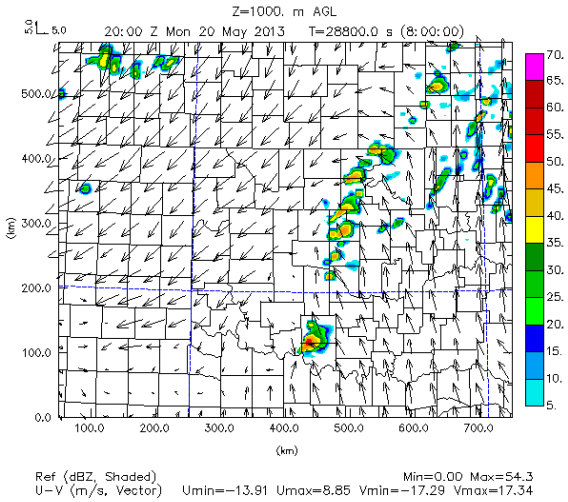
FMU02km108c, 108 stations, 30 min obs	FMU02km050c, 50 stations, 30 min obs
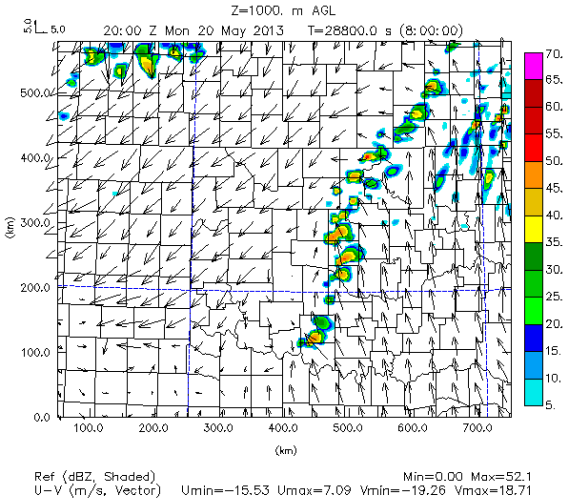	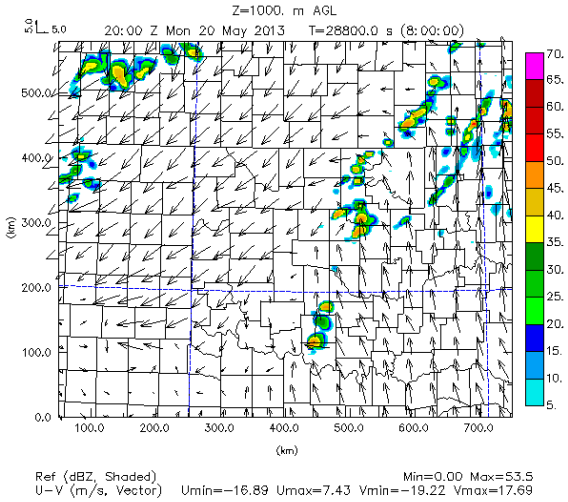

Figure 65. As in Figure 64, but at 2000 UTC.

By 2000 UTC, this lack of convective coverage along the warm front in north-central Oklahoma persists in the FMU02km050c experiment, is in better agreement with the Nature Run than the FMU02km108 and FMU02km108c experiments, which show too much convection in the corridor stretching from Oklahoma-Logan counties to Osage County. There is no high intensity convection centered over Cleveland County unlike the Nature Run, which also differs from the FMU02km108 and FMU02km108c experiment.

Nature Run	FMU02km108
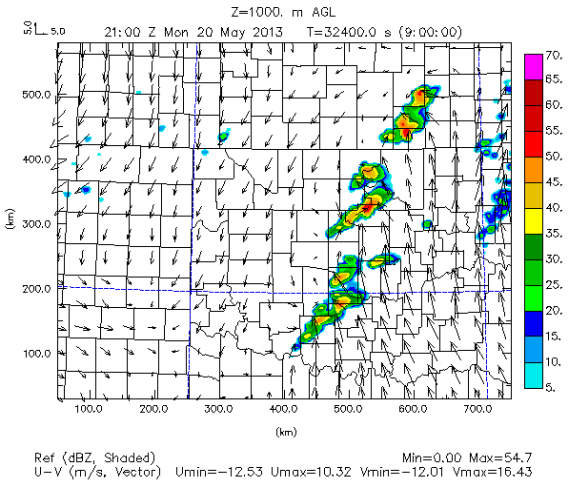	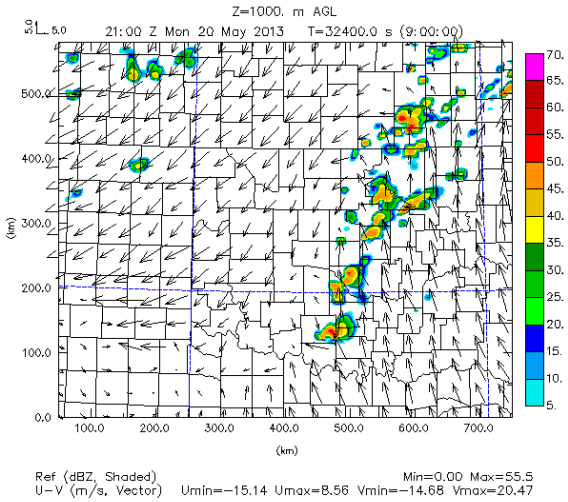
FMU02km108c, 108 stations, 30 min obs	FMU02km050c, 50 stations, 30 min obs
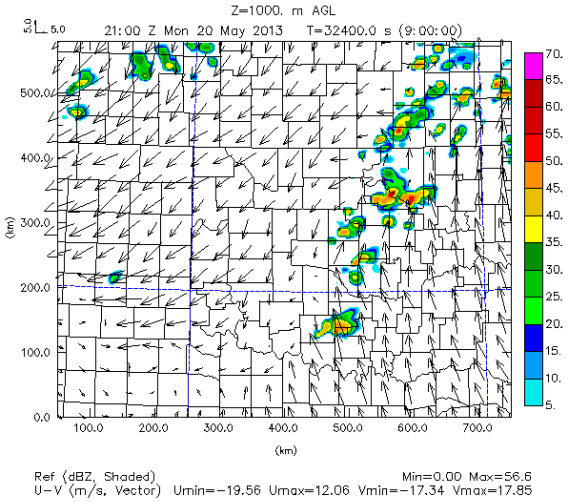	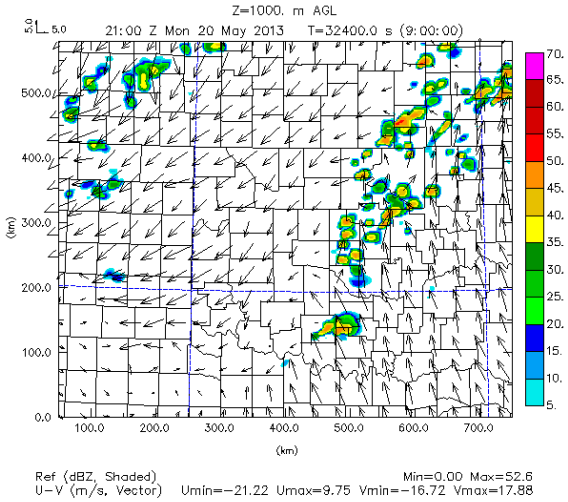

Figure 66. As in Figure 64, but for 2100 UTC.

By 2100 UTC, the FMU02km050c shows too much spotty convective activity in north-central Oklahoma compared to the Nature Run and FMU02km108 and FMU02km108c experiments. Particularly, there is no separation of defined convective cores along the dryline like in the Nature Run (where convective cores are separated into areas like Stephens to Cleveland County in southwest Oklahoma, Logan to Osage counties in Oklahoma, and southeast Kansas).

As observed, convective initiation is delayed when using UAV obs every 30 minutes with a maximum of 50 stations, but at least initially, using UAV obs every 30 minutes with a maximum of 50 stations (FMU02km050c) rather than 108 stations (FMU02km108c), convective activity in north-central Oklahoma is reduced in coverage, as in the Nature Run. This reduction persists for longer in the FMU02km050c experiment than in the FMU02km108 and FMU02km108c experiments, up until 2000 UTC, in better agreement with the Nature Run. The FMU02km050c

experiment was compared with the FMU02km108c and FMU02km108 experiments to also determine whether it improved on the FMU02km050 hourly.

However, already by 2000 UTC, the most significant convection over Cleveland County is missing at FMU02km050c compared to the FMU02km108 and FMU02km108c experiments and the Nature Run. So the closeness of the FMU02km050c experiment to the Nature Run has begun to break down approximately 1 hour after convective initiation.

By 2100 UTC, the FMU02km050c simulates too much spotty convection along the warm front in north-central Oklahoma compared to in the Nature Run and FMU02km108 and FMU02km108c experiments.

So while initially (up to 1 hour after convective initiation) the FMU02km050c experiment is able to better model placement and coverage of convection along the dryline in north-central Oklahoma, the similarity between the FMU02km050c and the Nature Run degrades over time, with reasons for this being missing convection over Cleveland County at 2000 UTC and too much spottiness of convection at 2100 UTC.

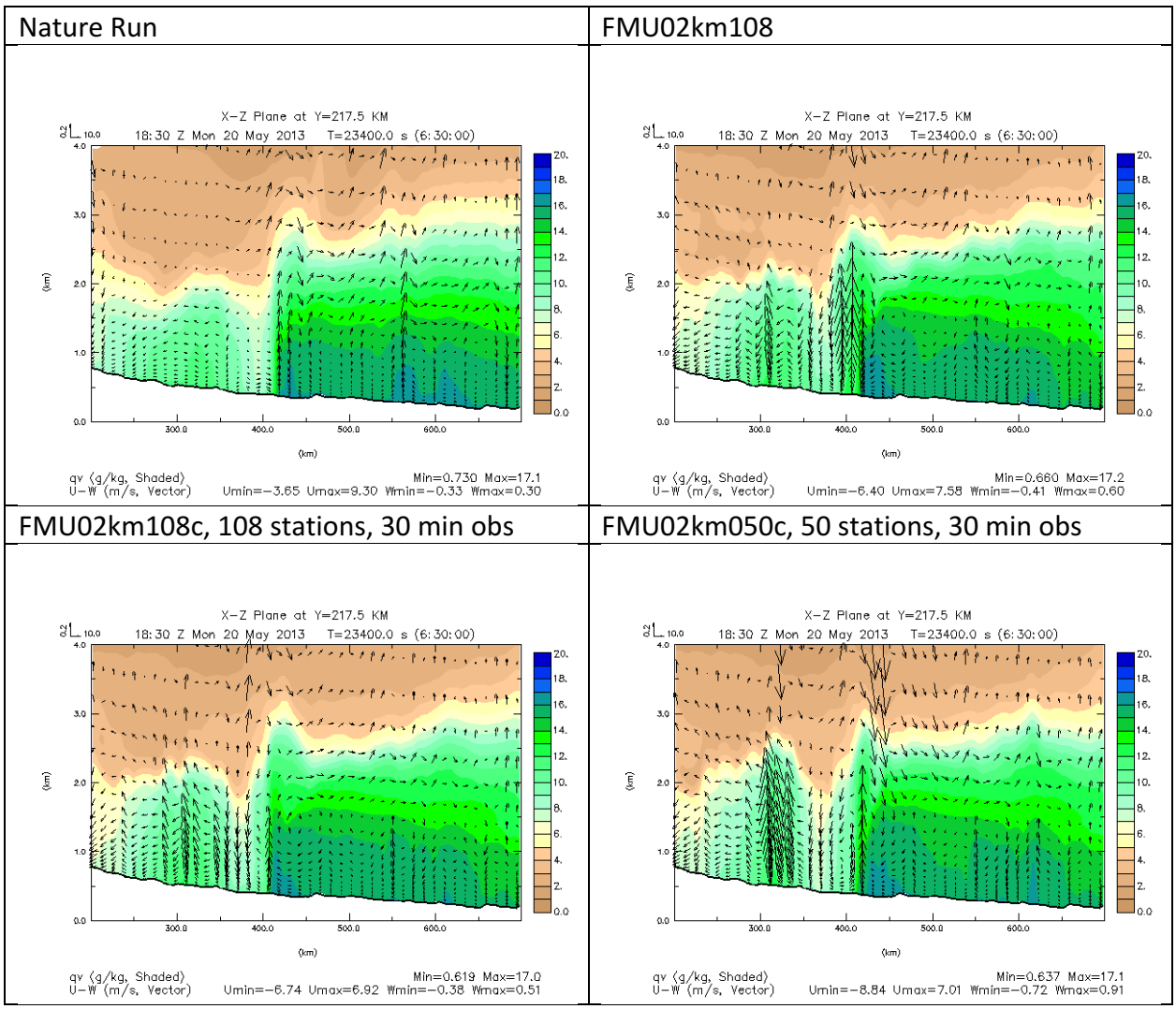

Figure 67. As in Figure 52, but for set of experiments where frequency of UAV obs for bottom experiments is 30 minutes instead of 1 hour.

Examination of the boundary layer at 1830 UTC prior to convective initiation and development of storms into Grady County (Figure 67) shows a much higher maximum vertical velocity along the dryline (0.91 m/s versus 0.51 m/s) when 50 stations are used for 30 minute interval UAV obs (FMU02km050c) rather than when 108 stations are used for 30 minute interval UAV obs (FMU02km108c). Additionally, the minimum vertical velocity in the FMU02km108c experiment (-0.38 m/s) is much closer to the value of minimum vertical motion in the Nature Run (-0.33 m/s) than in the FMU02km050c experiment (-0.91 m/s) The FMU02km108c experiment can already been seen to be hence more comparable with the Nature Run (where maximum vertical velocity is 0.30 m/s) than the FMU02km050c experiment concerning the magnitude and intensity of upward and downward motion along the dryline. The peak of the moisture intrusion (as defined by the 12 g/kg green contour of specific humidity) is broader and less well defined in the FMU02km050c experiment compared to the FMU02km108c experiment and shunted a bit farther to the east, with troughing of brown shaded contours west of this intrusion in the FMU02km050c experiment indicating too much mixing of drier aloft just west of the dryline. This shows that concerning

maximum vertical motion and height of moisture intrusion along the dryline, the FMU02km108c experiment is in better agreement with the Nature Run than the FMU02km050c experiment.

Examining of the wind vectors shows a smoother wind field in the moist intrusion for the FMU02km108c experiment compared to the FMU02km050c and FMU02km108 experiments and more in line with what is seen in the Nature Run. This more evidence that the FMU02km108c is in better agreement with simulation of overall moisture and vertical wind fields along the dryline than the FMU02km050c (but also the FMU02km108 experiment).

In the FMU02km050c experiment, the 16 g/kg dark green shaded contour at the lowest levels east of the dryline boundary is too broad and extends too far east compared to in the FMU02km108c experiment, FMU02km108 experiment, and Nature Run. This small but still noticeable difference suggests there is better pooling of more humid air near the dryline boundary when the number of stations is greater (108 compared to 50).

West of the dryline, the FMU02km050c experiment shows downward vertical motion in the troughing region where drier air is mixing down from aloft west of the dryline. This is not seen in the other experiments nor the Nature Run. Additionally, there is a secondary peak of higher moisture values and associated upward vertical motion around 300 km in Washita County that is not seen in the rest of the OSSE experiments nor the Nature Run. This shows that even considering the environment away from the immediate dryline (especially west of the dryline), reducing the number of stations down to 50 from 108 is not something that will preserve the desired moisture and wind fields in and around the region of the dryline.

It can be noted that there are a few similarities among the FMU02km050c experiment, FMU02km108c experiment, and the Nature Run. One similarity is that all experiments in this set of experiments show relatively humid air (indicated by the 14 to 16 g/kg dark green to blue shaded contours) extending from east of the dryline to 650 km (Grady to McIntosh counties) from the surface to 1.5 km MSL (although this layer is slanted downward with eastward distance away from the dryline in all of the OSSE experiments but not in the Nature Run).

Overall, comparison of the FMU02km108 and FMU02km108c, FMU02km050c experiments demonstrate that there is still degradation of the boundary layer structure and wind field along the dryline and particularly west of the dryline when the number of UAV obs is reduced from 108 to 50, even if the UAV obs interval for these 50 obs is every 30 minutes instead of every hour.

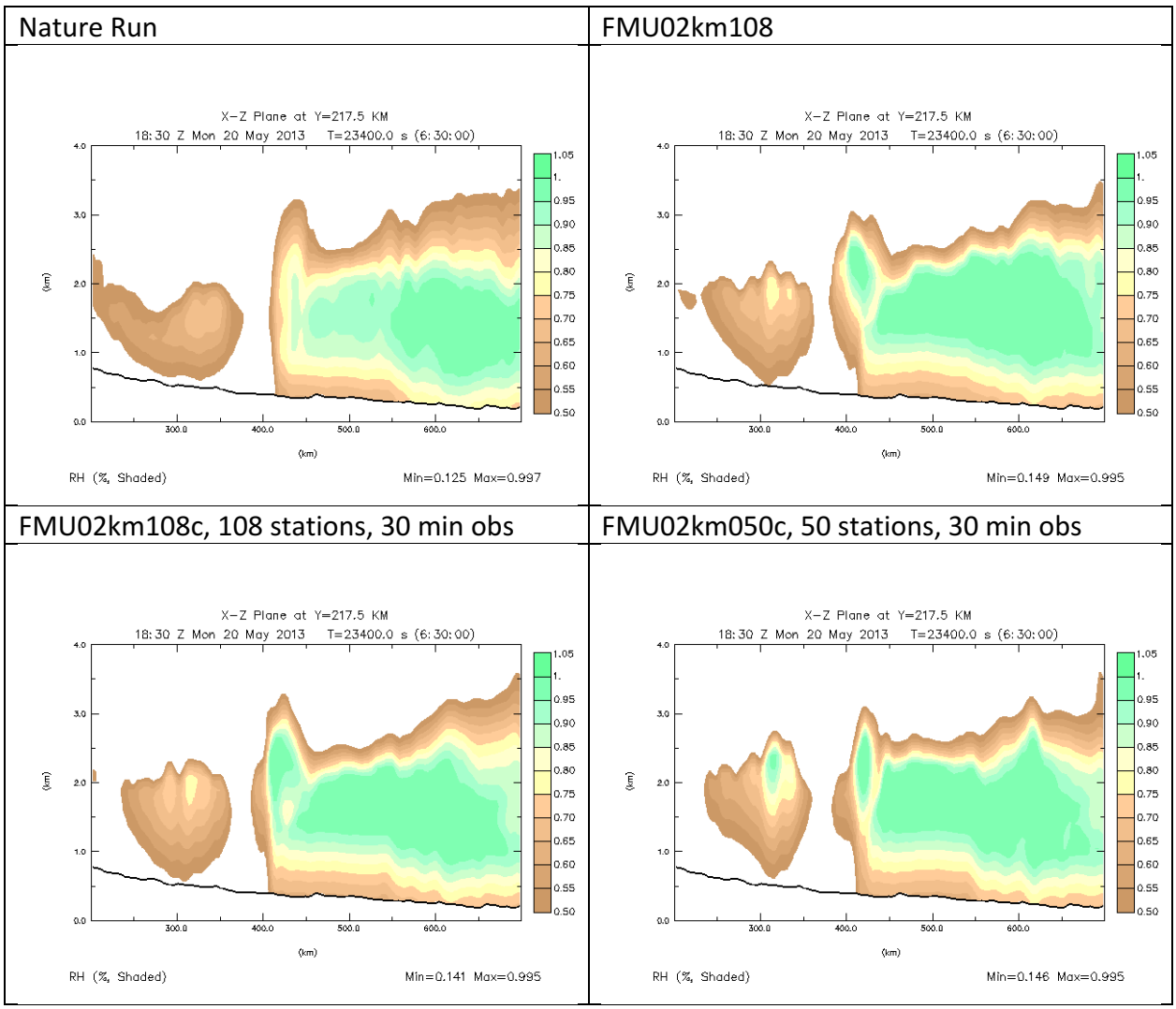

Figure 68. As in Figure 53, but for set of experiments where frequency of UAV obs for bottom experiments is 30 minutes instead of 1 hour.

Comparison of the relative humidity cross-section (Figure 68) for this set of experiments show that when reducing the number of stations from 108 to 50 for 30 minute interval UAV obs, there is increasing narrowness and higher intrusion into the atmosphere of air near saturation along the dryline (as indicated by the narrower 0.90 to 0.95 spring green shaded contour from 1.5 km to 3.0 km MSL at the dryline boundary at 400 km in the FMU02km050c experiment compared to the FMU02km108c and FMU02km108 experiments). While the air is closer to saturation 1.0 km AGL to 3.0 km AGL in the FMU02km108, FMU02km108c, and FMU02km050c experiments compared to the Nature Run (indicating more potential condensation and latent heat release throughout the column at the leading edge of the dryline compared to the Nature Run at this time), a secondary layer of air around 2.0 km MSL that is close to saturation west the dryline at 300 km (Washita County) for the FMU02km050c experiment but not the rest of the OSSE experiments nor the Nature Run suggests that more focused vertical motion along the dryline in the FMU02km050c experiment (owing to stronger downward motion west of the dryline in the FMU02km050c experiment compared to the FMU02km108c experiment, FMU02km108 experiment, and the

Nature Run). Owing to mass conversation, the resulting compensating increased upward motion along the dryline could explain both the presence of more moist air near the dryline at higher levels and this more humid air extending higher into the atmosphere (near 3.0 km AGL) near the dryline in the FMU02km050c experiment than in the other OSSE experiments

As before, comparison of the Nature Run, FMU02km108 and FMU02km108c, FMU02km050c experiments demonstrate that there is better pooling of higher moisture in the lower to mid portions (1.0 to 3.0 km MSL) of the boundary layer east of the dryline a(s shown by the greater areal coverage of spring green contours in this layer) when the number of stations is 108 instead of 50 for a UAV obs interval of 30 minutes. This shows that there are more realistic regions of imminent condensation and latent heating near the surface and further aloft near and east of the dryline and hence a broader region aloft (indicating weaker capping and entrainment of drier air west of the dryline) when the number of stations is 108, which can explain a part of why convection is faster to develop along the dryline in the experiments with 108 stations (FMU02km108 and FMU02km108c) than in the experiment with 50 stations (FMU02km050c). This is not unlike in the earlier in the set of experiments involving changing number of stations for UAV obs from a max height of 2 km, where there appears to be a cutoff below 75 stations where there is less utility in using UAV obs to simulate the correct configuration and magnitude of boundary layer moisture. Considering the experiment for UAV obs interval being 1 hour (FMU02km108) and both experiments for UAV obs interval being 30 minutes (regardless of whether there are 108 or 50 stations), there is more focused vertically oriented ascent along the dryline in Grady County prior to convective initiation when the interval of UAV obs is reduced from 1 hour to 30 minutes. This improvement is retained even if the number of stations used for 30 minute interval UAV obs is decreased from 108 to 50. So while the magnitude and placement of the vertical motion at the dryline and pooling of humid air in the near the surface and lower to mid levels (as shown in these specific vertical cross-sections) as shown by the relative humidity cross-sections) of the boundary layer is better simulated when the number of stations is at the maximum (108) irrespective of whether the interval of consecutive UAV obs is 1 hour or 30 minutes, when assimilating UAV obs every 30 minutes, reducing the number of stations to 50 when assimilating UAV obs every 30 minutes still simulates the focusing of moisture and latent heat release along the dryline prior to convective initiation and storms, but does a poorer job in simulating the broadness of regions of more humid air east of the dryline and dries out the lower levels of the atmosphere west of the dryline too much, with too much downward vertical motion west of the dryline associating with this drying. This can interfere with timing and placement of storms, specifically as mixing of drier air just west of the dryline and a secondary peak of moisture and vertical motion west of the dryline prevents the desired setup of a single region of upward vertical motion along the dryline and overall subdued descending air west of the dryline.

Chapter 5. Summary and Conclusions

OSSE experiments were conducted for various configurations of UAV profiles (i.e.: with and without UAV obs, different max heights of UAV obs, different number of UAV obs, etc.) to assess which setup best simulated timing of convective initiation and placement of storms along the dryline in Oklahoma in comparison with the Nature Run. Through conducting these experiments, we hope to determine which configuration of UAV networks is most suitable for deployment as a 3D Mesonet.

Both reflectivity/wind fields from 1800 UTC May 20 2013 to 0300 UTC May 21 (the forecast period) and moisture cross-sections at 1830 UTC May 20 (the end of the assimilation window and start of the free-forecast period) were examined when evaluating each experiment, and these fields and cross-sections were compared to the respective fields and cross-sections generated in the Nature Run to determine how well each experiment replicated the fields at the conclusion of data assimilation. The moisture cross-sections were examined for east-west oriented vertical slices from Y = 85.5 km (Red River region of southern Oklahoma) to Y = 295.5 km (north-central Oklahoma), with the width of the domain extending to 700 km east of the western boundary from the High Plains (including the Texas panhandle) to the eastern lowlands (encompassing eastern Oklahoma and extreme western Arkansas), and the depth of the atmosphere extending from the surface to a height of 4 km AGL. Variables examined in these cross-sections for 1830 UTC were: relative humidity, specific humidity and vertical winds (m/s), reflectivity (dBz), and cloud water mixing ratio. In order to determine which experiment produced results closest to that seen in the actual convective setup, qualitative and quantitative analysis was performed to determine which experiment generated reflectivity/wind fields and moisture cross-sections closest to the Nature Run.

Regardless of what experiment was run, there were a few main consistent features in the reflectivity/wind fields during the forecast period: initiation of storms around 1900 UTC to 1930 UTC May 20, development of supercell storms into Cleveland County anywhere from 1945 UTC to 2000 UTC at the latest, storms congealing and exiting Cleveland County by 2130 UTC to 2230 UTC, and from 0100 UTC May 21 to 0300 UTC May 21, and a pattern of two separate linear convective segments in southeast Oklahoma and northeast Oklahoma. Additionally, some other factors to note were that: there was initial initiation of convection from 1830 UTC to 2000 UTC across central Oklahoma (specifically Logan, Kingfisher, Canadian, and Oklahoma counties all north-northwest of Cleveland County), a northeastward moving supercell cluster in 2130 UTC to 2230 UTC that moves from southeast Oklahoma to northeast Oklahoma in this time frame, and organization of storms into an eastward moving QLCS segment that traverses northern Texas, the Red River region, and southern Oklahoma from 0100 UTC to 0300 UTC May 21

For the boundary layer moisture cross-sections, it was seen that no matter what horizontal slice was used, compared to the no data case, addition of more observations (to a large extent the Mesonet and FNL observations, and to a lesser extent UAV observations) increased the average height of the top of the moist layer. Addition of Mesonet and FNL observations increased the average height of the top of moist layer by several kilometers, while addition of UAV observations (as when comparing the No UAV experiment to the UAV experiments) increased the average height of the top of the moist layer by only a few tens to hundreds of meters. With addition of FNL and Mesonet observations, moisture intrusions (representing triggering of moist-unstable

convection that deepens the boundary layer) into higher levels of the atmosphere (such as 3 km MSL and above) became better defined, especially close to the dryline boundary. Similarly, with addition of more UAV observations such as the FMU02km108 experiments, there was better resolution of the narrow peak of moisture intrusion near the dryline, a precursor to convection initiation on that boundary. However, it was found that when comparing the FMU400ft108, FMU01km108, FMU02km108, and FMU03km108 experiments, the boundary layer moisture cross-section that best matched that from the Nature Run was the FMU02km108 experiment, with the next closest match being the FMU03km108 experiment.

These qualitative results from adding more observations were reflected in quantitative analysis as well, where for thermodynamic variables like potential temperature and water vapor, adding more observation data that encompassed a greater depth of the boundary layer (like FNL and UAV data) reduced the overall error, especially early in the assimilation period (0 to 6 hours) and for later in the forecast period (11 to 15 hours), especially for lower levels below 3 km. Adding Mesonet observations did not reduce error as much compared to the no data experiments, similar to how the height and depth of the moist boundary layer didn't not increase by much compared to the no data experiments. However, unlike with the boundary layer cross-section plots, addition of UAV observations from higher heights (3 km AGL compared to 1 km AGL) resulted in further reduced error in moisture during the assimilation and forecast periods except at the highest plotted level (3 km), which is different than how addition of higher heights in the boundary layer (UAV observations at 3 km AGL compared to UAV observations at 2 km AGL) reduced similarity of boundary layer cross-section moisture intrusion features around 2 km AGL compared to using UAV observations at 2 km AGL and from the Nature Run.

Fitting data to the average station spacing showed improvement only in better delineating the dryline boundary and more pooling of humid air of the lower boundary layer near the dryline prior to convective initiation compared to the Nature Run (which would result in more latent heat release and vertical motion in the lower levels of the atmosphere near the dryline), reducing overall extraneous convection spreading eastward in north-central and northeast Oklahoma, and reducing the amount of splitting supercell behavior (specifically when a lesser amount of stations are used such as 10 or 25) when storms are in the vicinity of Cleveland County. Additionally, fitting data had the best results in terms of preserving timing of convective initiation for the least number (10) of stations, whereas fitting the data had worsening results for a larger amount of stations (25 and 50), with the timing of convective initiation being pushed back as far as 1 hour for the 50 station fitted experiment (FMU02km050f). This is possibly due to overfitting of the sUAV data when 25 and 50 fitted station experiments are conducted, as well as the depth of the most humid air east of the dryline being less in the 25 and 50 station fitted experiments than in the 25 and 50 station unfitted experiments, which requires more lifting of the air east of the dryline to create convective clouds and precipitation.

When the maximum fixed number of stations (108) were used for UAV obs starting at 1200 UTC and ending at 1800 UTC, as expected, decreasing the interval of UAV obs from hourly to every half an hour improved not only timing of convection but placement of convection along the dryline, especially in southwest and central Oklahoma. However, these improvements were seen to a lesser extent when reducing the interval of UAV obs from 2 hours down to 1 hour, and there was not much improvement at all from reducing the UAV obs from 3 hours down to 2 hours. This indicates

that while more frequent UAV obs helped improve timing and placement of convection along the dryline, this relationship was not always linear, with the most improvement showing up when the interval of UAV obs was already relatively small (1 hour). A possible reason why timing of convective initiation was even closer to the Nature Run when frequency of UAV obs was reduced from every 1 hour to every 30 minutes was that when this was done, there was better pooling of moisture at the low levels near the dryline and a more singularly focused region of upward vertical motion. With narrower regions of rising, fairly humid air near the dryline and better simulation of moisture at low levels just east of the dryline, there is a singularly more focused region at the dryline where convective updrafts and latent heating are occurring, allowing for quicker initiation of storms along the dryline region. Because these regions of buoyant air are more limited in horizontal area when the frequency of UAV obs is reduced from 1 hour to 30 minutes, this could also explain why despite the maximum vertical motion not varying more than 1 m/s, there were more vigorous areas of convection and higher moisture intrusions seen when the frequency of UAV obs was every 30 minutes instead of every hour.

Delaying the start time for hourly UAV obs so that fewer data were used did not consistently generate as much degradation as expected in timing and placement of storms except for reducing small scale convection in north-central Oklahoma. However, it is interesting to note that when the start time of hourly UAV obs was closest to the time of convective initiation (as in the FMU02km108e experiment with start time at 1700 UTC), there was earlier timing of convective initiation and better placement of storms overall throughout the first two hours of the forecast period (1800 UTC to 2000 UTC) in comparison with the FMU02km108d experiment with start time at 1500 UTC, while by 2100 UTC, placement and coverage of storms over Cleveland County is still less similar to the Nature Run in the FMU02km108e experiment compared to the FMU02km108d experiment. Changing the start time for hourly UAV obs to being closer to the time of convective initiation reduced the defined moisture intrusion at the dryline and moisture gradient across the dryline, which presented a more muted lifting setup with less robust updrafts along the dryline. However, improvement in simulation of the structure and magnitude of boundary layer moisture along and east of the dryline with delayed start time could have resulted in less capping of the atmosphere and faster destabilization, also explaining why there was earlier convective initiation closer in timing to the Nature Run (although farther south along the dryline than in the Nature Run) in the FMU02km108e experiment compared to the FMU02km108d experiment.

Reducing the number of stations from 108 down to 50 while simultaneously reducing the interval of UAV obs from 1 hour to 30 minutes yielded some surprising results. For one, there was no less magnitude of moisture and vertical ascent along the dryline prior to convective initiation when 50 stations were used rather than 108 stations. Also, reducing the number of stations down to 50 reduced excess convective noise in north-central Oklahoma during the first hour to hour and a half after convective initiation (1930 UTC to 2100 UTC) compared to the experiments where 108 stations were used for hourly UAV obs from a max height of 2 km (FMU02km108) and 108 stations were used for 30 minute interval UAV obs from a max height of 2km (FMU02km108c). What this shows is that in the early portion of the forecast period, reducing the number of stations when UAV obs are more frequent (i.e.: 30 minutes rather than 1 hour) can result in better configuration of the boundary layer moisture and vertical fields farther north of the main area of convective initiation near the dryline in Grady County, as well as reduction of excess convective

noise in areas like north-central Oklahoma. However, this is outweighed by how important features like convection over Cleveland County at 2000 UTC and fragmentation of convection along the dryline at 2100 UTC are missing in the FMU02km050c experiment compared to the Nature Run and the FMU02km108 and FMU02km108c experiments.

Prior to convective initiation, vertical cross-sections of boundary layer moisture between the Nature Run, FMU02km108, FMU02km108c, and FMU02km050c experiments show that there was too much mixing of drier air aloft down to the surface just west of the and a secondary, extraneous maximum in upward vertical motion and moistening of the boundary layer west of the dryline when the number of stations was 50, even though the timing of UAV obs interval was 30 minutes. This prevented the desired setup seen in the Nature Run, FMU02km108, and FMU02km108c experiments where there is only one focused region of maximum ascent along the dryline and no excess drying or downward motion west of the dryline. So in addition to far less areal coverage of convection, reducing the number of UAV obs down to 50 from 108 even when the UAV obs interval was every 30 minutes was found to result in less accurate simulation of boundary layer moisture and wind fields and mis-placement of regions of ascent compared to when the number of UAV obs was 108 (regardless of whether the UAV obs interval was 1 hour or 30 minutes). This result is similar to how in earlier experiments, there was found to be a cutoff at 75 obs beyond which fewer obs meant less accurate simulation of moisture and wind fields.

As were the findings in Moore (2018), for convective situations like the one studied in this paper, the most relevant portion of the boundary layer where UAV obs appear to have the most use in reducing error in thermodynamic, moisture, and reflectivity fields compared to the reference Nature Run is the 1.0 km to 2.5 km AGL layer of the lower to mid portion of the boundary layer below 3.0 km AGL. In Moore's research, this portion of the boundary layer where the most improvement in adding UAV obs was seen was at 1 km AGL, in comparison to 2 km AGL in this experiment. Therefore, future research might focus on examination at a finer vertical resolution for this lower layer encompassing heights of 1 km and 2 km AGL, specifically concerning moisture pooling, moisture advection, and vertical motion in this layer prior to and following convective initiation. Focusing on this layer at a finer vertical scale might also be useful for case studies of how addition of UAV obs can help better simulate smaller-scale convective features that are strongly affected by the setup of moisture in the boundary layer, like mesocyclones and downdraft regions in diurnally occurring, synoptically forced severe thunderstorms in the Southern Great Plains.

This study looked at convection at a scale (3 km) that doesn't allow for precise modeling of smaller scale convective features like downdrafts and tornadoes. Hence, while this study did show that addition of UAV obs, increasing frequency of UAV obs, and (to a lesser extent) moving the start time of hourly UAV obs closer to the time of convective initiation definitely improved timing and placement of storms along the dryline for this setup of supercell storms outbreak in the Southern Great Plains in the springtime, there cannot be conclusions made about what improvements at the smaller scale might have also occurred. Neither can generalizations be made about whether these improvements will hold in similar such springtime convective weather outbreaks in the Southern Great Plains. Similar case studies examining the advantages and disadvantages of incorporating more frequent UAV obs for multiple supercell outbreak cases in the Southern Great Plains springtime might be an area to focus on for further research in order to further confirm the utility

of UAV obs to convective weather prediction at the scales examined in this study, as well as at smaller scales where phenomena like tornadoes and downdrafts are better resolved. As were the findings in Moore (2018), for convective situations like the one studied in this paper, the most relevant portion of the boundary layer where UAV obs appear to have the most use in reducing error in thermodynamic, moisture, and reflectivity fields compared to the reference Nature Run is the 1.0 km to 2.5 km AGL (concerning moisture intrusion at the dryline) layer of the lower to mid portion of the boundary layer below 3.0 km AGL. Future studies might focus on examination at a finer vertical resolution for this layer, specifically concerning moisture pooling, moisture advection, and vertical motion in this layer prior to and following convective initiation. Focusing on this layer at a finer scale might also be useful for case studies of how addition of UAV obs can help better simulate smaller-scale convective features that are strongly affected by the setup of moisture in the boundary layer, like mesocyclones and downdraft regions in diurnally occurring, synoptically forced severe thunderstorms in the Southern Great Plains.

References

Ackerman, E. and M. Koziol, 2019: In the Air with Zipline's Medical Delivery Drones, *IEEE Spectrum*, https://spectrum.ieee.org/robotics/drones/in-the-air-with-ziplines-medical-delivery-drones.

Atlas, R., 2017: 2.1 Core Science Keynote on Observing System Simulated Experiments (Invited Presentation), *21st Conference on Integrated Observing and Assimilation Systems for the Atmosphere, Oceans, and Land Surface*, Miami, FL, Amer. Meteor. Soc., https://ams.confex.com/ams/97Annual/webprogram/Paper314195.html.

Atmospheric and Environmental Research Inc., 2019: RRTM (Stand-Alone Model)/RRTMG (GCM Applications), http://rtweb.aer.com/rrtm_frame.html.

Barbieri, L., and Coauthors, 2019: Intercomparison of Small Unmanned Aircraft System (sUAS) Measurements for Atmospheric Science during the LAPSE-RATE Campaign, *Sensors*, **19(9)**, 2179.

Bratseth, A.M., 1985: Statistical Interpolation by means of successive correction, *Tellus,* Institute of Geophysics at the Unversity of Oslo, **38A**, 439-447 pp.

Brewster, K., 1996: Application of a Bratseth Analysis Scheme Including Doppler Radar Data, 15th Conf. On Weather Analysis and Forecasting, Norfolk, VA, August 1996, pp. 92-95.

Campbell, S.E., D.A. Clark, J.E. Evans., 2017: Preliminary Weather Information Gap Analysis for UAS Operations, Project Report ATC-437, MIT Lincoln Laboratory, 126 pp., https://archive.ll.mit.edu/mission/aviation/publications/publication-files/atc-reports/Campbell_2017_ATC-437.pdf.

Campbell, S.E., D.A. Clark, J. E. Evans, 2017: Preliminary UAS Weather Research Roadmap, Project Report ATC-438, MIT Lincoln Laboratory, 62 pp., https://archive.ll.mit.edu/mission/aviation/publications/publication-files/atc-reports/Campbell_2017_ATC-438.pdf.

Carlaw, L.B., J.A. Brotzge, F.H. Carr, 2015: Investigating the impacts of assimilating surface observations on high-resolution forecasts of the 15 May 2013 tornado event, *Electronic J. Severe Storms Meteor.*, **10**, pp.1-34, https://ejssm.org/ojs/index.php/ejssm/article/view/145/103.

Carr, F., J. Krause, K. Brewster, 1996: Application of the Bratseth scheme to high resolution analyses in inhomogeneous data regions, 15th Conf. On Weather Analysis and Forecasting, Norfolk, VA, August 1996, pp. 92-95.

Chilson, P.B., and Coauthors, 2019: Moving towards a Network of Autonomous UAS Atmospheric Profiling Stations for Observations in the Earth's Lower Atmosphere: The 3D Mesonet Concept, *Sensors*, **19(12)**, 2720.

Crook, N.A., 1996: Sensitivity of Moist Convection Forced by Boundary Layer Processes to Low-Level Thermodynamic Fields, *Monthly Weather Review*, **124**, 1767-1784.

de Boer, G., and Coauthors, 2020: Development of Community, Capabilities, and Understanding through Unmanned Aircraft-Based Atmospheric Research: The LAPSE-RATE Campaign, *Bull. Amer. Meteor. Soc.*, **101(5)**, E684, E699, https://doi.org/10.1175/BAMS-D-19-0050.1.

Dudhia, J., 2010: WRF Physics Options, slide 39, https://citeseerx.ist.psu.edu/viewdoc/download?doi=10.1.1.411.8782&rep=rep1&type=pdf.

Greene, B.R., A.R. Segales, T.M. Bell, E.A. Pillar-Little, P.B. Chilson, 2019: Environmental and Sensor Integration Influences on Temperature Measurements by Rotary-Wing Unmanned Aircraft Systems, *Sensors*, **19(6)**, 1470.

Hoffman, R.N., R. Atlas, 2016: Future Observing System Simulation Experiments, *Bull. Amer. Meteor. Soc.*, **97**, 1601-1616, https://doi.org/10.1175/BAMS-D-15-00200.1.

Koch, S.E., and Coauthors, 2018: On the Use of Unmanned Aicraft for Sampling Mesoscale Phenomena in the Preconvective Boundary Layer, *Journal of Atmospheric and Oceanic Technology*, **35**, Issue 11, 2265-2288, https://doi.org/10.1175/JTECH-D-18-0101.1.

Jacobs, A.M., T.M. Bell, B.R. Greene, P.B. Chilson, 2020: The Effect of Climatological Variables on Future UAS-Based Atmospheric Profiling in the Lower Atmosphere, *Remote Sensing*, **12(8)**, 2947, https://doi.org/10.3390/rs12182947.

Li, Y., Z. Li., Z. Zhang., L. Chen, S. Kurkute, L. Scaff, X. Pan, 2019: High-resolution regional climate modeling and projection over western Canada using a weather research forecasting model with a pseudo-global warming approach, *Hydrol. Earth Syst. Sci.*, **23**, 4635-4569, https://doi.org/10.5194/hess-23-4635-2019.

McFarquhar, G.M., and coauthors, 2020: Current and future uses of UAS for Improved Forecasts/Warnings and Scientific Studies, *Bulletin of Meteorological Society*, **101**, E1322-E1328, https://doi.org/10.1175/BAMS-D-20-0015.1.

Meteomatics, 2020: How Meteodrones Contribute to Weather Forecasting, Accessed 9 September 2020, https://www.meteomatics.com/wp-content/uploads/2020/03/Meteomatics_Whitepaper_Meteodrones_20.03.2020.pdf.

Moore, A., 2018: Observation system simulation experiment studies on the use of small UAV for boundary-layer sampling, University of Oklahoma M.S. Thesis, https://hdl.handle.net/11244/301347.

Morris, M.T., 2017: Assessing the impact of non-conventional observations on high-resolution analyses and forecast, University of Oklahoma M.S. Thesis, https://hdl.handle.net/11244/50799.

Morris, M.T., K.A. Brewster, F.H. Carr, 2021: Assessing the impact of non-conventional radar and surface observations on high-resolution analyses and forecasts of a severe hailstorm, *Electronic Journal of Severe Storms Meteorology,* **16**(1), 1-39, https://www.ejssm.org/ojs/index.php/ejssm/article/viewArticle/181.

NASA. Development and Application of Observing System Simulation Experiments (OSSEs), https://gmao.gsfc.nasa.gov/projects/osse/osseweb-1.htm.

National Research Council, 2009: Observing Weather and Climate from the Ground Up: A Nationwide Network of Networks. The National Academies Press, 250 pp.

National Research Council, 2012: Urban Meteorology: Forecasting, Monitoring, and Meeting Users' Needs. The National Academies Press, 176 pp.

National Research Council, 2018: The Future of Atmospheric Boundary Layer: Observing, Understanding, and Modeling, *National Academies Press*, 48 pp..

Thomas, A.J., S. Koch, Z. Li, 2017: Assimilating synthetic hyperspectral sounder temperature and humidity retrievals to improve severe weather forecasts, *Atmospheric Research*, **186**, 9-25, https://doi.org/10.1016/j.atmosres.2016.11.004.

Xue, M., M. Tong, K.K. Droegemeier, 2006: An OSSE Framework Based on the Ensemble Square Root Kalman Filter for Evaluating the Impact of Data from Radar Networks on Thunderstorm Analysis and Forecasting, *J. Atmos. Oceanic Technol.*, **23,** 46-66, https://doi.org/10.1175/JTECH1835.1.

Zeng, X., and coauthors, 2020: Use of Observing System Simulation Experiments in the United States, *Bulletin of American Meteorological Society*, **101**, E1427-E1438.

Appendix A

Parameters in namelist.input file for the Nature Run

```
&time_control
 run_days                            = 0,
 run_hours                           = 0,
 run_minutes                         = 0,
 run_seconds                         = 0,
 start_year                          = 2013, 2013,
 start_month                         = 05, 05,
 start_day                           = 20, 20,
 start_hour                          = 12, 12,
 start_minute                        = 00, 00,
 start_second                        = 00, 00,
 end_year                            = 2013, 2013,
 end_month                           = 05, 05,
 end_day                             = 21, 21,
 end_hour                            = 00, 00,
 end_minute                          = 00, 00,
 end_second                          = 00, 00,
 interval_seconds                    = 10800,
 input_from_file                     = .true.,.true.,
 history_interval                    = 15, 5,
 frames_per_outfile                  = 1, 1,
 restart                             = .false.,
 restart_interval                    = 8640,
 io_form_history                     = 2,
 io_form_restart                     = 2,
 io_form_input                       = 2,
 io_form_boundary                    = 2,
 debug_level                         = 1000,
 force_use_old_data                  = .true.,

 /

&domains
 time_step                           = 30,
 time_step_fract_num                 = 0,
 time_step_fract_den                 = 1,
 max_dom                             = 2,
 s_we                                = 1,
 e_we                                = 561, 901,
 s_sn                                = 1,
 e_sn                                = 441, 661,
 s_vert                              = 1,
 e_vert                              = 51, 51,
 eta_levels                                                  =
1.0000,0.9980,0.9940,0.9870,0.9750,0.9590,0.9390,0.9160,0.8920,0
```

```
.8650,0.8350,0.8020,0.7660,0.7270,0.6850,0.6400,0.5920,0.5420,0.
4970,0.4565,0.4205,0.3877,0.3582,0.3317,0.3078,0.2863,0.2670,0.2
496,0.2329,0.2188,0.2047,0.1906,0.1765,0.1624,0.1483,0.1342,0.12
01,0.1060,0.0919,0.0778,0.0657,0.0568,0.0486,0.0409,0.0337,0.027
1,0.0209,0.0151,0.0097,0.0047,0.0000,
 p_top_requested                     = 5000,
 dx                                  = 3000, 1000,
 dy                                  = 3000, 1000,
 grid_id                             = 1, 2,
 parent_id                           = 0, 1,
 i_parent_start                      = 1, 128,
 j_parent_start                      = 1, 111,
 parent_grid_ratio                   = 1, 3,
 parent_time_step_ratio              = 1, 5,
 num_metgrid_soil_levels             = 4,
 num_metgrid_levels                  = 27,
 force_sfc_in_vinterp                = 1,
 interp_type                         = 2,
 use_levels_below_ground             = .true.
 feedback                            = 1,
 smooth_option                       = 0,
 max_ts_locs                         = 30
 ts_buf_size                         = 200
 max_ts_level                        = 51

 /

 &physics
 physics_suite                       = 'CONUS'
 mp_physics                          = 8, 8,
 ra_lw_physics                       = 4, 4,
 ra_sw_physics                       = 4, 4,
 radt                                = 3, 3,
 sf_sfclay_physics                   = 5, 5,
 sf_surface_physics                  = 2, 2,
 bl_pbl_physics                      = 5, 5,
 icloud_bl                           = 1,
 bldt                                = 0, 0,
 scalar_pblmix                       = 1,
 mp_zero_out                         = 2,
 mp_zero_out_thresh                  = 1.0e-12,
 cu_physics                          = 0, 0,
 cudt                                = 0, 0,
 no_mp_heating                       = 0,
 isfflx                              = 1,
 ifsnow                              = 0,
 icloud                              = 1,
 surface_input_source                = 1,
```

```
 num_soil_layers                     = 4,
 num_land_cat                        = 21,
 sf_urban_physics                    = 0,     0,     0,
 slope_rad                           = 1,     1,     1,
 topo_shading                        = 1,     1,     1,
 shadlen                             = 25000.,
 do_radar_ref                        = 1,
 /
&fdda
 /
&dynamics
 tracer_opt                          = 0,     0,    1,
 w_damping                           = 1,
 diff_opt                            = 1,
 km_opt                              = 4,
 diff_6th_opt                        = 2,      2,    0,
 diff_6th_factor                     = 0.45,   0.30,   0.12,
 damp_opt                            = 3,
 zdamp                               = 5000.,  5000., 5000.,
 dampcoef                            = 0.15,    0.05,   0.01,
 khdif                               = 0,      0,     0,
 kvdif                               = 0,      0,     0,
 non_hydrostatic                     = .true., .true., .true.,
 moist_adv_opt                       = 1,      1,     1,
 scalar_adv_opt                      = 1,      1,     1,
 do_avgflx_em                        = 1, 1, 1, 1, 1, 1, 1, 1, 1,
 do_avgflx_cugd                      = 1, 1, 1, 1, 1, 1, 1, 1, 1,
 hybrid_opt                          = 0,
 base_temp                           = 290.
 gwd_opt                             = 0,
 /
&bdy_control
 spec_bdy_width                      = 15,
 spec_zone                           = 1,
 relax_zone                          = 12,
 spec_exp                            = 0.20,
 specified                           = .true., .false., .false.,
 nested                              = .false.,.true.,
 /
&maxhailw
 maxhailw_opt                        = 1,
 uh_inst_mag                         = 2.0,
 /

 &grib2
 /

 &namelist_quilt
```

```
 nio_tasks_per_group = 0,
 nio_groups = 1,
/
```

Appendix B

Namelist parameters in ARPS input file for ARPS model

```
&grid_dims
   nx   = 283,
   ny   = 213,
   nz   = 73,
 /


 &message_passing
   nproc_x = 2,
   nproc_y = 30,

   max_fopen = 20,

   nproc_x_out = 1,
   nproc_y_out = 1,
 /


 &comment_lines
   nocmnt  = 2,
   cmnt(1) = 'ARPS 5.4.2',
   cmnt(2) = 'May 20, 2013 3-km',
 /


 &jobname
   runname = 'FMU02km108_ar201305201200',
 /


 &model_configuration
   runmod = 1,
   hxopt = 0,
   memid = 1,
   hx_interval = 60,
 /
&initialization
   initime = '2013-05-20.12:00:00',
   initopt = 2,
     timeopt = 0,

     pt0opt  = 0,
       ptpert0(1) =     0.0,
       pt0radx(1) = 10000.0,
       pt0rady(1) = 10000.0,
```

```
      pt0radz(1) =  1500.0,
      pt0ctrx(1) = 48000.0,
      pt0ctry(1) = 16000.0,
      pt0ctrz(1) =  1500.0,

    rstinf                                                          =
'/scratch/vshenoy/ARPS_OSSE/FMU02km108/FMU02km108_ar201305201200
.rst021000',

    inifmt   = 3,
    inisplited = 0,
    inifile                                                         =
'/scratch/vshenoy/ARPS_OSSE/FMU02km108/FMU02km108_ar201305201200
.hdf021000',
    inigbf                                                          =
'/scratch/vshenoy/ARPS_OSSE/FMU02km108/FMU02km108_ar201305201200
.hdfgrdbas',

  inibasopt = 1,
    viniopt = 1,
      ubar0   = 0.0,
      vbar0   = 0.0,
      zshear  = 3000.0,

    sndfile = 'may20.snd',

    pttrop = 343.0,
    ttrop  = 213.0,
    ptground = 300.0,
    htrop   = 12000.0,
    qvmixed = 0.015,
    rhmixed = 0.95
    mixtop  = 1200.0,

  soilinitopt = 0,
    soiltintv   = 1800.0,

  tsfcopt = 0,
 /

 &assim
   assimopt = 1,
     iauintvl = 30.0,
     iaushape=    2,    2,    1,    2,    2,
     iaubegin=  21000, 21300, 0.,   0.,   0.,
     iauend  =  21600, 21600, 300., 600., 600.,
     iautmax =  21300, 21450, 300.,  90., 120.,
     iaugain  = 1.0,  1.0,  1.0,  1.0,  1.0,
```

```
     incrfnam                                                    =
'/scratch/vshenoy/ARPS_OSSE/FMU02km108/FMU02km108_ad201305201800
.incr',
     incrfmt = 3,
     iau_u   = 1,
     iau_v   = 1,
     iau_w   = 0,
     iau_p   = 0,
     iau_pt  = 1,
     iau_qv  = 1,
     iau_qc  = 2,
     iau_qr  = 2,
     iau_qi  = 2,
     iau_qs  = 2,
     iau_qg  = 2,
     iau_qh  = 2,
     iau_nc  = 0,
     iau_nr  = 0,
     iau_ni  = 0,
     iau_ns  = 0,
     iau_ng  = 0,
     iau_nh  = 0,

     df_tstart=1500.0,
     df_tinv=5.0,
     df_nstps=20,
     df_wght(1)=0.05,
     df_wght(2)=0.05,
     df_wght(3)=0.05,
     df_wght(4)=0.05,
     df_wght(5)=0.05,
     df_wght(6)=0.05,
     df_wght(7)=0.05,
     df_wght(8)=0.05,
     df_wght(9)=0.05,
     df_wght(10)=0.05,
     df_wght(11)=0.05,
     df_wght(12)=0.05,
     df_wght(13)=0.05,
     df_wght(14)=0.05,
     df_wght(15)=0.05,
     df_wght(16)=0.05,
     df_wght(17)=0.05,
     df_wght(18)=0.05,
     df_wght(19)=0.05,
     df_wght(20)=0.05,
 /
&terrain
```

```
   ternopt = 2,
   mntopt  = 0,
     hmount  =     0.000,
     mntwidx = 10000.000,
     mntwidy = 10000.000,
     mntctrx = 10000.000,
     mntctry = 10000.000,
   terndta                                                          =
'/home/kbrews/osse/static/gfs_2013051912a_03km.trndata',
     ternfmt = 3,
 /


 &grid
   dx       =  3000.000,
   dy       =  3000.000,
   dz       =   300.000,
   strhopt  = 2,
     dzmin    =    20.000,
     zrefsfc  =     0.0,
     dlayer1  =     0.0,
     dlayer2  =     1.0e5,
     strhtune =     1.0,
   zflat    =     1.0e5,
   ctrlat   =    36.0,
   ctrlon   =   -98.2,

   crdorgnopt = 0,

 /
&projection
   mapproj = 2,
     trulat1 =  30.0,
     trulat2 =  40.0,
     trulon  = -97.5,
     sclfct  =  1.0,

   mpfctopt = 1,
   mptrmopt = 1,
   maptest  = 0,
 /


 &timestep
   dtbig =   3.0,
   tstart=   21000,
   tstop =   54000,
 /
```

```
 &acoustic_wave
   vimplct  = 1,
   ptsmlstp = 0,

   csopt    = 1,
     csfactr  = 0.5,
     csound   = 150.0,

   tacoef   = 0.75,
   dtsml    = 1.5,
 /


 &equation_formulation
   buoyopt   = 1,
   buoy2nd   = 1,
   rhofctopt = 1,
   bsnesq    = 0,
   peqopt    = 1,
 /


 &numerics
   tintegopt = 1,
   madvopt = 3,
   sadvopt = 4,
     fctorderopt = 2,
     fctadvptprt = 1,
     fctfinalopt = 1,
 /

&boundary_condition_options
   lbcopt  = 2,
     wbc     = 5,
     ebc     = 5,
     sbc     = 5,
     nbc     = 5,
       c_phase = 300.0,
       rlxlbc  = 0.5,
       rbcopt  = 4,
       rbc_plbc= 1,

   tbc     = 1,
     fftopt  = 2,
   bbc     = 1,
```

```
  pdetrnd = 0,
 /


 &exbcpara
   exbcname = '/scratch/kbrews/GFS_051912z/gfs_2013051912a_03km',
   tinitebd = '2013-05-20.15:00:00',
   tintvebd =  10800,

   ngbrz    = 12,
   brlxhw   = 4.8,
   cbcdmp   = 0.02,

   exbcfmt  = 3,
 /


 &coriolis_force
   coriopt  = 4,
     earth_curvature = 0,
     coriotrm        = 1,
 /

&turbulence
   tmixopt  = 4,
     trbisotp = 0,
     tkeopt   = 3,
     tmixcst  = 0.0,
     tmixvert = 0,
     prantl   = 0.3300,

   trbvimp  = 1,

   kmlimit  = 1.0,
 /


 &computational_mixing
   cmix2nd = 0,
     cfcm2h  = 0.0,
     cfcm2v  = 4.0e-4,

   cmix4th = 1,
     cfcm4h  = 4.0e-4,
     cfcm4v  = 4.0e-4,

   scmixfctr = 0.8,
   cmix_opt = 3,
```

```
 /


 &divergence_damping
   divdmp    = 2,
     divdmpndh = 0.05,
     divdmpndv = 0.05,
 /


 &rayleigh_damping
   raydmp = 2,
     cfrdmp = 0.00333,
     zbrdmp = 12000.,
 /

 &asselin_time_filter
   flteps = 0.05,
 /
&microphysics
   moist    = 1,
   mphyopt  = 10,
   nmphystp = 1,
   dsdpref  = 1,
    ntcloud   = 1.0e8,
    n0rain  = 8.0e6,
    n0snow  = 3.0e6,
    n0grpl  = 4.0e5,
    n0hail  = 4.0e4,
    rhoice = 500.0,
    rhosnow = 100.0,
    rhogrpl = 400.0,
    rhohail = 913.0,
    alpharain = 0.0,
    alphaice = 0.0,
    alphasnow = 0.0,
    alphagrpl = 0.0,
    alphahail = 0.0,

   graupel_ON = 1,
   hail_ON    = 1,
   MFflg      = 0,

   mpthermdiag = 0,

   cnvctopt = 0,
     confrq   = 120.0,
     kffbfct  = 0.0,
```

```
      kfsubsattrig=0,
      wcldbs   = 0.005,
      qpfgfrq  = 120.0,
      idownd   = 1,

    impfallopt = 1,
    fallopt = 1,

    subsatopt = 0,
      rhsat = 0.98,
      rhsatmin = 0.98,
      dx_rhsatmin = 50000.,
      dx_rhsat100 = 5000.,

 /

&concentration
    ccin   = 0,
    cpoint = 1,
      icc     = 85,
      jcc     = 83,
      kcc     = 2,
      ccstart = 7200,
      ccend   = 10800,
    ccemit = 180000.0,
 /


 &radiation
    radopt  = 2,
      radstgr = 1,
      rlwopt  = 1,
      radshade = 0,
      dtrad   = 600.0,
      raddiag = 0,
 /


 &surface_physics
    sfcphy   = 4,
      landwtr  = 1,
      cdhwtropt= 0,
      cdmlnd   = 3.0e-3,
      cdmwtr   = 1.0e-3,
      cdhlnd   = 3.0e-3,
      cdhwtr   = 1.0e-3,
      cdqlnd   = 2.1e-3,
      cdqwtr   = 0.7e-3,
```

```
   pbldopt  = 2,
     pbldpth0 = 1400.0,
     lsclpbl0 = 0.25,

   tqflxdis = 1,
     dtqflxdis= 200.0,

   smthflx = 0,
     numsmth = 1,

   sfcdiag  = 0,
 /

&soil_ebm
   sfcdat   = 2,
     styp     = 10,
     vtyp     = 4,
     lai0     = 0.31,
     roufns0  = 0.01,
     veg0     = 0.3,

     sfcdtfl                                                          =
'/home/kbrews/osse/static/ar20130520a_03km.sfcdata',
     sfcfmt = 1,

   soilmodel_forced = 0,
     sitemeso = '../../arpsdata.dir/mts.dir/Meso',
     siteflux = '../../arpsdata.dir/mts.dir/Flux',
     siternet = '../../arpsdata.dir/mts.dir/Radd',
     sitesoil = '../../arpsdata.dir/mts.dir/Soil',
     siteveg =  '../../arpsdata.dir/mts.dir/Veg',

   soilmodel_option = 1,
     nzsoil   = 2,
     dzsoil   = 1.0,
     zrefsoil = 0.0,
     tsoilint(1)   =  283.2,
     tsoilint(2)   =  291.2,
     tsoilint(3)   =  293.65,
     tsoilint(4)   =  293.43,
     tsoilint(5)   =  292.76,
     qsoilint(1)   = 0.26,
     qsoilint(2)   = 0.2603,
     qsoilint(3)   = 0.2942,
     qsoilint(4)   = 0.3221,
     qsoilint(5) = 0.2979,
```

```
   soilstrhopt  = 0,
     soildzmin    =     0.01,
     soildlayer1  =     0.0,
     soildlayer2  =     1.0,
     soilstrhtune =     1.0,

soilinit = 3,
     ptslnd0  = 293.0,
     ptswtr0  = 288.0,
     wetcanp0 = 0.00,
     snowdpth0 = 0.0,
     ttprt    = 0.0,
     tbprt    = 0.0,
     wgrat    = 0.7,
     w2rat    = 0.7,

     soilinfl                                                    =
'/scratch/kbrews/GFS_051912z/gfs_2013051912a_03km.soilvar.086400
',
       soilfmt = 3,

   nstyp  = 3,

   tsoil_offset = 0,
   tsoil_offset_amplitude = 2.5,

   dtsfc    = 6.0,

   prtsoilflx = 0,

 /


 &grdtrans
   cltkopt = 0,
     tceltrk = 120.0,
     tcrestr = 1800.0,

   grdtrns = 0,
     chkdpth = 2500.0,
     twindow = 300.0,

   umove   = 0.0,
   vmove   = 0.0,
 /


 &history_dump
```

```
   hdmpopt    = 1,
   dmp_out_joined = 1111111,
   hdmpfmt    = 3,
   grbpkbit   = 16,
   hdfcompr   = 2,

   thisdmp    = 300.0,
   tstrtdmp   = 0.0,

   numhdmp    = 3,
     hdmptim(1) = 0.,
     hdmptim(2) = 3600.,
     hdmptim(3) = 7200.,
 /
&output
   dirname  = '/scratch/vshenoy/ARPS_OSSE/FMU02km108/',
   filcmprs = 0,
   readyfl  = 0,

   basout   = 0,
   grdout   = 0,
   varout   = 1,
   mstout   = 1,
   iceout   = 1,
   tkeout   = 0,
   trbout   = 0,
   rainout  = 1,
   sfcout   = 1,
   landout  = 0,
   prcout   = 1,
   radout   = 0,
   flxout   = 0,

   exbcdmp  = 0,
   exbchdfcompr = 5,
   extdadmp = 0,
     qcexout  = 1,
     qrexout  = 1,
     qiexout  = 1,
     qsexout  = 1,
     qhexout  = 1,
     qgexout  = 1,
     nqexout  = 0,
     zqexout  = 0,

   sfcdmp   = 0,
   soildmp  = 0,
   terndmp  = 0,
```

```
   tfmtprt  = 0.0,
   trstout  = 54000,
   tmaxmin  = 300.0,
   tenergy  = 0.0,

   imgopt   = 0,
     timgdmp  = 60.0,

   pltopt   = 0,
     tplots   = 600.0,
 /
&debug
   lvldbg = 0,
 /
```

Appendix C

Namelist parameters for ADAS

```
&incr_out
    incrdmp = 3,
    incrhdfcompr = 2,

incdmpf='/scratch/vshenoy/ARPS_OSSE/FMU02km108/FMU02km108_ad2013
05201800.incr',
    uincdmp = 1,
    vincdmp = 1,
    wincdmp = 1,
    pincdmp = 1,
    ptincdmp= 1,
    qvincdmp= 1,
    qcincdmp= 1,
    qrincdmp= 1,
    qiincdmp= 1,
    qsincdmp= 1,
    qgincdmp= 0,
    qhincdmp= 1,
    ncincdmp= 0,
    nrincdmp= 0,
    niincdmp= 0,
    nsincdmp= 0,
    ngincdmp= 0,
    nhincdmp= 0,
 /


&adas_const
   npass = 6,
   sprdist = 2000.,
   wlim = 1.E-03,
   zwlim = 1.E-04,
   thwlim = 1.E-04,
   spradopt = 2,
   ccatopt = 0,
 /


 &adjust
   hydradj = 0,
   wndadj = 2,
   obropt = 11,
   obrzero = 20000.,
 /
```

```
&adas_radaropt
   raduvobs = 0,
   radrhobs = 0,
   radistride = 1,
   radkstride = 1,
   refrh = 25.,
   rhradobs = 0.90,

   radcldopt = 0,
   radqvopt = 1,
   radqcopt = 1,
   radqropt = 1,
   radptopt = 1,
   refsat = 25.,
   rhrad = 0.90,
   refcld = 30.,
   cldrad = 0.001,
   ceilopt = 2,
   ceilmin = 1500.,
   dzfill = 3000.,
   refrain = 40.,
   radsetrat = 0.50,
   radreflim = 45.,
   radptgain = 1.1,
 /


&adas_cloud
   cloudopt = 1,
   clddiag = 0,
   cld_files = 0,

   range_cld = 100.0e03,

   refthr1 = 20.0,
   refthr2 = 15.0,
   hgtrefthr = 2000.0,

   thresh_cvr = 0.45,

   bgqcopt = 0,

   cldqvopt = 1,
   rh_thr1 = 0.5,
   cvr2rh_thr1 = 0.2,
   rh_thr2 = 1.00,
   cvr2rh_thr2 = 0.7,
```

```
   cldqcopt = 1,
   qvslimit_2_qc = 1.0,
   cldqropt = 1,
   cldrfopt = 2,
   qrlimit = 0.30,
   frac_qr_2_qc = 0.0,

   cldwopt = 0,
   wmhr_Cu = 0.0005,
   wmhr_Sc = 0.00005,
   wc_St = 0.05,

   cldptopt = 5,
   frac_qw_2_pt = 0.5,
   frac_qc_2_lh = 1.0,
   max_lh_2_pt = 8.0,

   smth_opt = 0,

   nirfiles     = 0,
   ir_fname(1)                                                    =
'/scratch/kbrews/20150424/goes/ad20150424_2345_goes13.satctt.hdf
4',
   ircalname(1) = '/home/kbrews/osse/adas/goes13ch4.adastab',

   nvisfiles    = 0,
   vis_fname(1)                                                   =
'/scratch/kbrews/20150424/goes/ad20150424_2345_goes13.satalb.hdf
4',
   viscalname(1)= '/home/kbrews/osse/adas/goes13vis.adastab',

 /


&adas_typ
   ianxtyp(1) = 21,
   ianxtyp(2) = 21,
   ianxtyp(3) = 21,
   ianxtyp(4) = 21,
   ianxtyp(5) = 21,
   ianxtyp(6) = 21,
   ianxtyp(7) = 21,
   ianxtyp(8) = 21,
 /

 &adas_range
   sfcqcrng = 100.E03,
```

```
  xyrange(1) = 320.E03,
  xyrange(2) = 240.E03,
  xyrange(3) = 160.E03,
  xyrange(4) = 110.E03,
  xyrange(5) = 70.E03,
  xyrange(6) = 40.E03,
  xyrange(7) = 20.E03,
  xyrange(8) = 20.E03,
 /

 &adas_kpvar
  kpvar(1) = 0.9,
  kpvar(2) = 0.9,
  kpvar(3) = 1.0,
  kpvar(4) = 1.0,
  kpvar(5) = 0.9,
 /

 &adas_zrange
  zrange(1) = 200.,
  zrange(2) = 250.,
  zrange(3) = 200.,
  zrange(4) = 150.,
  zrange(5) = 100.,
  zrange(6) =  75.,
  zrange(7) =  75.,
  zrange(8) =  75.,
 /

 &adas_thrng
  thrng(1) = 5.0,
  thrng(2) = 4.0,
  thrng(3) = 3.0,
  thrng(4) = 2.0,
  thrng(5) = 2.0,
  thrng(6) = 2.0,
  thrng(7) = 2.0,
  thrng(8) = 2.0,
 /

&adas_trnrng
  trnropt(1) = 1,
  trnropt(2) = 1,
  trnropt(3) = 1,
  trnropt(4) = 1,
  trnropt(5) = 1,
  trnropt(6) = 1,
  trnropt(7) = 1,
```

```
   trnropt(8) = 1,
   trnrcst(1) = 200.,
   trnrcst(2) = 200.,
   trnrcst(3) = 200.,
   trnrcst(4) = 200.,
   trnrcst(5) = 200.,
   trnrcst(6) = 200.,
   trnrcst(7) = 200.,
   trnrcst(8) = 200.,
   trnrng(1) = 1.8,
   trnrng(2) = 1.8,
   trnrng(3) = 1.8,
   trnrng(4) = 1.8,
   trnrng(5) = 1.8,
   trnrng(6) = 1.8,
   trnrng(7) = 1.8,
   trnrng(8) = 1.8,
 /


 &adas_backerf
   backerrfil = '/home/kbrews/osse/adas/ruc3herr.adastab',
 /


&adas_sng
   nsngfil = 1,

sngfname(1)='/home/kbrews/osse/Obs_OSSE/Meso/201305201800.lso',

sngtmchk(1)='/home/kbrews/osse/Obs_OSSE/Meso/201305201700.lso',

   blackfil='/home/kbrews/osse/static/blacklist.sfc',
   srcsng(1)='MESO',
      sngerrfil(1)='/home/kbrews/osse/adas/mesoerr.adastab',

iusesng(1,1)=0,iusesng(1,2)=0,iusesng(1,3)=1,iusesng(1,4)=1,

iusesng(1,5)=1,iusesng(1,6)=1,iusesng(1,7)=0,iusesng(1,8)=0,
   srcsng(2)='SA',
      sngerrfil(2)='/home/kbrews/osse/adas/saoerr.adastab',

iusesng(2,1)=0,iusesng(2,2)=0,iusesng(2,3)=0,iusesng(2,4)=0,

iusesng(2,5)=0,iusesng(2,6)=0,iusesng(2,7)=0,iusesng(2,8)=0,
   srcsng(3)='AUTO',
      sngerrfil(3)='/home/kbrews/osse/adas/autoerr.adastab',
```

```
iusesng(3,1)=0,iusesng(3,2)=0,iusesng(3,3)=0,iusesng(3,4)=0,

iusesng(3,5)=0,iusesng(3,6)=0,iusesng(3,7)=0,iusesng(3,8)=0,
   srcsng(4)='BUOY',
      sngerrfil(4)='/home/kbrews/osse/adas/buoyerr.adastab',

iusesng(4,1)=0,iusesng(4,2)=0,iusesng(4,3)=0,iusesng(4,4)=0,

iusesng(4,5)=0,iusesng(4,6)=0,iusesng(4,7)=0,iusesng(4,8)=0,
   srcsng(5)='MESOALPN',
      sngerrfil(5)='/home/kbrews/osse/adas/mesoalpnerr.adastab',

iusesng(5,1)=0,iusesng(5,2)=0,iusesng(5,3)=0,iusesng(5,4)=0,

iusesng(5,5)=0,iusesng(5,6)=0,iusesng(5,7)=0,iusesng(5,8)=0,
   srcsng(6)='MESOHYDR',
      sngerrfil(6)='/home/kbrews/osse/adas/mesohydrerr.adastab',

iusesng(6,1)=0,iusesng(6,2)=0,iusesng(6,3)=0,iusesng(6,4)=0,

iusesng(6,5)=0,iusesng(6,6)=0,iusesng(6,7)=0,iusesng(6,8)=0,
   srcsng(7)='MESOMET',
      sngerrfil(7)='/home/kbrews/osse/adas/mesometerr.adastab',

iusesng(7,1)=0,iusesng(7,2)=0,iusesng(7,3)=0,iusesng(7,4)=0,

iusesng(7,5)=0,iusesng(7,6)=0,iusesng(7,7)=0,iusesng(7,8)=0,
   srcsng(8)='MESOROAD',
      sngerrfil(8)='/home/kbrews/osse/adas/mesoroaderr.adastab',

iusesng(8,1)=0,iusesng(8,2)=0,iusesng(8,3)=0,iusesng(8,4)=0,

iusesng(8,5)=0,iusesng(8,6)=0,iusesng(8,7)=0,iusesng(8,8)=0,
   srcsng(9)='MESOTV',
      sngerrfil(9)='/home/kbrews/osse/adas/mesotverr.adastab',

iusesng(9,1)=0,iusesng(9,2)=0,iusesng(9,3)=0,iusesng(9,4)=0,

iusesng(9,5)=0,iusesng(9,6)=0,iusesng(9,7)=0,iusesng(9,8)=0,
   srcsng(10)='NFAWOS',
      sngerrfil(10)='/home/kbrews/osse/adas/nfawoserr.adastab',

iusesng(10,1)=0,iusesng(10,2)=0,iusesng(10,3)=0,iusesng(10,4)=0,

iusesng(10,5)=0,iusesng(10,6)=0,iusesng(10,7)=0,iusesng(10,8)=0,
   srcsng(11)='MOPED',
      sngerrfil(11)='/home/kbrews/osse/adas/mopederr.adastab',
```

```
iusesng(11,1)=0,iusesng(11,2)=0,iusesng(11,3)=0,iusesng(11,4)=0,

iusesng(11,5)=0,iusesng(11,6)=0,iusesng(11,7)=0,iusesng(11,8)=0,
   srcsng(12)='AMATSFC',
      sngerrfil(12)='/home/kbrews/osse/adas/amatsfcerr.adastab',

iusesng(12,1)=0,iusesng(12,2)=0,iusesng(12,3)=0,iusesng(12,4)=0,

iusesng(12,5)=0,iusesng(12,6)=0,iusesng(12,7)=0,iusesng(12,8)=0,
 /


 &adas_ua
   nuafil = 2,

uafname(1)='/home/kbrews/osse/Obs_OSSE/FNL/FNL_201305201800.fnl'

uafname(2)='/home/kbrews/osse/Obs_OSSE/UAV02km108/UAV02km108_201
305201800.uav'
   srcua(1)='OU_UAV',
      uaerrfil(1)='/home/kbrews/osse/adas/OU_UAVerr.adastab',
      iuseua(1,1)=0,iuseua(1,2)=0,iuseua(1,3)=1,iuseua(1,4)=1,
      iuseua(1,5)=1,iuseua(1,6)=1,iuseua(1,7)=0,iuseua(1,8)=0,
   srcua(2)='GFS_FNL',
      uaerrfil(2)='/home/kbrews/osse/adas/GFS_FNLerr.adastab',
      iuseua(2,1)=1,iuseua(2,2)=1,iuseua(2,3)=1,iuseua(2,4)=0,
      iuseua(2,5)=0,iuseua(2,6)=0,iuseua(2,7)=0,iuseua(2,8)=0,
   srcua(3)='MCLASS',
      uaerrfil(3)='/home/kbrews/osse/adas/mclasserr.adastab',
      iuseua(3,1)=1,iuseua(3,2)=1,iuseua(3,3)=0,iuseua(3,4)=0,
      iuseua(3,5)=0,iuseua(3,6)=0,iuseua(3,7)=0,iuseua(3,8)=0,
   srcua(4)='WPDN PRO',
      uaerrfil(4)='/home/kbrews/osse/adas/wpdnerr.adastab',
      iuseua(4,1)=1,iuseua(4,2)=1,iuseua(4,3)=0,iuseua(4,4)=0,
      iuseua(4,5)=0,iuseua(4,6)=0,iuseua(4,7)=0,iuseua(4,8)=0,
   srcua(5)='BLPROF',
      uaerrfil(5)='/home/kbrews/osse/adas/blproferr.adastab',
      iuseua(5,1)=1,iuseua(5,2)=1,iuseua(5,3)=0,iuseua(5,4)=0,
      iuseua(5,5)=0,iuseua(5,6)=0,iuseua(5,7)=0,iuseua(5,8)=0,
 /

&adas_radar
   grdtlt_flag = 0,
   nradfil = 0,
   radfname(1)                                                    =
'/scratch/kbrews/20150424/adas/KFDR.20150424.2354.hdf4',
```

```
   radfname(2)                                                      =
'/scratch/kbrews/20150424/adas/KFWS.20150424.2355.hdf4',
   radfname(3)                                                      =
'/scratch/kbrews/20150424/adas/KGRK.20150424.2352.hdf4',
   radfname(4)                                                      =
'/scratch/kbrews/20150424/adas/KSHV.20150424.2352.hdf4',
   radfname(5)                                                      =
'/scratch/kbrews/20150424/adas/XADD.20150424.2355.hdf4',
   radfname(6)                                                      =
'/scratch/kbrews/20150424/adas/XMDL.20150424.2355.hdf4',
   radfname(7)                                                      =
'/scratch/kbrews/20150424/adas/XUTA.20150424.2355.hdf4',
   bmwidth = 1.0, 1.0, 1.0, 1.0, 2.0, 2.0, 2.0,
   srcrad(1)='88D-AII',
      raderrfil(1)='/home/kbrews/osse/adas/rad88Derr.adastab',

iuserad(1,1)=0,iuserad(1,2)=1,iuserad(1,3)=0,iuserad(1,4)=0,

iuserad(1,5)=0,iuserad(1,6)=0,iuserad(1,7)=0,iuserad(1,8)=0,
   srcrad(2)='88D-NIDS',
      raderrfil(2)='/home/kbrews/osse/adas/radnidserr.adastab',

iuserad(2,1)=0,iuserad(2,2)=0,iuserad(2,3)=0,iuserad(2,4)=0,

iuserad(2,5)=0,iuserad(2,6)=0,iuserad(2,7)=0,iuserad(2,8)=0,
   srcrad(3)='CASA-IP1',
      raderrfil(3)='/home/kbrews/osse/adas/radcasaerr.adastab',

iuserad(3,1)=0,iuserad(3,2)=0,iuserad(3,3)=0,iuserad(3,4)=0,

iuserad(3,5)=0,iuserad(3,6)=0,iuserad(3,7)=0,iuserad(3,8)=0,
   srcrad(4)='TDWR',
      raderrfil(4)='/home/kbrews/osse/adas/radtdwrerr.adastab',

iuserad(4,1)=0,iuserad(4,2)=0,iuserad(4,3)=0,iuserad(4,4)=0,

iuserad(4,5)=0,iuserad(4,6)=0,iuserad(4,7)=0,iuserad(4,8)=0,
   srcrad(5)='88D-POL',
      raderrfil(5)='/home/kbrews/osse/adas/rad88dperr.adastab',

iuserad(5,1)=0,iuserad(5,2)=0,iuserad(5,3)=0,iuserad(5,4)=0,

iuserad(5,5)=0,iuserad(5,6)=0,iuserad(5,7)=0,iuserad(5,8)=0,
 /


 &adas_retrieval
   nretfil = 0,
```

```
   retfname(1) = 'KTLXret.960526.1700',
   srcret(1)='88D-RET',
      reterrfil(1)='/home/kbrews/osse/adas/ret88Derr.adastab',

iuseret(1,1)=0,iuseret(1,2)=0,iuseret(1,3)=0,iuseret(1,4)=0,

iuseret(1,5)=0,iuseret(1,6)=0,iuseret(1,7)=0,iuseret(1,8)=0,
 /
```